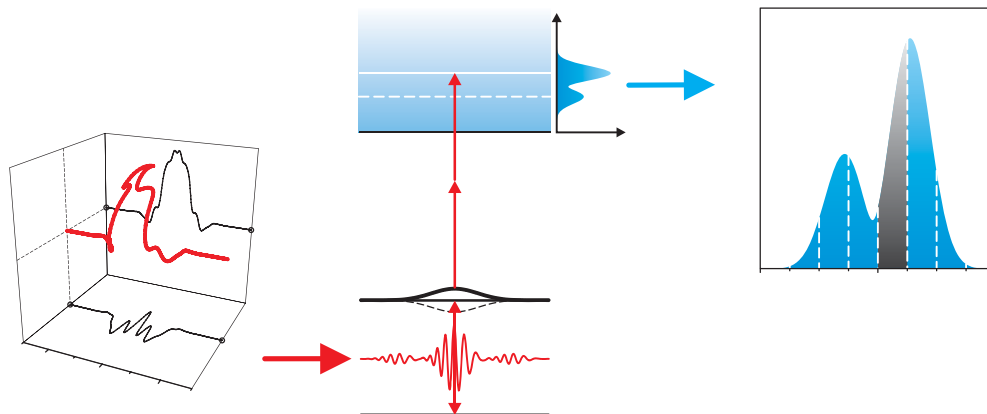


Adaptive Polarization Pulse Shaping and Modeling of Light–Matter Interactions with Neural Networks



Dissertation zur Erlangung des
naturwissenschaftlichen Doktorgrades der
Julius–Maximilians-Universität
Würzburg

vorgelegt von
Reimer Andreas Selle
aus Hof

Würzburg 2007

Eingereicht am: 16. November 2007
bei der Fakultät für Physik und Astronomie

1. Gutachter: Prof. Dr. T. Brixner
2. Gutachter: Prof. Dr. G. Gerber
der Dissertation

1. Prüfer: Prof. Dr. T. Brixner
2. Prüfer: Prof. Dr. J. Geurts
3. Prüfer: Prof. Dr. W. Kinzel
im Promotionskolloquium

Tag des Promotionskolloquiums: 19.12.2007

List of Publications

T. Brixner, C. Dietl, G. Krampert, P. Niklaus, E. Papastathopoulos, T. Pfeifer, R. Selle, G. Vogt, D. Walter, C. Winterfeldt and G. Gerber,
Adaptive femtosecond quantum control,
In F. Krausz, G. Korn, P. Corkum and I. A. Walmsley (Eds.), *Ultrafast Optics IV*,
Volume 95 of *Springer Series in Optical Sciences*, pp.119–128, Springer, Berlin (2004).

T. Brixner, G. Krampert, T. Pfeifer, R. Selle and G. Gerber,
M. Wollenhaupt, O. Graefe, C. Horn, D. Liese, and T. Baumert,
Quantum control by ultrafast polarization shaping,
Phys. Rev. Lett **92**[20], 208301-1–208301-4 (2004).

T. Brixner, G. Krampert, T. Pfeifer, R. Selle and G. Gerber,
M. Wollenhaupt, O. Graefe, C. Horn, D. Liese, and T. Baumert,
Adaptive polarization control of molecular dynamics,
In T. Kobayashi, T. Okada, T. Kobayashi, K. A. Nelson and S. DeSilvestri (Eds.),
Ultrafast Phenomena XIV,
Volume XX of *Springer Series in Chemical Physics*, Springer, Berlin (2005).

G. Vogt, P. Nuernberger, R. Selle, F. Dimler, T. Brixner, and G. Gerber,
Analysis of femtosecond quantum control mechanisms with colored double pulses,
Phys. Rev. A **74**, 033413-1–033413-8 (2006).

P. Nuernberger, G. Vogt, R. Selle, S. Fechner, T. Brixner, and G. Gerber,
Generation of femtosecond pulse sequences in the ultraviolet by spectral phase modulation,
In J. T. Sheridan, and F. Wyrowski (Eds.), *Photon Management II*,
Proceedings of SPIE 6187, No. 22, pp.151-162 (2006)

P. Nuernberger, G. Vogt, R. Selle, S. Fechner, T. Brixner, and G. Gerber,
Generation of shaped ultraviolet laser pulses at the third harmonic of titanium–sapphire femtosecond laser radiation,
Appl. Phys. B **88**, 519–526 (2007).

R. Selle, G. Vogt, T. Brixner, G. Gerber, R. Metzler and W. Kinzel
Modeling of light–matter interactions with neural networks,
Phys. Rev. A 76, 023810-1–023810-7 (2007).

R. Selle, T. Brixner, T. Bayer, M. Wollenhaupt and T. Baumert
Modeling of ultrafast coherent strong-field dynamics in potassium with neural networks,
submitted (2007).

R. Selle et al.
Femtosecond polarization pulse shaping in the ultraviolet,
in preparation.

Contents

List of Publications	i
1 Introduction	1
2 Quantum control of light–matter interactions	5
2.1 Introduction	5
2.2 Single–parameter control	6
2.3 Optimal control theory	9
2.4 Adaptive quantum control	11
3 Technological concepts	15
3.1 Mathematical description of femtosecond laser pulses	15
3.2 Generation of femtosecond laser pulses	20
3.3 Frequency conversion	23
3.3.1 Second–order nonlinear optical effects	24
3.3.2 Frequency doubling of shaped laser pulses	28
3.4 Femtosecond laser pulse shaping	30
3.4.1 Phase–only pulse shaping	32
3.4.2 Polarization laser pulse shaping	34
3.5 Laser pulse characterization	46
3.5.1 FROG and XFROG	46
3.5.2 Spectral interferometry	52
3.6 Joint time–frequency representations	56
4 Quantum control by ultrafast polarization shaping	59
4.1 Introduction	59
4.2 Ionization pathways and dynamics in the potassium dimer	60
4.3 Pump–probe experiments with varying polarization configurations	64
4.4 Quantum control of K_2	67
4.5 Conclusion	72
5 Polarization shaping in the UV	73
5.1 Introduction	73
5.2 Experimental implementation	75

5.2.1	The polarization pulse shaper	77
5.2.2	Dual–channel spectral interferometry	78
5.2.3	Characterization of the reference pulse	80
5.3	Results and discussion	81
5.4	Conclusions	86
6	Analysis of femtosecond quantum control mechanisms with double pulses	87
6.1	Introduction	87
6.2	Generation of double pulses	90
6.3	Interpretation of control mechanisms with fitness landscapes	90
6.3.1	Experimental setup	91
6.3.2	Results and discussion	92
6.4	Analysis of the intrapulse dumping mechanism	95
6.4.1	Experimental setup	96
6.4.2	Results and discussion	97
6.5	Conclusion	100
7	Modeling of light–matter interactions with neural networks	103
7.1	Introduction	103
7.2	Neural networks	105
7.3	Modeling of SHG and molecular fluorescence with neural networks	107
7.3.1	SHG simulation	107
7.3.2	Experimental implementation	109
7.3.3	Input parametrization and network architecture	112
7.3.4	Results and discussion	116
7.4	Modeling of coherent strong–field dynamics with neural networks	119
7.4.1	Simulation of the physical system	121
7.4.2	Input parametrization and network architecture	122
7.4.3	Results and discussion	123
7.5	Conclusion	128
8	Summary	131
9	Zusammenfassung	135
	Bibliography	138
	Acknowledgements	159
	Lebenslauf	163

Chapter 1

Introduction

God said:

$$\begin{aligned}\mathcal{L} &= \frac{1}{4}F_{\mu\nu}F^{\mu\nu}, \\ \nabla \cdot \mathbf{D} &= \rho, \\ \nabla \cdot \mathbf{B} &= 0, \\ \nabla \times \mathbf{E} + \frac{\partial \mathbf{B}}{\partial t} &= 0, \\ \nabla \times \mathbf{H} &= \mathbf{J} + \frac{\partial \mathbf{D}}{\partial t}.\end{aligned}$$

Let there be light!

The presence of light, and hence warmth and energy, is one of the prerequisites for life on Earth. Guided by evolution, nature developed molecules, cells and organisms that can harvest the plentiful energy offered by our star, the Sun, with an astonishing efficiency that is possibly matched only by their resilience to photophysical damage.

With the invention of the laser, the chemists' dream to investigate, initiate and control chemical reactions on the molecular scale seemed to come within grasp. However, the true beginnings of the realization of this dream had to wait until the time when the boundaries on the duration of laser pulses were pushed into the picosecond to femtosecond regime, the natural timescale of nuclear motions, i.e., vibrations and rotations in molecules. While such light sources allowed, for the first time, the direct observation of molecular dynamics, the breakthrough for the control of physical or chemical processes on the atomic or molecular scale came with the advent of pulse shaping techniques that made it possible to modify these ultrashort pulses, and hence to adapt them to the involved dynamics.

Especially the adaptive shaping of femtosecond laser pulses met great success, as the control over a variety of physical and chemical processes, such as the bond-selective dissociation or isomerization of molecules were successfully demonstrated with this method. It is intriguing that – just as nature adapted its molecules and more complex structures to the present natural light sources by evolution – it should be evolutionary algorithms that were most successful in adapting the artificial, coherent light of lasers to the dynamics of molecules, the building blocks of cells and organisms. While the shaping of ultrashort laser pulses and the adaptive optimization of physical or chemical processes have become well-established techniques, these fields still hold a variety of fascinating possibilities, opportunities, and challenges.

One of the most puzzling chemical aspects of life is that it is chiral. Biologically important molecules, such as amino acids and proteins, appear in only one geometrical configuration in nature, while their mirror-symmetric partners are absent. In artificial synthesis reactions however, both configurations (so-called enantiomers) of these molecules can be produced. As the tragic events surrounding thalidomide, a molecule used during the late 1950s and early 1960s in medicaments for pregnant women, illustrate, the ‘wrong’ enantiomer can have devastating effects on biological systems, in this case genetic damage to embryos. The enantiomer-selective production of chiral molecules, and the transformation of one enantiomer into its mirror image, remains one of the most challenging tasks for stereochemistry. It has been shown theoretically that the control over the time-dependent polarization state of laser pulses can be a crucial ingredient for achieving this goal in photochemical reactions. A part of this thesis is dedicated to one of the first adaptive polarization-control experiments on a molecular system, the potassium dimer, using near-infrared polarization-shaped laser pulses. A novel technique that allows the generation and characterization of polarization-shaped femtosecond laser pulses in the ultraviolet (UV) spectral range is also introduced. It is this spectral range, where a majority of organic molecules of chemical and/or biological relevance have their strongest absorption bands. This technique can be seen as another step in the direction of efficient selective control of stereochemical reactions in general, and of enantiomer-selective processes in particular.

Although it was possible to attain control over an impressive number of processes and reactions over the last ten years by adaptive optimization, the illumination of the control mechanisms and reaction pathways involved remains a formidable challenge. This challenge, known as the problem of inversion, is addressed in this thesis with systematic parameter scans and experimentally measured control landscapes.

The possibility to generate almost arbitrary electric fields with femtosecond pulse shapers also opens up possibilities apart from the optimal control of physical or chemical processes. With shaped laser pulses it is possible to experimentally measure the response of quantum systems to a large variety of electric fields, and thus it is possible to obtain a significant amount of information on the involved light-matter interaction that is not available with ordinary, unshaped laser pulses. Neural networks are introduced in this thesis as a method to evaluate this information, with the goal of obtaining

effective models for light–matter interactions.

This thesis is organized as follows. After this introduction, the theoretical basis for quantum control is detailed in chapter 2. The technological concepts that are needed for the understanding and implementation of experiments utilizing shaped femtosecond laser pulses are presented in chapter 3. They encompass the mathematical description and experimental generation of ultrashort laser pulses as well as their frequency conversion using nonlinear optical effects. Special emphasis is laid on the shaping of femtosecond laser pulses and the experimental characterization of these laser pulses. The technique of ultrafast polarization shaping introduced therein is applied to a model quantum system, the potassium dimer, in chapter 4. The polarization dependence of the multiphoton ionization dynamics in this molecule is first investigated in pump–probe experiments, and it is then more generally addressed and exploited in an adaptive quantum control experiment utilizing near–IR polarization–shaped laser pulses. The extension of these polarization shaping techniques to the UV spectral range is presented in chapter 5, where methods for the generation and characterization of polarization–shaped laser pulses in the UV are introduced. Chapter 6 is dedicated to the investigation and interpretation of control mechanisms based on experimental fitness landscapes obtained by systematic scans of double–pulse sequences. This concept is first introduced and illustrated for an optical demonstration experiment, and it is then applied for the analysis of the intrapulse dumping mechanism that is observed in the excitation of a large dye molecule in solution with ultrashort laser pulses. In chapter 7 shaped laser pulses are employed as a means for obtaining copious amounts of data on light–matter interactions. Neural networks are introduced as a novel tool for generating computer–based models for these interactions from the accumulated data. The viability of this approach is first tested for second harmonic generation (SHG) and molecular fluorescence processes. Neural networks are then utilized for modeling the far more complex coherent strong–field dynamics of potassium atoms. Finally, this work is summarized in chapter 8.

Chapter 2

Quantum control of light–matter interactions

The shaping of ultrafast laser pulses, and especially their application in the context of the adaptive control of quantum–mechanical systems, is of central concern for this thesis. In this chapter, the theoretical concepts used in quantum control are briefly introduced, from single–parameter control schemes and optimal control theory to adaptive quantum control.

2.1 Introduction

The advent of femtosecond (fs) laser systems allowed for the first time time–resolved studies of atomic processes and molecular dynamics and reactions [1, 2]. Moreover, these new light sources revived the dream to not only monitor, but to actively control these processes and reactions. Already shortly after the invention of lasers it was conceived that intensive narrowband laser radiation, tuned to match molecular vibrational resonances, could be used to selectively excite the vibrational mode of one particular chemical bond. It was hoped that by resonant absorption of several photons, the vibrational amplitude could be sufficiently increased so that the selected bond could be efficiently broken [3]. However, it turned out that in most molecules the energy would redistribute to other vibrational modes on a very short time scale due to the couplings between the vibrational modes. This process, known as ‘intramolecular vibrational energy redistribution’ (IVR) [4–6], limits the selectivity to such an extent that in many molecules predominantly the weakest bond would break, although a different, stronger bond was originally selectively excited. Therefore, this ‘mode selective chemistry’ remains limited to very few molecular systems. Another approach to steer molecular reactions by applying suitable light–fields aims to overcome or circumvent potential energy barriers in order to reach a desired product state. This method is again of limited applicability, as the molecular potential energy surfaces (PES) involved tend to be

rather complex. In general, these PES depend on the coordinates of all atoms of the molecule, and usually several reaction coordinates play a role in the progress of the reaction, which in turn means that the photoinduced reaction will not necessarily lead to the desired outcome. However, both IVR and the quantum–mechanical evolution of the involved states or wave–packets have a coherent character when induced by laser radiation, and can therefore be influenced and controlled by interference effects. Instead of using the obtainable spectral narrowness of laser radiation, this opens up the possibility to exploit the coherent properties of laser radiation for achieving the desired controllability. The aim of this ‘quantum control’ approach is to manipulate the temporal and/or spectral properties of the coherent light field in such a way, that an initial quantum–mechanical state is transferred into a desired final state. Various techniques for achieving this goal have been developed both theoretically and experimentally in recent years, which will be presented in the following sections.

2.2 Single–parameter control

The beginnings of the emerging field of quantum control was marked by three different approaches, which are shown schematically in Fig. 2.1 for some prototype systems. At first glance, the concepts involved seem to be very different, as they make use of different aspects of the coherent light–matter interaction. However, they have in common that they all rely on quantum–mechanical interference effects [7,8] to achieve control over the processes involved.

The phase–control scheme proposed by Brumer and Shapiro [9, 10] is based on exploiting interference effects between multiple excitation pathways in the frequency domain. It was first experimentally realized in 1989 on atoms and later also in small to medium–sized molecules [11–14]. In the model system depicted in Fig. 2.1(a), the ground state is coupled to degenerate final states $|\Psi\rangle$, $|\Psi'\rangle$ via two multi–photon transitions of different order, e.g., a one–photon transition (frequency 3ω) and a three–photon transition (frequency ω), which can be driven by continuous wave lasers. By tuning the relative phase between the ω and 3ω radiation, constructive or destructive interference between the probability amplitudes of the two degenerate final states can be achieved. By including all the different excitation pathways accessible with the broad spectra of ultrashort laser pulses, this intuitive scheme can be extended to experiments with pulsed lasers. A very illustrative example for this is the coherent control of the two–photon excitation of caesium atoms by the group of Y. Silberberg [15, 16]. They have shown both theoretically and experimentally that by a suitable choice of the spectral phase function, laser pulses can be generated that either do not excite the system at all (due to destructive interference) or have the same excitation efficiency as transform limited pulses – with a substantially lower peak intensity.

The second control scheme, known as pump–dump, was first introduced by Tannor,

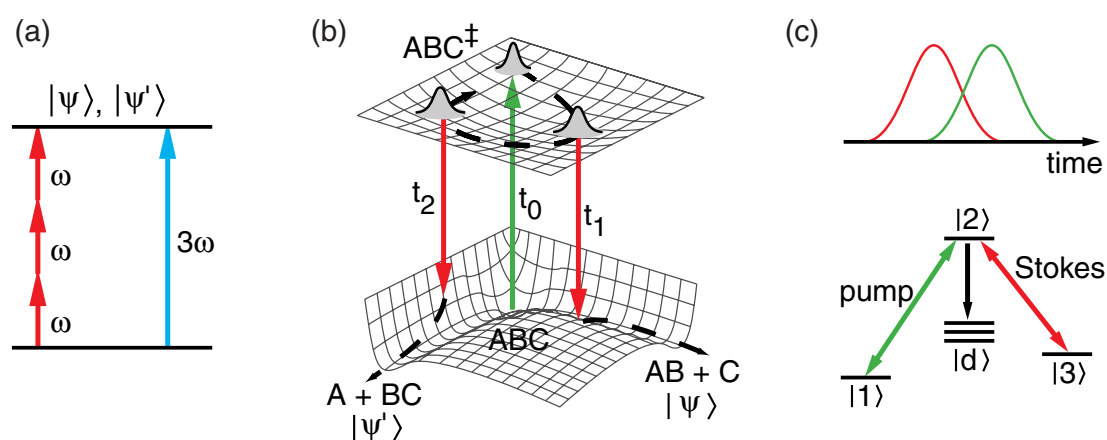


Figure 2.1: Simple quantum control schemes. The Brumer–Shapiro phase–control mechanism (a) exploits interference by coupling the initial and final states via a one–photon and three–photon transition. By varying the relative phase between the ω and 3ω radiation, selectivity in the population of the degenerate final states can be achieved. The Tannor–Kosloff–Rice pump–dump scheme (b) makes use of the coherent wave–packet evolution after an ultrashort excitation laser pulse to dump the wave–packet after a suitable time delay preferentially into one of the accessible exit channels. The STIRAP technique (c) by Bergmann and coworkers transfers the population from the initial state $|1\rangle$ to the final state $|3\rangle$ via the intermediate state $|2\rangle$ with a counter–intuitive sequence of nanosecond laser pulses. Thereby the transient population in state $|2\rangle$ remains zero throughout the process, and thus losses to dissipative channels $|d\rangle$ are avoided.

Kosloff and Rice [17, 18], and makes explicit use of the time–evolution of molecular vibrational wave–packets. As an example for this scheme, consider a molecule consisting of atoms A, B, and C, which can dissociate either into $A + BC$ or $AB + C$ (see Fig. 2.1(b)). After interaction with an ultrafast pump pulse at an initial time t_0 , and the resulting coherent superposition of several eigenstates, a vibrational wave–packet is created on the excited–state surface, where it will evolve freely with time. By applying a second laser pulse, the wave–packet can be transferred (or dumped) back onto the ground state. By choosing the time delay between the two laser pulses in such a way that the wave–packet is centered above one of the possible reaction channels, it is then possible to drive the molecule into the desired dissociative final state. Apart from this time delay, the wavelengths of the pump and dump pulses must be chosen appropriately, so that they match the energy difference between the involved points (or regions) of the potential energy surfaces, and of course the desired region on the excited state surface has to be accessible by the wave–packet dynamics. This technique has been experimentally demonstrated in the photo–dissociation of small molecules [19–21]. Not only the dumping of the wave–packet back to the ground state, but also a further excitation to higher–lying potential energy surfaces is feasible, in which case the process is termed pump–repump. The wave–packet will then also evolve for some time, until it decays back to lower lying potential energy surfaces and finally to some product state. It has been shown by Logunov et al. that this opens another possibility for influencing the molecular dynamics in a desired way [22]. A factor that limits the efficiency and applicability of the pump–dump method lies in the spreading of wave–packets due to the different temporal evolution of the various eigenstates that constitute the wave–packet. This spreading often leads to complex amplitude distributions that have little Franck–Condon overlap with the desired final state, resulting in a reduced selectivity. Chirped excitation and wave–packet revivals [23–25] can be utilized to influence or counter the effects of the wave–packet spreading.

Another control scheme, known as stimulated Raman adiabatic passage (STIRAP) has been proposed and experimentally demonstrated by Bergmann and coworkers [26, 27]. They applied nanosecond lasers for achieving non–dissipative population transfer in Λ –type systems. Such a Λ –type system consists of two states $|1\rangle$ and $|3\rangle$, coupled via a third, higher–lying state $|2\rangle$, as depicted in Fig. 2.1(c). Intuitively one would apply a laser pulse sequence that first transfers population from state $|1\rangle$ to the intermediate state $|2\rangle$ with a pump pulse, which is then transferred to state $|3\rangle$ by a second laser interaction, the Stokes pulse. However, if the intermediate state is coupled to dissipative loss channels $|d\rangle$, a complete population transfer to state $|3\rangle$ cannot be achieved with this procedure. It turns out that applying the laser pulses in a counter–intuitive sequence, where the Stokes pulse precedes the pump pulse, 100% population transfer can be achieved, provided that the two pulses have an optimal temporal overlap. Concerning the transient population in the intermediate state $|2\rangle$, there are two

light-driven contributions: a population increase related to the pump pulse, and a population depletion due to the Stokes pulse. With the counter-intuitive pulse sequence it is possible to transfer the population to state $|3\rangle$ in the temporal window where both pulses overlap, while the net population in state $|2\rangle$ remains zero throughout the process.

2.3 Optimal control theory

The rather simple control schemes presented in the previous section rely on the variation of only a few parameters, e.g., spectral phase or the time delay between two laser pulses, to achieve control over quantum mechanical processes. Furthermore, they focus solely on either the spectral or the temporal properties of laser radiation. While these methods have been very successful in the control of small molecular or atomic systems, their extension to more complex systems is often problematic. More advanced control schemes, which combine and utilize all aspects of coherent light-matter interactions to achieve selective control were developed in the 1980s by theoreticians.

The idea to employ light fields shaped both in the frequency and time domain that are tailored to the specific dynamics of a given optimization problem was first put forward by Tannor and Rice [17, 18], who used variational calculus to obtain an electric field that optimizes the outcome of the studied process. Since the time scale of molecular vibrations and many chemical reactions lies in the femtosecond to picosecond range, the shaping of femtosecond laser pulses, which will be covered in the next chapter, is the experimental tool of choice for realizing the control schemes presented in this section.

A more general theoretical approach, known as “optimal control theory” (OCT) was introduced by Rabitz and coworkers [28, 29], and independently Kosloff and coworkers [30]. The aim of OCT is to find an electric field that drives a quantum-mechanical system from an initial state $|\psi_0\rangle = |\psi(t=0)\rangle$ to a desired final state $|\psi_T\rangle$ at time t_f with maximum efficiency. Mathematically, this corresponds to the maximization of the functional J given by

$$J = |\langle \psi(t=t_f) | \psi_T \rangle|^2, \quad (2.1)$$

under the constraint that the wave-function of the quantum-mechanical system fulfills the Schrödinger equation

$$i\hbar \frac{\partial}{\partial t} |\psi(t)\rangle = H(t) |\psi(t)\rangle \quad (2.2)$$

at all times during the process. The time-dependent Hamiltonian $H(t)$ can be decomposed into H_0 , the time-independent Hamiltonian of the free, unperturbed system, and

the interaction Hamiltonian $H_I(t)$:

$$H(t) = H_0 + H_I(t). \quad (2.3)$$

$H_I(t)$ contains the light–matter interaction, which is given in the dipole approximation by the scalar product $-\boldsymbol{\mu}(t) \cdot \mathbf{E}(t)$ of the dipole moment vector $\boldsymbol{\mu}(t) = e\mathbf{r}(t)$ and the electric field vector $\mathbf{E}(t)$ (vectors are henceforth written in bold script). As the temporal development of the quantum–mechanical system depends on this scalar product, the control goal (Eq. 2.1) is a functional of the electric field $\mathbf{E}(t)$. By inspecting the interaction Hamiltonian it becomes clear that it is possible to reach the control objective by optimizing the temporal evolution (i.e., the momentary frequency and phase) of the electric field, as this allows to control the time–dependent amplitudes and relative phases of the involved transient states that are coupled via dipole moments. If the intensity of the electromagnetic light field is high enough, the laser pulse can also deform the potential energy surfaces by Stark shifting, thereby influencing both the propagation of wave–packets and the energy gaps between the states. Moreover, as both $\boldsymbol{\mu}(t)$ and $\mathbf{E}(t)$ are vectorial quantities, it is apparent that the polarization of the electric field can significantly influence the outcome of a given process. In recent years it has been shown by Brumer, Shapiro and coworkers [31, 32], by Bychkov et al. [33] and by Fujimura, Manz and coworkers [34–36] that the manipulation of the polarization state of the control field is a crucial ingredient for achieving selectivity in chiral systems. Chapters 3.4.2 and 5 deal with the questions how such time–dependent polarization profiles can be generated in the near–IR, and how they can be transferred to the visible/UV spectral range.

The problem of maximizing the functional J (Eq. 2.1) while satisfying the Schrödinger equation (Eq. 2.2) can be solved by applying the technique of Lagrange multipliers. Further constraints, like finite energy and spectrum of the control field, can be incorporated by introducing additional “cost functionals”. The maximization of the sum of all these functionals (to which the cost functionals contribute with a negative sign) can be achieved by variational methods and by solving the resulting coupled nonlinear differential equations numerically in a self–consistent iterative calculation.

While optimized control fields can now in principle be calculated with OCT, several issues – both of theoretical and experimental nature – remain that limit the practicality of this method. One problem is that OCT requires precise knowledge of the molecular Hamiltonian and the potential energy surfaces involved. However, the considerable computational effort and the finite numerical accuracy and stability limit *ab initio* calculations to small systems containing up to three or four atoms to date. To make calculations for more complex systems feasible, approximations and simplifications are necessary. For example, only a few reaction coordinates might be taken into account for the exact quantum–mechanical calculation instead of the complete set of variables. Other degrees of freedom, such as solvate–solvent interactions are treated classically as couplings to ‘bath modes’. However, the group of S.A. Rice has shown

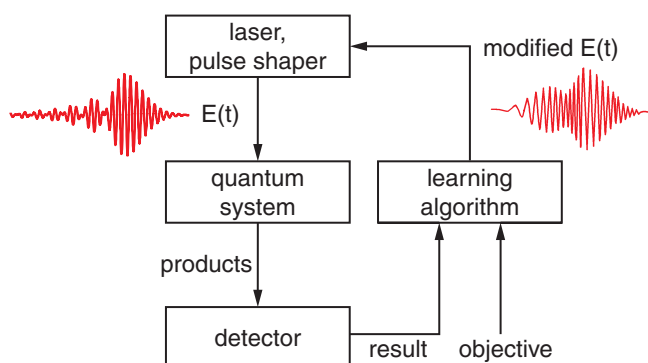


Figure 2.2: Closed-loop adaptive quantum control. The quantum system is excited by shaped femtosecond laser pulses provided by the combination of a femtosecond laser system and a pulse shaper. The resulting photoproduct yields of the photophysical or photochemical process are monitored by suitable detectors. This information is used by a learning algorithm to iteratively improve the pulse shape according to the specified control objective.

that such simplifications and approximations alter the resulting control field significantly [37]. They performed calculations with a varying degree of approximation on the rather small molecular system HCN, and its isomerization reaction $\text{HCN} \rightarrow \text{CNH}$. The results of these calculations show that the shape of the control field changes substantially with increasing system complexity, which leads to the conclusion that it is rather unlikely that control fields calculated for approximated systems will achieve the desired control in actual experiments [37]. Beside these difficulties encountered in calculating the optimal pulse shapes, additional problems arise for their experimental implementation, as it is almost impossible to exactly realize the conditions assumed for the calculations (e.g., focusing conditions, spectrum and duration of the laser pulse, etc.). Further unavoidable modifications of the pulse shape, e.g., due to the pixelation of the pulse shaper or material dispersion, will make it unlikely that the calculated electric field can be reproduced exactly at the point of the experiment. A related problem is the difficulty, or even impossibility, to fully characterize the light field exactly at the position where the experiment takes place.

2.4 Adaptive quantum control

An approach to quantum control that circumvents the aforementioned problems of OCT was put forward in 1992 by Judson and Rabitz in their work “Teaching lasers to control molecules” [38]. Instead of first calculating the optimal control field and then applying it in an experiment, they suggested to guide the search for the optimal control field with the experimental response of the investigated system to electric fields applied

to it. This can be achieved by employing learning algorithms that iteratively improve the pulse shape in a closed–loop scheme, as depicted in Fig. 2.2. A pulse shaper is used to generate modulated trial electric fields which interact with the quantum system. The outcome of the photoinduced process is monitored with suitable detection methods that are sensitive to observables related to the desired control objective. The trial fields and their corresponding detector signals – henceforth referred to as ‘feedback’ – are then entered into a learning algorithm, which iteratively generates new trial fields that are potentially better adapted to the given control objective.

As learning algorithms, simulated annealing [39] and evolutionary algorithms (EA) [40, 41] have been applied in closed–loop control experiments. The advantages and disadvantages of various optimization methods are discussed in Ref. [42].

The adaptive optimizations described in this work have been carried out using an EA that will briefly be described here. More detailed information can be found in the dissertations by Seyfried [42] and Brixner [43] and in Ref. [44]. EAs were originally developed as global search algorithms for solving optimization problems in engineering and were inspired by the evolutionary process in nature. Depending on the implementation, EAs can be classified as genetic algorithms, evolutionary strategies or a mixture of both. Characteristic features of genetic algorithms are the binary representation of the ‘genes’, i.e., the variables encoding the properties of a trial individual, and the application of crossover as the primary tool for generating individuals that are better adapted to achieving the desired objective. On the other hand, evolutionary strategies use a floating point representation of the genes and focus on mutation as source for evolutionary progress. The EA used here is a mixture of both approaches, employing floating point genes and both mutation and crossover as means for generating new trial pulses. The algorithm, depicted in Fig. 2.3, starts out with an initial population of individuals, which differ in their genes, i.e., the voltages applied to the pixels of an LCD pulse shaper. The individuals of the first generation of the optimization can either be randomly selected, or might consist of first guesses for the probable solution, provided there is enough information available. In cases where such guesses are not available and random pulses have a too low signal–to–noise ratio, it is also possible to start the evolution from an unmodulated pulse shape and mutations thereof. The electric field generated by each individual is then applied to the quantum system, and the feedback signals are recorded. From these signals, a ‘fitness’ value is calculated according to a user–specified control objective, which serves as an indicator for how well each individual is adapted to reaching the control objective. In analogy to ‘survival of the fittest’, the best individuals are kept (i.e., cloned) in the next generation of individuals. The remainder of the new population is generated by mutating the genes of an individual and/or by crossover of two individuals, which results in new individuals that inherit parts of the genetic code of each ‘parent’. Again, the fittest individuals are selected for crossover or mutation. This procedure is repeated until an optimal solution for the user defined control task is reached.

The question whether the found optimum is global or local in nature cannot be an-

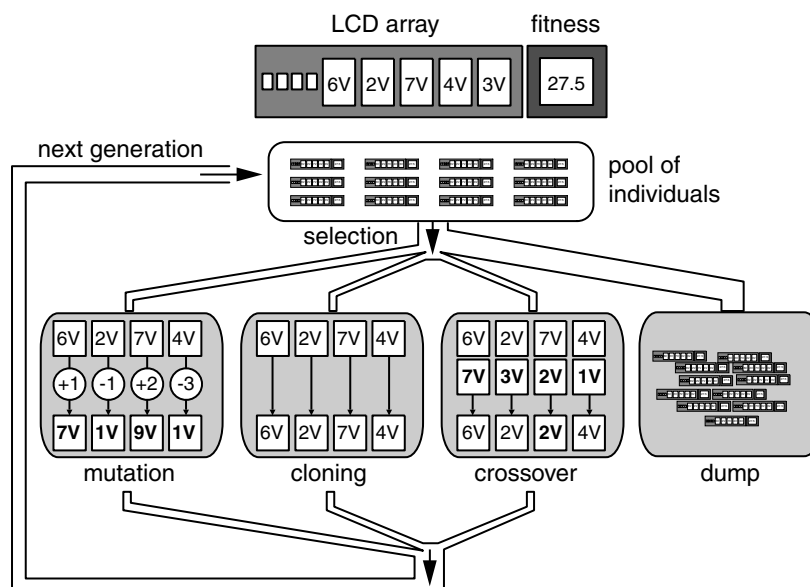


Figure 2.3: The diagram shows one cycle of the evolutionary algorithm used in the quantum control experiments described in this work. Each individual within the population (pool of individuals) represents a specific laser pulse shape, characterized by its genes, i.e., the specific LCD pixel voltage values. Depending on its experimentally determined fitness, an individual is either selected for reproduction or erased from the population. Reproduction operations include mutation, cloning, and crossover of the LCD voltage arrays. The individuals thus generated constitute the next generation, which is then evaluated and modified in the same way. This procedure is iterated until an optimized laser pulse shape is found.

swered in general. This is a problem common to all global search algorithms, which can be ameliorated to some extent by performing a series of optimizations under the same experimental conditions. However, the key advantages of the adaptive approach to quantum control (i.e., that no *a priori* knowledge about the Hamiltonian and the PES of the system is needed, and the fact that the experimental conditions are implicitly taken into account) have led to significant progress in the control of physical and chemical processes. Among the first demonstrations of this method were the optimization of the excited state population of a laser dye by Bardeen et al. [45] and the automated compression of femtosecond laser pulses [44, 46–48]. Since then, the dissociation of molecules in the gas phase [49–52], energy transfer in large biomolecular molecules [53], selective excitation of different vibrational modes [54, 55] and the control of the geometrical rearrangement in the liquid phase [56] and many other problems have been successfully controlled.

While obtaining control over such processes is a considerable achievement by itself, it is naturally desirable to extract information about the control mechanisms or

the molecular properties and states involved from such experiments. This non-trivial task, known as the ‘problem of inversion’, remains one of the primary challenges in the field of optimal control. In this context, the circumstance that all quantum states accessible with a given laser spectrum and a manifold of different control mechanisms (e.g., those mentioned in sections 2.2 and 2.3) can be exploited by the learning algorithm, is a two-edged sword. On the one hand, this ensures that optimal use can be made of all available factors that influence the investigated process. On the other hand, this means that the optimal pulse can be based on any of the possible control mechanisms or on some combination of these. This issue is further complicated by the possibility that any feature of the optimal pulse might either be crucial for some control mechanism or a redundant and superfluous ‘spectator’. At any rate, a careful characterization of the optimal control field (see chapter 3.5) has to be carried out, if any information is to be extracted from it. The comparison with theoretical findings can in some cases shed light on the control mechanisms [57–59]. Additional experimental evidence, e.g., from pump–probe scans, can provide supplementary information for identifying control mechanisms. For example, isotope–selective control of the K_2 dimer has been shown to depend primarily on the excitation wavelength [60]. Pulse sequences with time delays related to characteristic oscillation periods in molecules have been identified to play a central role in the manipulation and control of photodissociation reactions [61] and molecular vibrational dynamics [54, 62]. In this context the scanning of a reduced set of control parameters (see chapter 6) is noteworthy, which can be used to obtain illustrative and instructive control landscapes.

Chapter 3

Technological concepts

Femtosecond (fs) laser pulses are an ideal tool for the time-resolved observation or selective manipulation of ultrafast processes, such as molecular dynamics. Here, the mathematical description of such laser pulses is covered first, followed by the experimental details of their generation. The high intensities of these ultrashort laser pulses give access to nonlinear optical effects. The nonlinear processes relevant for the experiments presented in this thesis will be introduced in the section 3.3. The shaping of femtosecond laser pulses plays a vital role in all these experiments, and the experimental setups required for this shaping are presented in the next section. An overview of the various laser pulse characterization methods employed in this work concludes this chapter.

3.1 Mathematical description of femtosecond laser pulses

Laser light is a form of electromagnetic radiation, generated by stimulated emission. By a suitable coherent superposition of numerous light waves, laser pulses can be created with a duration of only a few femtoseconds. As the interaction of light with matter is dominated by effects related to the electric field (magnetic interactions being several orders of magnitude weaker), the mathematical discussion of fs laser pulses will be limited to their electric field. The polarization of the electric field is omitted here and will be recovered in section 3.4.2. Further simplification is possible if the spatial dependence of the electric field is neglected, and only its temporal variation $E(t)$ at one point in space is considered. Quite often, an alternative description of laser pulses in the frequency domain, $E(\omega)$, is very useful. Both descriptions are related via Fourier transformation:

$$E(t) = \frac{1}{\sqrt{2\pi}} \int_{-\infty}^{\infty} E(\omega) e^{i\omega t} d\omega, \quad (3.1)$$

$$E(\omega) = \frac{1}{\sqrt{2\pi}} \int_{-\infty}^{\infty} E(t) e^{-i\omega t} dt. \quad (3.2)$$

Since $E(t)$ is a real-valued observable, its Fourier transform $E(\omega)$ has to satisfy the relation $E(\omega) = E^*(-\omega)$, where * denotes complex conjugation. Therefore the values of $E(\omega)$ for positive frequencies are sufficient for a complete description of the electric field in the frequency domain:

$$E^+(\omega) = \begin{cases} E(\omega) & \text{if } \omega \geq 0, \\ 0 & \text{if } \omega < 0. \end{cases} \quad (3.3)$$

By inverse Fourier transformation of $E^+(\omega)$ one obtains the corresponding field $E^+(t)$ in the time domain, which is also complex-valued. The real-valued physical electric field can then be obtained via

$$E(t) = 2\text{Re}E^+(t), \quad (3.4)$$

where Re denotes the real part of the complex-valued argument. Both the spectral and the temporal representations can be expressed by a real-valued amplitude function A and a phase term ϕ :

$$E^+(\omega) = A(\omega) e^{-i\phi(\omega)}, \quad (3.5)$$

$$E^+(t) = A(t) e^{i\phi(t)}. \quad (3.6)$$

The amplitude factors describe an envelope function in the time or frequency domain, while the phase terms give rise to oscillations bounded by that envelope. First, the properties of the laser pulse that are related to the amplitude functions are considered. In experiments, the pulse energy is an important parameter, which can be obtained by integration of the temporal intensity $I(t)$ over the spatial and time coordinates. This intensity $I(t)$ is defined as the temporal average of $E^2(t)$ over one optical cycle T of the laser field:

$$I(t) = \epsilon_0 c n \frac{1}{T} \int_{t-T/2}^{t+T/2} E^2(t') dt' = 2\epsilon_0 c n A^2(t), \quad (3.7)$$

where ε_0 is the electric permittivity in vacuum, n is the index of refraction of the optical medium and c is the speed of light in vacuum. The spectral intensity $I(\omega)$ is obtained analogously by averaging in the frequency domain as

$$I(\omega) = 2\varepsilon_0 cn |E^+(\omega)|^2. \quad (3.8)$$

The pulse duration τ_p and the spectral bandwidth $\Delta\omega_p$ are defined in this thesis as the full width at half maximum (FWHM) of the temporal or spectral intensity profiles, respectively. However, these definitions are only meaningful for simple pulse shapes, and pulses with a more complex structure are better characterized by the full electric field, i.e., $E(t)$ or $E(\omega)$. As the temporal and spectral properties of the electric field are connected via Fourier transformation (see Eq. 3.1 and Eq. 3.2), the pulse duration and spectral bandwidth cannot be varied independently in an arbitrary way. From the theory of Fourier transformation, one obtains the ‘bandwidth product’, a relation between the two variables similar to the time–energy uncertainty relation in quantum mechanics:

$$\Delta\omega_p \tau_p \geq 2\pi k, \quad (3.9)$$

where k is a numerical constant of the order 1, which depends on the exact shape of the pulse. Pulses for which the bandwidth product is minimally fulfilled are called bandwidth–limited or Fourier–limited, and have the shortest time duration possible for a given spectrum. From this inequality relation it can be deduced that a broad spectrum $I(\omega)$ is necessary for obtaining temporally short laser pulses. However, a broad spectrum alone is not sufficient for obtaining short pulse durations, as the temporal electric field – and hence the pulse duration – also depends on the spectral phase function $\phi(\omega)$ (see Eq. 3.1 and Eq. 3.5).

The phase terms are considered in more detail now, beginning with the temporal phase $\phi(t)$. For a better understanding of the meaning of $\phi(t)$, it is convenient to perform a Taylor expansion of this function around a time t_0 (usually the time of the peak intensity, which is chosen as $t_0 = 0$ fs):

$$\begin{aligned} \phi(t) &= \phi(t=0) + \left[\frac{d\phi}{dt} \right]_{t=0} t + \frac{1}{2} \left[\frac{d^2\phi}{dt^2} \right]_{t=0} t^2 + \frac{1}{6} \left[\frac{d^3\phi}{dt^3} \right]_{t=0} t^3 + \dots \\ &= a_0 + a_1 t + \frac{1}{2} a_2 t^2 + \frac{1}{6} a_3 t^3 + \dots \end{aligned} \quad (3.10)$$

The first coefficient $a_0 = \phi(t=0)$ describes a constant absolute phase, which determines the temporal relation between the light oscillation and the pulse envelope $A(t)$. In Fig. 3.1 the effect of the absolute phase is illustrated for pulses with a duration of 5 fs and 25 fs. As can be seen, the influence of the absolute phase is already small for a pulse duration of 25 fs, and it becomes negligible for the 80 fs pulses used in

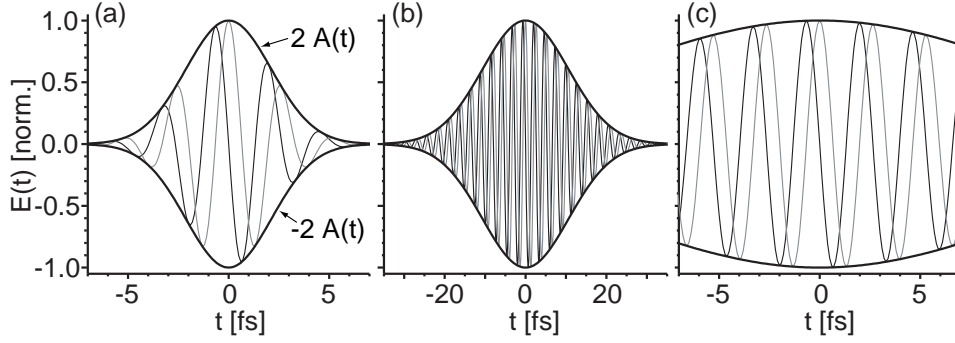


Figure 3.1: Absolute phase of femtosecond laser pulses. (a) A laser pulse with a duration of 5 fs is shown for two different values of the absolute phase a_0 , a “cosine pulse” with $a_0 = 0$ (gray line) and a “sine pulse” with $a_0 = \pi/2$ (black oscillating line). The temporal envelope function is identical in both cases. The same is plotted for a pulse with a duration of 25 fs in (b) and (c). As can be seen in (c) the difference in the electric field is minor for the two values of the absolute phase for 25 fs laser pulses compared to the significant changes in (a) for 5 fs laser pulses.

most experiments described in this thesis. However, it becomes important for pulse durations below 10 fs. While the value of the absolute phase changes from pulse to pulse in conventional laser systems, it can be stabilized with a suitable setup (‘carrier envelope phase stabilization’, see, e.g., Refs. [63, 64]).

The second coefficient, a_1 , is related to a shift in the frequency domain, which can be identified with the carrier frequency ω_0 of the electric field. This spectral shift is often subtracted from the phase $\phi(t)$:

$$\varphi(t) = \phi(t) - \omega_0 t, \quad (3.11)$$

introducing the time dependent phase $\varphi(t)$. With this relation, the momentary frequency $\omega(t)$, which is defined as the time-derivative of the temporal phase $\phi(t)$ can be written as:

$$\omega(t) = \frac{d\phi(t)}{dt} = \omega_0 + \frac{d\varphi(t)}{dt}. \quad (3.12)$$

From this definition it is apparent that the third coefficient, $a_2 = [d^2\phi/dt^2]_{t=0}$, describes the linear change of frequency with time. If a_2 is greater than zero, the time-dependent frequency increases monotonously and the pulse is called up-chirped in analogy to the acoustic phenomenon. Correspondingly, a monotonous decrease of the momentary frequency is called down-chirp. The higher order coefficients in the Taylor expansion are hence named ‘second-order chirp’, ‘third-order chirp’, and so on.

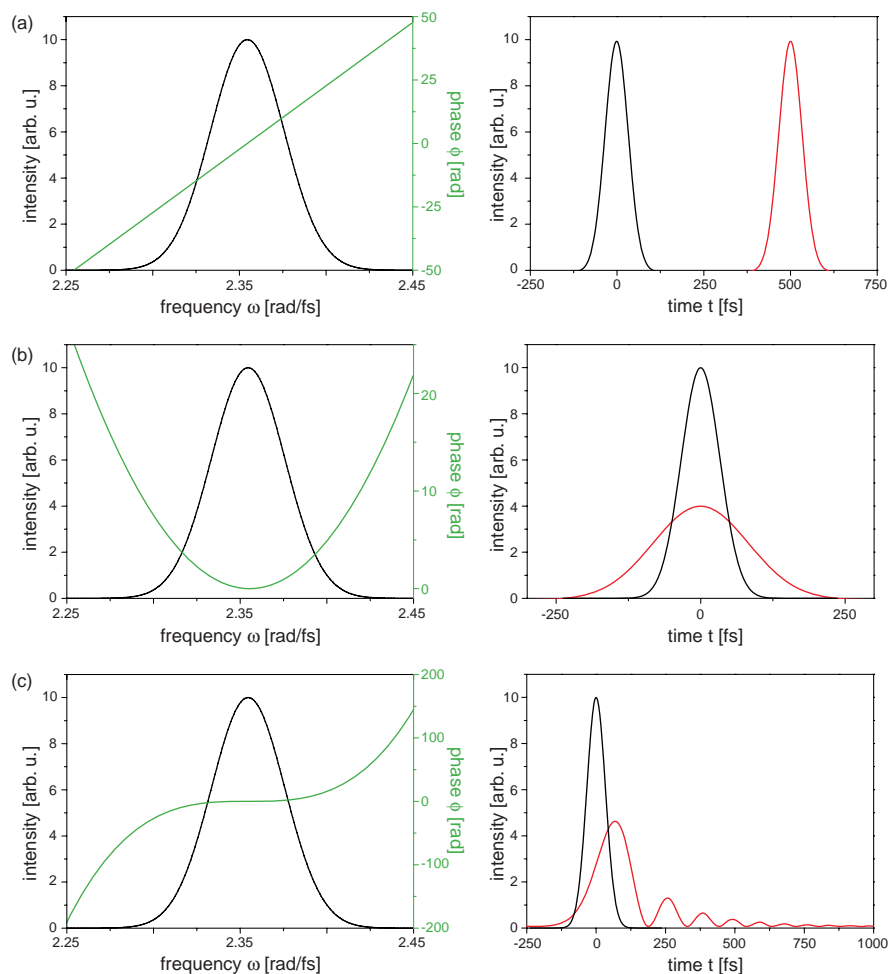


Figure 3.2: Effects of simple spectral phases on the intensity profile in the time domain. In the left column, the spectral intensity (black line) is shown together with the spectral phase (green line) for pulses with (a) a linear spectral phase of $b_1 = 500$ fs, (b) a quadratic spectral phase of $b_2 = 5000$ fs² and (c) a third order spectral phase of $b_3 = 10^6$ fs³. The corresponding intensity profiles in the time domain are shown in the right column (red line), together with the intensity profile of a bandwidth–limited pulse (black line).

Shaped femtosecond laser pulses, whose temporal characteristics can be manipulated on the timescale of a few femto– to picoseconds, are an essential ingredient for all experiments presented in this thesis. However, as the fastest electronic devices have a response time on the order of nanoseconds, the direct shaping fs laser pulses in the time domain is not viable. Therefore the shaping of fs pulses is carried out in the spectral domain (see section 3.4), which translates to the time domain via Fourier transformation (see Eq. 3.1). For a better understanding both of the shaping process and of the effects of material dispersion, it is instructive to perform a Taylor expansion

also on the spectral phase $\phi(\omega)$:

$$\begin{aligned}\phi(\omega) &= \phi(\omega_0) + \left[\frac{d\phi}{d\omega} \right]_{\omega_0} (\omega - \omega_0) + \frac{1}{2} \left[\frac{d^2\phi}{d\omega^2} \right]_{\omega_0} (\omega - \omega_0)^2 + \\ &\quad \frac{1}{6} \left[\frac{d^3\phi}{d\omega^3} \right]_{\omega_0} (\omega - \omega_0)^3 + \dots \\ &= b_0 + b_1(\omega - \omega_0) + \frac{1}{2}b_2(\omega - \omega_0)^2 + \frac{1}{6}b_3(\omega - \omega_0)^3 + \dots\end{aligned}\quad (3.13)$$

The first coefficient describes again a constant phase. The second coefficient is antiproportional to the group velocity and results in a shift in time. This becomes apparent by performing the inverse Fourier transformation and is illustrated in Fig. 3.2(a). The third coefficient is the derivative of the inverse of the group velocity and is therefore called ‘group velocity dispersion’ (GVD). It describes a change in the group velocity with frequency, and gives rise to up- or downchirp in the time domain, depending on its sign. This leads to temporal broadening, as illustrated in Fig. 3.2(b). The other terms are called after their order (‘third order dispersion’, TOD, ‘fourth order dispersion’, FOD, etc.). Non-zero TOD leads to pre- or post-pulses, depending on its sign, as shown in Fig. 3.2(c). Material dispersion, e.g., due to the beam passing through a lens or glass plate, introduces spectral phases mainly of second and third order, and thereby modifies the pulse shape.

Sinusoidal phases of the form

$$\phi(\omega) = A \sin(\omega\tau + \phi_0) \quad (3.14)$$

are also employed in this work. Such spectral phases create a pulse train in the time domain. The relative amplitudes of the subpulses is governed by the amplitude A , their temporal spacing by τ and their relative phases by ϕ_0 .

3.2 Generation of femtosecond laser pulses

As mentioned in the previous section, a broad spectrum and correct relative phases between the different frequency modes (known as ‘mode locking’) are required for the generation of ultrashort laser pulses [65]. Today, Ti:sapphire crystals are the standard laser medium for achieving both goals, due to their broad gain bandwidth that extends from about 700 nm to 1100 nm [66] and the possibility to achieve the desired mode locking by exploiting the Kerr-lens effect [67]. The laser system that has been used for most experiments in this thesis is shown schematically in Fig. 3.3 (the experiments described in chapter 4 have been performed in the labs of Prof. Dr. T. Baumert in Kassel). It produces ultrashort laser pulses at a central wavelength of 800 nm, a pulse

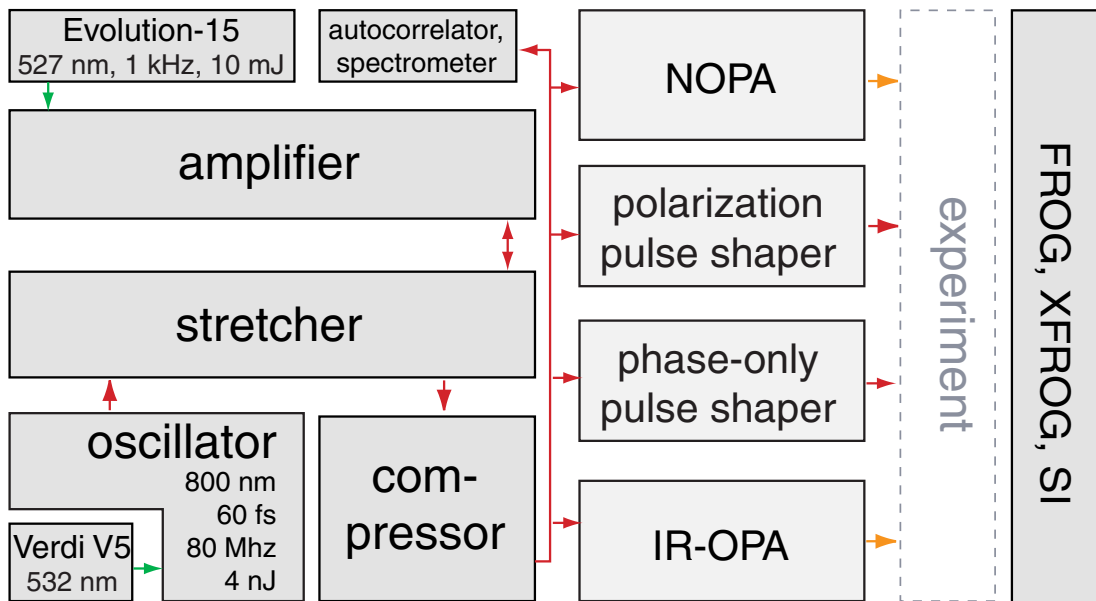


Figure 3.3: Schematic of the arrangement of the basic components of the laser system. The ultrashort pulses from the oscillator are stretched to 250 ps in the stretcher to avoid damaging of the amplifier components. The stretched pulses are then amplified by a factor of 10^6 and afterwards temporally recompressed to about 80 fs. The amplified pulses are generated with a repetition rate of 1 kHz and have a central wavelength of 800 nm and a pulse energy of 0.7 mJ. The diagnostic tools, the pulse shapers and different possibilities for converting light to different frequency regions are also shown. The components used for the experiments presented here will be introduced later in this chapter.

duration of about 80 fs and a pulse energy of 0.7 mJ at a repetition rate of 1 kHz. During this work, the laser system has been partly rebuilt and upgraded, in order to improve its pointing stability and to decrease the short- and longterm fluctuations in the pulse energy. The first stage in the generation of high-intensity ultrashort laser pulses is a home-built oscillator, which consists of a laser cavity, with a Ti:sapphire crystal as laser medium. It is now pumped by a solid state continuous wave (cw) laser (Verdi V5), replacing the previously used Ar-ion laser. Various components, such as the mirror mounts and posts, have been replaced in the course of the upgrade with more stable versions in order to reduce mechanical fluctuations. Two prisms, which have also been remounted, provide intra-cavity dispersion compensation. By utilizing the Kerr-lens mode locking effect in the Ti:sapphire crystal in conjunction with a slit aperture, as depicted schematically in Fig 3.4, pulsed operation can be achieved, which produces pulses centered around 800 nm with a duration of 60 fs and a pulse energy of 4 nJ at a repetition rate of 80 MHz.

As for most experiments – especially those which require the use of frequency conversion techniques – this pulse energy is not sufficient, the pulses from the oscillator

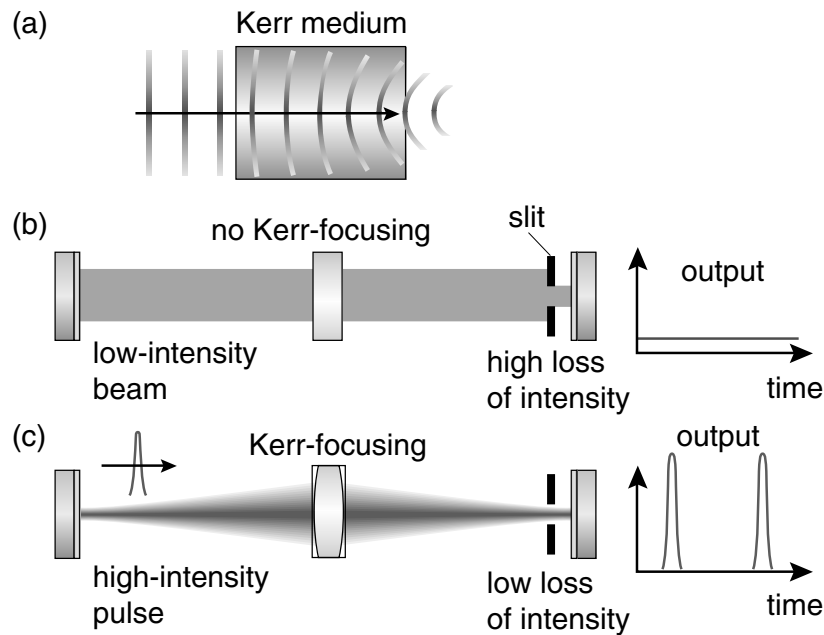


Figure 3.4: Kerr-lens mode locking. A Kerr medium shows an intensity-dependent index of refraction at very high intensities (a). This can be used to favour the pulsed operation (c) over continuous wave (cw) operation (b) of a laser (taken from [68]).

have to be amplified. However, direct amplification of these fs laser pulses is not possible, as the high temporal peak intensities involved would exceed the damage threshold of the amplifier gain medium. Therefore chirped pulse amplification (CPA) is employed, which was introduced by Strickland and Mourou [69]. Prior to amplification, the pulses from the oscillator pass through a ‘stretcher’, where a suitable setup of gratings introduces different optical pathlengths for the wavelengths in the oscillator spectrum. The resulting positive linear chirp leads to an increase in the pulse duration from 60 fs to about 250 ps. A Pockels-cell, in conjunction with polarization-dependent beamsplitters, is employed for selecting one of the oscillator pulses each millisecond for amplification. The regenerative amplifier consists of a Ti:sapphire resonator, which is pumped by a Q-switched ND:YLF laser. During the upgrade, the former lamp-pumped ND:YLF laser was replaced with an AlGaAs laser-diode pumped ND:YLF laser (Evolution 15 from Coherent) with an output power of 10 W and a repetition rate of 1 kHz, operating at 527 nm. The selected pulse is amplified by a factor of ca. 10^6 in the amplifier, and is then switched out, again by the combination of Pockels-cell and polarization dependent beamsplitters. The amplified pulse then proceeds through a compressor, i.e., a second setup of gratings that compensates the chirp introduced by the stretcher and during amplification. It compresses the laser pulse to a duration of about 80 fs, which is the minimum duration obtainable with a spectrum that is reduced from the FWHM of 16 nm of the oscillator to 12 nm by the amplification process due to nonlinear gain narrowing. After the compressor, a small portion of the laser pulse

is split off for monitoring with a spectrometer and an autocorrelator. Ultrashort laser pulses are now available for frequency conversion, e.g., into the visible spectral range with a NOPA or into the IR with an IR-OPA¹, and for fs pulse shaping. Besides the actual experiments, the setup is completed by various pulse characterization methods. Those components which are needed for the experiments presented in this thesis will be described in the remainder of this chapter.

3.3 Frequency conversion

The laser system described above has the drawback that the ultrashort laser pulses produced are limited to the spectral region around 800 nm. However, the absorption spectra and the allowed electromagnetic transitions in molecular and atomic systems often require different wavelengths. Fortunately, the electric field strength of the near-IR 800 nm pulses is sufficient to efficiently drive nonlinear processes which allow the generation of coherent radiation at different frequencies. The interaction of electric fields with matter is described by the wave equation, which can be derived from the Maxwell equations:

$$\left[\nabla \times (\nabla \times) - \frac{1}{c^2} \cdot \frac{\partial^2}{\partial t^2} \right] \mathbf{E}(\mathbf{r}, t) = \mu_0 \frac{\partial^2}{\partial t^2} \mathbf{P}(\mathbf{r}, t), \quad (3.15)$$

where c is the speed of light in vacuum, and μ_0 is the magnetic permeability in vacuum. $\mathbf{P}(\mathbf{r}, t)$ is the induced polarization, and acts as a source term in the wave equation. It includes both the light's effect on the medium and the medium's effect on the light wave. The induced polarization contains optical effects that are linear in the electric field strength, such as absorption, reflection, dispersion and refraction, and also non-linear optical effects. At low field strengths, the induced polarization is proportional to the electric field:

$$\mathbf{P} = \epsilon_0 \chi^{(1)} \mathbf{E}, \quad (3.16)$$

with the electrical permittivity in vacuum, ϵ_0 , and the linear electrical susceptibility $\chi^{(1)}$, which describes the linear optical effects. The electric field induces dipoles in the medium that oscillate at the frequency of the incident field, and these dipoles emit an additional electric field at the same frequency. The electric field strength in Eq. 3.15 contains both the incident and the emitted field. At higher intensities, the induced polarization is no longer a linear function of the electric field strength, and terms of higher order in \mathbf{E} have to be taken into account:

¹(N)OPA: (Non-collinear) optical parametric amplifier

$$\mathbf{P} = \varepsilon_0 \sum_{j=1}^{\infty} \chi^{(j)} \mathbf{E}^j = \varepsilon_0 \left[\chi^{(1)} \mathbf{E} + \chi^{(2)} : \mathbf{E}\mathbf{E} + \chi^{(3)} : \mathbf{E}\mathbf{E}\mathbf{E} + \dots \right]. \quad (3.17)$$

The $\chi^{(n)}$ are called n -th order electrical susceptibilities. They are in general tensors of the rank $n + 1$. The discussion of nonlinear optical effects is limited here to processes of second order in the electric field, as these are exploited in the experiments described in this thesis. More detailed discussions can be found, e.g., in [65, 70, 71].

3.3.1 Second-order nonlinear optical effects

Let us first consider an electric field which oscillates at a single frequency ω and propagates with wave-vector \mathbf{k} :

$$\mathbf{E}(\mathbf{r}, t) = \frac{1}{2} \mathbf{A}(\mathbf{r}, t) \exp[i(\omega t - \mathbf{k}\mathbf{r})] + c.c. \quad (3.18)$$

Squaring of this field yields:

$$\mathbf{E}^2(\mathbf{r}, t) = \frac{1}{4} \left[\mathbf{A}^2(\mathbf{r}, t) \exp[i(2\omega t - 2\mathbf{k}\mathbf{r})] + \mathbf{A}(\mathbf{r}, t) \mathbf{A}^*(\mathbf{r}, t) \right] + c.c. \quad (3.19)$$

If the second-order susceptibility is non-zero, the first term (and its complex conjugate) generates an electric field in the medium that oscillates at 2ω , the second harmonic of the incident light frequency. This process is therefore called second-harmonic generation (SHG), and it is important both for the frequency conversion of shaped pulses, and for the characterization of ultrashort laser pulses (see section 3.5). The remaining terms are non-oscillating and create a DC electric field. This phenomenon is known as ‘optical rectification’ and can be measured experimentally [72].

For a more general treatment of second-order processes, let us now consider an incident electric field that consists of two contributions with frequencies ω_1 and ω_2 and wave-vectors \mathbf{k}_1 and \mathbf{k}_2 :

$$\mathbf{E}(\mathbf{r}, t) = \frac{1}{2} \mathbf{A}_1(\mathbf{r}, t) \exp[i(\omega_1 t - \mathbf{k}_1 \mathbf{r})] + \frac{1}{2} \mathbf{A}_2(\mathbf{r}, t) \exp[i(\omega_2 t - \mathbf{k}_2 \mathbf{r})] + c.c. \quad (3.20)$$

Squaring this field gives:

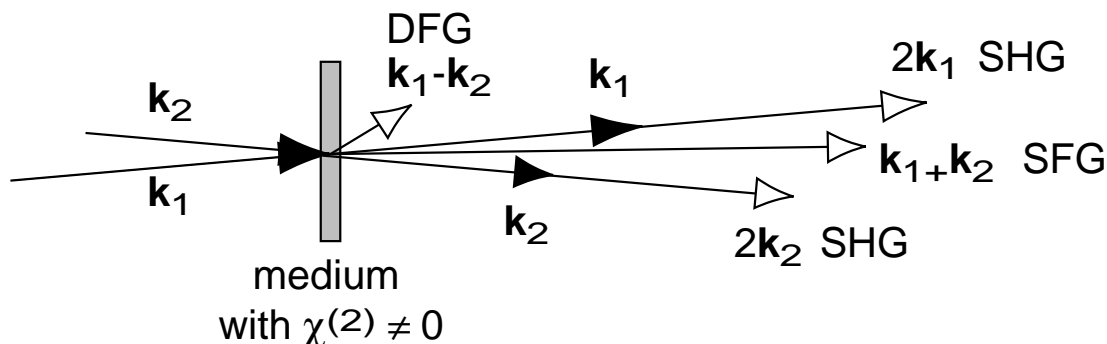


Figure 3.5: Second-order processes of two non-collinear beams with different frequencies. The quadratic term in Eq. 3.17 is responsible for second-harmonic generation (SHG), sum- and difference-frequency generation (SFG and DFG). Beams emerging from these processes are shown with a white arrow-head.

$$\begin{aligned}
 \mathbf{E}^2(\mathbf{r}, t) = & \frac{1}{4} \{ \mathbf{A}_1^2 \exp[i(2\omega_1 t - 2\mathbf{k}_1 \mathbf{r})] + \mathbf{A}_2^2 \exp[i(2\omega_2 t - 2\mathbf{k}_2 \mathbf{r})] \\
 & + \mathbf{A}_1 \mathbf{A}_1^* + \mathbf{A}_2 \mathbf{A}_2^* \\
 & + \mathbf{A}_1 \mathbf{A}_2 \exp[i(\omega_1 + \omega_2)t - (\mathbf{k}_1 + \mathbf{k}_2)\mathbf{r}] \\
 & + \mathbf{A}_1 \mathbf{A}_2^* \exp[i(\omega_1 - \omega_2)t - (\mathbf{k}_1 - \mathbf{k}_2)\mathbf{r}] \} + c.c.
 \end{aligned} \quad (3.21)$$

Apart from the SHG and optical rectification terms of the individual fields, additional terms arise at the frequencies $\omega_3 = \omega_1 + \omega_2$ and $\omega_4 = \omega_1 - \omega_2$, i.e., the sum or difference of the incident frequencies. These processes are therefore called sum-frequency generation (SFG, also sum-frequency mixing, SFM) and difference-frequency generation/mixing (DFG or DFM), respectively. These processes can be exploited for the characterization of UV-pulses by the XFROG-technique (see section 3.5), and also for the frequency conversion of shaped pulses. A noteworthy aspect is that the new frequencies are emitted in different directions (if \mathbf{k}_1 and \mathbf{k}_2 are non-collinear), e.g., in the direction $\mathbf{k}_1 + \mathbf{k}_2$ in the case of SFG. Fig. 3.5 shows the propagation of the incident electric fields and of the electric fields generated in the second-order processes.

The SFG process, which includes SHG as a special case, will now be studied in more detail. The fact that the new frequency ω_3 is the sum of the incident frequencies ω_1 and ω_2 ,

$$\omega_3 = \omega_1 + \omega_2, \quad (3.22)$$

reflects the conservation of energy. With $|\mathbf{k}| = \frac{\omega n(\omega)}{c}$, where $n(\omega)$ is the frequency-dependent index of refraction, one obtains the following relation between the wave-vectors:

$$\frac{\mathbf{k}_3}{n(\omega_3)} = \frac{\mathbf{k}_1}{n(\omega_1)} + \frac{\mathbf{k}_2}{n(\omega_2)}. \quad (3.23)$$

The conservation of momentum, on the other hand, yields

$$\mathbf{k}_3 = \mathbf{k}_1 + \mathbf{k}_2. \quad (3.24)$$

The transfer of energy from the incident fields is most efficient if not only Eq. 3.23, but also Eq. 3.24 is fulfilled. If this is not the case, the light wave with frequency ω_3 will get out of phase with the driving fields at ω_1 and ω_2 , depending on the pathlength l that the waves travel in the medium. This will result in destructive interference between the radiation at ω_3 generated at different positions in the medium. The amount by which Eq. 3.24 is violated is called phase-mismatch, which is given by:

$$\Delta\mathbf{k} = \mathbf{k}_1 + \mathbf{k}_2 - \mathbf{k}_3. \quad (3.25)$$

While the wave equation (Eq. 3.15) can be solved for $\Delta\mathbf{k} \neq 0$, the SFG process is most efficient for vanishing $\Delta\mathbf{k}$. With Eq. 3.22, 3.24 and 3.25 this condition can be written as:

$$\Delta k = \omega_1(n(\omega_3) - n(\omega_1)) + \omega_2(n(\omega_3) - n(\omega_2)). \quad (3.26)$$

This condition cannot be fulfilled in isotropic media which exhibit normal dispersion ($n(\omega_i) > n(\omega_j)$ for $\omega_i > \omega_j$). A possibility to solve this problem lies in the use of birefringent crystals, by which the tensorial character of $\chi^{(2)}$ can be exploited if the electric fields involved in the process have different polarizations. In this case phase-matching is possible, as the index of refraction for a given wavelength depends on the polarization of the electric field. Uniaxial birefringent crystals possess a symmetry axis (the ‘optical axis’). Light whose electric displacement field \mathbf{D}_o is perpendicular to this axis is called ‘ordinary beam’ and its index of refraction in the crystal, n_o , is independent of the direction of propagation. However, the index of refraction of the ‘extraordinary beam’ (with $\mathbf{D}_e \perp \mathbf{D}_o$) is a function of the angle θ between the optical axis and the direction of propagation [73]:

$$n_e(\theta) = \frac{n_o n_{e0}}{\sqrt{n_o^2 \sin^2 \theta + n_{e0}^2 \cos^2 \theta}}, \quad (3.27)$$

and it varies between $n_e(\theta = 0^\circ) = n_o$ and $n_e(\theta = 90^\circ) = n_{e0}$. If $n_{e0} < n_o$ the crystal is called negativ–uniaxial, otherwise positive–uniaxial. The condition $\Delta\mathbf{k} = 0$ can be achieved in uniaxial crystals in different ways. In the case of ‘type I’ phase-matching the two incident beams have the same polarization, while the sum–frequency field

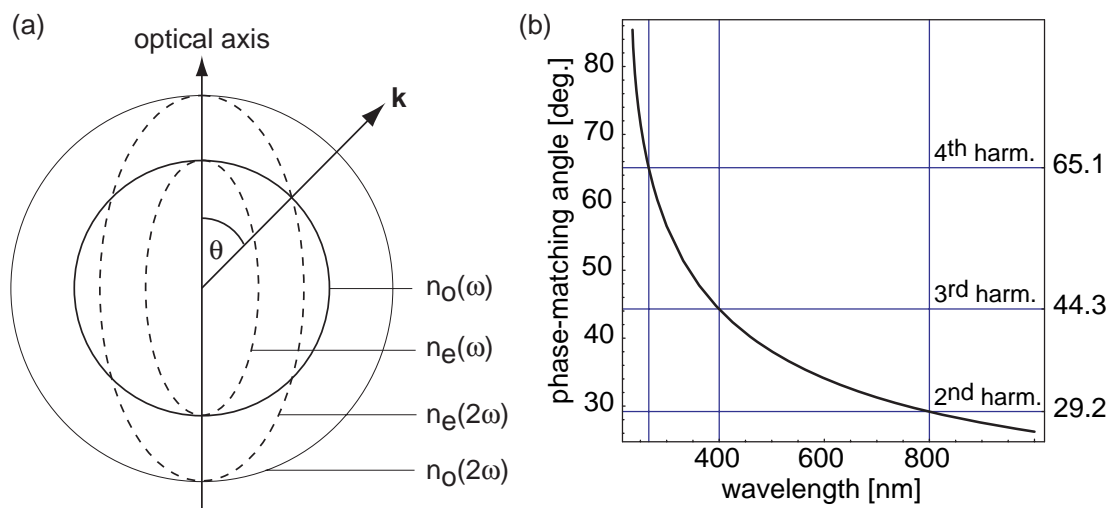


Figure 3.6: (a) Type I phase-matching for second-harmonic generation (SHG) in a negative-uniaxial crystal. The phase-matching condition $n_e(2\omega) = n_o(\omega)$ is fulfilled for the angle θ shown. The dependence of the phase-matching angle in BBO on the wavelength that is mixed with a fundamental at 800 nm is shown in (b). The generated sum-frequency is indicated for a mixing of 800 nm light with 800 nm, 400 nm and 266 nm radiation, resulting in the generation of the second, third and fourth harmonic, respectively.

is polarized perpendicular to the incident beams' polarization. For 'type II' phase-matching, one of the incident beams is polarized perpendicular to the other two beams. The birefringent crystals used in this thesis (BBO, β -barium-borate) are negative-uniaxial crystals, used in type I phase-matching configuration. The dependence of the indices of refraction for the fundamental and the second-harmonic on the angle θ is shown in Fig. 3.6(a). Fig. 3.6(b) depicts the phase-matching angle for which $\Delta\mathbf{k} = 0$ is fulfilled for SFG in dependence on the wavelength that is mixed with a fundamental at 800 nm. From Fig. 3.6(a) it is also apparent that a single BBO crystal can produce the second-harmonic efficiently only for a single polarization of the incident beam. Frequency conversion of polarization-shaped light can therefore not be realized by using a single crystal. A method for achieving this goal will be presented in chapter 5.

3.3.2 Frequency doubling of shaped laser pulses

Many molecules, especially organic molecules which are relevant for biochemistry, have strong absorption bands in the UV. While in some cases photodynamics in these systems can be triggered or influenced by multiphoton processes, this approach may not be advantageous or it is even impossible in other systems. Therefore, it is desirable to generate shaped pulses in the UV. Especially the wavelength region around 400 nm is easily accessible by frequency doubling of the 800 nm pulses generated by the laser system presented in section 3.2. There are various methods available for pulse shaping in this wavelength regime. Of course the most attractive option would be the direct shaping of 400 nm laser pulses. This is possible with deformable mirrors [74], which are limited to rather simple pulse shapes with smooth phase-functions. Also acousto-optical modulators [75, 76], which shape the optical electric field by diffracting it on a modulated acoustic wave, can be used for this purpose [77], albeit with a low diffraction efficiency and hence low throughput. Micro mirror arrays [78], which consist of individually addressable small mirrors, have also been introduced for this purpose [79]. While these devices are probably the most efficient solution to the problem, they were not commercially available until recently, and could therefore not be employed in the experiments presented here. The pulse shapers that were used feature liquid crystal displays (LCDs, see next section). These have the drawback that they absorb light below 450 nm and cannot be used for the direct shaping of 400 nm light. However, the nonlinear processes introduced above (namely SFG and SHG) can be exploited to convert shaped 800 nm pulses into the UV [80, 81]. Sum-frequency mixing of a shaped 800 nm pulse with another 800 nm pulse is feasible. However, as the shaped pulses may be a couple of picoseconds long, the second pulse must be stretched in time, e.g., by introducing a linear chirp, which results in low peak intensities and hence small conversion efficiency. However, this is a viable option for generating shaped pulses at the third harmonic (266 nm) of the fundamental. In [82, 83] we have shown that it is feasible to produce such shaped pulses by sum-frequency mixing of a shaped 800 nm pulse with a stretched 400 nm pulse. The second option, which was employed here, is

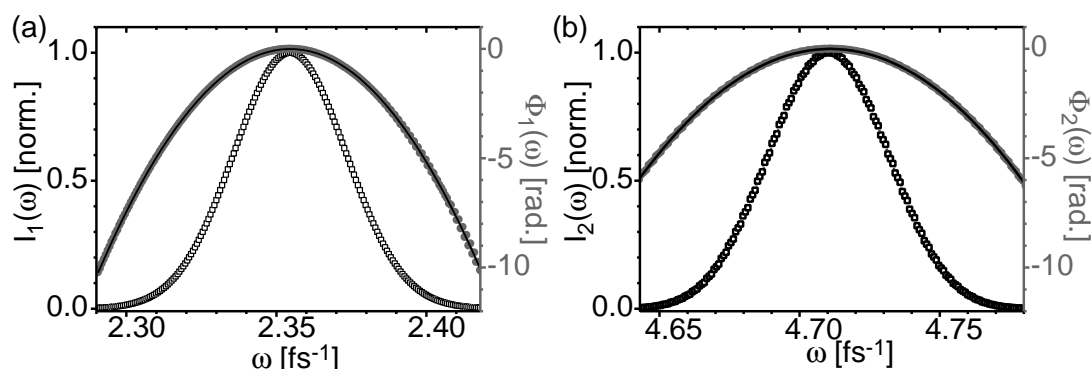


Figure 3.7: SHG with shaped laser pulses. The fundamental laser pulse (a) has a quadratic spectral phase with a Taylor coefficient $b_{2,FP} = -5000 \text{ fs}^2$. After SHG in a $400 \mu\text{m}$ thick BBO crystal this results in a 400 nm laser pulse (b) with a quadratic spectral phase of $b_{2,SH} = -2500 \text{ fs}^2$.

based on the frequency doubling of modulated laser pulses [80].

The discussion of the SHG process was limited so far to only one or two incident frequencies. However, as was pointed out before, temporally short laser pulses must have a broad spectrum. For pulse durations much longer than one optical cycle (about 2 fs for visible light), which is fulfilled for the laser pulses employed here, the wave equation (Eq. 3.15) can be simplified by using the slowly varying envelope approximation (SVEA) [65]. With this approximation, the electric field can be written as the product of a fast carrier wave and an envelope function A that varies slowly with respect to the carrier frequency. This allows us to neglect the second-order derivatives in the wave equation, as well as the group velocity dispersion and higher order dispersions. For electric fields propagating in the z direction, the wave equation can then be reformulated in two coupled differential equations for the fundamental (envelope function A_1) and the second harmonic (envelope function A_2):

$$\left(\frac{\partial}{\partial z} + \frac{1}{v_1} \frac{\partial}{\partial t} \right) A_1 = -i\chi^{(2)} \frac{\omega_1^2}{2c^2 k_1} A_1^* A_2 e^{i\Delta k z}, \quad (3.28)$$

$$\left(\frac{\partial}{\partial z} + \frac{1}{v_2} \frac{\partial}{\partial t} \right) A_2 = -i\chi^{(2)} \frac{\omega_1^2}{2c^2 k_1} A_1^2 e^{i\Delta k z}, \quad (3.29)$$

where $v_i = d\omega/dk|_{\omega_i}$ are the group velocities of the fundamental (ω_1) and the second harmonic ($\omega_2 = 2\omega_1$), and $\Delta k = 2k_1 - k_2$ is again the phase-mismatch. In the case of exact phase-matching at the carrier frequency and small conversion efficiency (i.e., below a few percent) this set of differential equations can be solved, which yields for the second-harmonic amplitude in the frequency domain [65, 71]:

$$A_2(\omega_2) \propto \int A_1(\omega_1)A_1(\omega_2 - \omega_1)d\omega_1. \quad (3.30)$$

The temporal field envelope can be calculated by

$$A_2(t) \propto A_1^2(t). \quad (3.31)$$

The temporal structure of the second-harmonic is therefore similar to that of the fundamental pulse. However, the convolution in Eq. 3.30 leads to significant and in general rather complex variations and changes in the frequency domain. As the mixing of different frequency components, e.g., $E(\omega - \Omega)$ and $E(\omega + \Omega)$, contributes to $E(2\omega)$, a fundamental pulse that is phase-modulated will result in a phase-and-amplitude modulated second-harmonic pulse. Also the energy of a frequency-doubled shaped pulse will therefore depend on the phase-modulation of the fundamental. The convolution integral in Eq. 3.30 can be solved analytically only for a few pulse shapes, e.g., for quadratic [43, 84] and sinusoidal spectral phases [80].

The spectra of a fundamental with a quadratic spectral phase of $b_{2,FP} = -5000 \text{ fs}^2$ and its second harmonic are shown in Fig. 3.7. The spectrum of the second-harmonic pulse is the same as the spectrum obtained with a bandwidth limited pulse, but has lower peak intensity. The spectral phase remains quadratic in nature, but is reduced to half the value of the fundamental, i.e., $b_{2,SH} = b_{2,FP}/2 = -2500 \text{ fs}^2$.

An example for the second-harmonic of a fundamental pulse with sinusoidal phase is displayed in Fig. 3.8. Fig. 3.8(c) shows that the temporal structure of the pulse is retained after frequency-doubling, although with reduced amplitudes. The spectrum, in contrast, changes dramatically, as can be seen in Fig. 3.8(b). For the second harmonic, the generated pulse train originates from spectral amplitude modulation, while the fundamental pulse train was due to spectral phase modulation.

For arbitrary pulse shapes, the second harmonic field has to be calculated numerically, which requires precise knowledge of the fundamental, as small variations in the spectral phase of the fundamental can lead to very different results for its second harmonic. Thus, as the relationship between phase-shaped fundamental and the corresponding second harmonic is highly non-trivial, the second-harmonic has in practice to be characterized experimentally rather than calculated from the fundamental pulse. The experimental techniques for this purpose will be introduced in section 3.5.

3.4 Femtosecond laser pulse shaping

As mentioned in section 3.1, the response time of the fastest electronic devices is on the order of nanoseconds. Therefore, the shaping of femtosecond laser pulses has to be carried out in the frequency domain, which is related to the time domain by the inverse Fourier transformation in Eq. 3.1.

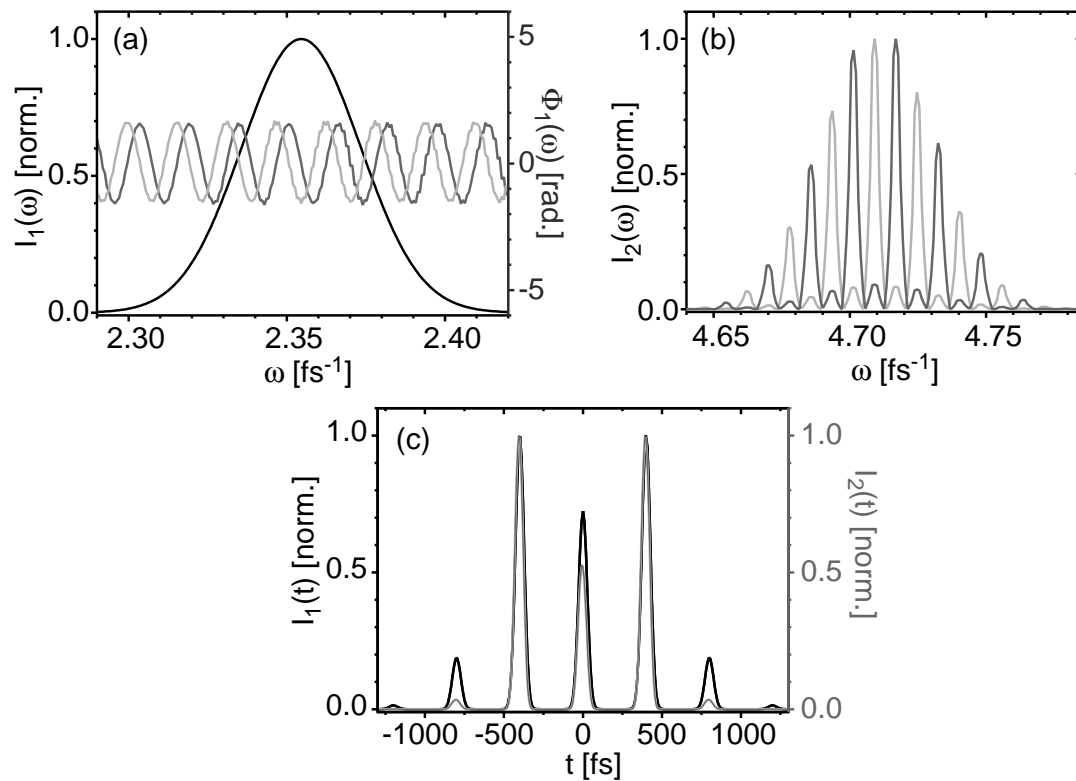


Figure 3.8: SHG of a sinusoidally phase-shaped laser pulse. The fundamental laser pulse (a) has a spectral phase with a sine (light gray) or cosine (dark gray) like shape. Both phase functions result in the same temporal profile $I(t)$ (c, black line), although with different temporal phase (not shown). The temporal profile of the second harmonic (c, gray line) is also identical for both cases. The spectrum at 400 nm (b), however, is different for the sine (light gray) or cosine (dark gray) case.

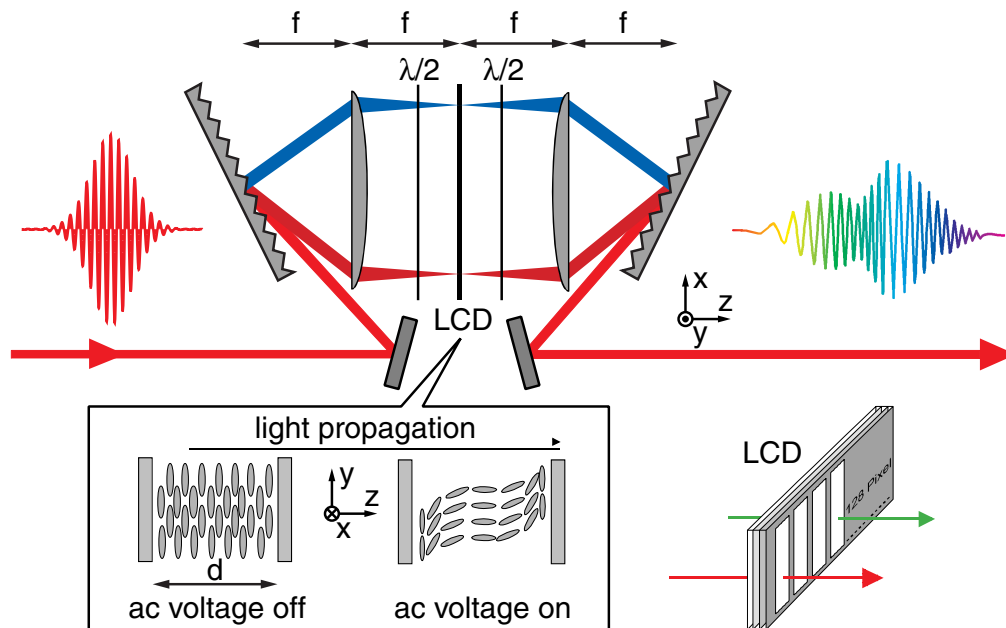


Figure 3.9: Femtosecond pulse shaper. A zero-dispersion compressor consisting of two gratings and two cylindrical lenses is used to spatially disperse the spectral components of a laser pulse. In the Fourier plane of the setup a LCD-SLM is placed, at whose 128 pixels the index of refraction – and thereby the spectral phase – can be modified for the individual frequency components.

A common ingredient in all setups used for frequency domain fs pulse shaping is the separation of the frequency components of the laser pulse in space. The individual frequency components of the spectrally dispersed pulse can then be modified by a spatial light modulator (SLM), followed by a reversion of the spectral dispersion. The most commonly used SLMs are liquid crystal displays (LCDs), acousto-optic modulators (AOMs) and deformable mirrors. An overview of these devices can be found in [85] and in [86], where also the advantages and disadvantages of the various approaches are discussed. As only pulse shapers employing LCD-SLMs have been used in this work, the discussion of pulse shapers will be limited to these devices here. In the following, the setups which allow phase-only or phase-and-polarization pulse shaping will be presented.

3.4.1 Phase-only pulse shaping

Like most pulse shaper designs, the employed pulse shaper which is shown schematically in Fig. 3.9 is based on a so-called $4f$ -setup. It consists of a pair of reflective gratings (1800 lines/mm), two cylindrical lenses (focal length $f = 80$ mm), two $\lambda/2$ -waveplates and a 128 pixel LCD-SLM. The incoming laser beam is spectrally dis-

persed by the first grating, which is positioned a focal length apart from the first lens. The beam is then collimated by the first cylindrical lens, and the different frequency components are focused into its focal plane, which is also called ‘Fourier plane’, as this part of the setup acts in principle as a Fourier transformation on the incident laser pulse. The second lens is positioned again at a distance of one focal length from the Fourier plane, and the second grating is placed at its focus. This second half of the $4f$ -setup acts like an inverse Fourier transformation and reassembles the pulse from its spectral components. Ideally (neglecting material dispersion), the temporal profiles of the incoming and exiting laser pulse are identical, and therefore this setup is also called zero-dispersion compressor [87]. The maximum frequency resolution (i.e., spatial separation of the different frequency components) is achieved in the Fourier plane, and hence the SLM is placed there. Depending on its design and the pulse shaper setup, the phase, amplitude and/or polarization of the incident laser pulse can be modified by the SLM.

The SLM used in this work for phase-only shaping is a liquid crystal display with 128 pixels (from Cambridge Research & Instrumentation) that are $97 \mu\text{m}$ wide and are arranged in a line along the x -axis (see Fig. 3.9) with a spacing of $3 \mu\text{m}$. As the pixels have a height of 2 mm, the beam diameter is reduced to this value with a Galilean telescope in front of the pulse shaper. The cylindrical lenses are employed, as they only focus along the x -direction for optimal spectral resolution, while the full height of the pixels is used in order to avoid the damaging of the display due to high intensities. Each pixel can be addressed individually and consists of a pair of substrates that are coated with indium tin oxide (ITO) electrodes. The volume between these substrates is filled with birefringent liquid crystal molecules that are aligned along the y -axis if no voltage is applied to the electrodes. By applying an AC electric field, the orientation of the liquid crystal molecules can be changed, and the molecules are tilted in the y - z plane (see the inset in the lower left of Fig. 3.9). This reorientation is accompanied by a change of the projection of the electric dipole moment of the molecules along the y -axis, which results in a change of the dielectric tensor ϵ and hence a change of the index of refraction n_y in the y -direction. By applying an appropriate voltage U it is therefore possible to adjust the refractive index and thereby the phase $\Delta\phi$ that is accumulated by the light passing through the pixel:

$$\Delta\phi(U, \omega) = \frac{\omega d}{c} [n_y(U, \omega) - n_y(0, \omega)], \quad (3.32)$$

where d is the spacing of the substrates and ω is the frequency of the incident light. In order to determine $\Delta\phi(U, \omega)$, it is necessary to perform two calibration measurements, which are described in detail in Ref. [88]. Briefly, the phase difference as a function of the applied voltage has to be measured, and it has to be determined which frequency components pass through each pixel. The voltage can in principle be varied between 0 and 10 V in 4096 steps, but for introducing a phase between 0 and 2π it is sufficient to use a voltage region of ca. 2000 steps. Still, as the display has 128 pixels, 2000^{128}

different pulse shapes can be generated.

The pixelation of the LCD leads to practical limitations for the pulse shapes that can be realized. Due to the finite number of pixels, not every phase function can be generated with sufficient accuracy. The approximation of continuous phase functions with a step-like function² due to the pixelation leads to discretization artifacts in the form of pre- or postpulses [89, 90], which have the same time structure as the main pulse, but much lower intensities. The pre- or postpulses appear periodically in distances δt from the main pulse. This temporal distance depends on $\delta\omega$, the width of each frequency interval that is modulated by a single pixel:

$$\delta t = 2\pi/\delta\omega. \quad (3.33)$$

With the parameters of the employed pulse shaper and laser system, δt is about 4 ps, and this is the maximum duration for shaped pulses if interference effects with pre- or postpulses are to be avoided. Further limitations of the employed pulse shaper are detailed in [43, 88, 91].

As the liquid crystal molecules are birefringent, the described modulation of the spectral phase is only feasible if the incident light is polarized along the extraordinary direction of the molecules. Because the employed LCD can only modulate the phase of s-polarized light, while the laser beam is p-polarized, a $\lambda/2$ -waveplate is inserted before the SLM in order to rotate the polarization by 90° . However, as the gratings are optimized for a maximum efficiency for p-polarized light, a second $\lambda/2$ -waveplate is placed after the SLM in order to restore the original polarization state. If the light incident on the LCD has a different polarization, the LCD can be used to change the polarization state (see next subsection), which can be transferred to an amplitude modulation by inserting a polarizer after the LCD. This property is exploited for the calibration measurements. If two layers of LCD-pixels are used, which have mutually perpendicular orientations of the liquid crystals molecules, the phase and amplitude of the different frequency components can be shaped simultaneously. Such a device can also be employed to shape the phase and the time-dependent polarization state simultaneously, which will be the subject of the next subsection.

3.4.2 Polarization laser pulse shaping

In principle, polarization-shaped laser pulses can be generated by splitting a laser pulse into two components which are shaped separately. One option, which has been proposed by Kakehata et al. [92], is to use a Mach-Zehnder interferometer and place a pulse shaper in each arm to shape the individual components. The polarizations of

²As the waist of each frequency component is about $30 \mu\text{m}$ at the Fourier plane, the applied phase function is smoothed to some extent.

both components should be orthogonal, which can be achieved, e.g., by using a polarizing beamsplitter to divide the incoming beam (which should have a polarization that is tilted by 45° relative to the s- or p-polarization) into two orthogonal polarization components of equal intensity. The components that are shaped separately in the arms of the interferometer can then be recombined to form a single polarization-shaped pulse. Recently, another setup has been proposed and implemented by Lindinger et al. [93, 94]. They split the initial beam into two components, which are then shaped individually in the same LCD-SLM, using one half of the 640 LCD pixels for each component. The polarization of one component is then turned by 90° with a $\lambda/2$ -waveplate in one arm of an interferometer, and the two components are then recombined with a polarizing beamsplitter. Both of these approaches have the drawback that they require a setup that is interferometrically stable. Already small variations of the optical pathlengths of the individual components by a fraction of the wavelength can lead to drastic changes in the polarization state. However, typical quantum control experiments usually take several hours, and it is difficult to provide interferometric stability on such timescales.

By employing a LCD-SLM with two liquid crystal layers which have mutually perpendicular optical axes, a polarization pulse shaper setup can be realized which does not require interferometric stability, as both components share the same optical path. After introducing the principle of operation, two such polarization pulse shaper setups are introduced that were implemented by our group [43, 91, 95] and used for the experiments described in chapters 4 and 5.

Principle of operation

Fig. 3.10 shows how a single LCD pixel can be used to change the polarization state of the incident frequency component. If the optical axis is tilted by 45° with respect to the polarization direction of the electric field, the pixel functions like a waveplate with variable retardation. The incident electric field can be decomposed into two orthogonal components 1 and 2, one perpendicular and one parallel to the optical axis of the liquid crystal molecules. By applying a voltage to the pixel, the index of refraction for the extraordinary component can be modified, leading to different optical pathlengths for the components 1 and 2. The resulting phase difference leads to a change of the polarization state of the frequency component passing through the pixel, as indicated in Fig. 3.10. In this way, either linear polarization along the x - or y -direction or elliptical polarizations can be generated. The degree of ellipticity depends on the relative phase difference $\Delta\phi$ between the components 1 and 2.

If only a single LCD layer is used, only the polarizations of the individual frequency components and at the same time the phase function of the extraordinary component can be modified. By adding a second LCD layer whose optical axis is perpendicular to the one of the first layer, the phase function of the second component can be modified as well. The total electric field in the time domain is then given by the superposition of all

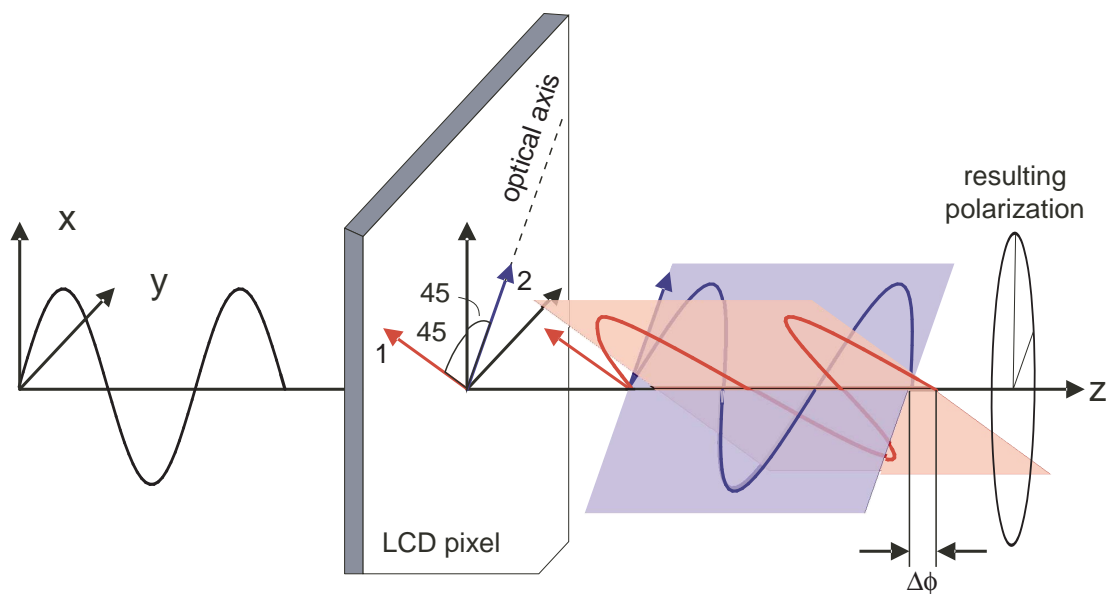


Figure 3.10: Modulation of the polarization state of one frequency component passing through an LCD pixel whose optical axis is tilted by 45° relative to the incident linear polarization. The x -polarized light can be decomposed into two orthogonal components 1 (red) and 2 (blue), which have different optical pathlengths, depending on the voltage applied to the pixel. The phase difference $\Delta\phi$ leads to an elliptical polarization of the output light.

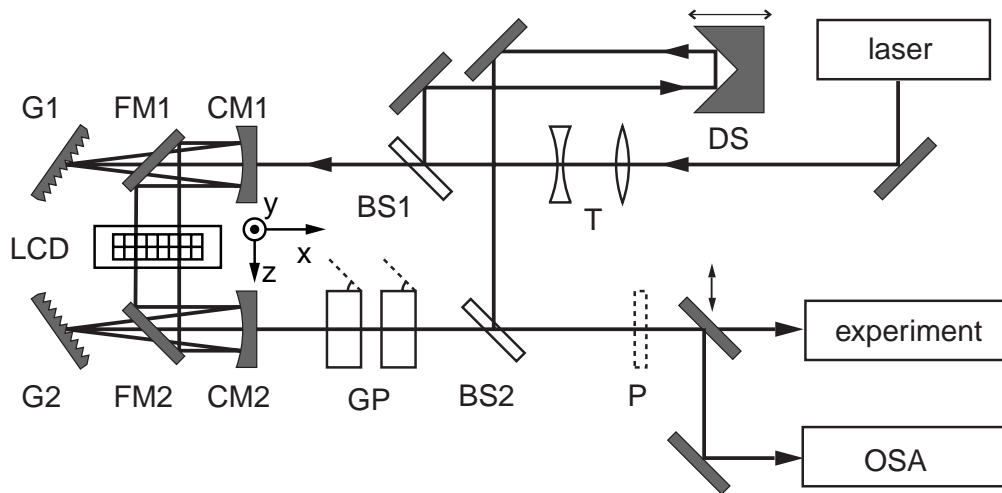


Figure 3.11: Setup of the prototype polarization pulse shaper. A telescope (T) is used to adjust the beam diameter of the Ti:sapphire femtosecond laser to the pixel height. Beam splitters (BS1 + BS2) and a delay stage (DS) provide an unshaped reference beam for the pulse characterization, which is carried out in the beam path towards the experiment. For that purpose a polarizer (P) can be introduced in the beam path. The pulse shaper itself consists of an all-reflective zero-dispersion compressor employing holographic gratings (G1 and G2), cylindrical mirrors (CM1 and CM2), planar folding mirrors (FM1 and FM2) and a two-layer liquid-crystal display (LCD). All mirrors have ‘protected silver’ coating. Compensation for the polarization-sensitive grating diffraction efficiency is achieved by transmitting the beam through a stack of glass plates (GP) tilted approximately by Brewster’s angle.

the individual elliptically polarized frequency components. Phase-only pulse shaping can also be achieved without adding any additional optics by applying identical phase functions to both LCD layers. By inserting a polarizer behind the two-layer SLM, the laser pulse can be shaped in phase and amplitude.

Polarization pulse shaper setups

Two different polarization pulse shapers were used for experiments presented in this thesis. The first ‘prototype’ setup, which is depicted in Fig. 3.11 was employed for the adaptive optimization experiment presented in chapter 4. The setup and the theoretical aspects of polarization shaping are presented in detail in the thesis of T. Brixner [43]. Like the phase-only pulse shaper introduced in chapter 3.4.1, the design is based on a zero-dispersion compressor in a $4f$ -geometry. The incoming beam travels along the z -direction and is polarized along the x -direction (the orientation of the different axes is shown in Fig. 3.11). A small portion of the beam is split off by a beamsplitter to pro-

vide an unshaped reference pulse for the characterization of the polarization-shaped laser pulses via spectral interferometry (see chapter 3.5.2). The time delay between the shaped pulse and the reference pulse, which are recombined after the $4f$ -setup with a second beamsplitter, can be adjusted with a delay stage. The incident beam is diffracted by a grating (1800 lines/mm) in Littrow configuration. Instead of the cylindrical lenses of the phase-only pulse shaper, cylindrical mirrors in conjunction with folding mirrors are employed here for collimating and focussing the beam in order to reduce aberrations. A two-layer LCD-SLM (Cambridge Research & Instrumentation) is placed in the Fourier plane of the zero-dispersion compressor. Each layer consists of 128 individually addressable pixels which have the same dimensions as those of the single-layer LCD. The optical axes of the birefringent liquid crystal molecules lie in the $x-y$ plane (see Fig. 3.11) and are tilted by $+45^\circ$ and -45° degrees with respect to the x -axis. The incident light is polarized along the x -direction and can be decomposed into two components 1 and 2 of equal magnitude, which are each parallel to the optical axis of one of the LCD-layers. By applying suitable voltages, each frequency component can be shaped in phase and polarization, as described in the previous subsection. The subsequent recollimation of the laser pulse is achieved via a second set of folding mirror, cylindrical mirror and holographic grating. A common problem of such gratings lies in the different efficiencies for x - and y -polarized light, in this case approximately 90% and 30%, respectively.

However, it is necessary to have equal intensities in both polarization components for performing unbiased polarization-shaping experiments. An option to compensate for the different grating efficiencies is given by reducing the magnitude of the more intense x -polarized component. This can be achieved by introducing a stack of glass plates ('Brewster stack') behind the $4f$ -setup, which are tilted at approximately Brewster's angle with respect to the x -polarized component. While the y -component passes through the glass plates without losses, the x -component is attenuated due to reflection. Four glass plates are employed to achieve equal intensities in both polarization components. By tuning the tilt angle of the glass plates, the variations in the pulse energy for different pulse shapes can be reduced to about 1% for the 80 fs pulses delivered by the laser system described in section 3.2. For the 30 fs laser pulses used in the experiments described in chapter 4, the obtainable pulse energy variation is increased to about 5%, because the wavelength-dependence of the grating efficiency becomes more significant for the broader spectrum. Mainly due to the low grating efficiency for y -polarized light and the reflective losses that have to be introduced with the Brewster stack, the energy throughput of this polarization pulse shaper setup is limited to about 15% (including the telescope for adjusting the beam diameter and the pulse characterization pickoff).

The energy throughput can be significantly increased, if so-called volume phase holographic (VPH) gratings [96] are employed. As illustrated by Fig. 3.12, such gratings can be designed with a high efficiency that is almost polarization-independent and that also exhibits a relatively small wavelength dependence. A new setup that is

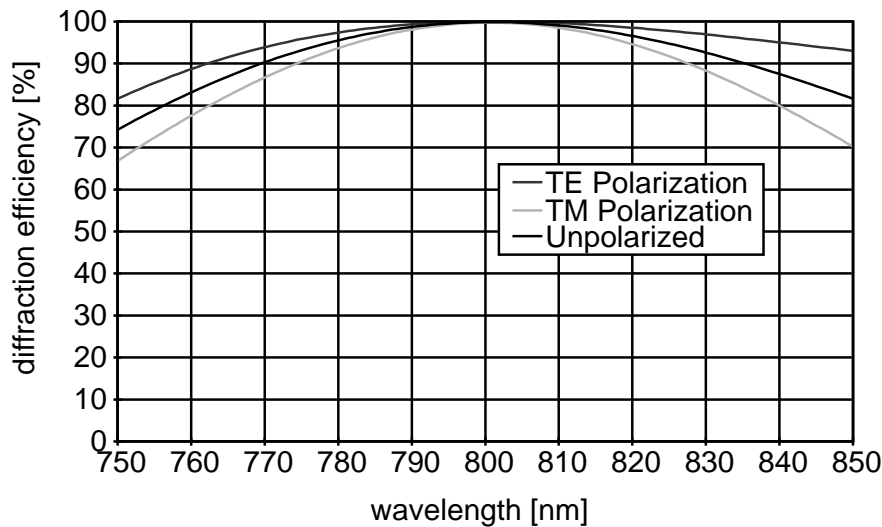


Figure 3.12: Diffraction efficiency of VPH gratings. This graph shows the theoretical performance curve (Kogelnik analysis) of a VPH grating of almost identical line spacing as the holographic reflection grating used in the prototype polarization pulse shaper setup. Note that the diffraction efficiency within the bandwidth of the used laser pulses does not differ by more than 3% for the two polarization components. Data shown is courtesy of Kaiser Optical Systems.

built around such gratings was therefore implemented, which is shown in Fig.3.13. It is described in detail in the diploma thesis of S. Fechner [95]. It is in principle very similar to the setup described above, but as the VPH gratings are operated in transmission rather than reflection, the components of the $4f$ -setup have to be rearranged. The almost equal efficiencies of the new gratings for both polarizations eliminate the need for a Brewster stack. With these modifications it was possible to increase the overall energy throughput from 15% to about 40% for both polarizations. Moreover, the new setup is more compact, and the mechanical stability has been increased significantly by mounting the optics on solid metal blocks and by minimizing the number of elements that have to be adjusted. This new setup was employed for the generation of polarization-shaped pulses in the UV, as described in chapter 5.

Mathematical description and representations of polarization-shaped pulses

For the description of a laser pulse with a time-dependent polarization state, it is in principle sufficient to represent its electric field \mathbf{E} with two linearly independent vector components \mathbf{E}_1 and \mathbf{E}_2 , which can be expressed either in the time or frequency domain. For convenience, the basis vectors can be chosen parallel to the LCD orientation axes, and as we are interested in the time-dependence of the polarization state, the discussion is limited to the time domain here. The electric field can then be represented by

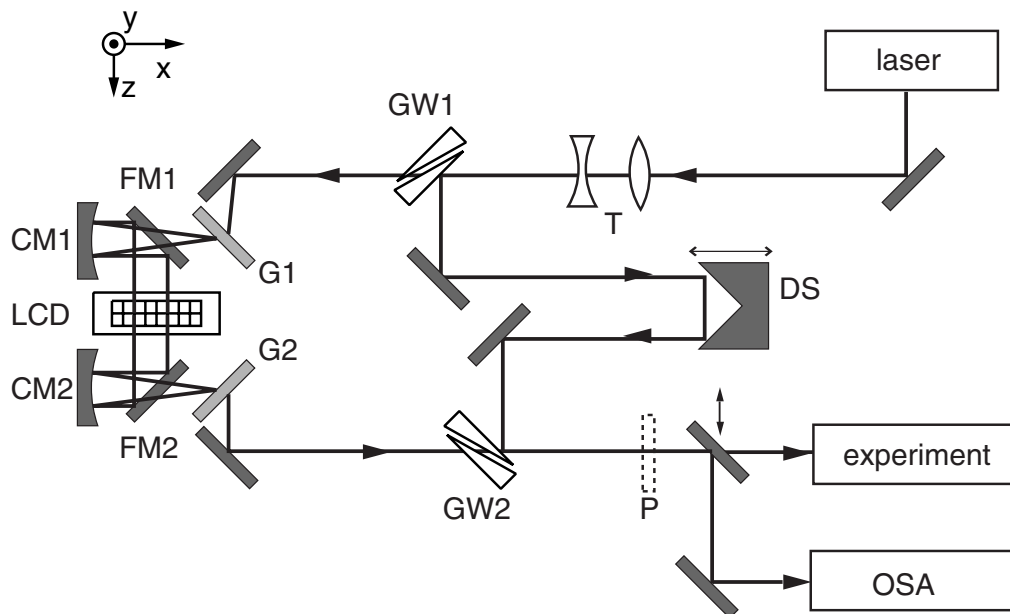


Figure 3.13: Setup of the revised polarization pulse shaper. A telescope (T) is used to adjust the beam diameter of the Ti:sapphire femtosecond laser to the pixel height. Pairs of glass wedges (GW1 + GW2) are used as beamsplitters, and together with a delay stage (DS) they provide an unshaped reference beam for the pulse characterization. For that purpose a polarizer (P) can be introduced in the beam path. The pulse shaper itself consists of a zero-dispersion compressor employing volume phase holographic (VPH) gratings (G1 and G2), cylindrical mirrors (CM1 and CM2), planar folding mirrors (FM1 and FM2) and a two-layer liquid-crystal display (LCD).

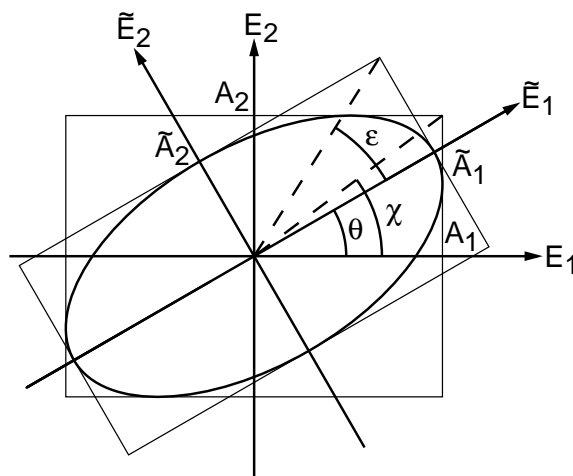


Figure 3.14: Elliptical pulse parameters. The light polarization ellipse is characterized by the major principal axis \tilde{A}_1 and the minor principal axis \tilde{A}_2 . These two amplitudes define the angle of ellipticity ε . The ellipse-inherent \tilde{E}_1 – \tilde{E}_2 coordinate system is rotated by the orientation angle θ with respect to the laboratory frame E_1 – E_2 coordinate system. In the laboratory system, the ratio of the amplitude components A_1 and A_2 defines the angle χ as indicated.

$$\begin{aligned} \mathbf{E} &= \mathbf{E}_1 + \mathbf{E}_2 = \begin{pmatrix} E_1(t) \\ 0 \end{pmatrix} + \begin{pmatrix} 0 \\ E_2(t) \end{pmatrix} \\ &= \begin{pmatrix} A_1(t) \cos[\omega_0 t + \varphi_1(t)] \\ A_2(t) \cos[\omega_0 t + \varphi_2(t)] \end{pmatrix}, \end{aligned} \quad (3.34)$$

where ω_0 is the center frequency, $A_1(t)$ and $A_2(t)$ are the temporal amplitudes and $\varphi_1(t)$ and $\varphi_2(t)$ are the temporal phase modulations of the two polarization components. While this representation of the electric field is mathematically convenient, it is difficult to extract the momentary polarization state from it. This is due to the fact that the polarization state results from the coherent superposition of the two components \mathbf{E}_1 and \mathbf{E}_2 . A more intuitive picture can be obtained if an elliptical parametrization is employed, where the time-dependent variables $I(t)$ (the total intensity), $\varepsilon(t)$ (the ellipticity), $\theta(t)$ (the orientation angle) and a total phase $\varphi(t)$ are used to describe the electric field. In the following discussion, which is based on [43], the time arguments are omitted for simplicity.

Within one oscillation period, the electric field vector \mathbf{E} will follow an ellipse that is tangential to the rectangle spanned by the amplitudes A_1 and A_2 ³, as shown in

³In the slowly varying envelope approximation (SVEA), i.e., under the assumption that the amplitudes can be treated as constant during one oscillation period.

Fig. 3.14. In general, this ellipse will be tilted by the orientation angle θ with respect to the E_1 axis in the laboratory frame coordinate system, and the ellipse–inherent principal axes \tilde{A}_1 and \tilde{A}_2 can be obtained via a principal axes transformation [43]. The total momentary intensity I is then given by

$$I = I_1 + I_2 = \tilde{I}_1 + \tilde{I}_2, \quad (3.35)$$

the sum of the individual intensities, and is independent of the chosen coordinate system. As shown in Fig. 3.14, the ellipticity ε is given by

$$\tan \varepsilon = \tilde{A}_2 / \tilde{A}_1. \quad (3.36)$$

After introducing the auxiliary angle χ and the phase difference δ between the two polarization components,

$$\begin{aligned} \chi &= \arctan \frac{A_2}{A_1} \in [0, \pi/2], \\ \delta &= \varphi_2 - \varphi_1 \in [-\pi, \pi], \end{aligned} \quad (3.37)$$

the ellipticity can be expressed as

$$\varepsilon = \frac{1}{2} \arcsin[\sin(2\chi) \sin \delta] \in [-\pi/4, \pi/4]. \quad (3.38)$$

With this definition, the sign of ε determines the helicity, i.e., the sense of rotation of the electric field vector. For $\varepsilon > 0$, the electric field is in a left–handed, and for $\varepsilon < 0$ in a right–handed elliptical polarization. If $\varepsilon = 0$, the electric field is linearly polarized. With

$$\tilde{\theta} = \frac{1}{2} \arctan[\tan(2\chi) \cos \delta] \in [-\pi/4, \pi/4], \quad (3.39)$$

the orientation angle θ of the ellipse can be obtained to be

$$\theta = \begin{cases} \tilde{\theta} & \in [-\pi/4, \pi/4] & \text{if } \chi \leq \pi/4, \\ \tilde{\theta} + \pi/2 & \in [\pi/4, \pi/2] & \text{if } \chi > \pi/4 \wedge \tilde{\theta} < 0, \\ \tilde{\theta} - \pi/2 & \in [-\pi/2, -\pi/4] & \text{if } \chi > \pi/4 \wedge \tilde{\theta} \geq 0. \end{cases} \quad (3.40)$$

The last elliptical pulse parameter, the total phase φ is given by [43]:

$$\varphi = \varphi_1 + \text{sign}\{\theta\varepsilon\} \arccos \left[\sqrt{\frac{I}{I_1}} \cos \theta \cos \varepsilon \right]. \quad (3.41)$$

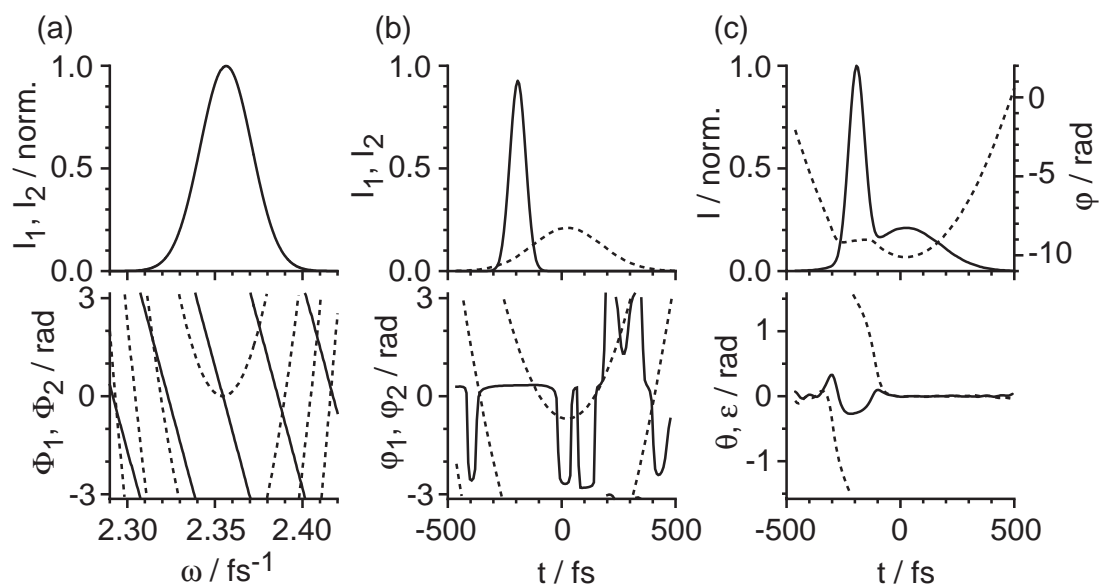


Figure 3.15: Representations of a polarization-shaped laser pulse. This figure shows (a) spectral intensities (top part) and spectral phases (bottom part) for component 1 (dashed line) and component 2 (solid line), (b) temporal intensities (top part) and temporal phase modulations (bottom part) for component 1 (dashed line) and component 2 (solid line), and (c) the temporal total intensity (top part, solid line) and total phase (top part, dashed line) as well as the temporal evolution of the ellipticity angle (bottom part, solid line) and the orientation angle (bottom part, dashed line).

It describes the rotation of the electric field vector on the polarization ellipse relative to the perihelion of the ellipse. If one polarization component is negligible (e.g., $A_2 \approx 0$), the total phase resembles the phase of the remaining component (in this case $\varphi \approx \phi_1$). In analogy to Eq. 3.12 the momentary frequency of the polarization shaped pulse can be obtained via

$$\omega(t) = \omega_0 + \frac{d\varphi(t)}{dt}. \quad (3.42)$$

The various representations of polarization shaped pulses are compared in Fig. 3.15. For a relatively simple pulse shape, the intensities and phases are shown in the frequency (a) and time (b) domain, together with the elliptical pulse parameters (c). The data shown results from a simulation for a bandwidth limited pulse with a Gaussian spectrum (equal intensities in both components) and a pulse duration of 80 fs. A quadratic spectral phase of $b_2 = 10^4 \text{ fs}^2$ for the E_1 component and a linear spectral phase of $b_1 = -200 \text{ fs}$ for the E_2 component were applied. A very descriptive graphical representation can be obtained with a pseudo-3D illustration, as shown in Fig.3.16. Alternatively, the time-evolution of the polarization state can be depicted by a series of snapshots or on a Poincaré surface [43].

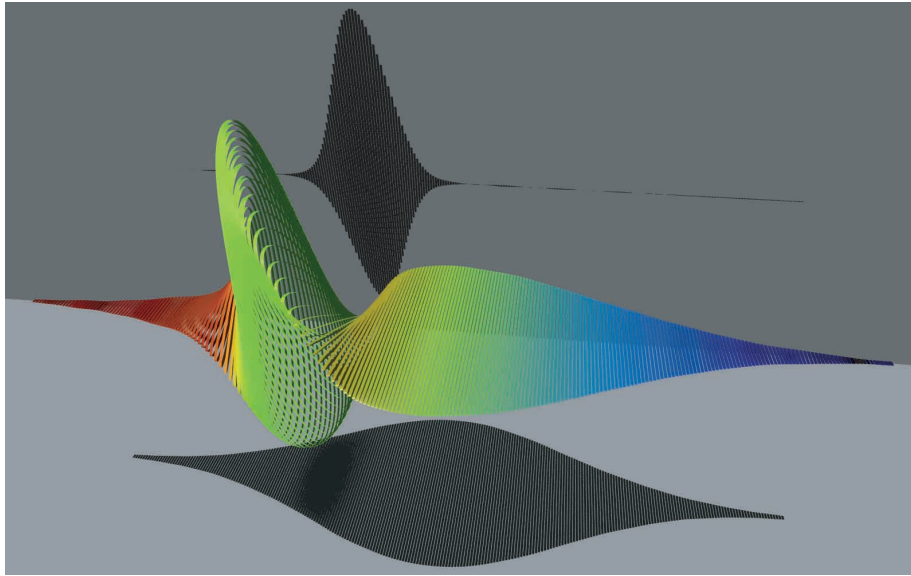


Figure 3.16: Pseudo-3D electric field representation for the simple laser pulse of Fig. 3.15. Time evolves from left to right, and electric field amplitudes are indicated by the sizes of the corresponding ellipses. The momentary frequency is indicated by colors, and the shadows represent the amplitude envelopes of component E_1 (bottom) and component E_2 (top) separately.

Experimentally, polarization-shaped pulses can be characterized by the dual-channel spectral interferometry method described in the section 3.5.2. For an accurate calculation of experimentally generated polarization-shaped pulses, the modification of the polarization state by optical components has to be taken into account. This can be achieved by experimental measurement of the Jones matrix, which will be briefly discussed in the next section.

Polarization modulation by optical elements and Jones matrices

Optical elements like mirrors, gratings or beamsplitters can modify the polarization state of a light wave upon reflection or transmission. The reflection and transmission properties can be calculated with the Fresnel formulas [97], and the effects of an optical element on the polarization state can be described by a 2×2 complex matrix, the so-called Jones matrix (see Ref. [98]). As the modification of the polarization state depends on the frequency of the incident light, a discussion of these effects in the frequency domain is appropriate.

Consider an incident electric field composed of two polarization components, $E_{1,\text{in}}^+(\omega)$ and $E_{2,\text{in}}^+(\omega)$ ⁴. The action of an optical element on the polarization state can

⁴For a definition of $E^+(\omega)$ see Eq. 3.3.

then be expressed for each frequency component by a 2×2 complex matrix \hat{J} , which transfers the incident electric fields $E_{1/2,\text{in}}^+(\omega)$ to the output electric fields $E_{1/2,\text{out}}^+(\omega)$:

$$\begin{pmatrix} E_{1,\text{out}}^+(\omega) \\ E_{2,\text{out}}^+(\omega) \end{pmatrix} = \begin{pmatrix} J_{11}(\omega) & J_{12}(\omega) \\ J_{21}(\omega) & J_{22}(\omega) \end{pmatrix} \begin{pmatrix} E_{1,\text{in}}^+(\omega) \\ E_{2,\text{in}}^+(\omega) \end{pmatrix}. \quad (3.43)$$

The diagonal elements J_{11} and J_{22} of \hat{J} can change the amplitude and/or phase of the two components, but they affect the original polarization components separately. The off-diagonal elements J_{12} and J_{21} , however, couple the two initial polarization components. For example, if J_{12} is non-zero, the resulting polarization component $E_{1,\text{out}}^+(\omega)$ will be modified by an amount which is proportional to the incident polarization component $E_{2,\text{in}}^+(\omega)$. This undesirable mixing effect warps the polarization state of the applied pulse shape, and therefore it is advisable to keep the number of additional optical elements between the polarization pulse shaper and the point of interaction in the experiment as small as possible. A Berek compensator [99] can be used to compensate for the coupling effects between the two polarization components (see chapter 5).

The modification of the polarization state by n subsequent optical elements is given by the matrix product of the corresponding Jones matrices:

$$\hat{J}(\omega) = \hat{J}^{(n)}(\omega)\hat{J}^{(n-1)}(\omega) \dots \hat{J}^{(1)}(\omega), \quad (3.44)$$

where $\hat{J}^{(1)}(\omega)$ is the Jones matrix of the first, and $\hat{J}^{(n)}(\omega)$ is the Jones matrix of the last optical element along the beam path. In the following, the frequency arguments are omitted for clarity. For an ideal LCD that only modifies the spectral phase of the two incident polarization components by Φ_1 and Φ_2 , the polarization state at the interaction point in a setup containing a polarization pulse shaper can be described by

$$\begin{pmatrix} E_{1,\text{out}}^+ \\ E_{2,\text{out}}^+ \end{pmatrix} = \begin{pmatrix} J_{11}^{(2)} & J_{12}^{(2)} \\ J_{21}^{(2)} & J_{22}^{(2)} \end{pmatrix} \begin{pmatrix} e^{i\Phi_1} & 0 \\ 0 & e^{i\Phi_2} \end{pmatrix} \\ \times \begin{pmatrix} J_{11}^{(1)} & J_{12}^{(1)} \\ J_{21}^{(1)} & J_{22}^{(1)} \end{pmatrix} \begin{pmatrix} E_{1,\text{in}}^+ \\ E_{2,\text{in}}^+ \end{pmatrix}. \quad (3.45)$$

The Jones matrix $\hat{J}^{(1)}$ contains the polarization modulation by all optical elements before the LCD, and likewise $\hat{J}^{(2)}$ describes the modulation by all elements after the LCD. While an exact calculation of the overall Jones matrix is not feasible due to the limited accuracy in determining the relevant experimental parameters (e.g., the angles of incidence), it can be derived from experimental measurements. The objective of this procedure is to determine the resulting pulse shape as a function of the applied spectral phases Φ_1 and Φ_2 . For this purpose it is advantageous that Eq. 3.45 can be transformed into an expression where the action of the active element, i.e., the LCD, is separated from the passive optical elements [43]:

$$\begin{pmatrix} E_{1,\text{out}}^+ \\ E_{2,\text{out}}^+ \end{pmatrix} = \begin{pmatrix} a_{11} & a_{12} \\ a_{21} & a_{22} \end{pmatrix} \begin{pmatrix} e^{i\Phi_1} \\ e^{i\Phi_2} \end{pmatrix}. \quad (3.46)$$

The matrix \hat{a} is identical for all pulse shapes, but it contains the incident electric fields $E_{1/2,\text{in}}^+(\omega)$. For an accurate calculation of an applied pulse shape it is therefore necessary to experimentally determine the Jones matrix under identical experimental conditions. The frequency-dependent components of \hat{a} can be determined from a set of pulse shapes with different phase functions Φ_1 and Φ_2 , which are characterized via dual-channel spectral interferometry (see chapter 3.5). The matrix elements of \hat{a} are then determined by a least squares fit for each frequency component (for details see [43]).

3.5 Laser pulse characterization

With the ability to create and manipulate ultrashort laser pulses on the fs timescale comes the need to characterize these pulses, i.e., to determine their electric field in the frequency or time domain. Without this knowledge, it is practically impossible to evaluate or interpret experiments carried out with ultrashort laser pulses. While the spectral intensity can easily be measured with a spectrometer, information on the spectral phase is lost during such a measurement. Measurements in the time domain suffer from the same dilemma as direct pulse shaping in the time domain, i.e., the fact that the fastest electronic devices have response times on the order of pico- or nanoseconds. However, for measuring a short event, one usually requires another event which has an even shorter duration. The solution to this dilemma lies in employing the laser pulse itself, or a reference pulse of comparable duration, for the characterization of the pulse in phase and amplitude. Several different techniques have been developed for this purpose, among them FROG (“Frequency Resolved Optical Gating”) [100–102], SI (“Spectral Interferometry”) [103], SPIDER (“Spectral Phase Interferometry for Direct Electric Field Reconstruction”) [104–110], and others, along with variations that are specifically designed for minimizing or augmenting certain inherent disadvantages of these techniques.

The task at hand here is the characterization of shaped pulses with durations from 80 fs up to a few ps, at central wavelengths of 400 nm and 800 nm. For the experiments presented here, the laser pulse characterization methods FROG, XFROG, and SI were employed, which will now be briefly introduced. A very comprehensive discussion of various pulse characterization techniques can be found in Ref. [111].

3.5.1 FROG and XFROG

Both FROG and XFROG are pulse characterization techniques that are based on a correlation of the unknown laser pulse either with a copy of itself (FROG) or with an-

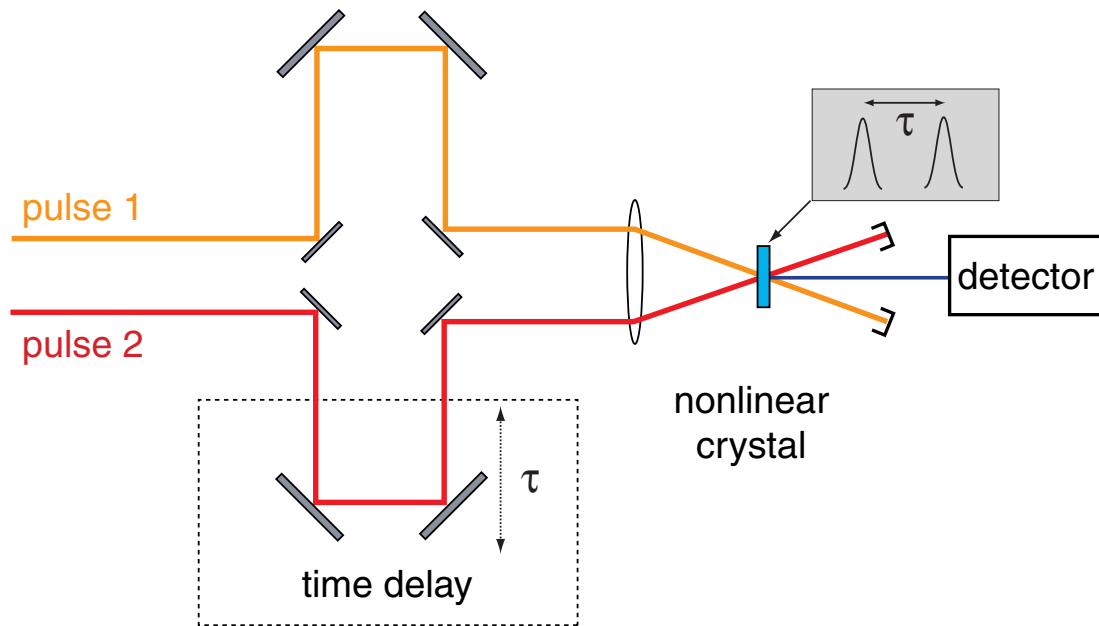


Figure 3.17: With this setup, four pulse characterization techniques can be realized: autocorrelator, cross-correlator, FROG and XFROG, depending on the nature of the employed laser pulses, the nonlinear process and the detector. In any case, two pulses, which can be temporally delayed relative to each other, are spatially overlapped in a nonlinear crystal. The resulting signal (SHG, SFG or DFG) can then be detected in dependence on the temporal delay τ . In the case of the autocorrelation, the pulse 1 and 2 are identical copies and only the intensity of their cooperative signal is detected. Therefore a complete characterization of the field is not possible, except in special cases. It is possible to get the complete information if the signal is recorded spectrally resolved. This variant is called FROG. If the two input pulses are not identical replica, but a known reference pulse is used for one of the two pulses, the setup is called either cross-correlator or XFROG, again depending on the employed detector. The advantages and disadvantages of the different methods are explained in the text.

other reference pulse (XFROG), in combination with a nonlinear optical process and the recording of the spectrally dispersed signal. For this purpose two pulses 1 and 2, which can be temporally delayed relative to each other within an interferometer setup, are spatially overlapped in a nonlinear crystal, as shown in Fig. 3.17. In the depicted setup, the two pulses overlap non-collinearly in the crystal. This has the advantage that only the cooperative signal that results from processes involving photons from both pulses is recorded in the detector. In a setup with collinear, overlapping incident pulses, the detector would register the signals from each individual pulse, together with the interference between them. Depending on the nature of the incident pulses 1 and 2, the exploited nonlinear process and the type of detector, four different pulse characterization methods can be realized with this setup: autocorrelator, cross-correlator, FROG and XFROG. In the case of the autocorrelator, pulse 2 is a copy of pulse 1 (obtained, e.g., with a beamsplitter), and a detector is used that only measures the intensity of the cooperative SHG signal (e.g., a photodiode or a photo-multiplier). The strength of this signal (the ‘intensity autocorrelation’), in dependence of the time delay τ between the two pulses, is given by:

$$I(\tau) = \int_{-\infty}^{\infty} I(t)I(t - \tau) dt, \quad (3.47)$$

where constant factors have been omitted for clarity. While being conceptually simple, autocorrelation measurements have several serious drawbacks. The major problem of the autocorrelator is that information on the phase of the electric field is not accessible. The autocorrelation is in general extremely ambiguous, and very different intensity profiles $I(t)$ can yield the same autocorrelation signal $I(\tau)$ [111]. The autocorrelation is also ambiguous regarding the temporal development, as a pulse with an intensity profile $I(t)$ yields the same autocorrelation signal as a pulse with the temporally inversed intensity profile $I(-t)$. While the ambiguities and the lack of information on the phase and on the temporal structure of a pulse make the autocorrelator a poor choice for an accurate pulse characterization, an autocorrelation gives a good indication of the pulse duration and is very helpful for monitoring the stability of a laser system.

A cross-correlator is very similar to an autocorrelator, but pulse 1 and pulse 2 are not identical copies of the same pulse. Instead, the unknown pulse is correlated with a reference pulse. In general the two pulses can have different spectra, and the resulting SFG or DFG signal is measured rather than a SHG signal. The propagation direction of the signal after the crystal depends on the nature of the exploited nonlinear process (see Fig. 3.5). The cross-correlation signal is of the form

$$I_c(\tau) = \int_{-\infty}^{\infty} I(t)I_{ref}(t - \tau) dt. \quad (3.48)$$

Compared to an autocorrelation measurement, a cross-correlation offers some advan-

tages. For example, it can also be used to measure pulses at wavelengths for which no SHG crystals are available. By resorting to SFG (or DFG) processes, pulses in the UV spectral range can also be measured. Moreover, the temporal inversion ambiguity of the autocorrelator is avoided, and at least the temporal envelope of the measured pulse becomes more apparent, provided that the reference pulse has a simple and well known structure. Another advantage is that also very weak pulses that generate a very low SHG signal themselves can be measured by employing a high-intensity reference pulse.

A SHG-FROG is basically an autocorrelator setup, in which the detector that is only sensitive to the total intensity is replaced with a detector that records the spectrally dispersed cooperative signal from the correlation of the two pulses (i.e., a spectrometer is used as a detector instead of a photodiode). The recorded signal, the so-called FROG trace, consists of the full spectra of the cooperative signal, recorded for varying time delays τ between the two pulses. It is given by the square of the electric field:

$$I_{FROG}(\omega, \tau) = |E_{sig}(\omega, \tau)|^2 = \left| \frac{1}{\sqrt{2\pi}} \int_{-\infty}^{\infty} E_{sig}(t, \tau) e^{-i\omega t} dt \right|^2, \quad (3.49)$$

where constant factors are again left out for clarity. $E_{sig}(t, \tau)$, the electric field that gives rise to the measured FROG trace in Eq. 3.49, is given by:

$$E_{sig}(t, \tau) = E(t)E(t - \tau) = A(t)A(t - \tau)e^{i[\phi(t) + \phi(t - \tau)]}, \quad (3.50)$$

where $A(t)$ is the amplitude and $\phi(t)$ is the phase of the electric field $E(t)$ that is to be characterized. For recovering this electric field from the FROG trace, it is useful to introduce the Fourier transform of $E_{sig}(t, \tau)$ with respect to τ :

$$E_{sig}(\Omega, t) = \frac{1}{\sqrt{2\pi}} \int_{-\infty}^{\infty} E_{sig}(t, \tau) e^{-i\Omega\tau} d\tau, \quad (3.51)$$

and its inverse transformation

$$E_{sig}(t, \tau) = \frac{1}{\sqrt{2\pi}} \int_{-\infty}^{\infty} E_{sig}(\Omega, t) e^{i\Omega\tau} d\Omega. \quad (3.52)$$

With these transforms, the FROG trace in Eq. 3.49 can be rewritten as a two-dimensional Fourier transformation:

$$I_{FROG}(\omega, \tau) = \frac{1}{2\pi} \left| \int_{-\infty}^{\infty} \int_{-\infty}^{\infty} E_{sig}(\Omega, t) e^{i\Omega\tau - i\omega t} d\Omega dt \right|^2. \quad (3.53)$$

The FROG trace can thus be re-expressed as a two-dimensional phase-retrieval problem, that – unlike the one-dimensional problem – can be solved iteratively [111].

An integration of $E_{sig}(t, \tau)$ over the time delay τ is given by setting $\Omega = 0$ in Eq. 3.51:

$$E_{sig}(\Omega = 0, t) = \frac{1}{\sqrt{2\pi}} A(t) e^{i\phi(t)} \int_{-\infty}^{\infty} A(t - \tau) e^{i\phi(t - \tau)} d\tau \quad (3.54)$$

$$= \frac{1}{\sqrt{2\pi}} A(t) e^{i\phi(t)} \int_{-\infty}^{\infty} A(\tau') e^{i\phi(\tau')} d\tau' \quad (3.55)$$

$$\propto A(t) e^{i\phi(t)}. \quad (3.56)$$

As the substitution of τ with $\tau' = t - \tau$ shows, this quantity is directly proportional to $E(t)$, and hence the electric field of the unknown laser pulse can be calculated if $E_{sig}(t, \tau)$ is known. The problem of obtaining $E_{sig}(t, \tau)$ can be solved by employing suitable iterative algorithms [112, 113]. These algorithms generally start with a random pulse shape, for which the FROG trace is calculated via Eq. 3.49. The resulting FROG trace is compared with the experimental data, and the electric field is then iteratively improved by minimizing the discrepancy between measured and calculated FROG trace. In this work, a commercial software is used for the FROG and XFROG retrieval process (FROG version 3.2.2 from Femtosoft Technologies [114]). By this procedure, the electric field can be retrieved both in the time and frequency domain, with only few remaining ambiguities. From Eq. 3.49 it is apparent that the FROG trace is symmetric with respect to time delay $\tau = 0$, and consequently the time structure of $E(t)$ is ambiguous regarding time inversion. Concerning the frequency domain, the intensity $I(\omega)$ can be determined unambiguously, while the retrieved spectral phase $\phi(\omega)$ can have the wrong sign. Besides, the coefficients of zero and first order in Eq. 3.13, which correspond to the absolute (constant) phase and a shift in time, cannot be determined, but this is of no consequence for our purposes. The sign of $\phi(\omega)$ can be determined with a second FROG measurement, where the spectral phase of the unknown laser pulse is modified in a known way, e.g., by introducing additional material dispersion, which adds linear chirp of a known sign to the spectral phase.

Apart from SHG, various other nonlinear processes, e.g., PG (‘Polarization Gating’), TG (‘Transient Grating’) or SD (‘Self Diffraction’) can be used for pulse characterization with the FROG technique. In these cases, the recorded FROG trace and the

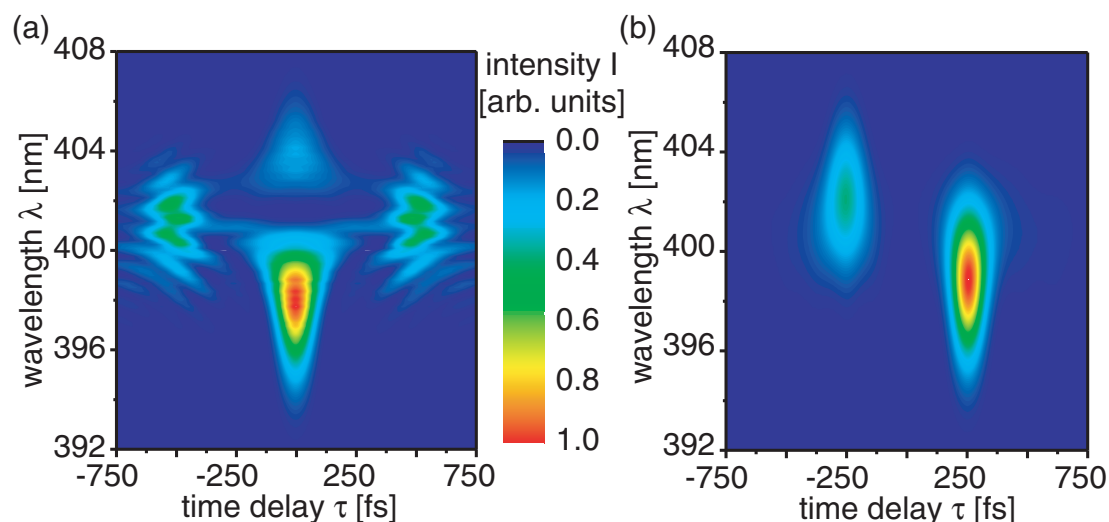


Figure 3.18: (a) FROG trace and (b) XFROG trace of a pulse with a spectral phase that creates a double pulse in the temporal regime. The individual pulses have a temporal separation of 500 fs, and they have different central wavelengths and intensities. Such a double pulse can be generated by separating the laser spectrum into two regions and applying linear spectral phases with opposite signs to both spectral regions. The resulting pulse structure can be easily read off from the XFROG trace of this shaped pulse with an unshaped Gaussian reference pulse that has the same central wavelength of 800 nm and FWHM of 15 nm. The interpretation of the FROG trace is less intuitive.

corresponding retrieval process differ from the SHG case described here. These alternative FROG designs are discussed in detail in Ref. [111], together with their inherent advantages and disadvantages.

As the SHG-FROG can be regarded as an extension of the autocorrelator setup, the XFROG corresponds to a cross-correlator setup with spectrally resolved signal detection. Consequently, the XFROG combines the advantages that both the cross-correlation and the FROG technique have over the autocorrelation. It should be noted, however, that a second pulse (the reference pulse) has to be characterized (e.g., with a FROG measurement), as a XFROG measures the correlation between the unknown pulse and a reference pulse. The electric field $E_{sig}(t, \tau)$ that generates the XFROG trace (which is mathematically equivalent to Eq. 3.49) is given by:

$$E_{sig}(t, \tau) = A(t)A_{ref}(t - \tau)e^{i[\phi(t) + \phi_{ref}(t - \tau)]}, \quad (3.57)$$

and hence the amplitude $A_{ref}(t)$ and the phase $\phi_{ref}(t)$ of the reference pulse have to be available for determining the electric field of the unknown laser pulse. In this work, a SFG-XFROG is used for characterizing 400 nm pulses, as no nonlinear crystals were available that were suited for generating the second harmonic of 400 nm light, precluding the applicability of the SHG-FROG technique. It is another inherent advantage of

the XFROG method over the FROG technique that in many cases an intuitive understanding of the measured pulse shape can be obtained directly from the XFROG trace. This is illustrated in Fig. 3.18, where (a) the FROG and (b) the XFROG trace are shown for the same shaped pulse. While the correlation of the shaped pulse with itself leads to a rather complex FROG trace, the cross-correlation of the shaped pulse with a bandwidth-limited pulse that has the same spectrum results in a XFROG trace that clearly exhibits the key features of the shaped pulse. From the XFROG trace it can be deduced that the shaped pulse consists of two subpulses which are 500 fs apart. Moreover, it is apparent that the first subpulse (at -250 fs) has a considerably lower intensity and that it is composed of longer wavelengths than the second pulse. This information is obscured in the FROG trace, and it will get apparent only after a successful retrieval process. It should be noted that the resolution of the XFROG technique depends on the reference pulse, as the XFROG trace contains simultaneously temporal and spectral information about both the reference and the unknown pulse. A temporally short reference pulse results in good resolution in the temporal delay, but its broad spectrum conceals details of the unknown pulse in the frequency direction. On the other hand, a reference pulse with a narrow spectrum results in good spectral resolution at the expense of poor temporal resolution. If the pulse widths of the reference and the unknown pulse are comparable, the resolution is distributed evenly between time and frequency [111].

As the phase-matching condition in the nonlinear crystals in a FROG or XFROG setup can only be realized for one specific set of polarizations for the incident electric fields, these techniques are impractical for the characterization of polarization-shaped pulses.

3.5.2 Spectral interferometry

The FROG technique introduced in the previous section is well suited for measuring pulses with energies down to the picojoule regime. A drawback of the FROG setup shown in Fig. 3.17 is the circumstance that only linearly polarized light can be measured, as the employed nonlinear crystal can only be aligned for the frequency doubling of a single polarization direction. For characterizing a laser pulse that contains two polarization components, it would therefore be necessary to either realign the nonlinear crystal, or to turn the polarization with a $\lambda/2$ -waveplate between the measurements for the two polarization components. However, as pointed out before, a FROG measurement does not yield information on the linear spectral phase, i.e., it is insensitive to an overall shift in time. Therefore, even if the FROG traces were measured for both polarization components, it would not be possible to deduce the momentary polarization state, which results from the coherent superposition of the two polarization components.

Fortunately, the complete characterization of an unknown laser pulse can also be realized by employing a linear technique, namely spectral interferometry (SI) [103,

115, 116], in conjunction with a well known reference pulse that is characterized, e.g., with a FROG measurement. Spectral interferometry involves the measuring of three spectra: the spectrum of the unknown laser pulse, the spectrum of the reference pulse, and the spectrum of the superposition of the two pulses which overlap spatially and are delayed by a constant time delay τ (the actual SI spectrum). From these measurements, the phase difference between the unknown pulse and the reference pulse, $\Delta\phi(\omega) = \phi_{ref}(\omega) - \phi(\omega)$ can be deduced, as will be shown below. Thus, if the phase $\phi_{ref}(\omega)$ of the reference pulse is known, the spectral phase of the unknown pulse can be calculated. Together with its measured spectrum, the unknown laser pulse is then fully characterized.

The combination of SI and FROG is called TADPOLE (‘Temporally Analysis of Dispersing a Pair of Light Electric fields’ [111, 117]). As the SI requires only linear optical measurements, it is possible to measure both very complex and very weak (down to $\approx 10^{-20}$ joules per pulse [111]) laser pulses. Once the electric field of the reference pulse has been retrieved from its FROG trace, unknown laser pulses can be characterized very fast and with low computational effort. Another important advantage is that the combination of SI and a reference FROG can also be employed for the full characterization of polarization-shaped laser pulses. For this purpose, the three spectra of an SI measurement are acquired for each polarization component. Optimal accuracy can be achieved if the SI spectra are measured simultaneously for both polarization components, e.g., with a 2D-CCD camera, as phase and intensity fluctuations can thereby be minimized. The combination of two SI measurements (one for each of the two orthogonal polarization components) and a reference pulse that is characterized with the FROG technique is also known as POLLIWOG (‘Polarization Labeled Interference versus Wavelength of Only a Glint’ [111, 118]).

The discussion of the SI technique is limited here to the case of linearly polarized laser pulses, as the extension to the measurement of two polarization components is straightforward. A setup for measuring the SI of shaped laser pulses is shown in Fig. 3.19(a). A small portion of the input laser pulse is split off by the first beamsplitter to serve as a reference pulse. After passing over a delay stage, the reference pulse is then recombined by the second beamsplitter with the shaped pulse at a fixed time delay τ . An example of the measured SI spectra is shown in Fig. 3.19(b), where identical spectra are assumed for the reference pulse and a shaped pulse (gray line). The modulated spectrum (black line) originates from the spectral interference of the two pulses. The modulation depth, i.e., the height of the minima in the interference spectrum, depends on the intensities of the two pulses and on their spatial overlap. For equally intense laser pulses and perfect spatial overlap, the minima have zero intensity. However, the method is very sensitive, and even a ratio of 1:100 of the intensities of the two pulses can lead to modulations of about 20% of the maximum intensity [111]. The spacing of the interference fringes in Fig. 3.19(b) is about $2\pi/\tau$, and deviations from this value are due to the difference in the spectral phase patterns of the reference pulse and the unknown laser pulse [91]. For the evaluation of the SI measurement it is

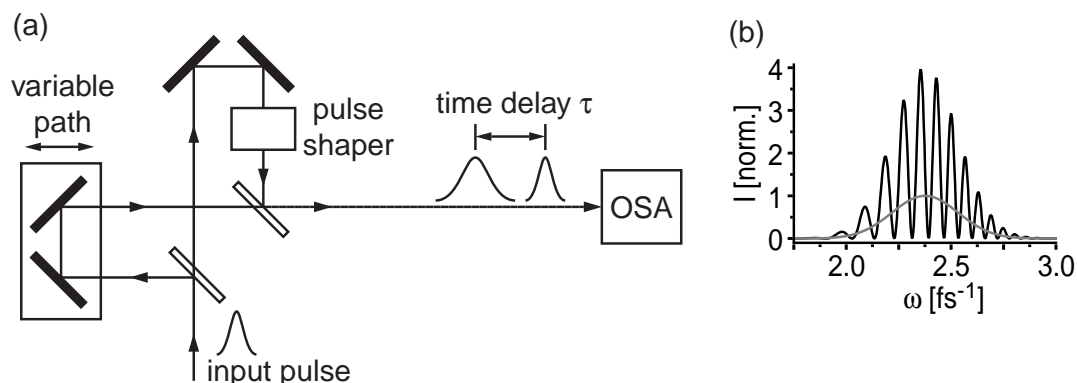


Figure 3.19: Spectral interferometry of shaped femtosecond laser pulses. The schematic setup (a) is shown along with (b) a simulated interference spectrum (black line) of a linearly chirped laser pulse (FWHM of 127 nm, center wavelength 800 nm, spectral phase coefficient $b_2 = 77.7 \text{ fs}^2$) and a bandwidth limited 7.5 fs laser pulse (the identical individual spectra of both laser pulses shown in gray) at a mutual time delay τ of 80 fs.

necessary to ascertain whether the reference pulse precedes the unknown laser pulse, or vice versa. The interference spectrum is given by

$$I_{\text{SI}}(\omega) = \left| \mathcal{F} \{ E_{\text{ref}}^+(t) + E^+(t - \tau) \} \right|^2 \quad (3.58)$$

$$= \left| E_{\text{ref}}^+(\omega) + E^+(\omega) e^{-i\omega\tau} \right|^2, \quad (3.59)$$

where \mathcal{F} denotes the Fourier transform and constant factors have been omitted for clarity. The shift in the time domain τ translates to the additional phase factor $e^{-i\omega\tau}$ in the frequency domain. With the electric fields $E_{\text{ref}}^+(\omega) = A_{\text{ref}}(\omega) e^{-i\phi_{\text{ref}}(\omega)}$ and $E^+(\omega) = A(\omega) e^{-i\phi(\omega)}$, the SI signal in Eq. 3.59 can be rewritten as

$$I_{\text{SI}}(\omega) = \left| A_{\text{ref}}(\omega) e^{-i\phi_{\text{ref}}(\omega)} + A(\omega) e^{-i(\phi(\omega) + \omega\tau)} \right|^2 \quad (3.60)$$

$$= I_{\text{ref}}(\omega) + I(\omega) + 2A_{\text{ref}}(\omega)A(\omega) \cos[\phi_{\text{ref}}(\omega) - \phi(\omega) - \omega\tau], \quad (3.61)$$

where $I_{\text{ref}}(\omega) = A_{\text{ref}}^2(\omega)$ and $I(\omega) = A^2(\omega)$ are the intensities of the individual pulses. The starting point for the data evaluation is the quantity $S(\omega)$, which is defined as the SI-signal of Eq. 3.61, from which the intensities of the two individual pulses are subtracted:

$$S(\omega) = I_{SI} - I(\omega) - I_{ref}(\omega) \quad (3.62)$$

$$= 2A_{ref}(\omega)A(\omega) \cos[\phi_{ref}(\omega) - \phi(\omega) - \omega\tau]. \quad (3.63)$$

The information on the phase difference

$$\Delta\phi(\omega) = \phi_{ref}(\omega) - \phi(\omega) - \omega\tau \quad (3.64)$$

can in principle be obtained from Eq. 3.63 via the arccos function. However, it was shown in [103] that the evaluation of the arccos function is very sensitive to experimental fluctuations, and these can lead to values of the argument of the arccos function that lie outside the domain of the arccos function, $[-1; +1]$. It is therefore advantageous to process the experimental SI data in such a way that the relevant information, i.e., the phase difference $\Delta\phi(\omega)$, can be obtained by evaluating the phase of a complex number. This procedure is much less sensitive to noise than the application of the arccos function to a real-valued number. First, the Fourier transform of $S(\omega)$ is calculated:

$$S(t) = \frac{1}{\sqrt{2\pi}} \int_{-\infty}^{\infty} S(\omega) e^{i\omega t} d\omega \quad (3.65)$$

$$= \frac{1}{\sqrt{2\pi}} \int_{-\infty}^{\infty} [E_{ref}^+(\omega)]^* E^+(\omega) e^{i\omega(t-\tau)} d\omega$$

$$+ \left(\frac{1}{\sqrt{2\pi}} \int_{-\infty}^{\infty} [E_{ref}^+(\omega)]^* E^+(\omega) e^{i\omega(-t-\tau)} d\omega \right)^* \quad (3.66)$$

$$= \tilde{S}(t-\tau) + \tilde{S}^*(-t-\tau), \quad (3.67)$$

where $\tilde{S}(t)$ is given by

$$\tilde{S}(t) = \frac{1}{\sqrt{2\pi}} \int_{-\infty}^{\infty} [E_{ref}^+(\omega)]^* E^+(\omega) e^{i\omega t} d\omega. \quad (3.68)$$

As $S(\omega)$ is a real-valued quantity, its Fourier transform $S(t)$ is subject to the condition $S(t) = S^*(-t)$, and it can therefore be written as the sum of two symmetric terms. If the time delay τ between the two pulses is longer than the duration of either pulse, it is sufficient to consider only the positive-delay part $S^+(t)$ of $S(t)$, as the contribution

around time $t \approx \tau$, $\tilde{S}(t - \tau)$, can then be separated from the contribution $\tilde{S}^*(-t - \tau)$ around $t \approx -\tau$. For $\tau > 0$, $S^+(t)$ is given by

$$S^+(t) = \tilde{S}(t - \tau), \quad (3.69)$$

which is non-zero only for positive times t . The inverse Fourier transform of $S^+(t)$ into the frequency domain yields

$$\begin{aligned} S^+(\omega) &= \frac{1}{\sqrt{2\pi}} \int_{-\infty}^{\infty} \tilde{S}(t - \tau) e^{-i\omega t} dt \\ &= [E_{ref}^+(\omega)]^* E^+(\omega) e^{-i\omega\tau} \\ &= A_{ref}(\omega) A(\omega) e^{i[\phi_{ref}(\omega) - \phi(\omega) - \omega\tau]}. \end{aligned} \quad (3.70)$$

With this equation, the goal of expressing the determination of the phase difference $\Delta\phi(\omega) = \phi_{ref}(\omega) - \phi(\omega) - \omega\tau$ as the evaluation of the phase of a complex number is achieved. The linear factor $\omega\tau$ in the phase difference, which describes the temporal delay between shaped pulse and reference pulse, is not important for the pulse characterization and can be removed by a linear fit. As the phase of the reference pulse, $\phi_{ref}(\omega)$, is obtained from a separate FROG measurement, the phase $\phi(\omega)$ can be determined, and together with its already measured spectrum, the unknown pulse is fully characterized.

3.6 Joint time–frequency representations

During the discussion of the XFROG technique in section 3.5.1, it became apparent that the XFROG trace shown in Fig. 3.18 is an invaluable aid for the intuitive understanding of complex pulse structures. More generally, joint time–frequency representations [119] that indicate which frequencies appear at which times during the laser pulse can be employed to illustrate the nature of shaped pulses. Examples for such representations include the Wigner distribution [120–122], the Wavelet transform [123, 124] and the Husimi distribution [125]. The discussion is limited here to the Wigner distribution that was originally introduced as a phase–space representation in quantum mechanics [120], and the Husimi distribution, which can be derived from the Wigner distribution. The Wigner distribution $W(E^+; t, \omega)$ of a laser pulse with the electric field E^+ is given by

$$W(E^+; t, \omega) = \int_{-\infty}^{\infty} E^+(\omega + \Omega) [E^+(\omega - \Omega)]^* e^{i2\Omega t} d\Omega, \quad (3.71)$$

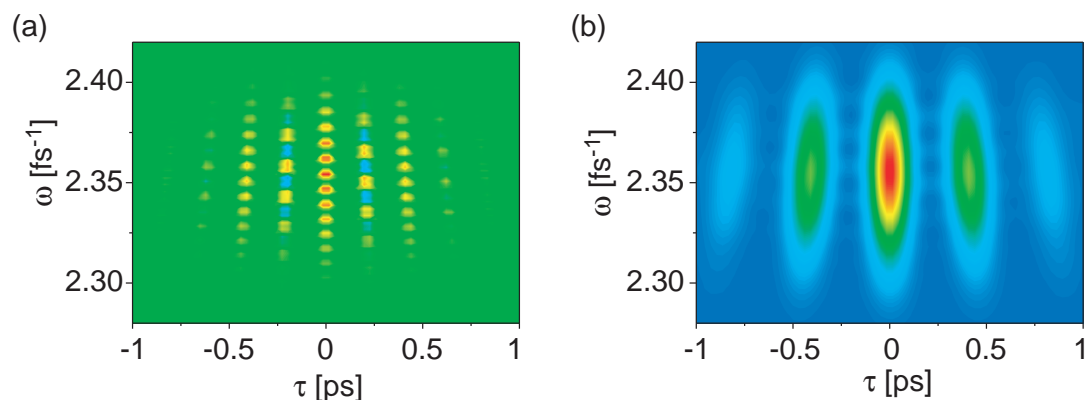


Figure 3.20: (a) Wigner and (b) Husimi representation of an ultrashort laser pulse. The joint time–frequency representations are shown for a pulse train with a temporal spacing of the subpulses of 400 fs.

or equivalently by

$$W(E^+; t, \omega) = \int_{-\infty}^{\infty} E^+(t + \tau) [E^+(t - \tau)]^* e^{-i2\omega\tau} d\tau. \quad (3.72)$$

The Wigner distribution is real–valued and bounded, but it may reach both negative and positive values, which precludes an interpretation in terms of a probability distribution. The Wigner distribution is shown in Fig. 3.20(a) for a pulse train with a temporal spacing of the subpulses of 400 fs. The presence of rapidly oscillating terms, which appear for example at time delays τ of -200 fs and $+200$ fs in Fig. 3.20(a), complicate the interpretation of the depicted pulse shape. On the other hand, the Wigner distribution has the advantageous property that integrations over the delay or frequency (the so–called marginals) yield the spectrum or temporal intensity, respectively:

$$I(\omega) = \int_{-\infty}^{\infty} W(E^+; t, \omega) dt, \quad (3.73)$$

$$I(t) = \int_{-\infty}^{\infty} W(E^+; t, \omega) d\omega. \quad (3.74)$$

However, the Wigner distribution is not easily accessible experimentally. From Eq. 3.72 it can be seen that a measurement of the Wigner distribution of a laser pulse would require a time–reversed replica of the pulse. Instead, the Wigner distribution can be calculated from the retrieved electric field if the laser pulse is accurately characterized, e.g., with the FROG technique. The Husimi distribution can be derived

from the Wigner distribution by two-dimensional smoothing that fulfills the minimum uncertainty relation. The smoothing can be implemented, e.g., by employing a two-dimensional Gaussian function with a temporal width of σ_τ and a spectral width of σ_ω . While the product of both widths has to fulfill the condition

$$\sigma_\tau \sigma_\omega = 4 \ln 2, \quad (3.75)$$

the choice of σ_τ and σ_ω is not unique. Where Husimi representations are shown in this work, a symmetrical smoothing with $\sigma_\tau = \sigma_\omega = 2\sqrt{\ln 2}$ is chosen, which distributes resolution evenly between time and frequency. The advantage that the Husimi distribution offers over the Wigner distribution is that it is positive definite and that it can be interpreted as a probability distribution. The value of the Husimi distribution at a point with coordinates τ and ω can be interpreted as the probability of finding a photon with frequency $\omega \pm \frac{1}{2}\sigma_\omega$ at time $\tau \pm \frac{1}{2}\sigma_\tau$ in the laser pulse. For comparison, the Husimi distribution is plotted in Fig. 3.20(b) for the same pulse that yields the Wigner distribution shown in Fig. 3.20(a). The disadvantage of the Husimi distribution is that the marginals do not correspond to the spectral or temporal intensities. At a first glance, the Husimi distribution of a shaped pulse looks very similar to the corresponding XFROG trace. It should be noted however, that they are not equivalent, and that the frequency axis of the XFROG shows the sum- or difference-frequency of the shaped pulse and the reference pulse, while the frequency axis of the Husimi distribution shows the frequency of the shaped pulse itself.

Another joint time-frequency representation that has recently been introduced by our group to the context of pulse shaping is the von Neumann distribution. It has been proposed in Ref. [126] as a means for parametrizing shaped pulses in terms of meaningful subsets, namely subpulses which are Gaussian in time and frequency. Such a parametrization has the potential that it leads to less complex pulse shapes in optimization experiments which can give better access to the identification of the control mechanisms exploited by the optimal pulse, while still covering a substantial part of the control parameter space.

Chapter 4

Quantum control by ultrafast polarization shaping

The generation and characterization of polarization-shaped femtosecond laser pulses were introduced in the previous chapter. Here, these techniques are applied in an adaptive optimization experiment, with the potassium dimer as a model quantum system. After introducing the possibilities and advantages of using polarization as an active agent in quantum control experiments (section 4.1), the polarization sensitivity and wavelength dependence of multiphoton ionization pathways in the K_2 molecule are discussed in section 4.2. In order to verify that polarization does indeed play a significant role in the dynamics involved in the ionization process, pump-probe experiments are carried out with various linear polarizations of the pump and probe pulses (section 4.3). These polarization-dependent dynamics are addressed and exploited in a more general fashion in an adaptive quantum control experiment that employs ultrafast polarization shaping (section 4.4), by which the polarization of the light field can be varied on the timescale of the initial laser pulse duration.

4.1 Introduction

As stated in chapter 2, the objective of coherent control is to ‘steer’ a quantum mechanical system from an initial state towards the desired final state. The main experimental tool for achieving this goal has been spectral phase (or phase-and-amplitude) shaping of femtosecond laser pulses [85, 127]. This ‘conventional’ approach to pulse shaping addresses only the scalar properties of laser pulses, i.e., momentary frequency, phase and intensity. However, the electric field and the transition dipole moment interacting with it are vectorial quantities. As quantum systems and their wave functions are three-dimensional objects, the ability to manipulate and tailor the momentary polarization state of light fields has therefore the prospect of increasing the degree of achievable control substantially. Simple time-dependent polarization profiles (without using

pulse shapers) had already been exploited in several experiments on optical [118, 128], atomic [92], and molecular systems [129]. With the polarization pulse shaping technique developed in our group (see previous chapter), the polarization state of light (i.e., the degree of polarization ellipticity and orientation of the elliptical principal axes) can be varied as a function of time within a single femtosecond laser pulse, in addition to the temporal intensity and momentary oscillation frequency.

The application of time-dependent polarization states that can thus be generated has been suggested, for example, for the generation [130, 131] and characterization [132] of attosecond light pulses, for the optical control of lattice vibrations [133] and the selective production of enantiomers [31–36]. The adaptive shaping of complex polarization profiles within a learning loop has been demonstrated by our group in an optical demonstration experiment [134], and Oron et al. have used spectral modulation of phase and polarization direction in coherent anti-Stokes Raman spectroscopy (CARS) [135].

Yet, the general prospect for manipulating light-matter interactions in three dimensions using complex polarization-shaped laser pulses goes beyond these initial suggestions or demonstrations. While this interaction is governed by the scalar product $\boldsymbol{\mu}(t) \cdot \mathbf{E}(t)$, the vectorial character of $\mathbf{E}(t)$ is ignored completely in most experimental and theoretical studies on quantum control or nonlinear spectroscopy, and only the scalar $\boldsymbol{\mu}(t)E(t)$ is considered. However, if the momentary polarization of the applied electromagnetic field is varied appropriately, the quantity $\boldsymbol{\mu}(t) \cdot \mathbf{E}(t)$ can be optimized throughout the complete temporal evolution of a quantum system. This opens many experimental perspectives, e.g., controlling which dipole transitions are allowed at any particular time during a wave-packet evolution. Thus, one can address and exploit the spatio-temporal properties of quantum wavefunctions with polarization-shaped laser pulses.

The advantages of making explicit use of polarization variation on an ultrafast time scale are demonstrated in a quantum control experiment where the photoionization of the potassium dimer K_2 is maximized (section 4.4). The corresponding results presented in this chapter are published in [136] and were among the first applications of polarization-shaped laser pulses for the control of quantum systems (together with [137]). Additional experiments employing polarization-shaped laser pulses have since then been conducted by Polack et al. [138] and Weise et al. [139].

4.2 Ionization pathways and dynamics in the potassium dimer

Alkali dimers have proven their value as prototype systems for ultrafast dynamics, and are therefore well investigated and understood both experimentally and theoretically [140–146]. Especially the photoionization process in the potassium dimer lends itself to studies of polarization effects. This is due to the fact that one of the competing

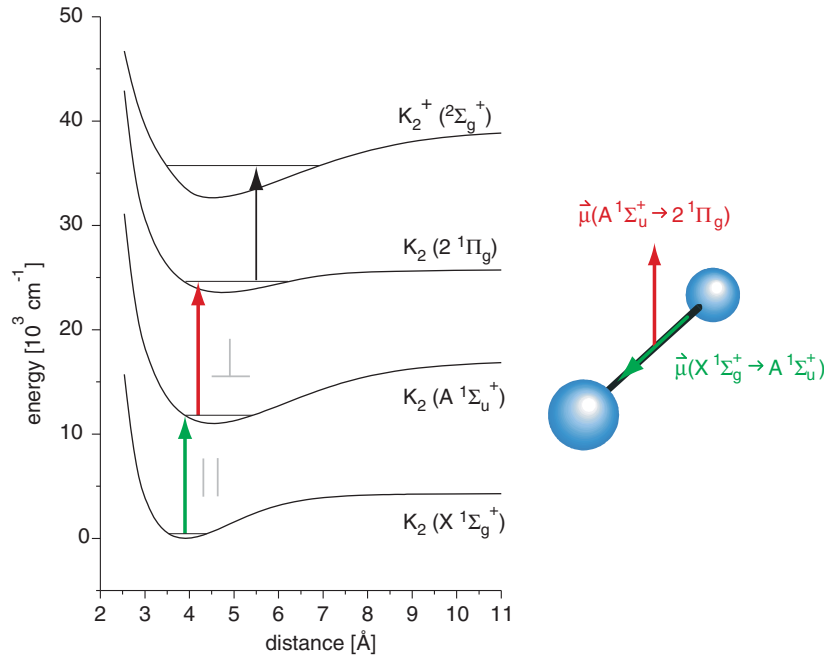


Figure 4.1: Calculated potential energy curves of the potassium dimer system, adapted from Ref. [146]. Only those curves are shown which are relevant for the excitation wavelengths used in the experiment. The arrows indicate the one-photon transitions that lead to the production of K_2^+ ions. The gray symbols indicate the light polarization with respect to the molecular axis, as required by the selection rules for the one-photon transitions involved (the two-photon process that directly connects the $X^1\Sigma_g^+$ and $2^1\Pi_g$ states is omitted for clarity). On the right side an illustration of the K_2 molecule together with the orientation of the first two transition dipole moments is shown.

transition pathways leading to the K_2^+ ion is strongly polarization dependent. The relevant potential energy curves and transitions are displayed in Fig. 4.1. Simulations show that only the $X^1\Sigma_g^+$, $A^1\Sigma_u^+$, $2^1\Pi_g$ and $K_2^+(2^1\Sigma_g^+)$ (the ionic ground state) need to be considered for the wavelengths used in our experiment, as other electronic states do not contribute to the K_2^+ yield [146]. Also, the rotational degrees of freedom can be neglected, as they are irrelevant on the short timescale of the dynamics involved.

Starting from the molecular ground state $X^1\Sigma_g^+$, the $2^1\Pi_g$ state is populated as an intermediate state before photoionization. The $2^1\Pi_g$ state can be reached from the ground state either directly by a two-photon process, or sequentially by two one-photon processes, with the first transition populating the $A^1\Sigma_u^+$ as an intermediate state. It is the latter of these pathways that is strongly polarization dependent, because according to selection rules the two electronic transitions involved, i.e., $X^1\Sigma_g^+ \rightarrow A^1\Sigma_u^+$ and $A^1\Sigma_u^+ \rightarrow 2^1\Pi_g$, require electromagnetic fields with polarizations parallel and perpendicular to the molecular axis, respectively. Hence, for maximizing the population

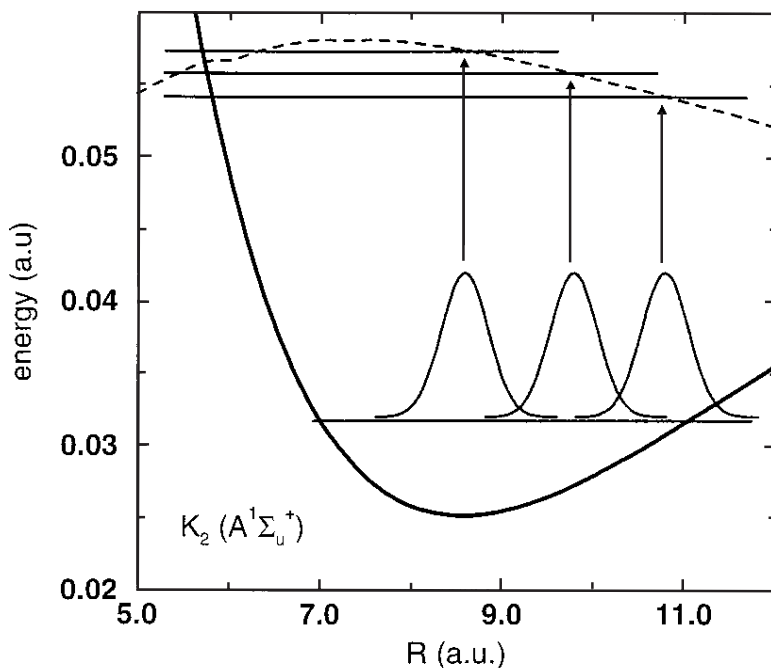


Figure 4.2: Difference potential analysis illustrating the shifting of the transient Franck–Condon point, adapted from Ref. [146]. The dashed line is the difference between the potential energy curves of the $2^1\Pi_g$ and the $A^1\Sigma_u^+$ states, and the arrows indicate the internuclear distances R where the laser frequency equals the difference potential for 800 nm (left), 816 nm (middle) and 837 nm (right).

of the $2^1\Pi_g$ state via this pathway, a pulse sequence is needed in which the polarization of the light fields are parallel to the relevant dipole moments at the appropriate Franck–Condon windows reached during the vibrational wave–packet motion.

The enhancement of the K_2^+ yield that can be achieved by using these optimal polarizations – instead of employing only one linear polarization – can be estimated by a simple model. Consider an isotropic ensemble of quantum systems in which two sequential transitions require two electromagnetic fields with mutually perpendicular polarizations. If two pulses with the same linear polarization are employed, only the projections of the polarization vector onto the involved dipole moments of the randomly oriented systems contribute to the transition rates. The total transition rate is then given by averaging over the isotropic ensemble. However, if the polarizations of the two laser pulses are perpendicular to each other, the averaging procedure gives a yield that is enhanced by a factor of two. The enhancement obtainable with polarization–shaped light can be further improved if the quantum systems are appropriately aligned or oriented with respect to the incoming light fields [147–150].

Apart from the polarization, the excitation wavelength also has a strong impact on the dynamics in the K_2 system, as the one–color pump–probe experiments carried out

by Nicole et. al. [146] reveal. Their pump–probe transients, recorded with parallel pump and probe polarizations, show a variety of structures which reflect the complicated interplay of nuclear dynamics and the ionization process. In these experiments, a relatively narrowband Ti:sapphire laser system (8 nm FWHM) was used, and the central wavelength was varied between 779 nm and 837 nm. The results show that ionization occurs predominantly at the outer turning point of the $2^1\Pi_g$ state for longer wavelengths, and shifts towards the inner turning point with decreasing wavelength. This can be explained by a difference potential analysis between the $A^1\Sigma_u^+$ and the $2^1\Pi_g$ states (confer Fig. 4.2), which shows that the Franck–Condon point shifts towards smaller internuclear distances with decreasing wavelength. A more detailed analysis of the wavelength dependent features in the pump–probe dynamics reveals that the intermediate population in the $A^1\Sigma_u^+$ is more dominant for longer wavelengths, while the pump pulse leads to significant population in the $2^1\Pi_g$ state for shorter wavelengths [146]. Taking into account the large bandwidth of the laser system used in our experiment (30 fs FWHM, spectrum shown in Fig. 4.3), one can therefore expect that a large number of transition pathways with differing dynamics is accessible. Optimal control of the multiphoton ionization process therefore requires both adjustment of the temporal intensity profile and momentary frequency as well as a variation of the polarization direction to meet the selection–rule requirements. Such a scheme cannot be achieved with shaped laser pulses with only one polarization component.

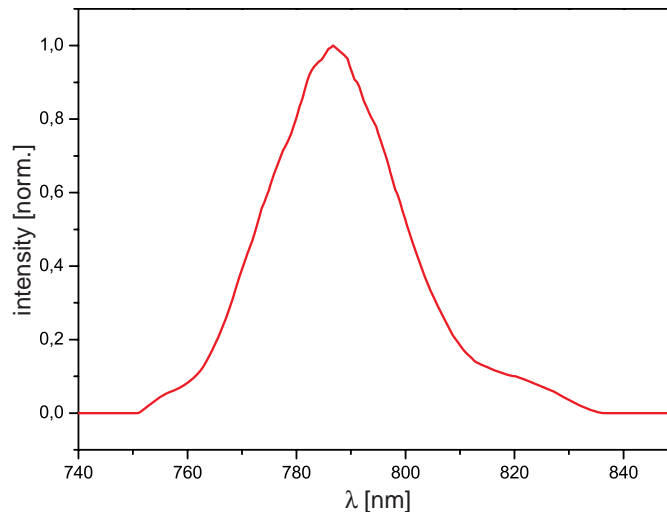


Figure 4.3: Spectrum of the laser system used for the experiments on the potassium dimer. The 30 fs (FWHM) pulses were generated with a central wavelength of 787 nm.

4.3 Pump–probe experiments with varying polarization configurations

In order to verify and demonstrate the expected influence of the polarization on the ionization yield and the dynamics involved, a series of pump–probe experiments is carried out. The experimental setup, shown in Fig. 4.4, consists of a supersonic molecular beam apparatus with a linear time–of–flight (TOF) mass spectrometer. The vacuum apparatus consists of two differentially pumped chambers, separated by a skimmer with a hole diameter of 1.5 mm. In the first chamber, the molecular beam is generated by supersonic expansion from an oven (nozzle diameter 100 μm) by evaporating metallic potassium at a temperature of 500 $^{\circ}\text{C}$, seeded with argon gas of 1.5 bar pressure. Both pump and probe laser pulses have an energy of 150 nJ and are focused with a 500 mm lens onto the potassium dimer beam. These experimental parameters ensure that strong–field effects are avoided.

In the TOF mass spectrometer ions of charge state q are accelerated to a kinetic energy of $E_{kin} = mv^2/2 = qU$, where U is the accelerating voltage of the mass spectrometer. After this initial acceleration the ions pass through a field–free drift region and are registered by a micro channel plate (MCP) detector. The time of flight, i.e., the time between the acceleration of the ions and their detection by the MCP, is therefore proportional to the square root of their mass for singly charged ions. The voltage pulse generated by their impact in the detector is then recorded either via boxcar integration (SR250 from Stanford Research Systems) and subsequent analog–to–digital conversion in a computer card or via direct transient analysis in a digital oscilloscope (LC574A from LeCroy). The mass resolution of the employed TOF mass spectrometer is sufficient to separate the potassium isotopes ^{39}K (93% natural abundance) and ^{41}K

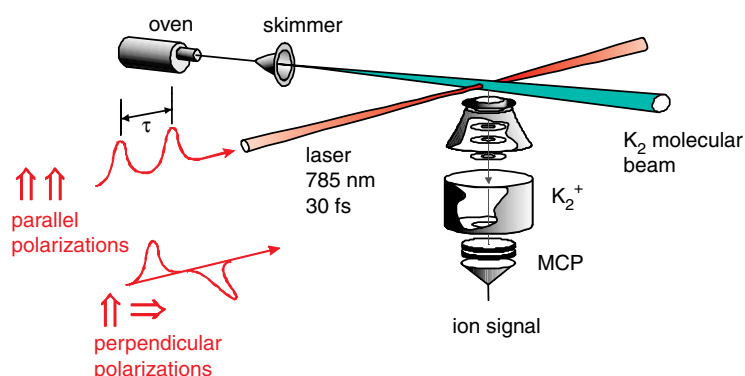


Figure 4.4: Pump–probe setup. The pump and probe laser pulses intersect with a supersonic beam of potassium dimers. The produced K_2^+ ions are detected in the TOF mass spectrometer with a micro channel plate (MCP) detector.

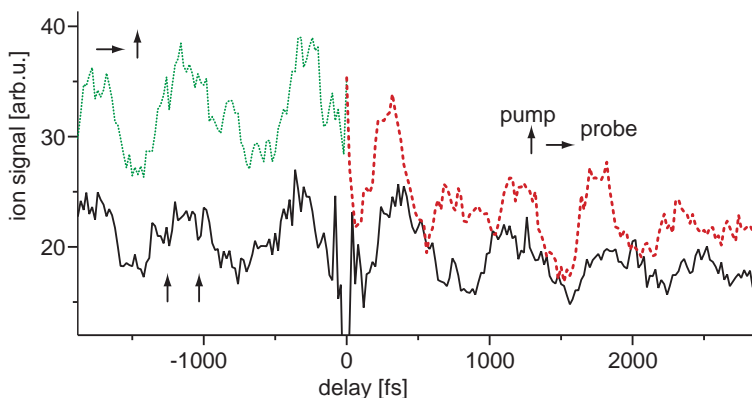


Figure 4.5: Section of pump–probe transients recorded with mutually parallel (solid black line) or perpendicular (dotted green and dashed red lines) linear polarizations. The polarization directions of the pump and probe pulses, depending on the time delay, are indicated by the arrows.

(7% natural abundance). The observable analyzed in all subsequent experiments was the ion signal of the most abundant dimer, $^{39,39}\text{K}_2$.

In the first pump–probe experiment, the equally intense pump and probe pulses are both polarized parallel to the TOF axis (and hence perpendicular to the molecular beam direction). The resulting K_2^+ yield is shown as a function of the pump–probe time delay in Fig. 4.5 (solid black line). This transient is symmetric with respect to (and shows a minimum at) time zero. After inserting a periscope that turns the polarization by 90° into the optical path of the second laser pulse, pump–probe experiments can be carried out with mutually perpendicular polarizations. The periscope is used instead of a waveplate in order to ensure a clean linear polarization over the complete spectral range. The resulting transient (Fig. 4.5, dotted green and dashed red lines) is asymmetric with respect to time zero. For both negative and positive delay times, the measured K_2^+ yield exceeds the signal of the previous experiment. Especially for negative time delays, where the pump pulse is polarized parallel and the probe pulse is polarized perpendicular to the molecular beam direction, the K_2^+ production is significantly enhanced. The general signal enhancement verifies the polarization dependence of the K_2^+ ionization pathways, and it indicates that a certain final state (in this case the K_2^+ ion) can be reached more efficiently by applying a control laser field with time-dependent polarization.

The observed asymmetry in the pump–probe transient, i.e., higher average signal for negative delay times, is a clear indication for a partial alignment of the K_2 molecules. Since the pump pulse is polarized parallel to the molecular beam direction in this case, and the dipole moment for the $X^1\Sigma_g^+ \rightarrow A^1\Sigma_u^+$ transition is parallel to the molecular axis (confer Fig. 4.1), it can be concluded that the majority of the potassium dimers fly with their angular momentum vector perpendicular to the flow direction. This ‘edge-on’

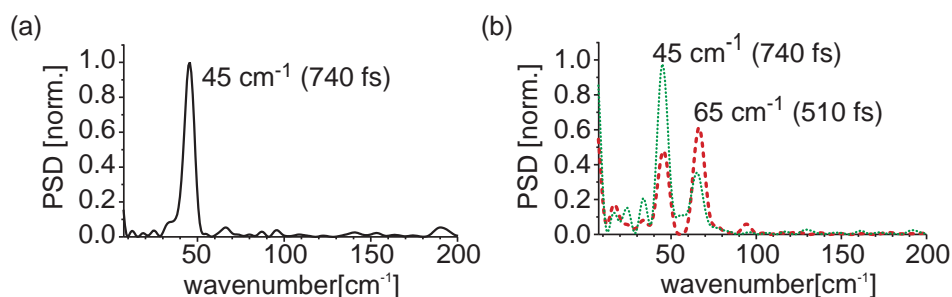


Figure 4.6: Fourier analysis of the pump–probe transients with mutually (a) parallel and (b) perpendicular polarizations. The numbers in brackets indicate the vibrational period of the associated wave packet motion. The FFTs have been performed over time periods from 0 ps to +3 ps for parallel polarizations (a) (solid black line, identical at negative delay times), from -4 ps to 0 ps for perpendicular polarizations (b) (negative delays, dotted green line) and 0 ps to +4 ps for perpendicular polarizations (b) (positive delays, dashed red line).

configuration is the most common molecular alignment observed in molecular beams [150, 151]. It can be attributed to the collisional alignment of the angular momentum in supersonic beams seeded with light carrier gases [151]. A descriptive explanation for this is given by the Gorter mechanism [152], which argues that molecules with this orientation offer a smaller target cross-section to collisions and therefore suffer less randomizing events than those molecules with total angular momentum parallel to the flow. However, the Gorter mechanism is not a universally valid description, as both elastic and inelastic processes have to be taken into account [151]. The degree of molecular alignment in a supersonic beam depends on a variety of experimental details, such as source pressure, nozzle geometry, angular displacement from the beam axis and the carrier gas used in the experiment. The degree of collisional alignment can in principle be studied, e.g., by laser induced fluorescence [153], but it was not monitored during the experiments presented here.

Additional information can be extracted from the pump–probe experiments by Fourier transformation of the transients, the results of which are shown in Fig. 4.6. For parallel pump and probe polarizations (Fig. 4.6(a)) only dynamics in the $2^1\Pi_g$ state (average vibrational quantum number $\bar{\nu} = 24$) with a vibrational period of 740 fs [146] (corresponding to 45 cm^{-1}) is observed. The appearance of dynamics in the $2^1\Pi_g$ state shows that the ionization depends on the internuclear distance and occurs predominantly at the outer turning point. In simulations, a dipole moment for the transition $2^1\Pi_g \rightarrow K_2^+(^2\Sigma_g^+)$ that grows linearly with the internuclear distance has been used successfully to recover the experimental results [146]. In the case of mutually perpendicular pump and probe polarizations (Fig. 4.6(b)) an additional Fourier peak appears at 65 cm^{-1} (corresponding to 510 fs), which can be attributed to vibrational dynamics in the $A^1\Sigma_u^+$ state ($\bar{\nu} = 14$). The different relative contributions of the dynamics in the

$A^1\Sigma_u^+$ and $2^1\Pi_g$ states for negative versus positive delay times can be attributed to the partial alignment of the molecules.

Overall, the results of the pump–probe experiments show that a laser field with time–dependent polarization can give access to additional dynamics and different intermediate states. Note that all other experimental conditions, such as pulse intensity, were identical for the different polarization configurations, and therefore all the differences visible in the transients are entirely due to the polarization properties of the applied light fields. This type of polarization sensitivity can be exploited much more generally by adaptive polarization pulse shaping, which provides a qualitatively novel tool for the control of quantum systems. In the following section, flexible and automated polarization–and–phase shaping of femtosecond laser pulses is used in combination with an evolutionary algorithm in order to control molecular dynamics and, in this case, maximize the ionization yield of the potassium dimer.

4.4 Quantum control of K_2

For the adaptive control experiment, the prototype polarization pulse shaper setup described in chapter 3.4.2 is used, slightly realigned in order to cope with the spectrally broad 30 fs laser pulses. The complete experimental setup is shown in Fig. 4.7. The pulse characterization is carried out by dual–channel spectral interferometry (see chapter 3.5.2), with an appropriately delayed reference pulse that is characterized using the FROG technique introduced in chapter 3.5.1. The energy of the shaped pulses was attenuated to 300 nJ, which equals the sum of the pump and probe pulse intensities used in the pump–probe experiments of the previous section. This pulse energy ensures that the K_2^+ ion yield can be recorded with good signal–to–noise ratio even for the arbitrary pulse shapes in the initial population of the evolutionary algorithm, while strong–field effects are avoided.

For comparison, two types of adaptive control experiments with different strategies are performed: spectral polarization–and–phase laser pulse shaping as well as phase–only shaping. As mentioned in chapter 3.4, conventional phase–only pulse shaping can be realized by applying the same phase function to both LCD layers of the polarization pulse shaper setup. Hence, optimizations both with linearly polarized shaped pulses and with polarization shaped laser pulses can be performed without mechanical changes to the pulse shaper setup. In both cases, the $^{39,39}K_2^+$ ion yield measured in the TOF mass spectrometer is used as feedback signal in an evolutionary algorithm.

In order to ensure identical experimental conditions, e.g., concerning the laser pulse energy and molecular beam conditions, the two optimizations are run in a parallel implementation, where the strategy is switched after each individual of either evolution. As was shown in [154], the number of parameters varied by the optimization algorithm can significantly influence the achievable degree of control. Therefore the same number of parameters is chosen for both strategies, which was

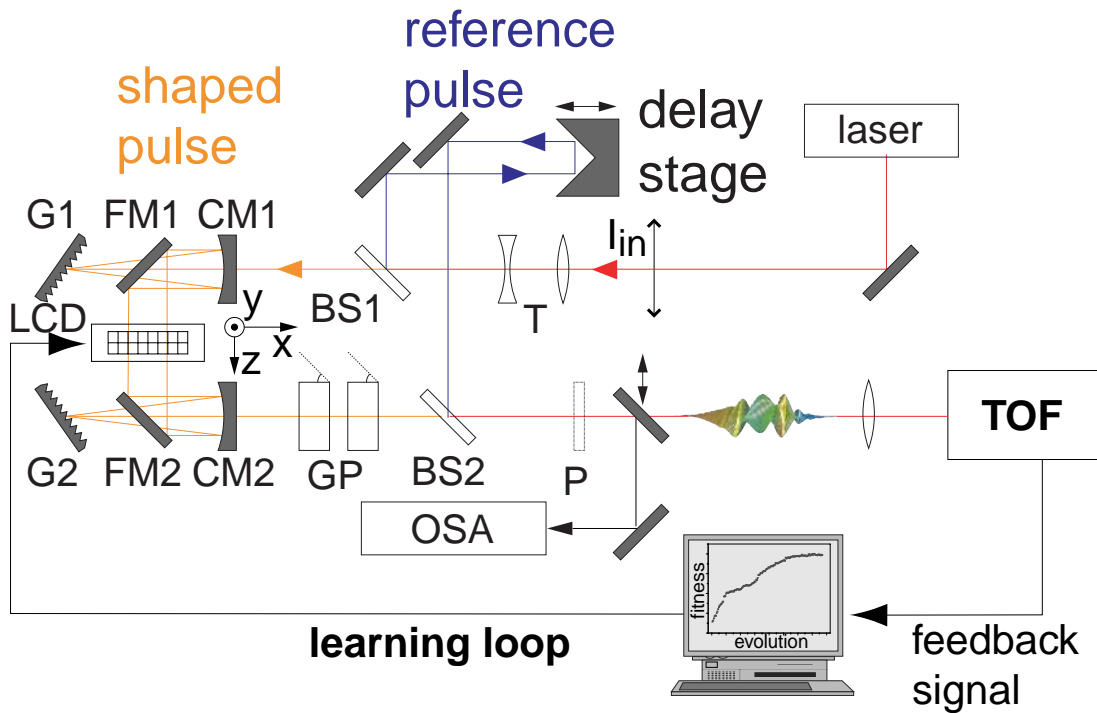


Figure 4.7: Experimental setup. The pulse shaper that creates time-dependent polarization profiles consists of a telescope (T), cylindrical mirrors (CM), optical gratings (G), folding mirrors (FM), a two-layer liquid-crystal display (LCD), and a stack of glass plates at Brewster's angle (GP) to provide equal intensity and independently shaped polarization components at the output. Pulse characterization is carried out by dual-channel spectral interferometry with a characterized and appropriately delayed reference pulse. For this purpose, shaped pulse and reference pulse are recombined collinearly along the beam path towards the experiment by a beam splitter (BS2), and the spectral interferences are recorded by an optical spectrum analyzer (OSA). A polarizer (P) selects the polarization component to be analyzed. During the actual experiment, the polarizer is removed and the reference pulse is blocked. Shaped pulses then interact with the seeded molecular beam of K_2 . The $^{39,39}K_2^+$ ion yield measured in the TOF mass spectrometer is used as feedback signal in an evolutionary algorithm.

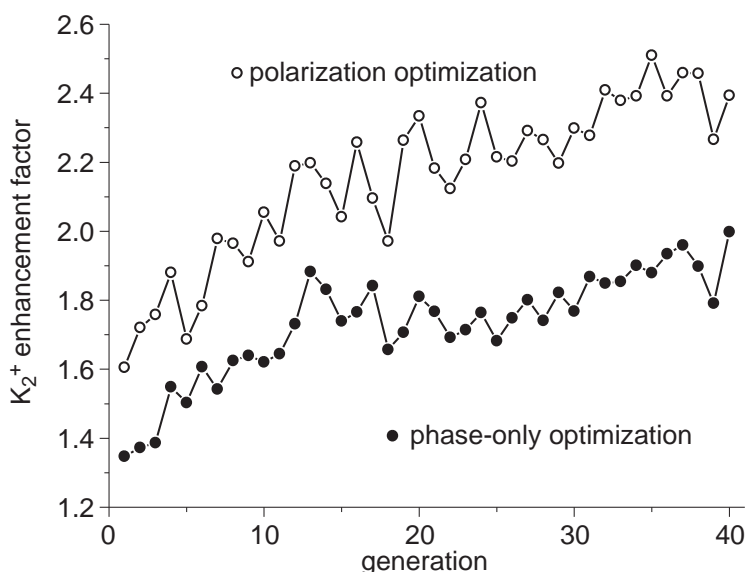


Figure 4.8: Evolution curves showing the K_2^+ ion yield relative to that obtained with an unshaped laser pulse. The signal obtained with the best individual of each generation for the polarization–and–phase optimization (open circles) and phase–only optimization (solid circles) is plotted.

achieved by binning two neighboring pixels in the case of polarization shaping. Under these conditions, a direct comparison of the results of both optimizations is possible. For this purpose, the ratio of the K_2^+ signal for the best individual of each generation, divided by the K_2^+ signal for the unshaped reference pulse, is shown in Fig. 4.8 as a function of generation number. The evolution curves show that both strategies lead to a significant enhancement of the K_2^+ yield.

The increase in the case of phase–only pulse shaping (solid circles) can be attributed to the adaptation of the laser pulse structure to the vibrational dynamics of the potassium dimer, providing high laser intensities when the wave packet is in a suitable Franck–Condon region. This general type of mechanism is what had been exploited and discussed in the theoretical and experimental literature on quantum control to date. However, when the additional mechanism of polarization control is used (open circles), one can go beyond the limitations set by linearly polarized fields and achieve significantly higher product yields. This demonstrates not just a quantitative improvement, but rather a qualitative extension of quantum control mechanisms, because it goes beyond one–dimensional addressing of transition dipoles and rather makes use of their directional properties by shaping the polarization state of the controlling laser pulse.

Figure 4.9 shows a representation of the best laser pulse shape reached in the final generation of the polarization–and–phase optimization. The momentary frequency and the polarization state of the optimized pulse changes substantially in a complex

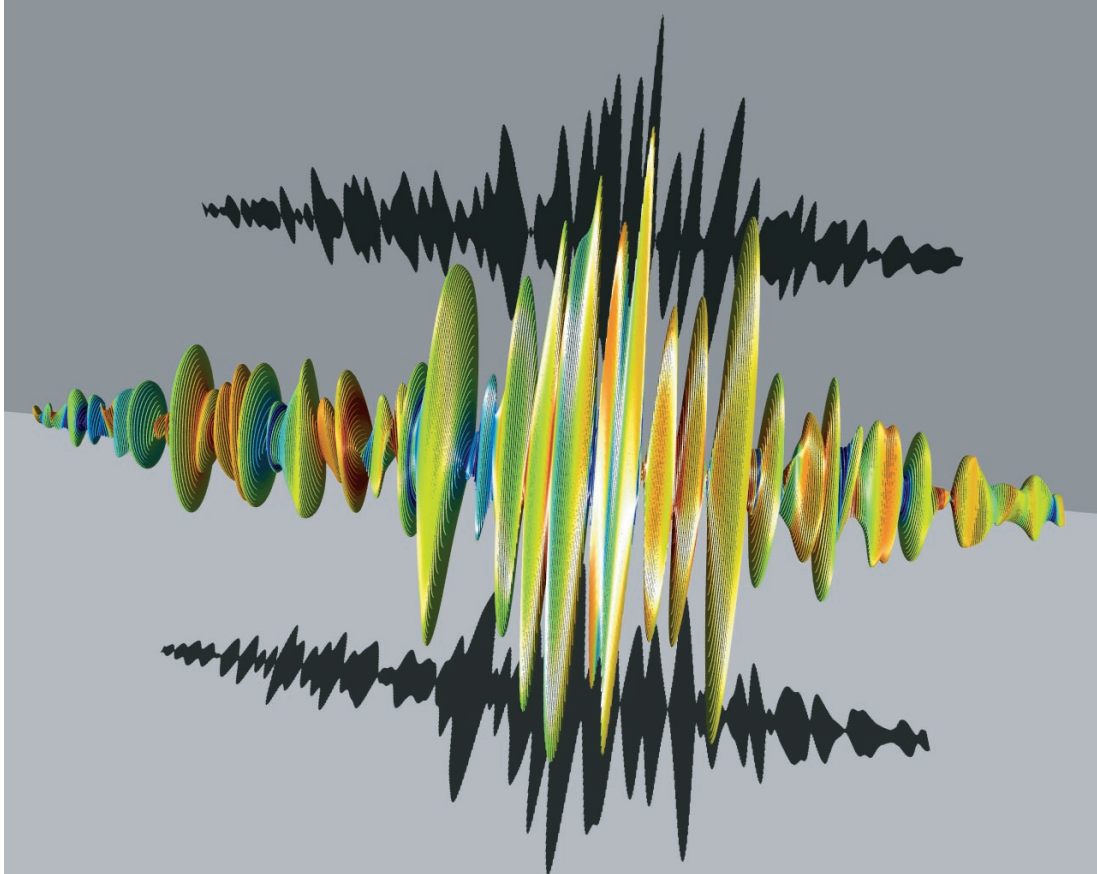


Figure 4.9: Quasi-three-dimensional representation of the optimal polarization-shaped laser pulse. Time evolves from -1.5 ps (left) to $+1.5$ ps (right), the electric field amplitudes are indicated by the sizes of the corresponding ellipses, and the momentary frequencies are indicated by colors. The shadows represent the amplitude envelopes of the two orthogonal components parallel to the shaping directions of LCD layers.

fashion as a function of time. Some reasons for this complexity are briefly discussed now. First, the detection step in this experiment (i.e., the ionization) needs to be considered in more detail. The observation of $2^1\Pi_g$ state dynamics in the pump–probe measurement (Figs. 4.5 and 4.6) proves that ionization from the $2^1\Pi_g$ state is dependent on the internuclear distance and occurs predominantly at the outer turning point [146]. In addition, another potential ionization channel could involve doubly excited autoionizing states, which was observed in experiments with molecular beams of Na_2 alkali dimers [155]. Excitations of these doubly excited states via the outer turning point in the $2^1\Pi_g$ state as well as transitions involving the $4^1\Sigma_g^+$ state have not been considered in the previous simplified discussion. A significant contribution to the complicated pulse structure can also be expected from the broad spectrum of the ultrashort 30 fs laser pulses employed in the experiment, which gives access to a large number of transition pathways with differing dynamics. As was discussed in detail in section 4.2, the vibrational dynamics of the potassium dimer are known to depend strongly on the center wavelength of the excitation laser pulse, and the Franck–Condon point shifts towards smaller internuclear distances with decreasing wavelength. In the context of the adaptive polarization shaping experiment carried out this means that the optimal polarization needs to be provided for a wide distribution of both wavelengths and timings.

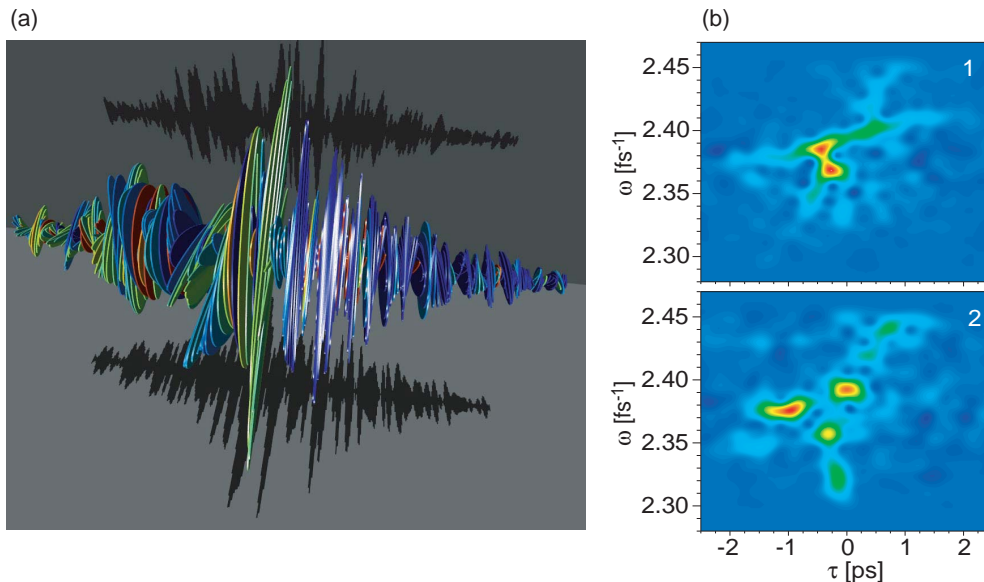


Figure 4.10: Optimal polarization–shaped laser pulse with “hot” molecular beam. (a) shows the optimal pulse in the quasi–three–dimensional representation and (b) shows the Husimi distributions of the polarization components 1 and 2 of the same pulse. The two Husimi plots display some indications for the simple pulse sequence with varying linear polarizations discussed for the simple model given in Section 4.2.

A series of optimizations carried out with different molecular beam conditions reveal that these conditions also have a strong impact on the optimal pulse shape. During these optimizations, the seed gas (Ar) of the molecular beam is heated up to approximately 150 °C. Under these circumstances the partial alignment effects in the pump–probe transients vanish, and an increase in the vibrational temperature of the K_2 can be expected. Fig. 4.10 shows an example of an optimal polarization–shaped laser pulse obtained under these molecular beam conditions. In comparison to the optimal pulse shape from experiments with ‘cold’ molecular beam (Fig. 4.9) remarkable differences can be observed. These cannot be attributed to statistical variations of the pulse shape for different optimizations, because also with the cold molecular beam several optimizations were performed, and the optimal pulse shapes obtained are similar to the one shown in Fig. 4.9. Interestingly, the pulse shapes with the ‘hot’ molecular beam resemble much more the expectation from the simple model given in section 4.2, i.e., a pulse sequence with varying linear polarizations. However, without detailed calculations and simulations of the interaction between the optimal field and the K_2 dimer one has to refrain from speculations about the underlying control mechanism.

While all these factors complicate the analysis and interpretation of the optimal pulse shape, the important point is that despite the complexity an optimized electric field with time–varying polarization has indeed been exploited by the evolutionary learning algorithm as a novel control agent.

4.5 Conclusion

In conclusion, the experiments presented in this chapter demonstrate that time–dependent shaping of femtosecond light polarization can give access to a further level of control in quantum systems. Already the pump–probe measurements with different linear polarizations show that a time–dependent polarization can give access to additional dynamics and different intermediate states. Comparative optimizations of the K_2^+ yield show that polarization–and–phase laser pulse shaping is superior to phase–only shaping, because the vectorial electric field can adapt to the time evolution of the transition dipole moment vectors. Hence, the vectorial properties of light–matter interaction have been exploited to achieve quantum control in a molecular model system. This opens the door to a number of qualitatively new experimental schemes, which exploit the full vectorial temporal response of quantum systems. It allows to address stereochemical aspects in quantum control such as chiral selectivity, where polarization–shaped laser pulses are a crucial ingredient [31–36]. The optical control of lattice vibrations [156] and the generation and characterization of attosecond light pulses [130, 131] are further examples of numerous new perspectives.

Chapter 5

Polarization shaping in the UV

In this chapter, a technique for generating and characterizing polarization-shaped pulses in the UV spectral region will be presented. After introducing the experimental concepts and the envisaged applications in section 5.1, the experimental implementation will be presented in section 5.2. The feasibility of polarization shaping in the UV is then demonstrated with a variety of different pulse shapes in section 5.3, where also the influence of mixing effects and material dispersion will be investigated.

5.1 Introduction

The advantages and possibilities that the polarization-and-phase shaping of fs laser pulses offers over phase-only pulse shaping were demonstrated in the experiments on the potassium dimer described in the previous chapter. It should be noted, however, that in order to address and exploit the polarization-dependent dynamics in this model quantum system, it was required that the relevant transitions were accessible with the employed laser spectrum.

The most intriguing and promising prospects and applications for ultrafast polarization pulse shaping lie in the manipulation and control of stereochemical reactions of organic molecules that are of chemical or biological relevance. Examples for such processes include ring opening reactions, isomerizations and the enantiomer-selective excitation or production of chiral molecules. Such reactions depend on the geometry of the molecule at hand, and entail changes of this geometry during the reaction, which in turn will lead to significant changes of the involved quantum states and hence to changes of the orientation and magnitude of the transition dipole moments connecting the states relevant for the reaction. Polarization-shaped laser pulses have the potential to adapt to the changing conditions, and therefore to initiate, guide or follow the geometrical rearrangements. However, organic molecules usually have their main absorption bands in the UV, and two-photon processes may not always be feasible

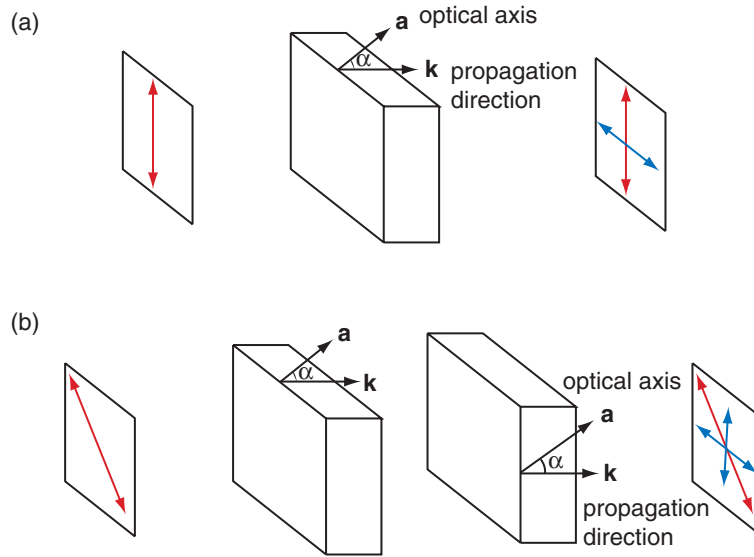


Figure 5.1: Frequency-doubling of shaped near-IR laser pulses. (a) In conventional type-I SHG, the fundamental at 800 nm is polarized as the ordinary wave (direction indicated by the red arrow), and the resulting second harmonic as the extraordinary wave. (b) For the frequency-doubling of polarization-shaped pulses, one component of the fundamental is doubled in the first crystal, whereas the other passes the first crystal undergoing only material dispersion and is then frequency-doubled in the second crystal. The orientation of the crystals is shown on their side faces by the direction of the optical axis \mathbf{a} and the propagation direction \mathbf{k} , where \mathbf{a} and \mathbf{k} lie in the plane of the respective side face.

or desirable, e.g., due to low two-photon absorption cross-sections and/or unwanted high intensity effects such as white-light generation in the solvent in the case of liquid-phase experiments. Once again, the fact that the liquid-crystal displays of the pulse shapers introduced in chapter 3.4 absorb light below ≈ 450 nm precludes the direct polarization shaping of UV light with such setups, leaving the frequency conversion of polarization-shaped near-IR pulses as an option.

While the frequency doubling of phase-only shaped laser pulses can be achieved with a single nonlinear crystal (e.g., BBO, β -barium-borate), as discussed in chapter 3.3.2, this is not feasible in the case of polarization-shaped laser pulses. This is due to the fact that a nonlinear crystal effectively acts as a polarizer. In the exemplary case of type-I phase-matching, only fundamental light polarized as the ordinary wave is phase-matched to its second harmonic, which is polarized as the extraordinary wave (i.e., $n_o(\omega) = n_{eo}(2\omega)$), as depicted in figures 3.6 and 5.1(a). Any component of the fundamental laser pulse that is polarized as the extraordinary wave is not phase-matched, and hence not efficiently frequency-doubled, and is only affected

by material dispersion when passing through the birefringent nonlinear crystal. Recalling that the polarization shaping of near-IR laser pulses was achieved with two mutually perpendicular layers of LCD-pixels (see chapter 3.4.2), the employment of two nonlinear crystals with mutually perpendicular optical axes should make the frequency-doubling of polarization-shaped near-IR pulses, and hence the generation of polarization-shaped UV pulses, feasible, as illustrated in Fig. 5.1(b). For example, an incoming laser pulse with a linear polarization that is tilted by 45° with respect to the ordinary polarization directions of the two nonlinear crystals can be decomposed into two orthogonal components of equal magnitude, one parallel to the ordinary direction of the first crystal, and the other one parallel to the ordinary direction of the second crystal. Hence, the first component will be frequency-doubled in the first nonlinear crystal, and its second harmonic will then be subject to material dispersion in the second crystal. Likewise, the fundamental of the second component will be affected by material dispersion in the first crystal and will then be frequency-doubled in the second crystal.

In order to determine the electric field of the polarization-shaped UV laser pulse, it is not sufficient to characterize the fundamental and compute its second harmonic. As mentioned in chapter 3.3.2, already small errors in the characterization of the fundamental pulse can lead to significant discrepancies in the calculated second harmonic pulse shape. Also the dispersion effects mentioned above would have to be taken into account. Therefore, an experimental setup has to be implemented that allows a direct characterization of the polarization-shaped UV pulses, which will be introduced in the next section.

5.2 Experimental implementation

The experimental setup for the generation and characterization of polarization-shaped UV pulses on the femtosecond time scale is shown in Fig. 5.2. The revised polarization pulse shaper depicted in Fig. 3.13 was employed for this experiment, and some of its properties that are of relevance here will be discussed in section 5.2.1. The polarization-shaped near-IR pulses exiting the pulse shaper (red line) pass through a $\lambda/2$ -waveplate, which rotates the polarization state by 45° . The polarization components 1 and 2 that are effectively shaped by the two-layer LCD¹ are thereby rotated in such a way that their second harmonics are s-polarized or p-polarized, respectively, relative to the polarizing beamsplitter cube (PC) further down the beam path. The polarization component 1 of the shaped laser pulse is then frequency doubled in the first 100 μm thick nonlinear crystal (BBO 1), and component 2 is frequency doubled in the second 100 μm thick nonlinear crystal (BBO 2). The optical axes of these two nonlinear crystals are mutually perpendicular. After recombination of the second harmonics

¹The components 1 and 2 are tilted by $\pm 45^\circ$ relative to the incoming polarization direction, see chapter 3.4.2

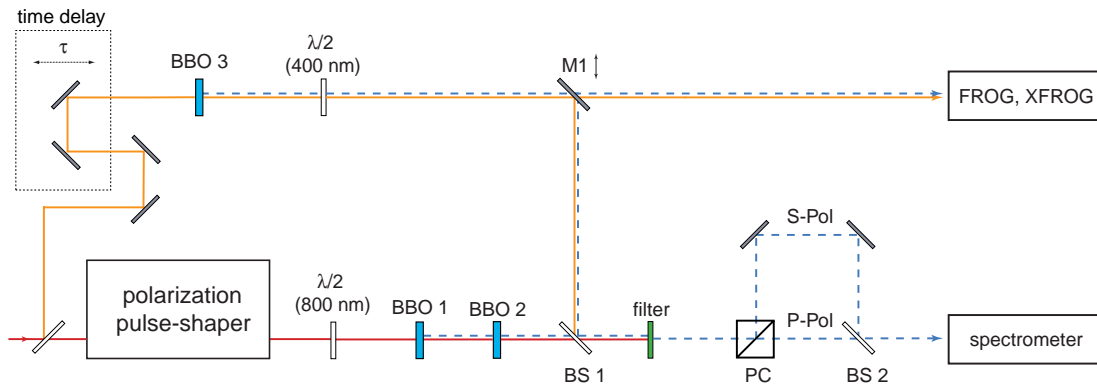


Figure 5.2: Setup for the generation and characterization of polarization-shaped UV pulses. The polarization-shaped 800 nm pulse (red line) passes through a $\lambda/2$ -waveplate, where the polarization is turned by 45° . After frequency-doubling in two nonlinear crystals (BBO 1 and BBO 2), it is recombined with the frequency-doubled reference pulse with a beamsplitter (BS 1). After removing the fundamental with a filter (BG38, Schott), the pulse is decomposed into two orthogonal polarization components with a polarizing beamsplitter cube (PC), and the spectra of reference and shaped pulse, as well as the SI spectra are recorded with a spectrometer. The reference pulse (yellow line) passes over a delay stage, where the temporal delay τ between shaped pulse and reference pulse can be adjusted. It is then frequency doubled in a nonlinear crystal (BBO 3), and its polarization direction is rotated by 45° with a $\lambda/2$ -waveplate, in order to provide reference pulses for both polarization directions. It can then either be recombined with the shaped pulse, or characterized separately via FROG and XFROG measurements.

of shaped and reference pulse on the first beamsplitter (BS 1), the fundamental is removed by a filter (BG38, Schott). A polarizing beamsplitter cube (PC) is employed to separate the s- and p-polarized components. Via a second beamsplitter (BS 2) both components travel parallel, but slightly displaced vertically, to a high-resolution spectrometer, where their spectra can be recorded simultaneously with a 2D-CCD camera for the purpose of dual-channel spectral interferometry (SI, see section 5.2.2). The reference pulse (yellow line) that is split off in front of the $4f$ -setup would normally be recombined via a pair of glass wedges (GW 2 in Fig. 3.13) with the polarization-shaped near-IR pulse. However, as this could lead to unwanted mixing of the shaped and reference pulse during the SHG process, this is not advisable here. The reference pulse is therefore sent over an external delay stage, where the time delay τ between shaped and reference pulse can be adjusted for the subsequent characterization via dual-channel spectral interferometry. The reference pulse is then frequency-doubled in a third nonlinear crystal (BBO 3), and its linear polarization is turned by 45° with a $\lambda/2$ -waveplate in order to provide both s- and p-polarized reference pulses. The reference pulse can then either be recombined with the shaped pulse via the mirror M 1 and the beamsplitter BS 1 for the SI measurements, or directed to FROG and XFROG

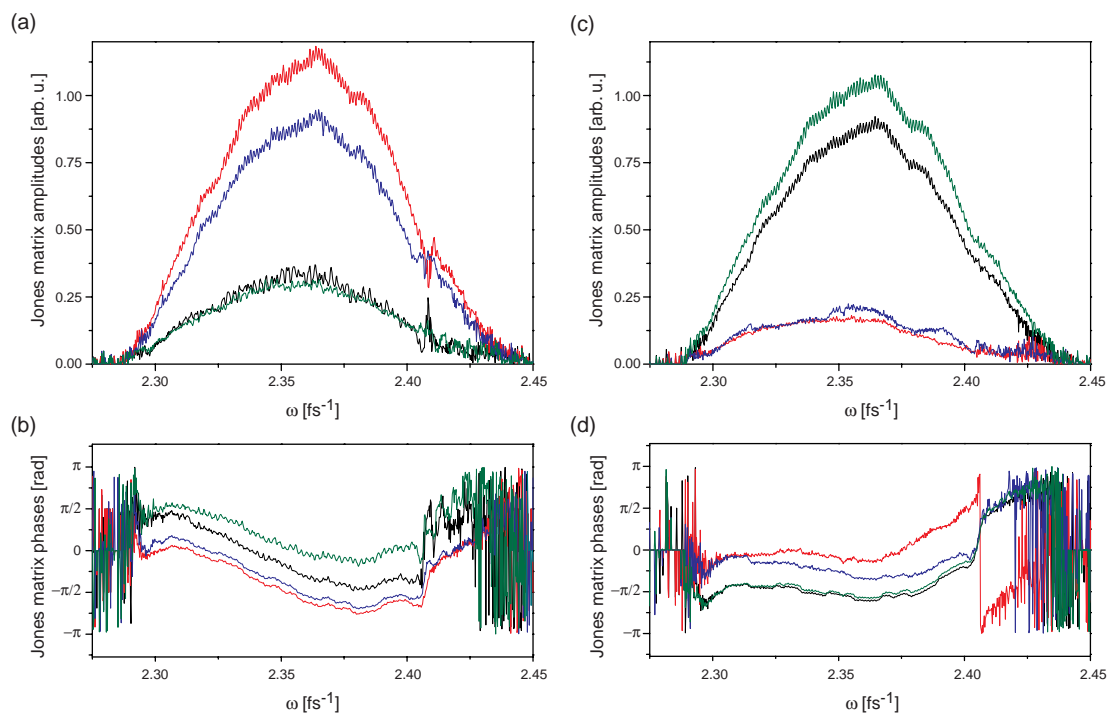


Figure 5.3: Measured Jones matrix elements of the revised polarization pulse shaper. The amplitudes are shown in the top row for (a) the unmodified pulse shaper and (c) with a suitably adjusted Berek compensator after the $4f$ -setup. The diagonal matrix elements are a_{11} (black line) and a_{22} (green line), the off-diagonal matrix elements are a_{12} (red line) and a_{21} (blue line). The corresponding phases of these matrix elements are shown in the bottom row, for (b) the unmodified pulse shaper and (d) with a suitably adjusted Berek compensator after the $4f$ -setup.

setups for characterization (see section 5.2.3).

5.2.1 The polarization pulse shaper

The revised polarization pulse shaper setup shown in Fig. 3.13 was chosen for the generation of polarization-shaped UV pulses. The key advantages of the revised setup over the prototype design are the significantly increased energy throughput, and the potentially lower mixing effects of the two shaped polarization components. The Jones matrix calculus introduced in chapter 3.4.2, and the experimental determination of the Jones matrix (for details see Ref. [43]) are suitable for understanding and measuring these mixing effects. By applying a variety of different pulse shapes, each of which is characterized by dual-channel spectral interferometry, and a subsequent fit-procedure (see Ref. [43]), the amplitudes and phases of the Jones matrix elements a_{11} , a_{12} , a_{21} and a_{22} (see Eq. 3.46) can be determined. For an ideal pulse shaper, only the diagonal elements a_{11} and a_{22} would be non-zero and of equal magnitude. They describe the

amplitude and phase modifications of each polarization component separately. The off-diagonal elements a_{12} and a_{21} however, describe the mixing effects between the two polarization components. For example, the matrix element a_{12} describes how the polarization component 1 is modified by a contribution proportional to the polarization component 2. The frequency-dependent amplitudes and phases of the Jones matrix elements for the revised polarization pulse shaper setup, as measured with the oscillator of the laser system, are shown in Fig. 5.3(a) and (b), respectively. From Fig. 5.3(a) it is apparent that the amplitudes of the off-diagonal elements a_{12} (red line) and a_{21} (blue line) that describe the mixing effects are about a factor of 4 larger than the diagonal elements a_{11} (black line) and a_{22} (green line). This means that the mixing effects are so strong, that effectively the two polarization components 1 and 2 are switched after leaving the pulse shaper. Such characteristics were not observed for the prototype setup, and they are probably related to the volume phase holographic (VPH) gratings employed in the revised setup, as their use constitutes the main difference between the two designs.

By placing a carefully adjusted Berek compensator [157], which is basically a waveplate with variable retardation and rotation angle, after the $4f$ -setup, this situation can be reversed. This can be seen in Fig. 5.3(c), as now the diagonal matrix elements (a_{11} (black line) and a_{22} (green line)) dominate the mixing terms, again by about a factor of 4. While the experiments described here were carried out with the Berek compensator, the residual mixing effects will still affect the SHG process (see section 5.3).

5.2.2 Dual-channel spectral interferometry

The dual-channel spectral interferometry (SI) method described in chapter 3.5.2 is the method of choice for characterizing polarization-shaped pulses. As discussed there, in total six spectra have to be measured for the characterization of a shaped pulse. For both polarization components, the spectra of the shaped pulse and the reference pulse have to be measured separately, as well as the spectrum resulting from the spectral interference of the two pulses. Examples for these spectra are shown in Fig. 5.4(a) for the reference pulse, (b) for the shaped pulse and (c) for their interference, for a polarization-shaped pulse where a flat (zero) spectral phase was applied to polarization component 1 (black lines), and a linear phase of +60 fs was applied to polarization component 2 (red lines). The spectra of the two polarization components of the shaped pulse shown in Fig. 5.4(b) suggest that component 2 (red line) is much more intense than component 1 (black line). However, this is misleading, as the optical elements that the two components pass have transmission, reflection, or diffraction properties that depend strongly on the polarization and wavelength of the incident light. The beamsplitters BS 1 and BS 2 show the strongest dependence of their transmission and reflection properties on the polarization and wavelength. Also the grating that is used to disperse the incoming light in the spectrometer has polarization- and wavelength-dependent efficiencies, and even the two additional aluminum coated mirrors that the

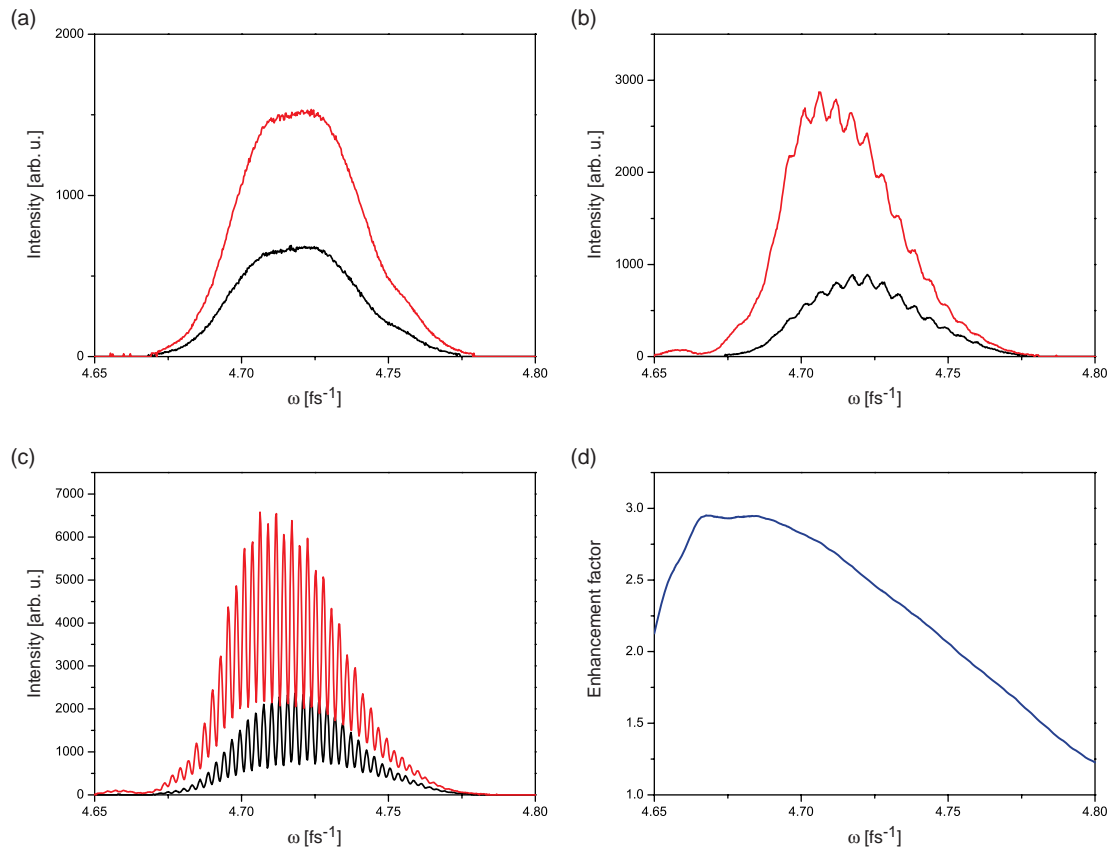


Figure 5.4: The spectra that have to be measured for the characterization of polarization-shaped UV pulses via dual-channel spectral interferometry are shown for a sample pulse with a flat (zero) phase applied to polarization component 1 (black lines) and a linear phase of +60 fs applied to polarization component 2 (red lines). The spectra for the two polarization components are shown (a) for the reference pulse, (b) for the shaped pulse, and (c) for their spectral interference. The polarization- and wavelength-dependence of the transmission, reflection, or diffraction properties of the optical elements in the experimental setup can be compensated by weighting the intensity of the measured spectrum of polarization component 1 ((b), black line) with the wavelength-dependent enhancement factor shown in (d).

s-polarized component has to pass will reduce the amplitude of this component by about 10% each.

The SI measurements mainly serve to determine the phase of the shaped pulse, which is not significantly influenced by these polarization- and wavelength-dependent properties. This is due to the circumstance that only the relative phase between the shaped pulse and the reference pulse is determined with the SI measurement, and both pulses pass the same optical components after their recombination. However, the corresponding intensities for the two polarization components of the shaped pulse obtained

during this measurement are inaccurate. In order to compensate for the polarization- and wavelength-dependent efficiencies, two additional measurements are carried out. With only a single nonlinear crystal (BBO 1), two spectra are measured with a $\lambda/2$ -waveplate in front of the first beamsplitter (BS 1). Depending on the orientation of the waveplate, the 400 nm light generated in the nonlinear crystal can be made linearly polarized either along the s- or p-direction. Thus, the spectrum can be measured for an identical pulse that travels either along the path of the s-polarized light, or along the path of the p-polarized light (see Fig. 5.2). As the pulse is otherwise unmodified, the ratio of these two measurements yields a wavelength dependent enhancement factor shown in Fig. 5.4(d), with which the less intense spectrum of the s-polarized component 1 has to be multiplied in order to obtain its correct intensity. All spectra of the s-polarized component shown in section 5.3 are rescaled accordingly after the SI evaluation.

5.2.3 Characterization of the reference pulse

As discussed in chapter 3.5.2, the phase difference between a shaped pulse and a reference pulse can be determined with spectral interferometry up to a linear term that can be removed with a linear fit (see Eq. 3.64). In order to obtain the phase of the shaped pulse itself, the phase of the reference pulse has to be determined in a separate measurement. Because the reference pulse has a central wavelength of about 400 nm, it is not possible to determine its phase with a FROG measurement, as no nonlinear crystals were available for generating the second harmonic of the 400 nm light (see chapter 3.5.1). However, it can be characterized using the XFROG technique (see chapter 3.5.1). For this purpose, the fundamental of the reference pulse is separated from its second harmonic by a dichroitic mirror, and the cross-correlation of these two pulses is then measured in a XFROG setup. As the reference pulse is very weak (only about 4% of the light entering the pulse shaper), and its second harmonic is even weaker, measuring the cross-correlation of these two pulses is rather tedious and time-consuming. In order to retrieve the electric field and hence the phase of the 400 nm reference pulse from the measured XFROG trace, an additional FROG measurement of its fundamental has to be carried out. The measured FROG and XFROG traces are shown in Fig. 5.5(a) and (c), respectively, along with the FROG (b) and XFROG (d) traces of the electric fields retrieved by the FROG algorithm [114]. Together with the measured SI spectra, and after appropriate rescaling of the s-polarized component, the polarization-shaped UV pulses can now be fully characterized, and several instructive examples of such pulses are presented in the next section.

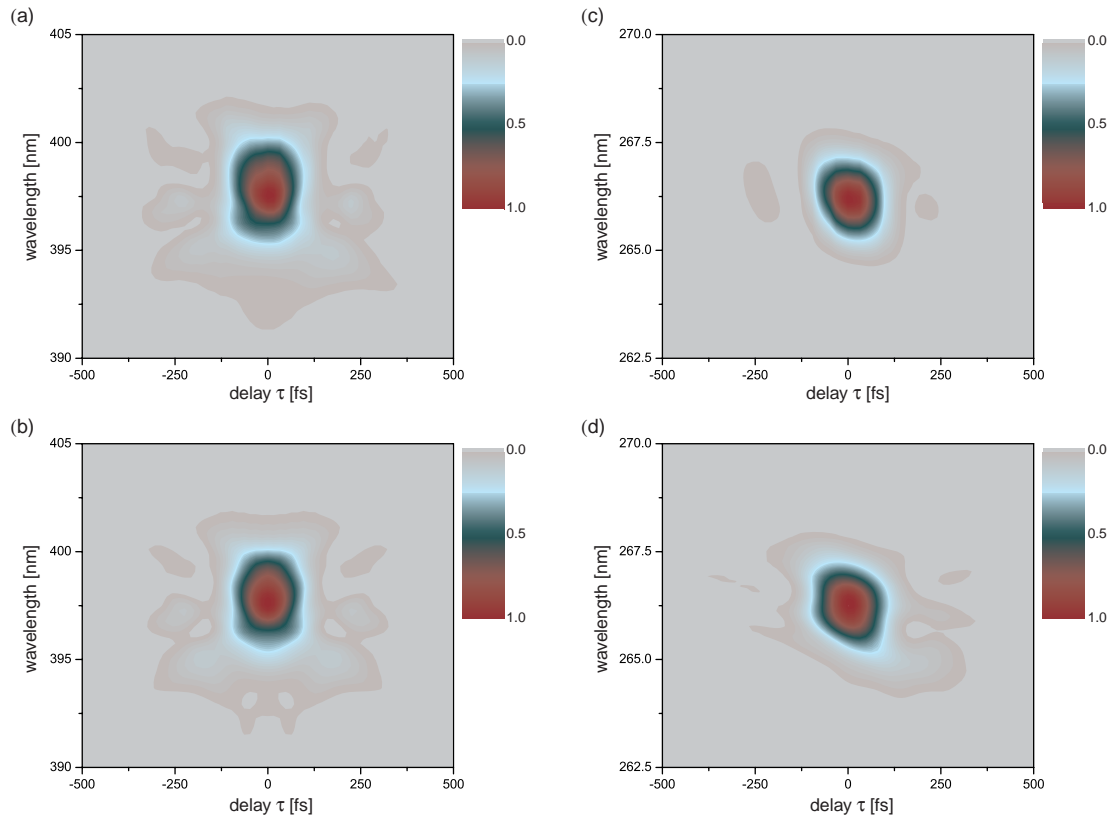


Figure 5.5: Characterization of the reference pulse. The measured FROG and XFROG traces are shown in (a) and (c), respectively. The corresponding FROG and XFROG traces of the electric fields retrieved by the FROG algorithm are shown in (b) and (d), respectively.

5.3 Results and discussion

In order to demonstrate the feasibility of generating polarization-shaped UV pulses with the setup shown in Fig. 5.2, a variety of different types of pulse shapes with analytical phase-functions are generated and characterized. As will become apparent below, this also serves to illuminate various aspects of the experiment, such as the influence of the mixing of the polarization components, and the effects that are due to dispersion in the nonlinear birefringent crystals.

Naturally, the first pulse shape that is applied and characterized is the one that results from applying zero phases to both layers of the LCD-SLM. The spectral intensities are shown in Fig. 5.6(a) along with the spectral phases (b) and the temporal intensity profiles (c) for the s-polarized (black lines) and p-polarized (red lines) components. From examining the spectral phase, it is apparent that the p-polarized component (red line) that is generated by frequency-doubling in the second nonlinear crystal (BBO 2) clearly exhibits a linear phase, which corresponds to a shift in time, while the phase

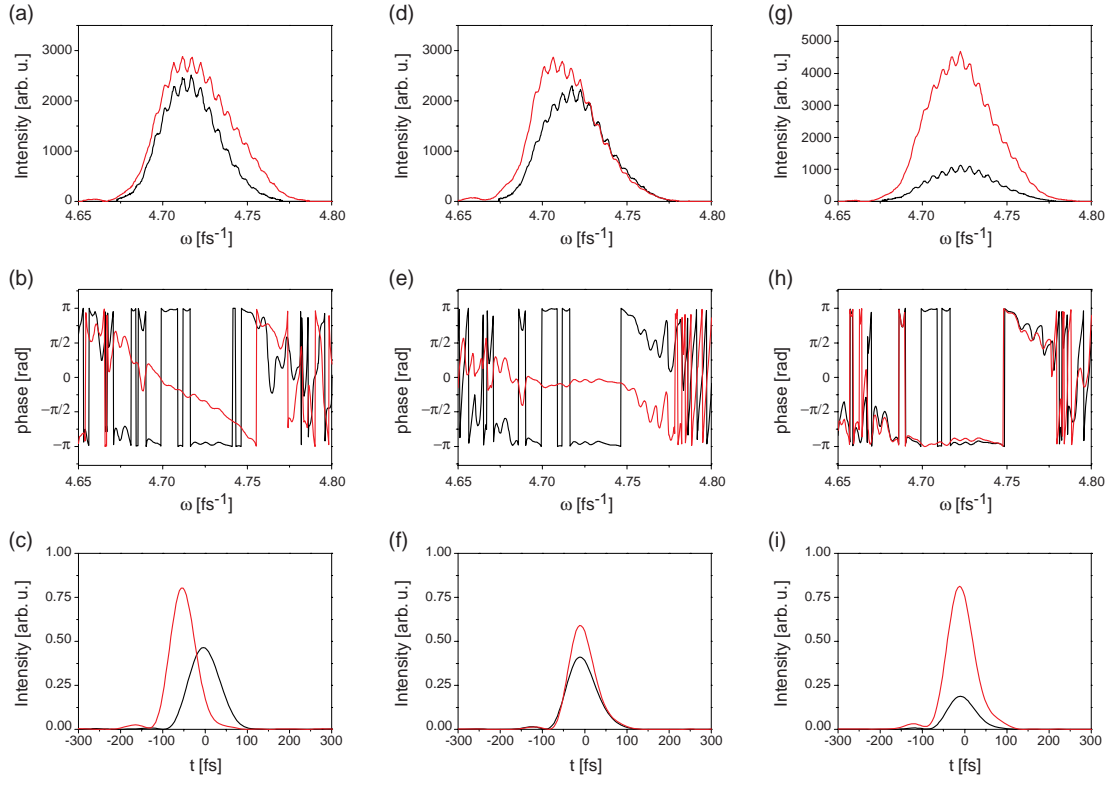


Figure 5.6: The spectral intensities for three different simple pulse shapes (see text) are displayed in the top row, for the s-polarized (black lines) and the p-polarized component (red lines). The corresponding spectral phases are shown in the second row, and the temporal development of the intensities is displayed in the bottom row.

of the s-polarized component (black line) is very flat and practically constant. This can also be seen in the temporal intensity profiles (Fig. 5.6(c)), where the p-polarized component precedes the s-polarized component by about 60 fs. The temporal intensities are shown here (and in all similar subsequent graphs in this chapter) normalized with respect to the maximum of the total temporal intensity $I_{tot}(t) = I_s(t) + I_p(t)$. The shift in time between the two polarization components can be attributed to the group velocity mismatch (GVM) of the two orthogonally polarized 400 nm subpulses, which is due to the difference of their respective indices of refraction in the second nonlinear birefringent crystal (confer Fig. 3.6), and similarly to the different dispersion of the two 800 nm subpulses in the nonlinear crystals.

In Fig. 5.6(d)–(f) the spectral and temporal properties are shown for a pulse where a linear phase of +60 fs has been applied to the polarization component 2. From Fig. 5.6(f) it is apparent that the GVM can indeed be compensated by applying this phase, which is therefore adopted as the default offset phase for component 2, which will be applied additionally for all of the following pulse shapes. The spectral phase of this pulse, which is shown in Fig. 5.6(e), reveals another feature, namely the presence

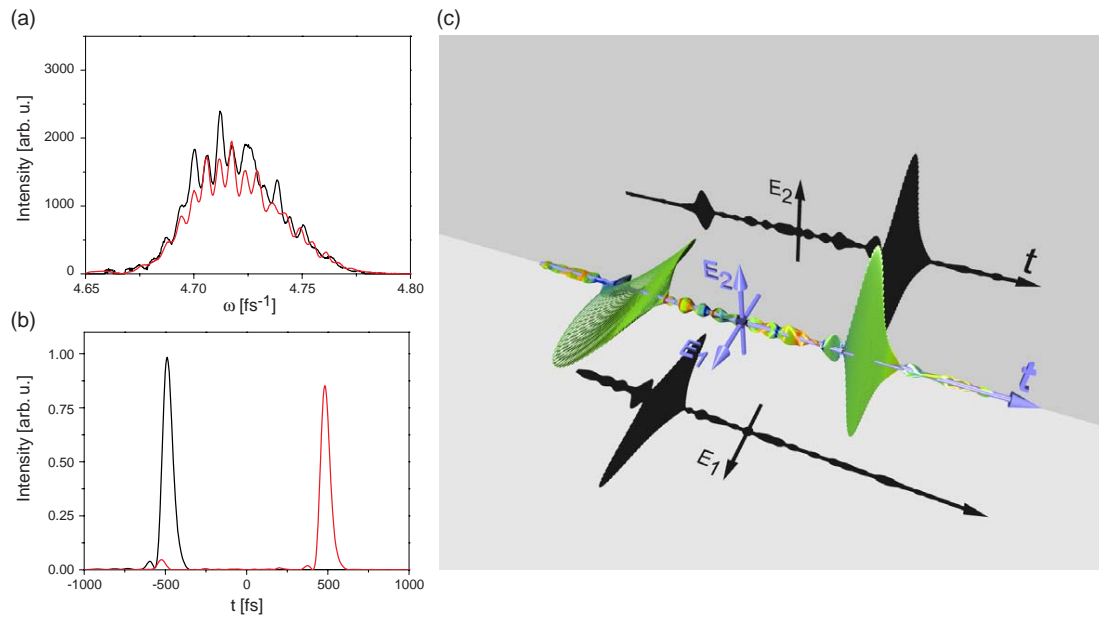


Figure 5.7: The spectral (a) and temporal (b) intensities of a shaped pulse with linear phases of -500 fs applied to component 1 (black lines) and of $+500$ fs applied to component 2 (red lines) are shown together with a pseudo-3D plot of the electric fields in the time domain (c).

of a constant phase difference between the two components of about π . This phase difference can probably be attributed to a difference in the rotation of the shaped and reference pulse by the $\lambda/2$ -waveplates in Fig. 5.2. If one pulse is rotated by $+45^\circ$, and the other one by -45° , a relative constant spectral phase of π will be introduced between the two polarization components during the SI-evaluation. By applying a constant phase of $\pi/2$ to component 1, which leads to a constant phase of π for the second harmonic, the spectral phases of both polarization components can be made practically identical, as shown in Fig. 5.6(h).

The application of different linear phases to both LCD layers should result in the generation of two temporally separated subpulses with mutually perpendicular polarizations. Linear phases of -500 fs applied to component 1 and of $+500$ fs applied to component 2 does indeed produce such a pulse sequence, as illustrated in Fig. 5.7. The spectral and temporal intensities are shown in Fig. 5.7(a) and (b), respectively, and the temporal evolution of the electric field is visualized in a pseudo-3D plot (Fig. 5.7(c)). It is noteworthy that the first subpulse at -500 fs is slightly elliptical, due to a temporally coincident, but less intense, subpulse of the other polarization, which can be attributed to the mixing effects between the two polarization components discussed above.

The influence of these mixing effects is more pronounced if, e.g., a quadratic phase is applied to one of the LCD-layers, as illustrated in Fig. 5.8 for a pulse with a quadratic

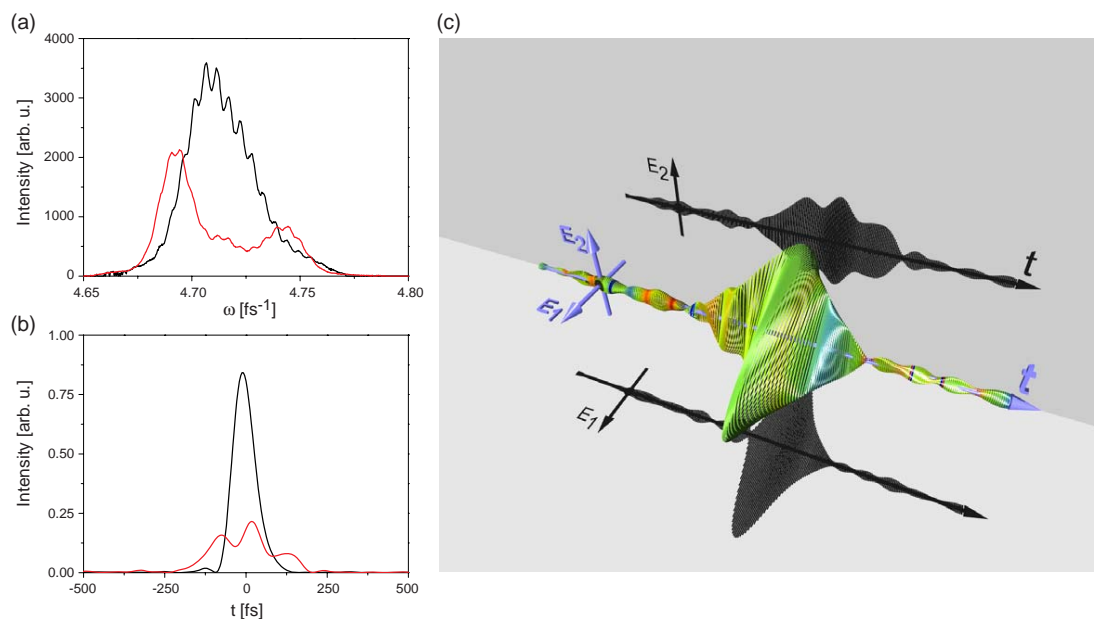


Figure 5.8: The spectral (a) and temporal (b) intensities of a shaped pulse with zero phase applied to component 1 (black lines) and a quadratic phase of $+10^4$ fs² applied to component 2 (red lines) are shown together with a pseudo-3D plot of the electric fields in the time domain (c).

phase of $+10^4$ fs² applied to polarization component 2. In the temporal domain, this quadratic phase will lead to a chirped, temporally broadened pulse centered around time zero with a substantially reduced peak intensity. The mixing of the polarization components results in another, temporally shorter, contribution from component 1 with the same polarization direction, also centered around time zero. As the temporal intensity of the second harmonic is proportional to the square of the intensity of the fundamental, the superposition of the two contributions can significantly alter the temporal intensities of the second harmonics. As component 2 is linearly chirped, the spectral intensity of the p-polarized second harmonic will also be affected. Both effects are observed in Fig. 5.8(a) and (b). The resulting pulse is shown in the time domain in Fig. 5.8(b) and (c). It starts linearly p-polarized, changes to elliptical polarization where both polarization components overlap temporally, and ends again linearly p-polarized.

As discussed in chapter 3.1, sinusoidal spectral phases of the form

$$\phi(\omega) = A \sin(\omega\tau + \phi_0) \quad (5.1)$$

will lead to pulse trains with a temporal separation τ of the individual subpulses. The frequency doubling of such a pulse train will result in a periodically modulated spectrum, as shown in Fig. 3.8. Hence, a sinusoidal phase of $\phi_1(\omega) = \pi \sin(\omega 670\text{fs})$

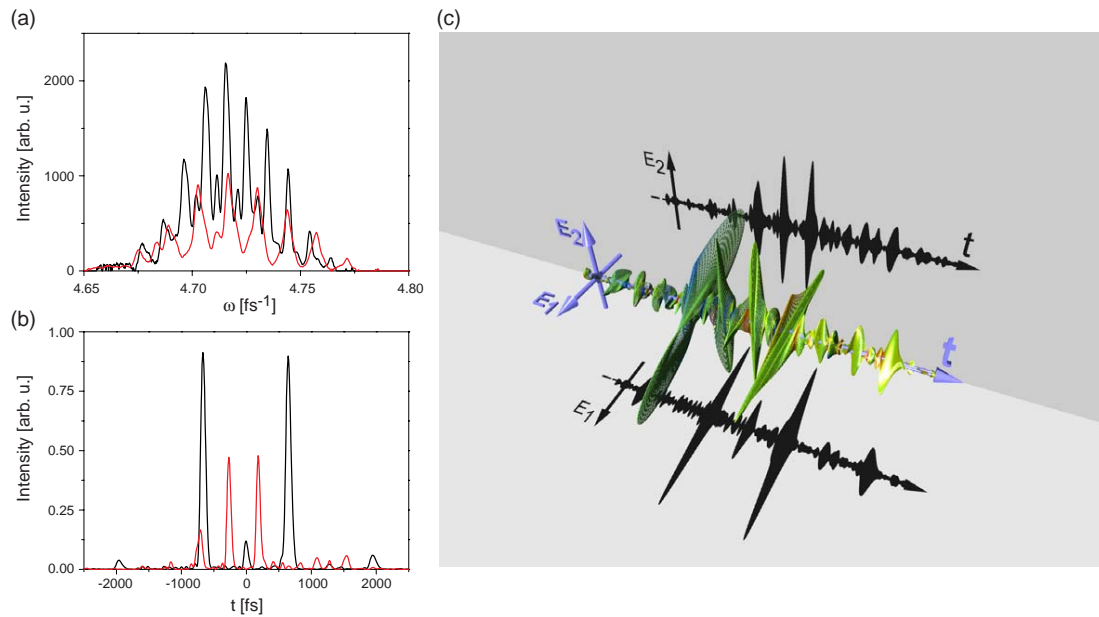


Figure 5.9: The spectral (a) and temporal (b) intensities of a shaped pulse with sinusoidal phases, as described in the text, applied to both polarization components 1 (black lines) and 2 (red lines) are shown together with a pseudo-3D plot of the electric fields in the time domain (c).

applied to component 1 and a phase of $\phi_2(\omega) = \pi \sin(\omega 470\text{fs} + \pi/2)$ applied to component 2 should lead to pulse trains in both polarization directions. Both the spectral and temporal intensity profiles of this shaped pulse, displayed in Fig. 5.9(a) and (b) show the aforementioned characteristic features. In the pseudo-3D plot of this pulse (Fig. 5.9(c)), which shows the corresponding electric fields, the periodic appearance of subpulses with low peak intensities is better visible. Again, some subpulses are elliptically polarized rather than linearly polarized due to temporally coinciding subpulses with low intensities in the orthogonal polarization direction.

For practical purposes, not only the temporal and spectral structure of the generated pulses, but also their pulse energy is important. While the pulse energy of the polarization-shaped near-IR pulses is almost independent of the applied spectral phases, the energy of the corresponding frequency-doubled pulses is expected to vary considerably with the applied pulse shape, due to the SHG process. From the initial 500 μJ at the pulse shaper entrance, about 135 μJ are available at its output, corresponding to a total throughput of about 27%. For linearly polarized pulse sequences such as the one shown in Fig. 5.7, the energy of the UV pulses is about 500 nJ. The pulse train shown in Fig. 5.9 has a total energy of about 50 nJ. For different sine parameters, e.g., $\phi_1(\omega) = \phi_2(\omega) = \frac{\pi}{2} \sin(\omega 470\text{fs})$, considerably higher pulse energies can be achieved, in this case 175 nJ. Pulse energies in this region are sufficient for many applications. However, the pulse energy can be increased by a variety of mea-

tures. For example, the initial pulse energy entering the pulse shaper can be increased, thicker nonlinear crystals can be employed, and the beam diameter can be decreased in front of the nonlinear crystals.

5.4 Conclusions

The generation and characterization of polarization-shaped pulses in the UV on the femtosecond timescale has been successfully implemented and demonstrated for the first time. It could be shown that polarization-mixing and dispersion effects have to be taken into account. With due care and consideration, these effects can be compensated if the generation of shaped pulses with analytical phase-functions is desired. However, in adaptive polarization pulse shaping experiments such effects should be taken care of by the optimization algorithm, and the introduced experimental setup in conjunction with the presented pulse characterization method are up to the task of performing such optimization experiments.

If the near-IR input laser were replaced by a coherent light source in the visible spectral region, such as a NOPA, the accessible spectral range in the UV could be tremendously increased, utilizing the techniques presented here.

Polarization-shaped pulses in the UV are especially of interest in the context of stereochemical applications, such as the manipulation and control of isomerization reactions or the selective excitation, transformation or production of enantiomers in chiral systems. An entirely different application for polarization-shaped UV pulses lies in the manipulation of forces on the nanometer scale, which has been proposed in Ref. [158] as a means for controlling the trapping and dynamic mechanical control of small particles like atoms or molecules in the vicinity of metal nanostructures.

Chapter 6

Analysis of femtosecond quantum control mechanisms with double pulses

In this chapter, the possibilities of analyzing quantum control mechanisms with parameter scans and fitness landscapes utilizing colored double pulses will be presented. After an introduction to the concept of fitness landscapes and pulse parametrizations in the first section, the generation of colored double pulses will be illustrated in section 6.2. The capability of fitness landscapes obtained by scanning colored double pulses to investigate control mechanisms is then first displayed in an optical demonstration experiment in section 6.3. In a second experiment, the dependence of the excitation efficiency of the solvated dye molecule IR140 on selected pulse shapes will be investigated, using transient absorption spectroscopy. In addition to the parametrization with colored double pulses, the second order spectral phase (linear chirp) is scanned for comparison. The results show that very different pulse profiles can be equivalently adequate to maximize a given control objective.

6.1 Introduction

Adaptive femtosecond quantum control has proven to be a very powerful tool to control a variety of chemical reactions and physical processes [15,45,49,52,53,56,59,127,159]. However, in many cases it is quite difficult to extract the control mechanism(s) utilized by the optimal pulse shape obtained in the optimal control experiment, a problem already encountered in chapter 4. The optimal solution may consist of substructures that contribute to a certain control mechanism to different degrees, or that even make use of different control mechanisms towards optimizing the fitness [160–162]. Also, in some cases, pulse shapes with very different electric fields can lead to similar fitness values, again because there may be more than one possibility to optimize the fitness. All substructures of the pulse may contribute to the control mechanism in a crucial way. However, the optimal solution can also contain meaningless parts that have no

influence on the optimization, but do not affect the found solution negatively, either.

While in some cases the optimal pulse shape allows a straightforward interpretation of the control mechanism [45,50,57,58,163], more complicated pulse shapes are often much harder to decipher. Closed-loop optimizations often result in such complicated pulses, as the number of pulse shapes accessible by the algorithm is usually held as large as possible, in order to make the search for the optimal solution as global as possible.

However, in order to make the control mechanisms involved in an optimal solution apparent, a restriction of the pulse shapes accessible during the optimization might be helpful. This approach may lead to a lower degree of control [154], but it can help to understand how control may be achievable if the accessible pulse shapes can be connected to intuitive physical processes. The restriction to a subspace of the possible pulse shapes can be achieved by parametrizing the spectral phases that can be applied by the pulse-shaper during the experiment. Such a parametrization typically involves the choice of a mathematical basis set for the spectral phases. For example, a Taylor expansion of the spectral phase function may be carried out, with the Taylor coefficients as the parameters to be scanned. A suitable parametrization of the spectral phases can also give a handle on time-domain parameterizations, e.g., by scanning only pulse sequences with a certain temporal spacing [164]. In several demonstrations of closed-loop quantum control, the additional information gained from closed-loop optimizations in restricted subspaces facilitated the interpretation of possible control mechanisms [45,53,54,165–172]. The obtained results can also be used to change the basis of the search space, further simplifying the optimization procedure in subsequent experiments [165,166,170,173].

If only a few parameters are varied to change the electric field, illustrative fitness landscapes [160–162] can be recorded by systematically scanning them. These landscapes, in which the fitness value is plotted as a function of the selected parameters [165,166,174,175], directly reflect the system's response to the different pulse shapes and give an indication about possible control mechanisms. Thus, testing different parameterizations that represent putative control scenarios allows to draw conclusions whether these play a decisive role or not. Several disadvantages remain, e.g., the difficulty to determine the interplay of different control mechanisms in the optimal solution. The optimal pulse shape might also contain control mechanisms that can not be accessed by the employed parameterizations.

Parameter scans [23,164,176–179] and fitness landscapes [165,166,174,175] have been employed to investigate reaction mechanisms and to control chemical reactions in an open loop. These works have shown that restricting the pulse shape to certain subspaces can provide valuable information on how a molecular system can be controlled with shaped femtosecond laser pulses.

Very often pump-dump- or pump-*repump*-like processes influence reactions significantly. These processes involve two sequential pulses, the first of which prepares a molecule in a certain state. The second pulse then influences the excited molecule in a desired way. Depending on the process under study, different parameters concern-

ing the pump and the dump (or repump) pulses can play an important role. Among these parameters are for example the time delay between the two pulses, the central wavelengths, the amplitudes and the difference of the absolute phase of the individual pulses [19, 22, 54, 62, 180, 181]. This makes the usage of colored double pulses, the generation of which will be explained in the following section, a method of choice for studying the dynamics and control mechanisms of systems in which pump–dump or pump–repump schemes may be of importance.

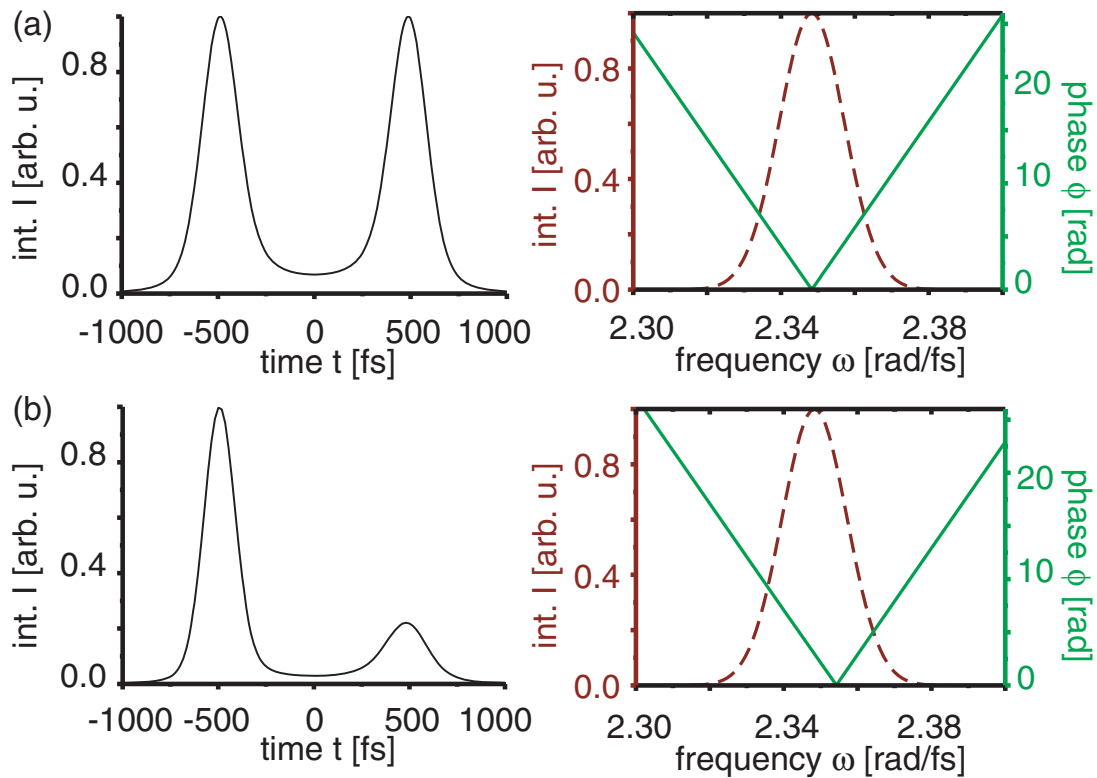


Figure 6.1: Simulated normalized temporal amplitudes for different spectral phase functions and a Gaussian spectrum. The left column presents the calculated temporal intensity profiles, the right column the assumed spectral intensity (bordeaux dashed) and spectral phase (green solid). (a) Triangular spectral phase for a double triangular phase slope $\Delta\tau = 1000$ fs and for a spectral breakpoint at $(\omega_0 + \delta\omega) = \omega_0 = 2.348$ rad/fs. (b) Triangular phase with the same phase slope as in (a), but for a spectral breakpoint $(\omega_0 + \delta\omega) = 2.354$ rad/fs.

6.2 Generation of double pulses

Colored double pulses can easily be generated by applying a certain spectral phase $\phi(\omega)$ to a femtosecond laser pulse. As illustrated in chapter 3.1, a linear phase in the frequency domain corresponds to a temporal shift of the laser pulse in the time domain. Intuitively, a colored double pulse can then be generated by applying a triangular spectral phase which shifts a part of the spectrum forward and the other part backward in time [182]:

$$\phi(\omega) = \text{sign}[\omega - (\omega_0 + \delta\omega)] \frac{\Delta\tau}{2} [\omega - (\omega_0 + \delta\omega)]. \quad (6.1)$$

In this equation $\frac{\Delta\tau}{2}$ is the triangular phase slope and $(\omega_0 + \delta\omega)$ the point at which the spectrum is divided and shifted either forward or backward in time. Thus $\Delta\tau$ determines the temporal separation between the two subpulses and the ‘spectral breakpoint’ $(\omega_0 + \delta\omega)$ determines the spectral width, the central wavelengths, and the amplitudes of the individual subpulses.

Two illustrative examples are shown in Fig. 6.1 for a double triangular phase slope of 1000 fs resulting in a pulse separation of the same value of 1000 fs. In Fig. 6.1(a), the spectral breakpoint is set to the carrier frequency $\omega_0 = 2.348$ rad/fs and thus the two individual pulses are of equal peak intensity. In Fig. 6.1(b) the influence of the spectral breakpoint $\omega_0 + \delta\omega$, with $\delta\omega$ being different from zero, on the temporal profile of the individual subpulses is clearly visible. Due to the fact that one part of the spectrum is shifted backward in time and one forward, the individual subpulses have different central frequencies [82, 182]. In the presented scheme, the pulse separation and amplitude ratio can be adjusted by two parameters, triangular phase slope and spectral breakpoint. By scanning these two control parameters a fitness landscape can be measured in which the effect induced by varying separation, spectra and amplitudes of the two pulses is directly visible.

6.3 Interpretation of control mechanisms with fitness landscapes

In this section, an optical demonstration experiment is used to show that fitness landscapes generated by scanning colored double pulses can indeed elucidate the control mechanisms of adaptively obtained optimal pulse shapes. The experimental setup that will be presented in the next subsection has been specifically designed in such a way, that a double pulse best fulfills the control objective. This objective, the maximization of the yield of third harmonic generation (THG) in the given setup, has the additional benefits that the effects of different pulse shapes can be mathematically calculated and intuitively understood.

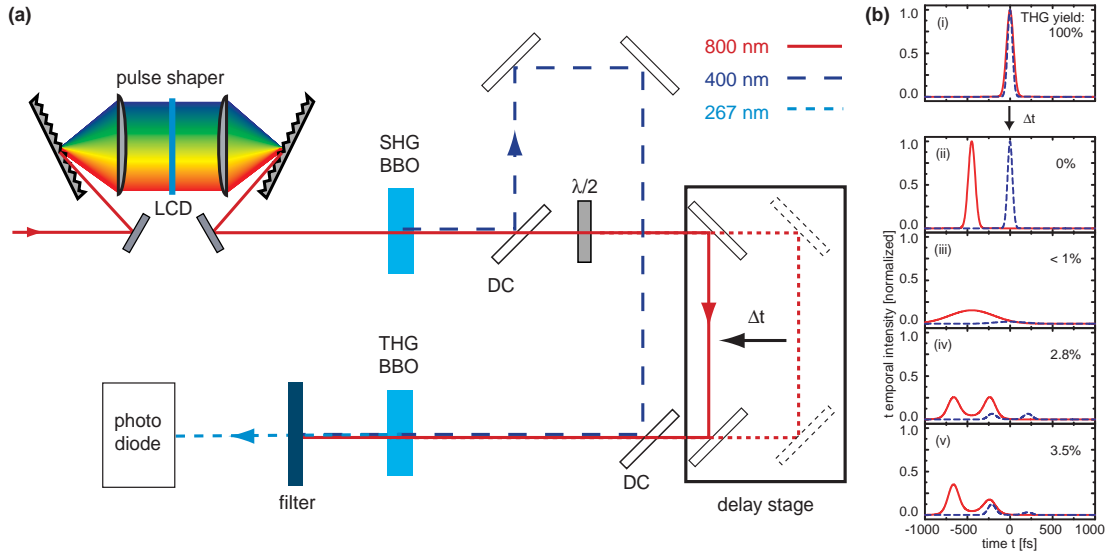


Figure 6.2: (a) Setup for an experiment in which a double pulse leads to the highest third harmonic yield. It is based on a standard design for THG. The 800 nm laser beam coming from the pulse shaper is frequency-doubled in a SHG crystal. Second harmonic (400 nm) and fundamental (800 nm) are separated by a dichroic mirror (DC). The 800 nm pulse passes over a delay stage (dotted red line) and is temporally and spatially overlapped with the 400 nm pulse in a THG crystal. The $\lambda/2$ -waveplate ensures the correct polarization of the 800 nm beam for the SFG-process. When a temporal delay is introduced (indicated by the delay stage moved to the left, so that the unshaped 800 nm pulse is Δt ahead of the 400 nm pulse at the THG crystal), there will be less temporal overlap in the THG crystal, and thus, less third harmonic (267 nm) radiation. However, with the pulse shaper it is possible to generate laser pulses whose shapes are adapted to the introduced temporal delay, so that the generation of 267 nm light is increased. (b) Sketch of the temporal intensity profiles revealing the influence of the pulse shape on the THG. In the case of temporal overlap ($\Delta t = 0$ fs, Fig.[i]), the THG yield is maximal. When a temporal delay Δt (here: 450 fs) between the 800 nm (red) and the 400 nm (blue) beam is introduced, unshaped laser pulses will not create any 267 nm light [ii]. Chirping the initial 800 nm pulse, and thus elongating it, improves the overlap between the 800 nm and 400 nm pulses in the THG crystal, but only little 267 nm light is produced [iii]. A double pulse with a pulse separation of 450 fs where the energy is spread equally over the two subpulses yields more 267 nm light [iv]. A double pulse where the first subpulse has twice the peak intensity of the second subpulse leads to even more 267 nm light. The asymmetry in the intensity of the subpulses accounts for the nonlinear SHG process [v].

6.3.1 Experimental setup

The standard method to produce the third harmonic (267 nm) of the fundamental (800 nm) laser pulse of our laser system is given by first frequency-doubling the

800 nm pulse in a SHG crystal (BBO, β -barium borate, thickness: 100 μm , $\phi=29.2^\circ$) and consecutive sum-frequency generation (SFG) of the second harmonic (400 nm) with the fundamental 800 nm pulse (see Fig. 6.2(a)) in a THG crystal (BBO, 300 μm , $\phi=44.3^\circ$). Such a setup is generally called ‘tripler’. In order to obtain a high conversion efficiency, a good temporal overlap of the 800 nm and 400 nm pulses has to be ensured. If the temporal overlap and/or the phase matching angles of the crystals are not perfectly adjusted, a bandwidth-limited pulse will not produce the highest yield. The setup in Fig. 6.2(a) can easily be modified in such a way that the yield of THG is maximal for a double pulse, simply by introducing a temporal delay Δt between the fundamental and the second harmonic pulse. If the optical path of the 800 nm beam is made slightly shorter than necessary, so that the 800 nm pulse arrives $\Delta t = 450$ fs earlier at the THG crystal than the 400 nm pulse, nearly no 267 nm yield can be measured for unshaped pulses. The outcome of such an experiment is outlined for exemplary pulse shapes in Fig. 6.2(b). Due to the temporal delay Δt , unmodulated or linearly chirped pulses will lead only to very little third harmonic light, while significantly more can be generated with a double pulse. Fig. 6.2(b) also reveals that an even higher THG yield is achieved by a double pulse whose first subpulse has a higher intensity than the second subpulse. As SHG is a second-order process, while the subsequent SFG is only linear in the 800 nm pulse intensity, it is advantageous for maximizing THG to invest substantially more intensity in the initial second-order step of SHG (i.e., to produce a 400 nm double pulse with an intense first subpulse), and then to mix this intense first 400 nm subpulse with the second 800 nm subpulse of lower intensity at the optimal temporal delay (see Fig. 6.2(b)[v]). According to this intuitive picture, an evolutionary algorithm controlling the pulse shaper and using the THG signal as a feedback should find optimal pulses which show a clear double-pulse structure.

6.3.2 Results and discussion

In a first experiment, the optimal pulse for producing the highest third harmonic yield for the THG setup in which the temporal overlap between the fundamental and the second harmonic is slightly detuned by $\Delta t = 450$ fs (see Fig. 6.2(a)) is determined. Fig. 6.3(a) shows the evolution curve obtained for the optimization. Clearly, the algorithm finds an optimal laser pulse shape that is much better adapted to the experimental situation than the randomly shaped laser pulses from the first generation of the evolution. Unshaped laser pulses produce nearly no third harmonic in comparison to the optimally shaped laser pulses, as expected from Fig. 6.2(b).

Fig. 6.3(b) visualizes the temporal intensity and phase of the optimal pulse as measured by SHG-FROG (see chapter 3.5), and in Fig. 6.3(c), the optimal pulse shape is shown in the Husimi representation. In both figures, a dominant double-pulse structure can be seen, for which the intensity of the first subpulse is much higher than that of the second. This is again in excellent agreement with the intuitive picture of

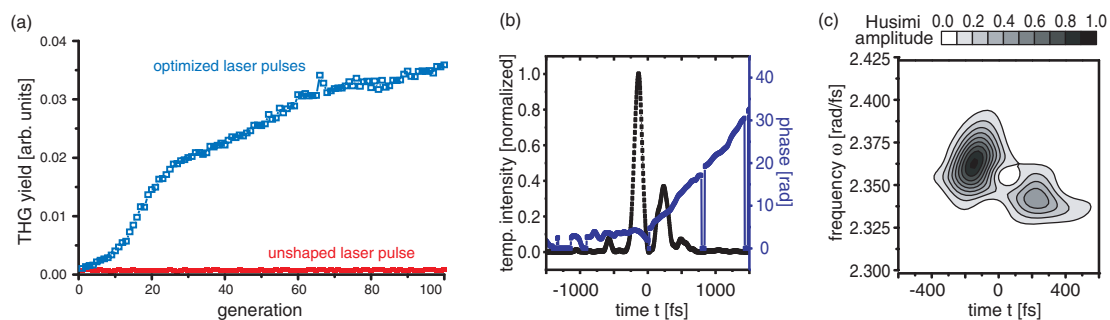


Figure 6.3: (a) Evolution curve for optimizing the THG yield with a time delay of 450 fs between the 800 nm and 400 nm pulses. Open blue squares: Each data point is the average of the ten best individuals of one generation. Solid red squares: reference signal of an unshaped laser pulse. Clearly the learning algorithm succeeded in finding a pulse shape that can produce a much higher third-harmonic yield than the initial randomly shaped laser pulses or unshaped laser pulses. (b) Temporal intensity and phase as derived from an SHG-FROG measurement. As expected from the sketch in Fig. 6.2(b)[v], a double-pulse-like feature is visible, with the first subpulse having significantly more amplitude. (c) Corresponding Husimi representation of the optimal pulse shape for the third-harmonic optimization. The second subpulse is clearly red-shifted.

Fig. 6.2(b). Additional features such as slight pre- and post-pulses are visible as well.

For a systematic study and explanation of the optimization results, a fitness landscape of the third harmonic yield was measured by scanning the parameters of the colored double pulses. This fitness landscape is shown in Fig. 6.4(a), where the THG yield is shown as a function of the two control parameters, double triangular phase slope $\Delta\tau$ and spectral breakpoint $\omega_0 + \delta\omega$. Two regions for a high third-harmonic yield can be identified. One local maximum occurs for a double triangular phase slope of +450 fs (double pulse with 450 fs pulse separation and the red-shifted pulse comes first) and a spectral breakpoint of ≈ 799 nm (the red pulse has a higher intensity than the blue one). The second and larger maximum in the fitness landscape of Fig. 6.4(a) is at a double triangular phase slope of -450 fs (double pulses with 450 fs pulse separation and the blue-shifted laser pulse precedes the red-shifted one) and a spectral breakpoint of ≈ 802 nm (thus, the blue-shifted laser pulse has a higher intensity than the red-shifted one). The pulse shape responsible for the global maximum as well as the corresponding measured value of the 267 nm yield are very similar to the pulse shape and the 267 nm yield found by the adaptive femtosecond quantum control experiment. However, it is possible that the algorithm would have found an even higher fitness value at a later generation than tested.

Fig. 6.4(b) shows the calculated fitness landscape for an idealized case, where no misalignments are present, such as deviations of the phase matching angles of the nonlinear crystals from the ideal value. The effects of the pixelation of the LCD are included in the simulations. The simulated fitness landscape is very similar to

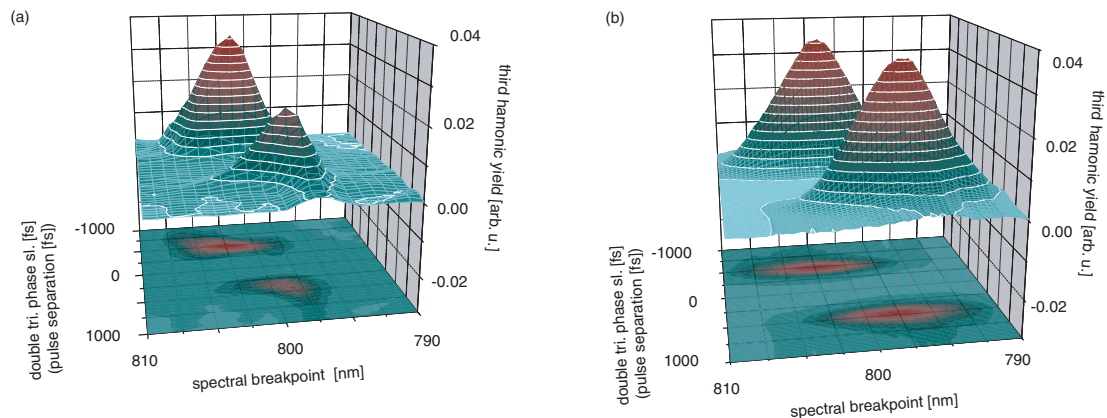


Figure 6.4: (a) 3D representation of the measured colored double pulse fitness landscape of THG. (b) Calculated third-harmonic yield. The differences between the calculated and measured fitness landscapes are due to experimental imperfections (especially slight misalignments of the phase-matching angles of the used crystals).

the measured landscape except that the two maxima are of equal height and slightly different shape. This suggests that it is necessary to have a double pulse, with the first pulse having a higher amplitude than the second.

Both the calculated and the measured results are in accordance with the intuitive picture discussed above (Fig. 6.2(b)). The reason for the experimental measurement having two maxima of different height can be explained by phase-matching imperfections. Therefore certain central frequencies for the individual pulses are better adapted to the given experimental situation.

Based on the information that can be gathered from the fitness landscape (Fig. 6.4(a)), one can easily explain the optimal pulse shape obtained from the adaptive control experiment (Fig. 6.3). The pulse separation in Fig. 6.3(b) of the two dominant sub-pulses matches the pulse separation that gives the highest yield in the parameter scan of Fig. 6.4(a). Just like there, the maximum is achieved with a double pulse whose first subpulse has a higher peak intensity compared to the second one. Also, the first subpulse in the adaptive experiment contains higher frequencies than the second one, as can be seen from the Husimi trace in Fig. 6.3(c), again in accordance with the parameter scan. The additional small pre- and post-pulses can be explained as slight adaptations to the given experimental situation or as features not yet smoothed out by the learning algorithm, either because they will not contribute substantially to the fitness or because the algorithm would have to run for a longer time.

6.4 Analysis of the intrapulse dumping mechanism

Many investigations in time-resolved femtosecond molecular spectroscopy have revealed that pump-dump-like processes can influence molecular dynamics significantly and that such processes can be responsible for reaching certain control objectives. A prominent example for this is intrapulse dumping [176, 183], where two electronic transitions occur within the same adequately linearly chirped laser pulse (where the momentary frequency of the laser pulse changes linearly with time). Other possibilities are two-pulse pump-dump-scenarios [180, 181], where two laser pulses of different colors and with a certain temporal delay between the pulses interact with the system under study. In both cases, the observed effects originate from wave-packet dynamics on the first excited-state (S_1) potential energy surface (PES). After an initial excitation by the first interaction with the electric field, the wave-packet generated on the S_1 PES propagates away from the Franck-Condon region (see Fig. 6.5). The energy gap between the excited-state (S_1) and the ground-state (S_0) potential energy surfaces is in general shrinking during this wave-packet propagation. Therefore, if a second interaction with the electric field is to take place that connects the S_1 and the S_0 potential energy surfaces, thereby transferring the wave packet partially or completely back to the ground-state, a photon of lower frequency in comparison to the first interaction is required.

C. V. Shank and coworkers have shown in 1996 that in the case of one photon excitation, the amount of excited molecules depends significantly on the linear chirp imposed on the exciting laser pulse [176]. A downchirped pulse, where high frequen-

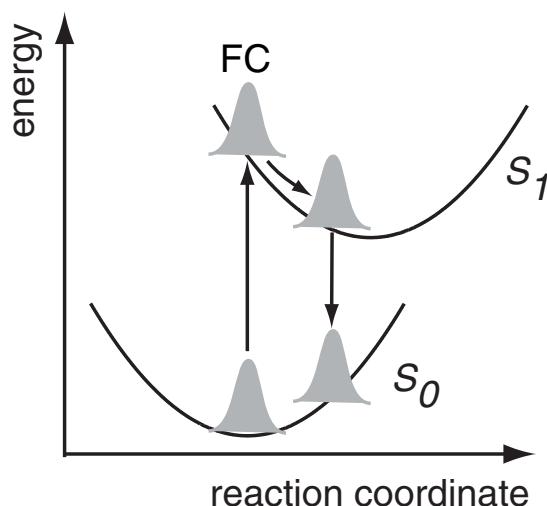


Figure 6.5: Scheme of the potential energy surfaces illustrating the intrapulse dumping and pump-dump mechanisms (adapted from Ref. [176]). The excited-state wave-packet is initially created in the Franck-Condon (FC) region of the S_1 PES.

cies precede low ones, excites significantly less molecules than an upchirped pulse of the same pulse energy. This is due to the fact that the decreasing photon frequencies match the shrinking molecular energy gap between the relevant PESs, and a part of the wave-packet can therefore be efficiently transferred back to the lower PES. In the case of the upchirped pulses, this intrapulse dumping mechanism is minimized, so that the excitation of the molecules is more efficient [176].

We have chosen an example of such an intrapulse dumping mechanism for a systematic study of parameter scans with different basis sets. With this method it can be investigated whether it is equivalent to guide the wave-packet along the shrinking energy gap, i.e., by a linearly chirped pulse, so that both interactions occur within the same elongated laser pulse, or to split the laser pulse energy into two subpulses, one for each of the two interactions. Thus, two time-domain parameterizations will be used: linearly chirped laser pulses and colored double pulses. The influence of the different pulse shapes on a molecular system is studied by monitoring the stimulated emission from a solution of the dye molecule 5,5-dichloro-11-diphenylamino-3,3-diethyl-10,12-ethylene thiatricarbocyanine perchlorate (IR140) under strong-field illumination.

6.4.1 Experimental setup

In order to show the mapping of molecular control parameter landscapes, the transient absorption spectroscopy setup shown in Fig. 6.6 is employed. With this setup it is possible to determine the amount of IR140 molecules excited by the shaped 800 nm pulses by measuring their stimulated emission. The initial 800 nm laser beam is split

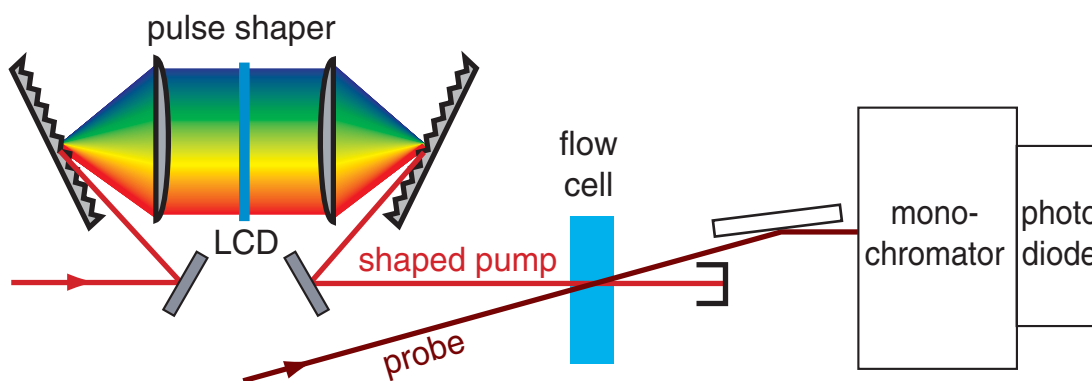


Figure 6.6: Transient absorption pump-probe setup. The pump and the probe pulses are spatially overlapped in the sample. The pump pulse, which can be modulated by a pulse shaper, excites a certain amount of molecules, and the probe pulse monitors the stimulated emission and thereby the amount of excited molecules. The time delay between the two pulses can be varied by a delay line. The 870 nm part of the probe pulse is isolated with a monochromator after the sample, and the signal is recorded with a photodiode.

into two parts in front of the pulse shaper. One part is sent through the pulse shaper and is used as the modulated pump, while the other part is used for the probe beam. The shaped 800 nm pump pulse is focused by a lens with a focal length of 200 mm into a flow cell containing the IR140 sample dissolved in methanol. To measure the stimulated emission at 870 nm, the second part of the initial beam is focused into a sapphire plate to generate a white-light continuum centered around 800 nm. Using a lens of 150 mm focal length, the white-light probe laser pulse is spatially overlapped with the shaped 800 nm pump pulse in the sample. Pump and probe laser pulses can be delayed with respect to each other by employing a computer-controlled delay stage. The excited state lifetime of the IR140 molecule dissolved in ethanol is reported to be 500 ps [184]. This is for example observable in the stimulated emission decay, which can be probed at a wavelength of 870 nm. Therefore the transient absorption signal at a fixed probe delay time of 150 ps and at a probe wavelength of 870 nm is proportional to the amount of excited molecules. This observable is examined in the following experiments.

6.4.2 Results and discussion

The aim of the experiments presented here is to investigate whether the intrapulse dumping or pump-dump mechanism can be driven with a similar efficiency by different electromagnetic fields. More specifically, measurements are carried out that compare the achievable excitation of molecules by either the continuous electric field of linearly chirped laser pulses or by splitting the energy into two subpulses whose central frequencies are adjusted appropriately in order to facilitate the dumping mechanism.

For this comparison it is worthwhile to examine the relationship between the momentary frequencies of linearly chirped laser pulses and colored double pulses. The momentary frequency $\omega_m(t) = d\phi(t)/dt$ of a chirped laser pulse with central frequency ω_0 , a spectral intensity at full width at half maximum (FWHM) $\Delta\omega$ and a second-order spectral phase Taylor coefficient b_2 is given by [176, 185]

$$\omega_m(t) = \omega_0 + \frac{b_2}{\frac{(4\ln 2)^2}{\Delta\omega^4} + b_2^2} \cdot t \quad . \quad (6.2)$$

For a double pulse with a symmetric separation of the spectrum (i.e. $\delta\omega = 0$), as defined by Eq. (6.1), the momentary frequency at the temporal positions $\pm\Delta\tau/2$ can be determined as [185]

$$\omega_m(t = \pm\Delta\tau/2) = \omega_0 \pm \frac{\Delta\omega}{\sqrt{2\pi \ln 2}} \quad , \quad (6.3)$$

where $\Delta\tau$ is again the pulse separation and its sign determines whether the red subpulse precedes the blue subpulse or vice versa. In order to make an appropriate comparison,

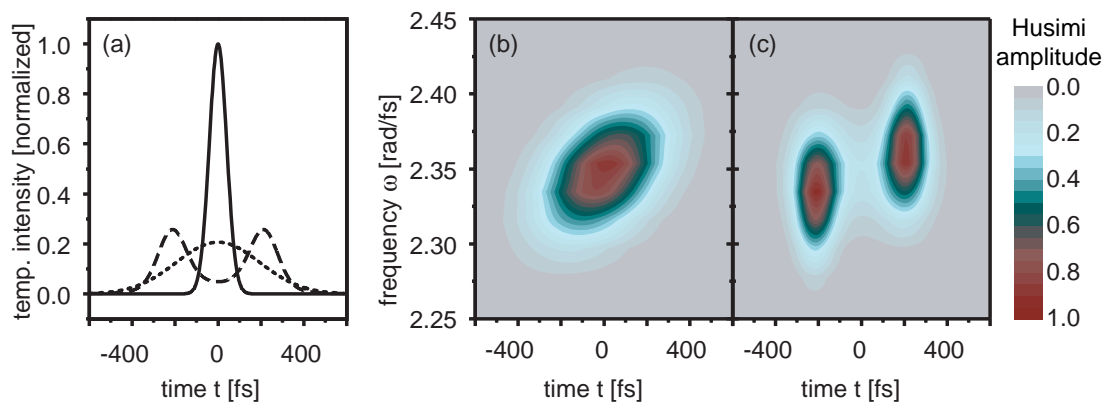


Figure 6.7: (a) Simulation of the temporal intensity of a colored double pulse with $\Delta\tau = 450$ fs (dashed), and a chirped pulse with second order spectral phase coefficient $b_2 = 15400$ fs² (dotted), according to Eq. (6.4). The solid line shows the temporal intensity of a bandwidth-limited pulse for comparison. On the right, the corresponding normalized Husimi representations for the chirped pulse (b) and for the colored double pulse (c) can be seen.

we compare each colored double pulse to the linearly chirped pulse which has the same momentary frequency at $t = \pm\Delta\tau/2$. This leads to the formula

$$\Delta\tau = \frac{2\Delta\omega}{b_2\sqrt{2\pi\ln 2}} \left(\frac{(4\ln 2)^2}{\Delta\omega^4} + b_2^2 \right). \quad (6.4)$$

For values of $\Delta\tau$ which are close to the minimum pulse duration or even smaller, one cannot really speak of a clear double pulse, which complicates an adequate comparison. However, if $\Delta\tau$ is larger than the minimum pulse duration, two separated sub-pulses are generated. In that case, Eq. (6.4) can be approximated to the linear equation

$$\Delta\tau \approx \frac{2\Delta\omega b_2}{\sqrt{2\pi\ln 2}}. \quad (6.5)$$

For a Gaussian laser spectrum centered at $\omega_0 = 2.348$ rad/fs with $\Delta\omega = 0.029$ rad/fs (which corresponds to the same minimum pulse duration of 95 fs as used in the experiment), the colored double pulse corresponding to a linear chirp of $b_2 = 20000$ fs² has a pulse separation of 575 fs according to Eq. (6.4), or 560 fs according to the approximation in Eq. (6.5), respectively. Thus, we make use of Eq. (6.5) in the juxtaposition of linearly chirped pulses and colored double pulses in Fig. 6.8.

Fig. 6.7 shows that although the temporal pulse profiles are extremely different (see Fig. 6.7(a)), chirped pulses and colored double pulses can be generated whose momentary frequencies coincide at times of highest intensity in the double pulse (visualized by the slope in the Husimi traces of Fig. 6.7(b) and (c)). In order to investigate whether the

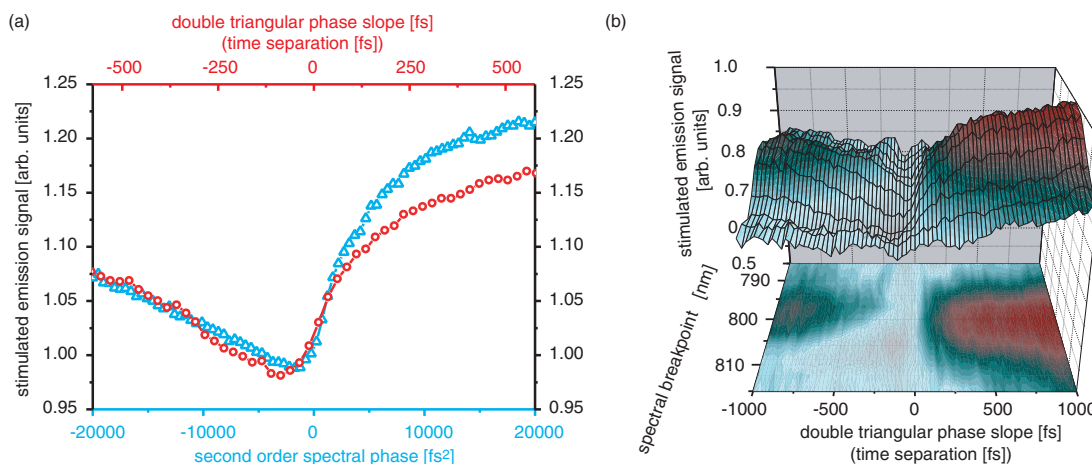


Figure 6.8: (a) Stimulated emission of IR 140 pumped with shaped 800 nm laser pulses and probed at 870 nm at a delay time of 150 ps. The graph shows two parameter scans. In the one corresponding to the lower abscissa (blue triangles), the second order spectral phase (i.e., the linear chirp) is varied from -20000 fs^2 to $+20000 \text{ fs}^2$. In the second parameter scan corresponding to the upper abscissa (red circles), double pulses (spectral breakpoint at $\omega_0 = 2.348 \text{ rad/fs}$) are generated with the time separation varied from -560 fs to $+560 \text{ fs}$. The interrelation between the two abscissae is calculated according to Eq. (6.5). (b) 3D representation of the stimulated emission in dependence on a double pulse separation from -1000 fs to $+1000 \text{ fs}$ and a variation of the spectral breakpoint from 785 nm to 815 nm.

intrapulse dumping effect can also be realized and confirmed by colored double pulses, several experiments are carried out. First, the dependence of the excitation on the linear chirp is measured (Fig. 6.8(a), blue triangles). From this figure, it is clearly visible that downchirped pulses excite significantly less molecules than upchirped pulses of the same chirp magnitude, which is in agreement with the observations made for other molecular systems [45, 176, 177, 183].

In a second experiment, a double pulse fitness landscape is obtained for the molecular excitation process, which shows the stimulated emission of IR140 after the excitation as a function of the two control parameters double-pulse separation and spectral breakpoint (Fig. 6.8(b)). This figure shows that the amount of stimulated emission and hence the amount of excited molecules clearly varies for different pulse parameters. The highest yield can be achieved for double pulses with a spectral breakpoint of 800 nm and for positive double-triangular phase slopes.

To understand this effect, a cut of this fitness landscape for a fixed breakpoint value of 800 nm is shown together with the chirp scan in Fig. 6.8(a) (red circles). For positive values of the double triangular phase, the first subpulse is red-shifted and the second subpulse is blue-shifted, and vice versa for negative double-triangular phase

slopes. As can be seen from Fig. 6.8(a), double pulses with positive double-triangular phase slope excite the system much more efficiently than those with a negative double-triangular phase slope of the same magnitude. This effect can be explained analogously to the intrapulse dumping mechanism of chirped pulses. If the first subpulse that induces a wave-packet on the upper PES has higher frequencies, then a second subpulse containing lower frequencies matches the decreasing energy gap upon wave-packet propagation and thus, the dumping of the wave-packet to the ground state is enhanced. The efficiency of the dumping process depends both on the pulse amplitudes and on the pulse separation as can be seen in the fitness landscape (Fig. 6.8(b)). Appropriately colored double pulses are equivalent to single chirped pulses for the case of intrapulse dumping. This is seen in the similar behavior of the two curves in Fig. 6.8(a).

These experiments demonstrate that two parameterizations leading to clearly different pulse shapes can fulfill a control objective by the same underlying mechanism. The Husimi plots of the pulses in Fig. 6.7 show that matching the momentary frequency to the S_0 - S_1 energy gap at two points in time results in a similar outcome as when the momentary frequency is continuously adapted by a linear chirp.

In general, using colored double pulses and scanning of fitness landscapes can provide insight in basic color-dependent pump-dump-like control mechanisms.

6.5 Conclusion

The experiments presented in this chapter demonstrated the capability of colored double-pulse fitness landscapes to investigate molecular dynamics and to assist in the interpretation of optimal laser pulse shapes found in adaptive femtosecond quantum control experiments. Differently colored double pulses were produced by a pulse shaper with varying subpulse amplitudes and pulse separations. The resulting control landscapes illuminate the system's response to colored double pulses.

In a purely optical demonstration experiment, the yield of the third harmonic generation was studied in a setup where certain double pulses represent the best solution. This experiment had the advantage that the optimal pulse shape from an adaptive femtosecond quantum control experiment as well as the double-pulse fitness landscape could be intuitively understood and compared to calculations.

In order to establish the scanning of colored double pulses as a valuable tool among systematic parameterizations for investigating control mechanisms with regard to more complex problems, the control of molecular excitation of the dye IR140 dissolved in methanol under strong-field laser illumination was studied. It was shown that two clearly different pulse parameterizations can result in similar effects. The experiments showed that well-known effects like intrapulse dumping usually observed under chirped-pulse excitation can be induced in an equivalent way by colored double pulses. This scenario demonstrated that parameter scans and fitness landscapes can give an indication how a molecular system can be controlled.

Often very different control pulse shapes can fulfill a control objective with simi-

lar efficiency. Such pulse shapes correspond to different local extrema in the space of all possible laser pulses, which can lead to difficulties in finding the global optimum and in the interpretation of adaptively found optimal pulses. A combination of several adequately chosen parameterizations is proposed as a means to identify viable control mechanisms involved in an optimal pulse found in a closed-loop optimization. Thus, with the assistance of parameter scans like the colored double pulses presented here, a better understanding of molecular systems and their controllability is a realistic objective. However, in a closed-loop control experiment, the optimization algorithm may take advantage of several mechanisms to optimize the control goal. Determining the interplay of these mechanisms will still pose a challenging task.

Chapter 7

Modeling of light–matter interactions with neural networks

Despite the considerable increase in computing power, *ab initio* calculations, e.g., for the prediction of light–matter interactions, remain limited to small molecular systems to date. An intriguing option for gaining information about this interaction is to extract it from experimental data. In this context, the manipulation of light fields with femtosecond laser pulse shapers opens up new possibilities, as the ability for almost–arbitrary field tailoring provides an opportunity for testing the response of quantum systems with respect to a large number of different electromagnetic fields.

In this chapter, the possibilities for the generation of models for light–matter interactions from simulated or measured data with the help of neural networks (NNs) will be examined. After an introduction to the general concept of this approach in section 7.1, the basic properties of neural networks will be presented in section 7.2. In a first application, NNs will be utilized to model the processes of second–harmonic generation (SHG) and molecular fluorescence (section 7.3). A more sophisticated quantum system will be investigated in section 7.4, where the ultrafast coherent strong–field dynamics in potassium will be modeled with a neural network.

7.1 Introduction

As illustrated in chapter 2, and demonstrated in chapter 4, adaptive optimal control involves an iterative search for suitable electromagnetic fields that drive a quantum system along desired trajectories or into certain final states. This approach has proven to be an excellent method for reaching specific control objectives [15, 45, 49, 52, 53, 56, 59, 127, 159]. However, it is usually difficult to gain insight into the reaction mechanisms at play or to extract information on the interaction of the investigated system with electromagnetic fields from the optimized field shapes. While the previous chap-

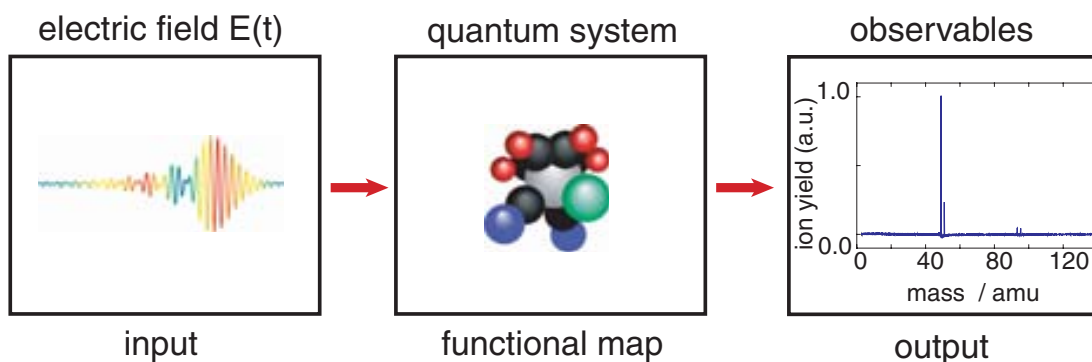


Figure 7.1: Correspondence between optical experiments with shaped femtosecond laser pulses and functional input–output maps.

ter addressed the first of these issues, we will focus on the second topic here. The ability of almost–arbitrary field tailoring opens the opportunity for testing the response of quantum systems with respect to a large number of input parameters, and thus it should be possible to obtain a significant amount of information not available with ordinary, unshaped laser pulses. Hence the question arises how to process this data, i.e., which pulse shapes to employ and in which form to evaluate the complex system responses. Optimization schemes such as evolutionary algorithms or simulated annealing are well suited for finding the best laser pulse shape according to a specific optimization objective. However, they are not designed to ‘keep track’ of the information gathered during the optimization process, and they are not capable of evaluating the system’s responses in a systematic fashion. Hence other methods might be better suited for the specific purpose of analyzing light–driven quantum processes. The objective of such methods should not be to optimize a certain quantum–mechanical process or to reach user–specified quantum states, but rather to obtain some kind of model for the system response to applied light fields.

In formal terms, a pulse–shaping quantum control experiment can be viewed as shown schematically in Fig. 7.1. The electric field $E(t)$ of the shaped laser pulse is an input to the quantum system (say, molecule), and the observable (e.g., mass spectrum) is an output, with the molecule itself acting as a functional input–output map. If it is possible to determine this input–output map, one has obtained an effective model of the system’s response. The usage of input–output maps has been discussed theoretically before [186, 187]. In both these works from the group of H. Rabitz, simulated input–output pairs are utilized for generating linear [186] or nonlinear [187] functional maps that describe the impact of various electric fields on a quantum–mechanical system. The input–output pairs used there consist of electric fields, expanded in simple bases, as input and the value of an observable at a final time t_f , e.g., the population in a certain final state, or a time–history/trajectory, as output. These maps are obtained by interpolating between the explicitly sampled fields.

Here a concept for the automated generation of input–output maps by employing

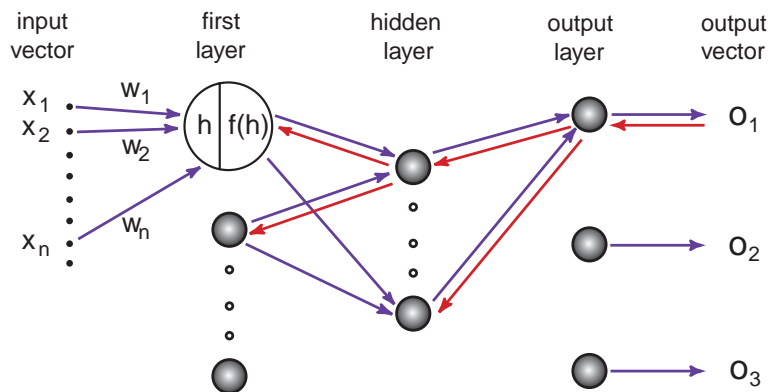


Figure 7.2: Schematic representation of a feedforward–backpropagation NN architecture and working principle. Neurons are depicted as spheres, and the flow of information and error correction is indicated by right–pointing and left–pointing arrows, respectively. If the weights w_i are adjusted correctly, the input vector is mapped onto the desired output vector by the underlying functional map.

a neural network is introduced. It will be shown both in simulations as well as in experiments that NNs are able to learn such maps with suitable trial inputs and that they can then generalize beyond this trial data in order to predict the system behavior even for complex pulse shapes that have not been introduced to the NN before. In this way, one transfers the functional behavior of the laboratory quantum system onto the NN contained within a computer.

7.2 Neural networks

Originally, neural networks were conceived for modeling biological processes in neural systems, consisting of neurons, synapses and axions. As it turned out, NNs were far too simplified to lead to significant progress in this field. On the other hand, it was soon recognized that they had properties which were rather desirable for various other applications, such as pattern recognition and function approximation [188–190]. A NN consists of neurons, which are basically simple processors, arranged in layers and connected to inputs, outputs and/or other neurons. There are many options how the input, output and neural elements can be connected, and how the network parameters are then adjusted. As we want the network to learn the response of physical systems to the electric fields of shaped laser pulses from a variety of sample pulses, we have chosen a network type that uses ‘supervised learning’ for adjusting the network parameters. More specifically, we employed networks of the so–called feedforward–backpropagation type, as depicted schematically in Fig. 7.2.

As in Feynman diagrams, there is no material entity connected to the elements of

such a network graph. It merely serves to illustrate the flow of information, and each symbol (connecting lines, neurons) stands for certain mathematical operations. The ‘feedforward’ in the network classification means that information is passed through the network in the forward direction only, i.e., from inputs towards outputs; there are no connections between neurons of the same layer or between layers other than one layer and the next one towards the output. Information is treated in terms of real-valued numbers x_i that travel along connecting lines. For information processing, each number is multiplied with a weight w_i associated with this connection. All (weighted) information entering a neuron is then subjected to a so-called propagation function h . Here, the weighted sum is formed according to $h = \sum_i w_i x_i$. The resulting ‘internal field’ h is then inserted into the ‘activation function’ $f(h)$, in our case the error function,

$$f(h) = \frac{2}{\sqrt{\pi}} \int_0^h e^{-t^2} dt, \quad (7.1)$$

and the resulting output is transmitted to the receiving neurons or output–channels in the same manner. The choice of this nonlinear activation function allows for varying output signal strength and saturation effects.

It should be noted here that the use of nonlinear activation functions is one of the prerequisites for approximating nonlinear mappings, the other is the presence of at least one hidden layer of neurons, which is not directly connected to input and/or output nodes [188]. We fulfill both requirements by employing a three–layer NN and the activation function in Eq. 7.1. The approximation of the functional map then involves finding both the optimal input parametrization and network architecture and adjusting the weights w_i such that the input parameters are mapped onto the output channels in the desired way. As the choice of the input parametrization and network architecture depends on the specific problem at hand, it will be covered in the relevant sections 7.3 and 7.4. The weights, however, are the most important parameters of the NN, and the terminus ‘backpropagation’ in the network classification describes how these weights are adjusted to the values suited for the function we want the network to approximate: The weights are initially assigned random values, which is a prerequisite for a successful performance of the NN; during a training process a large number of examples, consisting of input–output pairs, are presented to the NN. The input is entered into the network, processed as described above and delivers certain values o_j at the output nodes. These values are then compared to the correct, desired outputs t_j . If there are any deviations, the error – or rather its correction – is then propagated backwards through the NN (from the output towards the input nodes) using the ‘generalized delta rule’ [188]. This leads to the following modifications of the weights:

$$\Delta w_{ij} = \eta x_i \delta_j, \quad (7.2)$$

$$\delta_j = \begin{cases} f'(h_j)(t_j - o_j), & \text{for output neurons } j, \\ f'(h_j) \sum w_{jk} \delta_k, & \text{else.} \end{cases} \quad (7.3)$$

According to Eq. 7.2, the amount by which the weight w_{ij} , connecting neurons (or inputs/outputs) i and j , is changed after each training sample, is given by the product of the learning rate η , the input x_i of neuron i , and its ‘error signal’ δ_j . For output neurons, this error signal consists of the derivative of the neuron activation function and the difference between the desired, correct output t_j and the actual neuron output o_j . For neurons in deeper layers (towards the input side), the error signal contains the sum over $w_{jk}\delta_k$, where the sum runs over neurons k of the next higher layer (towards the output side) that are connected to neuron j . During the training process the weights of the NN are therefore adjusted in such a way that the errors on all outputs are minimized simultaneously. This procedure is repeated until the accuracy of the NN calculations for the training data set cannot be further improved. After this training process is completed, the NN can be used to generalize beyond the data presented to it. The degree to which this generalization is accurate depends on several factors, including suitable network architecture, input parametrization, representative training data, and so forth. How these questions have been tackled in several cases of interactions with shaped femtosecond laser pulses and how well the neural networks performed both during training and in tests of the generalization abilities, will be the subject of the following sections.

7.3 Modeling of SHG and molecular fluorescence with neural networks

The optimization, i.e., maximization, of second-harmonic generation (SHG) was among the first applications of closed-loop adaptive femtosecond pulse-shaping. It is still an important method for pulse compression, as the SHG signal is maximal for the shortest possible pulse duration for a given laser spectrum, and by maximizing the SHG signal with a pulse shaper, dispersion effects can be compensated. Apart from its relevance and the fact that SHG maximization is a well-understood process, it is also a straightforward task in both simulation and experiment. This makes SHG an ideal candidate as a first test for the capabilities of NNs for predicting the physical effects of various electric fields.

7.3.1 SHG simulation

As experimental data is subject to noise and as it is more difficult to reproduce exactly the same laboratory conditions for different measurements, we selected SHG simulation data for a first investigation of the question whether the modeling of light-matter interactions with neural networks is feasible or not. During these simulations a Gaussian spectrum, of similar width to that of our actual laser system, was subjected to a variety of spectral phases. For each such shaped pulse the electric field in the time

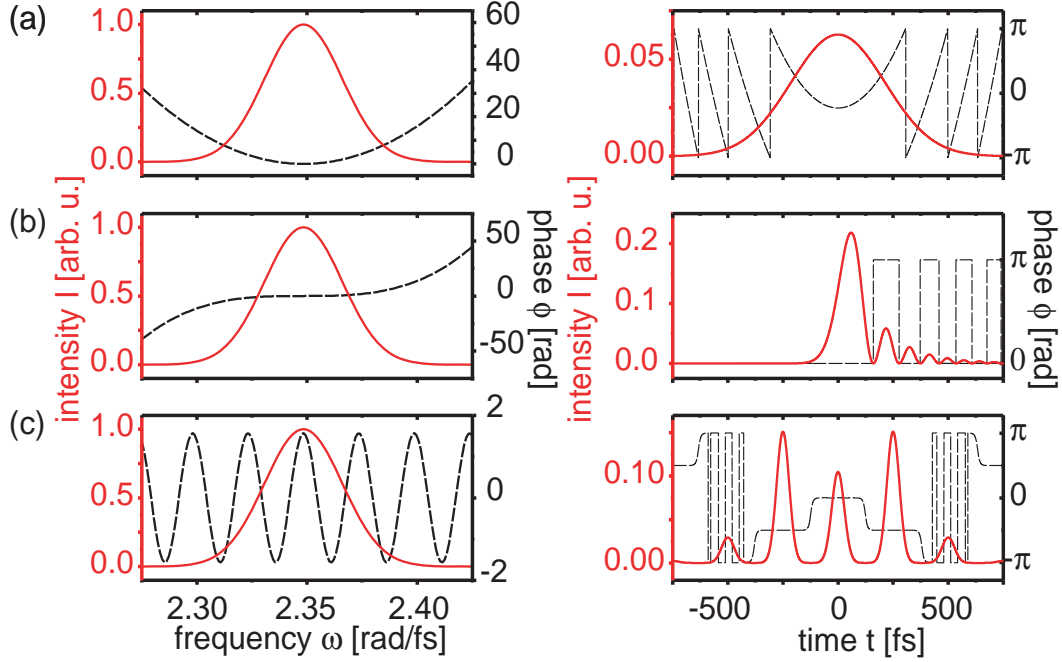


Figure 7.3: Simulated examples for the pulse shapes used during the training process. The first column displays the spectral phase (dashed black line) and intensity (red solid line) while the second column shows the respective temporal phase (dashed black line) and intensity (solid red line) profile. (a) Second–order spectral phase of 6000 fs^2 , (b) third–order spectral phase of 10^5 fs^3 , (c) sinusoidal spectral phase with $A = \pi/2$, $\tau = 250 \text{ fs}$, $\phi_0 = \pi/2$.

domain $E(t)$ was obtained by Fourier transformation. The temporally integrated SHG signal S , as generated in a nonresonant nonlinear crystal, was then obtained via

$$S = \int_{-\infty}^{\infty} I^2(t) dt, \quad (7.4)$$

where $I(t)$ is the intensity envelope associated with $E(t)$.

As a first step, training data had to be generated for teaching the NN how much second harmonic is generated by various electric fields. This training data should feature important parameters for the process under study and cover a reasonable part of the parameter space. The data points should also be systematically chosen, rather than randomly selected. As training data, pulse shapes with quadratic, cubic and sinusoidal [$\phi(\omega) = A \sin(\tau\omega + \phi_0)$] spectral phase structure were chosen. The temporal shaping window of our pulse shaper is about 4 ps [44]. In order to suppress the generation of unwanted pulse replicas, the parameter ranges for the different phase structures were chosen such that the phase difference between neighbouring pixels

remains well below 2π over the whole spectral range of the pulse shaper. Hence, quadratic phases from $-4 \times 10^4 \text{ fs}^2$ to $4 \times 10^4 \text{ fs}^2$, cubic phases from $-3 \times 10^6 \text{ fs}^3$ to $3 \times 10^6 \text{ fs}^3$ and sinusoidal phase patterns with amplitude A , $\frac{\pi}{4} \leq A \leq \pi$, delay τ , $16 \text{ fs} \leq \tau \leq 480 \text{ fs}$ and phase offset ϕ_0 with $0 \leq \phi_0 \leq \frac{11}{6}\pi$ were used. For each of these phase types ca. 1500 pulse shapes have been generated. Examples for these different parametrizations are depicted in Fig. 7.3.

During the training process itself, the simulated SHG signal that was calculated according to Eq. 7.4 was compared for each pulse shape to the SHG signal predicted by the NN and the error correction for the weights w_i was applied as described above (Eq. 7.2). This procedure was repeated – with reshuffled training samples – until the residual error could not be further improved. At the end of this stage, the learning process was completed and the performance of the NN could be tested.

In order to evaluate the network's ability to generalize beyond the training data, complex pulse shapes covering a wide range of both the input parameters and the resulting output signal strength are desirable as test data. One way to obtain such a variety of pulse shapes is to perform a closed-loop adaptive optimization. We therefore carried out an automated optimization with the aim of maximizing the SHG signal using an evolutionary algorithm. As mentioned above, the optimal pulse shape for maximizing the SHG signal is of course the shortest possible laser pulse for the given spectral bandwidth, but starting with an initial set of random pulse shapes many different pulse shapes are applied – and recorded – until this result is reached. Thus, during the optimization a variety of pulse shapes is generated with output signals covering the whole range between almost zero and maximum signal strength. The algorithm treated the values of the 128 spectral phases that can be applied by the LCD pulse shaper described in chapter 3.4.1 as independent genes. The pulse shaper phase-settings were adjusted by mutation and crossover during the optimization as described in chapter 2. During the optimization procedure, the NN was not involved. As pointed out before, we merely employed evolutionary optimization to generate complex trial pulses. After the optimization was finished, we then subjected each of its pulse shapes to the NN in order to find out what it would have predicted as compared to the correct result. If the NN approximates the functional map (in this case for SHG) well, then the SHG values predicted by the NN and those calculated exactly according to Eq. 7.4 during the evolutionary optimization should correspond to each other. The SHG simulation data was also used to determine the optimal input parametrization and architecture for the NN by testing its performance on both training and test data sets, which will be the subject of section 7.3.3.

7.3.2 Experimental implementation

As we intended to apply the method of mapping by NNs also to experimental data, the setup of Fig. 7.4 has been implemented for demonstration purposes. The 80 fs pulses

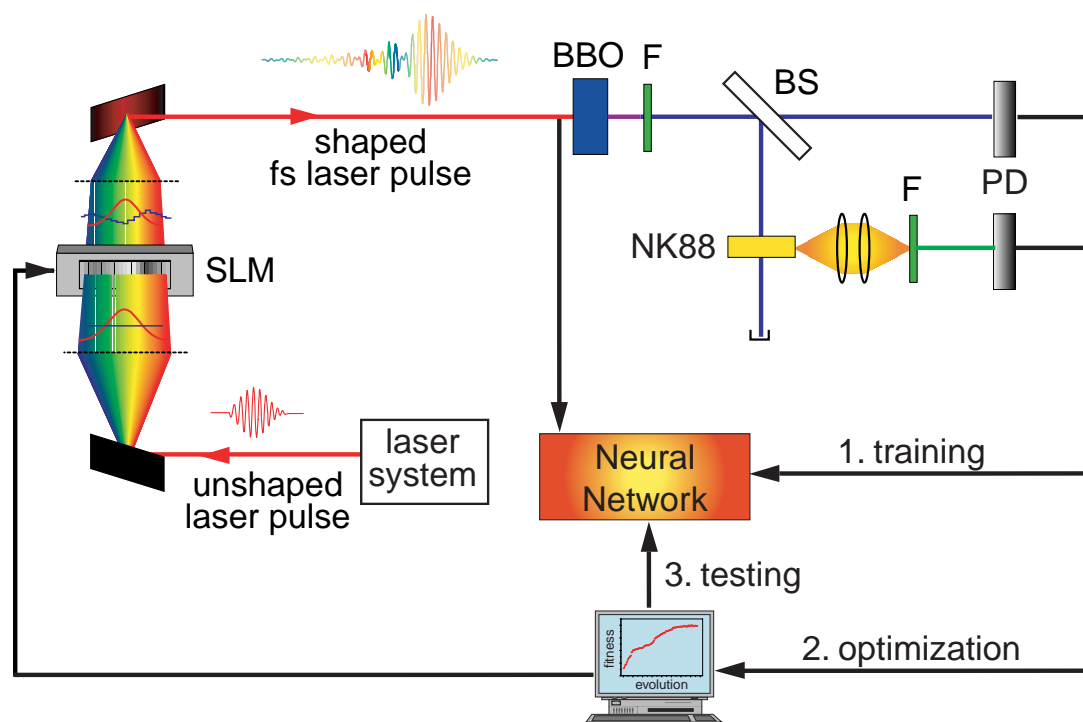


Figure 7.4: Experimental setup. Using a 128–pixel LCD pulse shaper, a variety of pulse shapes is first generated, and the corresponding values of observables (SHG signal and NK88 fluorescence) are recorded. This data is then used for the training of a NN. In a second step, an evolutionary optimization is carried out, with the goal of maximizing the SHG signal. Finally, the data gained in this optimization is used for testing the accuracy of the NN predictions for pulse shapes not present in the training data set.

from our laser system (800 nm, 1 kHz, 800 μ J) are phase–shaped by the computer–controlled 128–pixel liquid–crystal display (LCD) spatial light modulator ($4f$ –setup) described in chapter 3.4.1. After frequency doubling in a nonlinear β –barium borate (BBO) crystal, the fundamental is removed by a filter (BG38, Schott). The energy of the resulting SHG signal is recorded by a photodiode (PD). Due to the nonlinear nature of the SHG–process, the pulse energy will vary with the different applied pulse shapes.

In order to demonstrate that the NN is capable of modeling multiple observables simultaneously and that the NN can also make predictions for a molecular system, we additionally recorded the spontaneous emission yield (fluorescence) of the molecule 3,3′–diethyl–2,2′–thiacyanine iodide (NK88, Fig. 7.5(a)) dissolved in methanol, after excitation with the shaped 400 nm laser pulses. The molecular solution is cycled by a peristaltic pump through a flow cell. At room temperature the molecule NK88 is in the *trans* configuration. After excitation with a 400 nm photon it can then decay back into the *trans* configuration or undergo a *trans*–*cis* isomerization (see Fig. 7.5(b)). The ground–state absorption spectrum of the *trans*–isomer is shown in Fig. 7.5(c). From

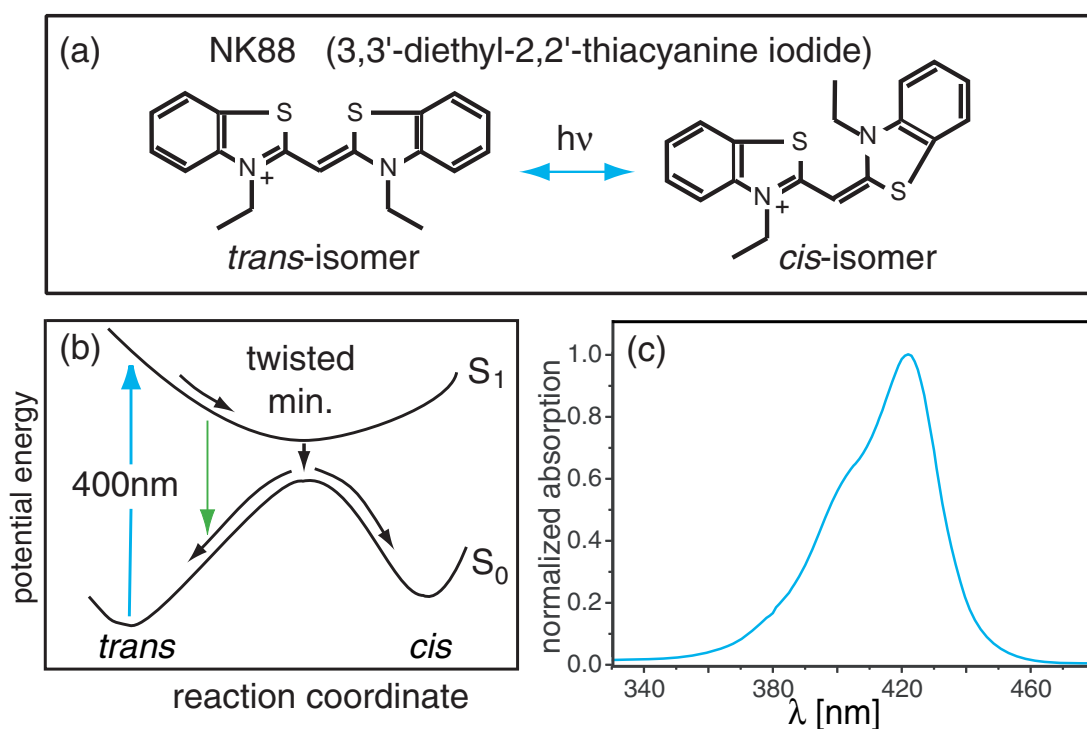


Figure 7.5: (a) Molecular structure of the two isomer configurations of the cyanine dye NK88. Irradiated by light of the proper wavelength, this molecule can undergo *trans*–*cis* isomerization. (b) Simplified potential energy surfaces. The reaction coordinate is the twist angle about the $C = C$ double bond. The excitation at 400 nm and the molecular fluorescence at 500 nm are indicated by blue and green arrows, respectively. (c) The ground–state absorption spectrum of the *trans* isomer.

the fluorescence accompanying the transition back to the ground state, the radiation at 500 nm is filtered out and recorded by a photodiode. The fluorescence signal acts as an indicator for the number of excited molecules. For a more detailed discussion, both theoretically and experimentally, of the molecular properties of NK88 after photo-excitation, confer Refs. [191, 192].

In analogy to the procedure described in the SHG simulation section above and as illustrated in Fig. 7.4, the experimental data is used in a sequence of three steps. First, a NN with the same architecture – apart from a second network output for the fluorescence yield – and input parametrization as for the SHG simulation is trained with pulse shapes within the same parameter ranges as for the SHG simulation, but with NK88 fluorescence at 500 nm as additional observable besides the SHG signal. In the second step, an evolutionary optimization of SHG is carried out, recording the fluorescence yield simultaneously. Finally, the NN performance is tested by using it to predict the experimental signals measured during the evolutionary optimization.

7.3.3 Input parametrization and network architecture

So far, only the employment of input–output pairs of a variety of pulse shapes for the training of NNs has been mentioned. How the information content of such input–output pairs has to be processed, i.e., how the inputs and outputs have to be parametrized, for use with a NN will be the first subject of this section. Later on it will also be investigated how the optimal network architecture, i.e., the optimal number of neurons in the network, can be found. Both issues are highly dependent on the specific process the network is supposed to model. While the parametrization of the outputs o_j of the network is straightforward, as the measured (or computed) values of the observables can be employed for this purpose, the parametrization of the inputs is less obvious. This is due to the fact that our control agent, i.e., the spectral phases and the electric field generated by them, can be expressed in many different ways, e.g., by the 128 values of the spectral phases $\phi(\omega)$ (LCD settings), or by a variety of temporal or spectral representations of the electric field. Several input parametrizations were tested using the SHG–simulation data, with the NN prediction for the simulated SHG signal t as the single network output o . For each of these parametrizations we have carried out the NN training procedure as described in section 7.2, with the pulse–shapes from section 7.3.1 as training data set. The adequacy of the different parametrizations depends on their ability both to reproduce the training data, and the ability to generalize beyond this training data. As a first candidate for the parametrization of the NN inputs x_i we considered the values of the 128 spectral phases, as these are the parameters varied in the simulation and experiment. It turned out that a NN trained with the spectral phases $\phi(\omega)$ as inputs has very limited capability of reproducing the data presented during training, as can be seen in Fig 7.6, where the network predictions and the exact simulation results are shown for (a) quadratic and (b) cubic spectral phases. Apparently the NN is incapable of reflecting both the axial symmetry of the quadratic phases and the inversion symmetry of the cubic phases at the same time with this input parametrization.

In order to solve this problem, as well as to reflect the 2π –periodicity of the phases, another parametrization was obtained by taking both the sine and cosine of the 128 spectral phases, totalling 256 network inputs. As a spectral representation of the electric field, the real and imaginary parts of $E(\omega) = A(\omega)e^{-i\phi(\omega)}$ were also examined as input parametrization, where $A(\omega) = \sqrt{I(\omega)}$ is obtained from the laser spectrum with intensity $I(\omega)$, again totalling 256 inputs. Both of these parametrizations do not show the symmetry problems encountered with the spectral phases $\phi(\omega)$ as inputs, and the error in reproducing the training data is significantly reduced, as can be seen in Fig 7.7. Another detail apparent in this figure is that the NN outputs can also reach (unphysical) negative values. This is due to the fact that the mapping by the NN is not necessarily positive definite.

As the overall training errors are still quite sizeable for these alternate input parametrizations in the frequency domain, a representation of the electric field in the

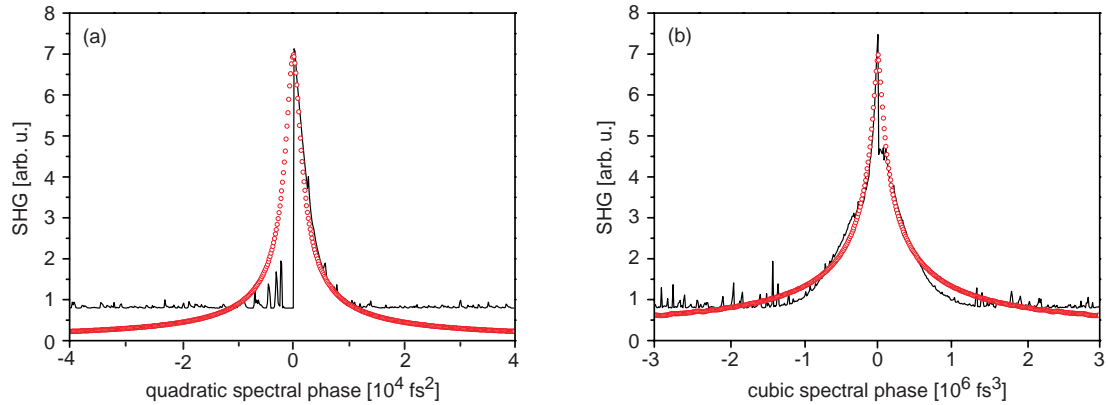


Figure 7.6: Training results of a NN trained with the spectral phases $\phi(\omega)$ as inputs. The network predictions (black line) and the simulation results (red circles) are shown for (a) quadratic and (b) cubic spectral phases, respectively.

time domain was also employed for parametrizing the network inputs. For this purpose, the envelope of the electric field in the time domain, evaluated at 128 discrete points, was used. The electric field was computed from the laser spectrum and the 128 spectral LCD phases by Fourier transformation. With this input parametrization, the errors of the NN mapping could be dramatically reduced; the corresponding training results will be shown in section 7.3.4. For comparison, the mean square errors of the NN predictions for the training data set were calculated. The results are shown in Fig. 7.8 for (A) the spectral phases, (B) sine and cosine of the spectral phases, (C) real and imaginary parts of the spectral field and (D) the temporal field envelope as input parametrizations. It is evident that the envelope of the electric field $E(t)$ in the time

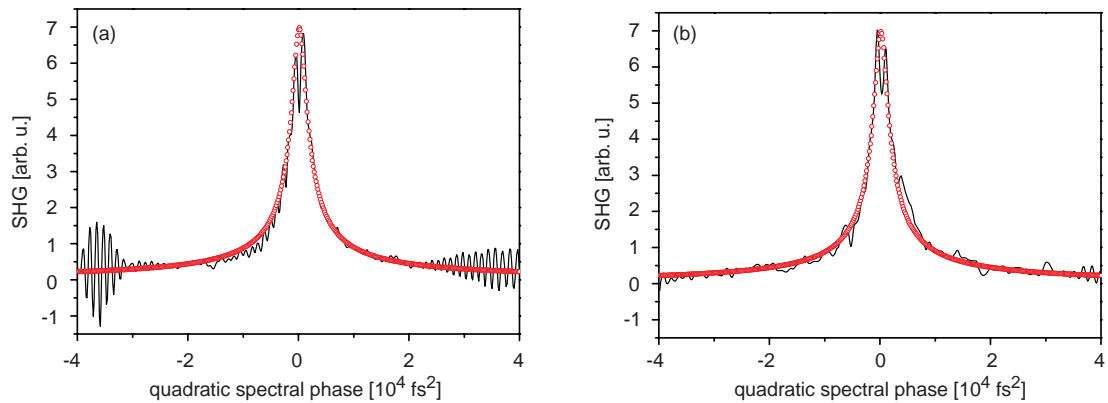


Figure 7.7: Training results for quadratic spectral phases of a NN trained with (a) the sine and cosine of the spectral phases and (b) the real and imaginary parts of $E(\omega)$ as inputs. The network predictions are shown as black lines and the simulation results as red circles.

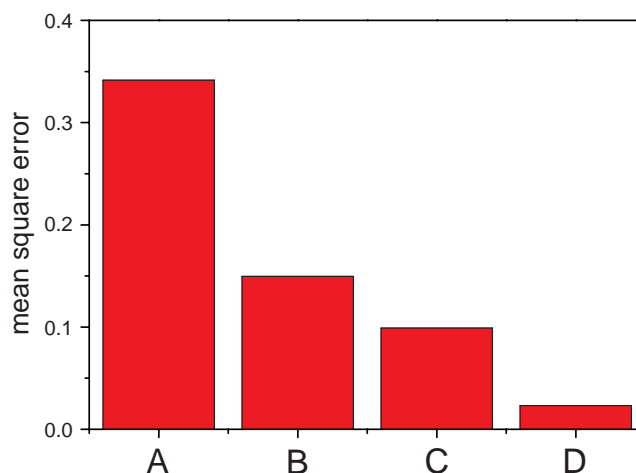


Figure 7.8: Mean square errors, obtained by averaging the squared deviation $(o - t)^2$ between the NN output o and the simulated SHG signal t over the training data set for the following input parametrizations: (A) the 128 spectral phases, (B) the sine and cosine of the spectral phases, (C) the real and imaginary parts of $E(\omega)$ and (D) the envelope of the electric field in the time domain, $E(t)$.

domain delivered by far the smallest errors for the training data set.

As mentioned above, another important factor for the evaluation of the input parametrization is the quality of the NN predictions for a test data set, i.e., the networks ability to generalize beyond the data presented during training. In our case this test data set consisted of the pulse shapes obtained during an evolutionary SHG maximization. Fig 7.9 illustrates that the failure of the phase and spectral representations as input parametrizations is even more dramatic than indicated by the training performance in figures 7.6 and 7.7. Obviously none of these representations delivered results that resembled even vaguely the simulation data. The input parametrization by the envelope of the electric field in the time domain however performed this task extremely well; the corresponding results will also be shown in section 7.3.4. This behaviour can be explained by the fact that the SHG signal depends on the temporal structure of the laser pulse (confer Eq. 7.4). Due to its convincing performance in the case of SHG simulation, the envelope of the electric field $E(t)$ was also adopted for the NN trained with the experimental data, which generates the two network outputs o_1 and o_2 , corresponding to the measured observables SHG–signal (t_1) and NK88–fluorescence (t_2), respectively.

While an appropriate choice for the input parametrization turned out to be of crucial importance for the NN performance, the optimization of the network architecture proved to have a less significant impact. For the determination of the ideal number of neurons and the connections between them, various methods can be applied; these can be as sophisticated as using genetic algorithms for finding the optimal architecture, or

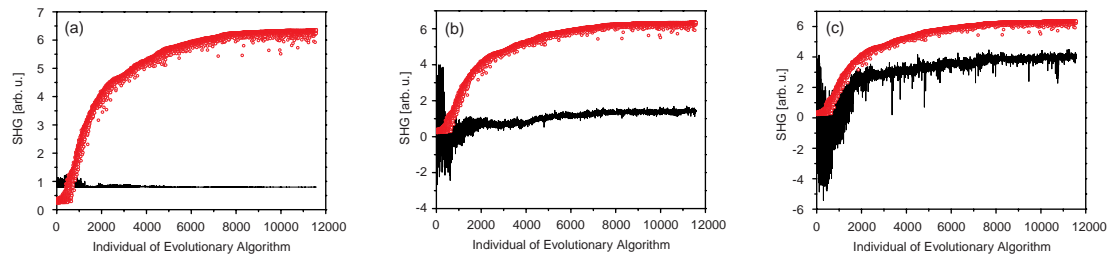


Figure 7.9: Generalization abilities for inputs parametrized with (a) spectral phases $\phi(\omega)$, (b) the sine and cosine of the spectral phases and (c) the real and imaginary parts of the spectral field $E(\omega)$. The network predictions are shown as black lines and the simulation results as red circles.

a simple trial-and-error for smaller networks, like the one used here. The optimization of the NN architecture was carried out for the $E(t)$ input parametrization by evaluating the training and generalization performance for various combinations of neurons connected to the inputs and in the hidden layer. As Fig 7.10 illustrates, an architecture with 16 neurons connected to the input layer and 16 neurons in the hidden layer yielded the best correspondence between NN prediction and exact results in both cases. This architecture was also adopted for the experimental data.

Finally, one or two neurons were connected to the outputs, depending on the number of observables the NN should be able to predict. While the connections between the inputs and the neurons of the first two layers are shared in the case of multiple outputs, the connections between the intermediate (hidden) layer and the output nodes are dedicated exclusively to either output, thus allowing the NN to simultaneously describe

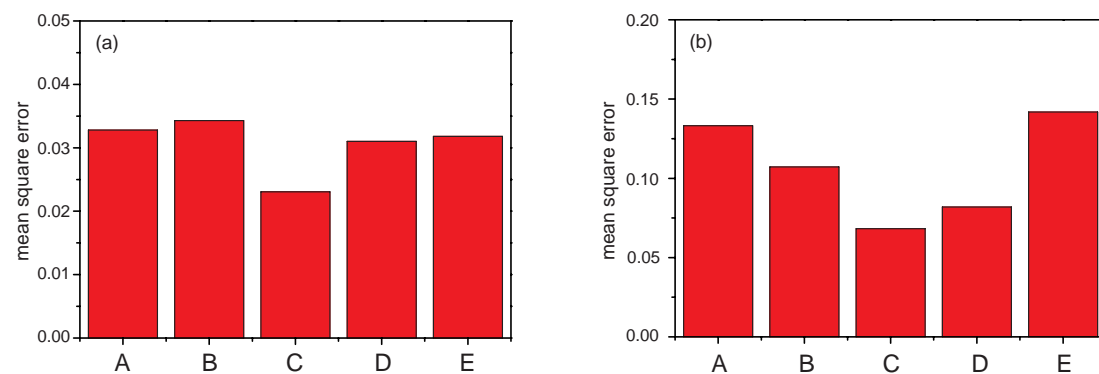


Figure 7.10: Mean square errors, obtained by averaging the squared deviation $(o - t)^2$ between the NN output o and the simulated SHG signal t over (a) the training data set and (b) for the data from the SHG maximization. The following combinations $[N_i|N_h]$ of neurons N_i of the input layer and neurons N_h in the hidden layer have been evaluated: (A) [8|8], (B) [8|16], (C) [16|16], (D) [16|24] and (E) [16|32]. In all cases, the input was parametrized by the envelope of the electric field in the time domain, $E(t)$.

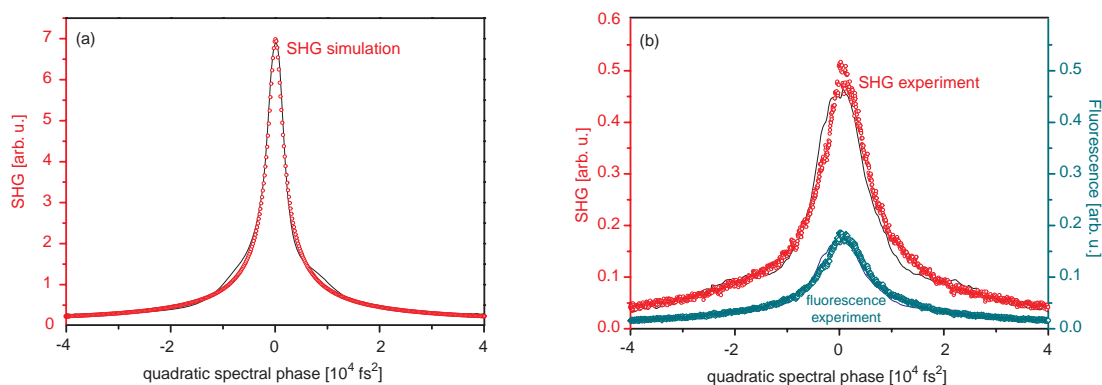


Figure 7.11: Capability of the NN to reproduce the data presented during training, illustrated for pulses with quadratic spectral phase. The solid lines correspond to NN predictions, the symbols to the actual results of (a) SHG simulation and (b) SHG experiment (red circles/upper curve), as well as molecular fluorescence from NK88 in methanol (blue diamonds/lower curve).

the mapping of the inputs onto multiple observables.

7.3.4 Results and discussion

The quality of functional maps generated by NNs depends on their ability both to reproduce the training data, and the ability to generalize beyond this training data. In the previous section the importance of finding an adequate input parametrization and optimal network architecture has been illustrated. In this section, the achievable training performance and generalization capabilities of NNs for SHG simulation and SHG/fluorescence experiments will be demonstrated. In both cases, the input was parametrized by the envelope of the electric field in the time domain, and the networks had 16 neurons in both the input and the hidden layer. Figures 7.11(a) and 7.11(b) show the ability of the NN to learn the mapping of the simulated or measured training data, respectively. For the variation of the quadratic spectral phase as an example, the simulated SHG signal calculated by Eq. 7.4 is shown in Fig. 7.11(a) (circles). In Fig. 7.11(b) the measured SHG and fluorescence yields are displayed by red circles (upper curve) and blue diamonds (lower curve), respectively. The NN predictions after training completion are indicated by solid lines. As can be seen, the exact values and the NN results match well for both simulated SHG and the measured SHG and fluorescence data. Qualitatively similar agreements were found for the other training pulses with cubic or sinusoidal spectral phases (results not shown). It can hence be concluded that the response of the studied systems to the training pulses can be successfully reproduced by the NN.

For applications of system mapping by NNs as described in the introduction, the ability of the NN to generalize, i.e., to inter- and extrapolate when confronted with

unfamiliar inputs, is crucial. As pointed out before, a successful completion of the training phase is necessary for this, but it is not sufficient. Therefore the NN has to be tested with data that was not part of the training data set. In order to generate a wide variety of different electric fields for this test, we performed evolutionary optimizations, both in simulation and experiment, as described in sections 7.3.1 and 7.3.2. In both cases the SHG yield was maximized. In the experiment, the fluorescence of NK88 was simultaneously recorded for each individual. The electric field of each individual from all generations of the evolutionary optimizations was then inserted into the trained NN as new input. The predicted output of the NN is compared to the actual values in Fig. 7.12(a) for simulated SHG and in Fig. 7.12(b) for experimentally measured SHG and fluorescence data. Again, the correct results (symbols) and the NN predictions (solid lines) match reasonably well over the complete parameter range of possible output signals. However, it is emphasized that here this correspondence does not simply mean that the NN has learned the behaviour of previously presented pulse shapes. Hence the NN is indeed able to approximate the input–output map associated with our problem, and it can extrapolate with rather good accuracy beyond the training data set. The electric fields tested in Fig. 7.12 are much more complex than those from the training set, and the NN has never encountered them before. An example of the electric fields generated by the evolutionary algorithm during the experiment can be seen in Fig. 7.13. In comparison with the rather simple pulse shapes resulting from analytic spectral phases used for the training process, examples of which are shown in Fig. 7.3, the electric fields from the optimization show much more structure and complexity, because the spectral phases at the LCD–pixels are first randomly selected and then independently modified during the optimization process.

While the presence of noise on the experimental data (both for training and testing

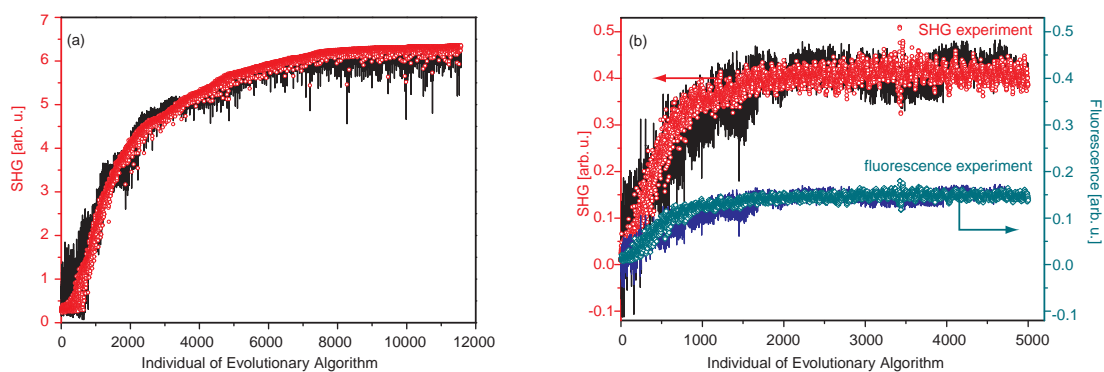


Figure 7.12: Ability of the NN to generalize beyond the data presented during training, illustrated for pulses obtained during an evolutionary optimization. The solid lines correspond to NN predictions, the symbols to the actual results of (a) SHG simulation and (b) SHG experiment (upper curve), as well as molecular fluorescence from NK88 in methanol (lower curve). Signal values are shown for all individuals of all generations of the optimization, hence they do not correspond to a monotonous function.

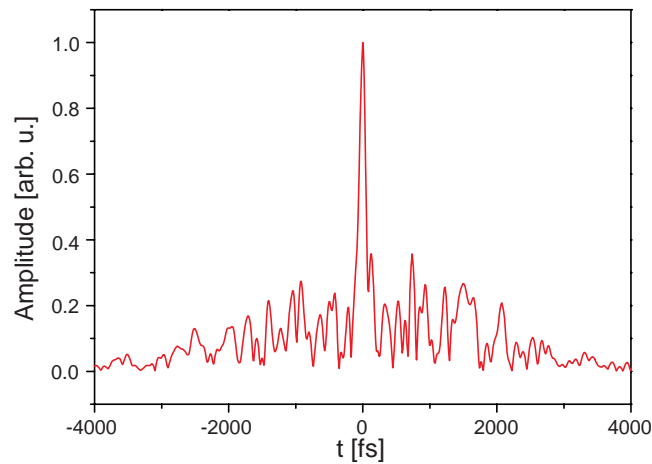


Figure 7.13: Sample electric field generated by the evolutionary algorithm during the experimental SHG maximization. The electric field of the individual number 300 is shown.

data) reduces the accuracy of the NN somewhat, it is still capable of yielding acceptable results, which is illustrated in Fig. 7.14, where the frequency distribution of the absolute error ($o_1 - t_1$) between o_1 , the SHG signal predicted by the NN, and t_1 , the experimentally measured SHG signal, is shown. This frequency distribution resembles a Gaussian distribution, centered around zero, with a standard deviation of 0.041, which corresponds to approximately 10% of the maximum SHG signal measured.

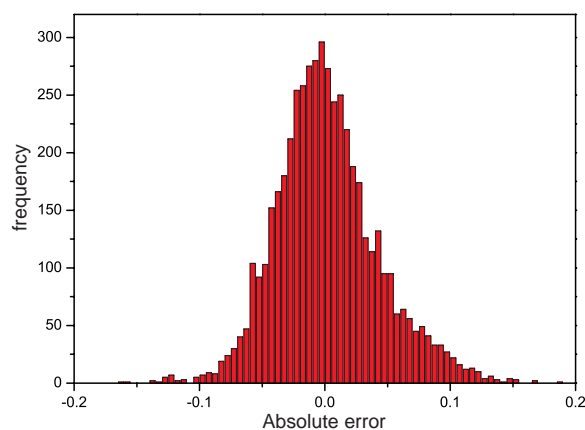


Figure 7.14: Frequency distribution of the absolute error ($o_1 - t_1$) between o_1 , the SHG signal predicted by the NN, and t_1 , the experimentally measured SHG signal.

It can be concluded that neural networks were used successfully for the automated generation of input–output maps for the processes of second–harmonic generation (SHG) and an example of molecular excitation. Apart from reproducing the training data, the employed network was also able to generalize beyond its teaching, as it was shown that the response of the investigated systems to arbitrarily shaped femtosecond laser pulses can be predicted.

7.4 Modeling of coherent strong-field dynamics with neural networks

The systems studied in the previous section, i.e., SHG and molecular excitation, were rather simple test cases. For investigating the applicability of neural networks for the generation of effective computer models for fully coherent light–matter interactions, the simulation of Autler–Townes doublets from strong-field ionization of potassium atoms is chosen as a model system that exhibits distinct quantum–mechanical effects. The ability of NNs to predict photoelectron spectra from strong-field ionization of potassium atoms is investigated in this section.

The potassium atom, irradiated by an intense femtosecond laser field, represents a fully coherent system, i.e., no decoherence mechanisms are operative on the interaction time scale, and thus the quantum–mechanical phase is well defined and preserved. As described in section 7.4.1, the process considered here is based on a REMPI–type (resonance–enhanced multiphoton ionization) excitation scheme. However, unlike conventional REMPI schemes, which usually are related to the weak–field regime, excitation by strong laser fields will effectively induce population depletion and Rabi–cycling within the resonant subsystem. REMPI excitation of coherent systems in strong laser fields provides an ideal test bed to evaluate the performance of NNs in approximating the response of coherent quantum–mechanical systems. In general, the dynamics of the potassium atom induced by shaped strong laser fields will depend critically on all details of the laser pulse such as the pulse energy, the pulse envelope, the instantaneous frequency and phase jumps. Strong–field ionization of potassium atoms by resonant, shaped laser fields has been studied recently [193]. It was pointed out that the control mechanism at play in the light–atom interaction is the selective population of dressed states (SPODS) [174, 175, 194, 195]. Besides the sensitivity to the pulse shape – as exemplified by variations of the absolute pulse intensity as well as the relative intensities of pulses within a sequence [195, 196] – SPODS critically depends on variations of the optical phase. The influence of changes in the instantaneous frequency has been demonstrated using chirped pulses [194] and was discussed in terms of rapid adiabatic passage (RAP) [197]. Likewise, discrete temporal phase jumps are capable of realizing SPODS with high efficiency as was demonstrated by the use of double pulses and multipulse sequences [195, 196]. In this case, the physical mechanism is based on photon locking (PL) [198, 199]. Together with the non–linearity

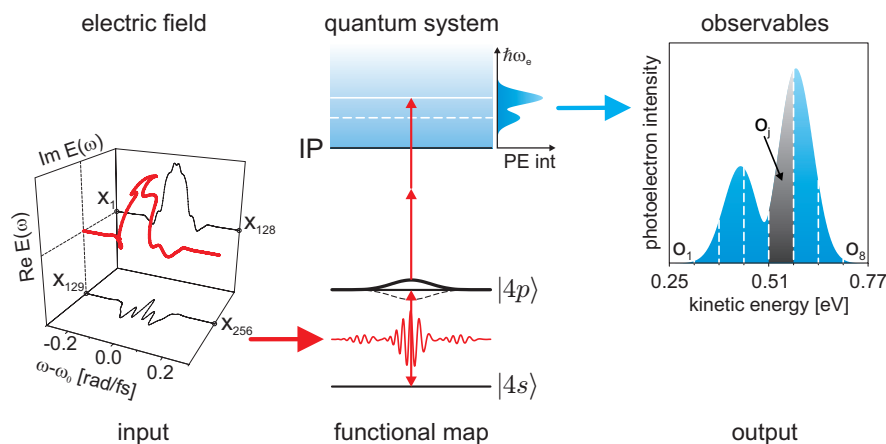


Figure 7.15: Schematic of the input–output map for the physical model system. The quantum system, i.e., the potassium atom (center), comprises the two–level system $|4s\rangle$ – $|4p\rangle$ (thin black lines) coupled to an ionic continuum. Interaction with an intense shaped femtosecond laser field displayed in the frequency domain (left) yields energy resolved photoelectron spectra (right). With regard to the NN, the laser electric field, suitably parameterized and taken at discrete sampling points x_i , serves as an input for the NN to model the quantum system. The resulting photoelectron spectrum, sampled at a finite number of energy intervals o_j , represents an output, with the laser–atom interaction providing a functional input–output map.

of the photoelectron signal due to the multi–photon ionization step, the prediction of photoelectron spectra for a given input electric field is a complex and challenging task for a NN.

The pulse–shaping experiment shown schematically in Fig. 7.1 is concretized for the investigated quantum system, the potassium atom, in Fig. 7.15. Again, it can be interpreted as the electric field of the shaped laser pulse serving as an input to the quantum system, and the resulting photoelectron spectrum can then be regarded as the output, with the atom–laser interaction providing a functional input–output map. The goal here is to approximate this input–output map, and hence the atom’s response to electric fields, by employing a neural network. Various trial pulses and the corresponding photoelectron spectra obtained from a simulation of the REMPI process in the potassium atom will be used to train the NN, which will then be employed to generalize beyond the training data set by predicting control landscapes. If only a few parameters are varied to change the electric field, illustrative control landscapes (see chapter 6 and Refs. [160–162]) can be recorded by systematically scanning them. Experimentally, these landscapes, in which a control objective derived from observables is plotted as a function of selected parameters [165, 166, 174, 200, 201], directly reflect the system’s response to the different pulse shapes and give an indication about possible control mechanisms.

7.4.1 Simulation of the physical system

The physical system that the network is to approximate consists of the two potassium bound states $|4s\rangle$ and $|4p\rangle$, strongly driven by a resonant shaped femtosecond laser pulse and weakly coupled to a continuum of ionic states, as depicted in Fig. 7.15 (center). Resonant one-photon excitation and absorption of two further photons from the same laser field constitute a $1 + 2$ photon REMPI process. As was shown recently [193], photoelectrons produced during the strong-field excitation of the atom directly map the non-perturbative dynamics of the neutral system. Thus, information on both the population and the quantum-mechanical phase of the bound states can be extracted from the photoelectron spectrum [196]. An intuitive physical picture of this scenario was devised in terms of SPODS, i.e., the selective population of dressed states. A description in the framework of dressed states is especially suited for this process, since ionization occurs simultaneously to excitation, and the dressed states, i.e., the eigenstates of the two-level system and the light field, are probed, rather than the bare atomic states. The splitting of the dressed-state eigenenergies (thick and dotted black lines in Fig. 7.15 (center)), which is proportional to the laser field strength, is mapped into the photoelectron spectrum, which gives rise to the well-known Autler-Townes (AT) doublet [202].

Making use of the fact that the coupling among the two bound states is much stronger than the coupling of either bound state to the continuum, the numerical calculation of the photoionization process is divided into two steps. At first, the strong-field interaction of the shaped laser pulse with the neutral system is treated by solving the time-dependent Schrödinger equation (TDSE) [203]

$$i\hbar \frac{d}{dt} \begin{pmatrix} c_{4s} \\ c_{4p} \end{pmatrix} = -\frac{\hbar}{2} \begin{pmatrix} 0 & \Omega(t) \\ \Omega^*(t) & 0 \end{pmatrix} \begin{pmatrix} c_{4s} \\ c_{4p} \end{pmatrix} \quad (7.5)$$

in the interaction picture, applying the rotating-wave approximation (RWA) and using the short-time propagator method. Herein, c_{4s} and c_{4p} are the time-dependent probability amplitudes of the corresponding quantum states and $\Omega(t)$ denotes the complex Rabi frequency. Introducing the $4s \rightarrow 4p$ transition dipole moment (along the laser polarization) μ , the Rabi frequency is related to the laser electric field $E(t)$ by $\hbar\Omega(t) = \mu E(t)$.

In the second step, the two-photon ionization starting from the $4p$ state is evaluated in the framework of second-order perturbation theory. The final photoelectron amplitude then reads [15, 16, 204]

$$c(\omega_e) \propto \int_{-\infty}^{\infty} c_{4p}(t) E^2(t) e^{i(\omega_e + \omega_{IP} - \omega_{4p})t} dt, \quad (7.6)$$

with $\hbar\omega_e$ being the kinetic excess energy of the emitted electron, $\hbar\omega_{IP}$ the potassium ionization potential and $\hbar\omega_{4p}$ the eigenenergy of the $4p$ state.

Pulse shaping is carried out in frequency domain, as summarized in [205]. To this end a bandwidth–limited 30 fs full width at half maximum (FWHM) Gaussian laser pulse with amplitude $A(\omega)$ is spectrally phase modulated, allowing for second– and third–order polynomial phase functions $\varphi(\omega) = \phi^{(n)}/n! (\omega - \omega_0)^n$, sinusoidal phase functions $\varphi(\omega) = A \sin[(\omega - \omega_0) \tau + \phi_0]$ as well as linear combinations of the form:

$$\varphi(\omega) = A \sin[(\omega - \omega_0) \tau + \phi_0] + \frac{\phi^{(2)}}{2} (\omega - \omega_0)^2. \quad (7.7)$$

The laser central frequency ω_0 coincides with the $4s \rightarrow 4p$ transition frequency. From the modulation function $\varphi(\omega)$ the modulated spectral electric field is calculated as

$$E(\omega) = A(\omega)e^{-i\varphi(\omega)}, \quad (7.8)$$

and the temporal electric field is obtained via inverse Fourier transformation $E(t) = \mathcal{F}^{-1}[E(\omega)]$. The pulse energy was chosen such that the dressed states exhibit a maximum energy splitting of 210 meV in accordance with the experimental observations in Ref. [175].

7.4.2 Input parametrization and network architecture

The modeling of light–matter interactions for SHG and molecular fluorescence (section 7.3) has shown that an appropriate input parametrization is of crucial importance for a successful application of neural networks. Moreover, it became apparent that an input parametrization that reflects the physically relevant information (e.g., the envelope of the electric field in the time domain in the case of SHG) delivers the best results. As the process we want to approximate with a NN here depends strongly on both the intensity and the phase of the electric field, it is sensible to use representations of the electric field, either in the frequency domain (see Eq. 7.8) or in the time domain, as inputs to the network.

The spectral phases are applied in the simulation of the potassium atom at 128 discrete frequencies, and hence the spectral electric field is evaluated at 128 points. Both spectral and temporal electric field representations are used as input parametrizations, with the real and imaginary parts of the electric field as inputs to the NN, in total 256 variables (see Figs. 7.15(left) and 7.16 (left)). Concerning the network architecture, the following structure yielded good results: the first layer of neurons processes the real ($x_1 \dots x_{128}$) and imaginary ($x_{129} \dots x_{256}$) parts separately, each with eight neurons. The outputs of this first layer of neurons is then transferred to the hidden layer, consisting of 24 neurons. These are connected to the eight neurons of the output layer that deliver the photoelectron spectrum for eight photoelectron energy intervals (o_1 to o_8 , confer Fig. 7.15) of equal width between 0.25 and 0.77 eV. The activation function and the modification of the weights during training are stated in section 7.2.

Examples of the different input parameterizations are shown in Fig. 7.17. In Fig. 7.17(a) the spectral intensity (grey shaded) and phase (black line) are shown for

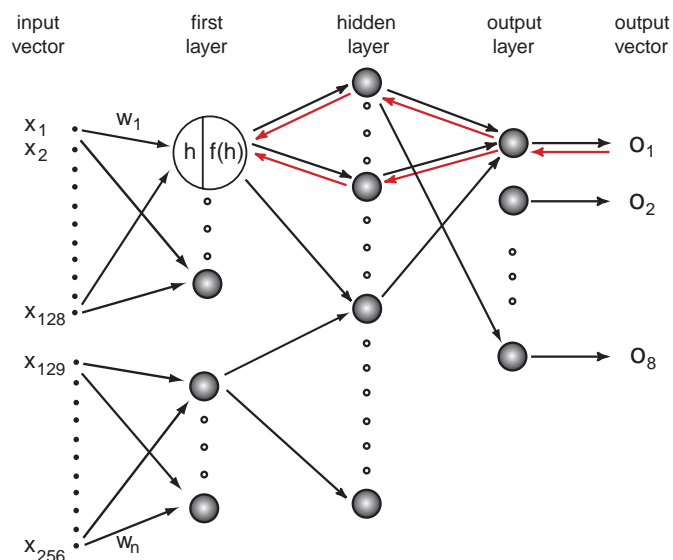


Figure 7.16: Schematic representation of the employed NN architecture and working principle. Neurons are depicted as spheres, and the flow of information and error correction is indicated by right-pointing and left-pointing arrows, respectively.

the spectral phase $\varphi(\omega) = 0.3 \text{ rad} \sin[(\omega - \omega_0)140 \text{ fs} - \pi/2] + \frac{1}{2} \cdot 400 \text{ fs}^2(\omega - \omega_0)^2$. The real and imaginary parts of the resulting electric field are shown in the frequency (Fig. 7.17(b)) and in the time (Fig. 7.17(c)) domain. How well these parametrizations are suited to the modeling task at hand will be examined in the next section.

7.4.3 Results and discussion

In order to provide a comprehensive set of data for training and testing the NN, photoelectron spectra for different classes of shaped laser pulses were generated, using the phase functions and the numeric model described in section 7.4.1. The polynomial phase parameters $\phi^{(n)}$ were varied within the following limits: from -2000 to $+2000 \text{ fs}^2$ for quadratic phases, and from -15000 to $+15000 \text{ fs}^3$ for cubic phases. For the sinusoidal phases the frequency τ was fixed to 140 fs and amplitudes A of $0.1, 0.2, \dots, 0.5 \text{ [rad]}$ were used; the phase ϕ_0 , which is the sine parameter the studied process is most sensitive to, was varied from 0 to 2π . In total, circa 5000 pulses and the corresponding photoelectron spectra were employed for the training procedure: 1000 for second and third order modulation each, and 630 for each value of the sine amplitude.

Simulated pulse shapes with either purely polynomial or sinusoidal phases and the resulting photoelectron spectra were used for the training of the NN. The ability of the NN to learn the mapping of the shaped electric field onto the photoelectron spectrum from the training data set is shown in Fig. 7.18 for two representative classes of pulse shapes. The contour plots in the upper row show the photoelectron spectra

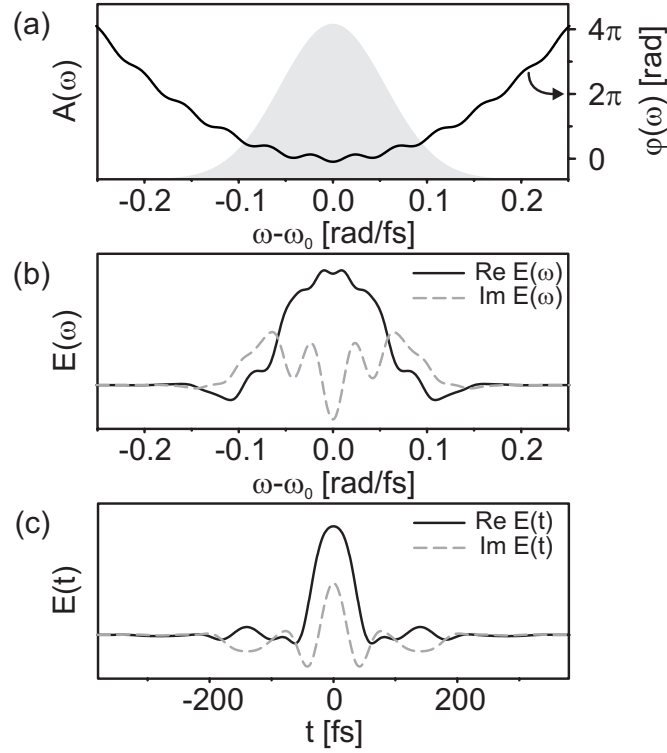


Figure 7.17: (a) The spectral amplitude $A(\omega)$ (shaded background) and spectral modulation function $\phi(\omega)$ are shown for the modulation parameters $A = 0.3$ rad, $\tau = 140$ fs, $\phi_0 = -\pi/2$ and $\phi^{(2)} = 400$ fs² in Eq. 7.7. Different input parameterizations used for the electric field are shown in (b) for the decomposition of the spectral electric field $E(\omega)$ into its real and imaginary part and in (c) for the decomposition of the temporal electric field $E(t)$ into its real and imaginary part.

resulting from the numeric model of section 7.4.1 for second–order spectral phases (left) and sinusoidal phases (right). The second row shows the corresponding photoelectron spectra generated by a NN with the spectral electric field $E(\omega)$ as input after the training is completed. In both cases, the agreement between the NN results and the exact results from the simulation is satisfactory, both qualitatively and quantitatively (compare Figs. 7.18(a) and (b) as well as Figs. 7.18(d) and (e)). The last row shows the photoelectron spectra generated by a NN with the temporal electric field $E(t)$ as input. Compared to the spectral input parametrization, the results are poor. While the photoelectron spectra for phases of second order (Fig. 7.18(c)) resemble qualitatively the expected results (Fig. 7.18(a)), the spectra for sinusoidal phases (Fig. 7.18(f)) show little variation depending on the phase parameter ϕ_0 . Apparently, for this input parametrization, the minimization of the training error led to a network which always delivers the average spectrum. Due to these findings, the network with $E(\omega)$ as input was used for predicting the control landscapes in the remainder of this work, as it is able to reproduce the training data accurately.

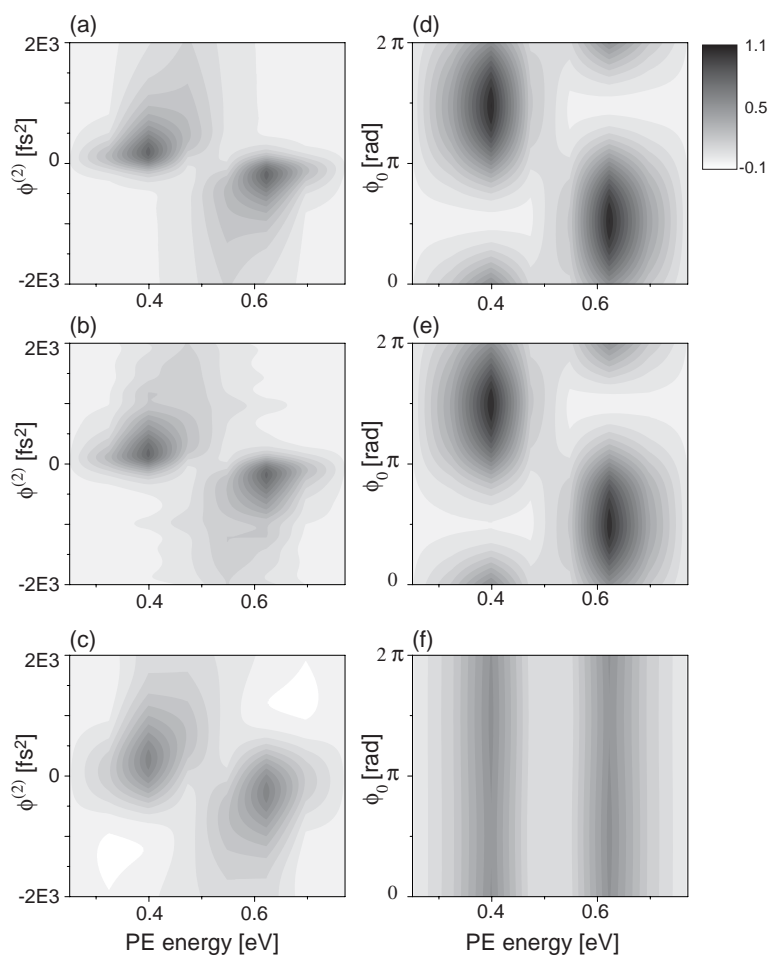


Figure 7.18: Contour plots of the photoelectron spectra for second-order spectral phases $\varphi(\omega) = \phi^{(2)}/2 (\omega - \omega_0)^2$ (left column) and sinusoidal phases $\varphi(\omega) = 0.2 \text{ rad} \sin[(\omega - \omega_0)140 \text{ fs} + \phi_0]$ (right column). The top row shows the simulation. In the second row, results from the NN with $E(\omega)$ used as input are displayed. Results obtained from the NN when $E(t)$ is used as input are shown in the bottom row.

Ideally, one would hope that a network trained with purely polynomial and sinusoidal phases could be able to predict the outcome resulting from a linear combination of second-order and sinusoidal phases. However, this expectation turns out to be rather naive, given the complexity of the coherent strong-field dynamics involved. As was pointed out before, the physical process considered here is sensitive to virtually all details of the laser pulse such as the pulse energy, the pulse envelope, the instantaneous frequency and phase. Therefore – also taking into account the nonlinearity of the photoionization – a simple interdependence of the parameters is not to be expected. The mutual interdependence of chirps and phase jumps is illustrated in Fig. 7.19, where exemplary photoelectron spectra from (a) a purely sinusoidal modulation, (b) a purely quadratic modulation and (c) a linear combination of both types of modulation are

compared. While both the sinusoidal and the quadratic modulations alone lead to the exclusive production of slow photoelectrons, i.e., the low energetic AT component, this picture is completely inverted in case of the combined modulation. Now the production of fast electrons is favored and only the high energetic AT component shows up in the spectrum. This reflects the fact that in general the shape of the AT doublet resulting from a combined phase modulation cannot be decomposed into contributions of each elementary modulation, but arises from a complex interplay of the modulation parameters, exemplifying the quantum mechanical nature of the underlying effects. Taking into account this complexity of the strong–field induced dynamics it is not surprising that additional information is needed for the NN to accurately predict two–dimensional control landscapes. Shaped pulses resulting from a linear combination of second–order and sinusoidal phases were used to generate such control landscapes. The contour plots of these control landscapes show the total photoelectron count belonging to the high energetic component of the Autler–Townes doublet (from 0.51 to 0.77 eV in Fig. 7.19) as a function of the second–order phase (from -1000 to $+1000$ fs²) and the varied sinusoidal phase parameter, here ϕ_0 (from 0 to 2π), for varying sine amplitude A and τ again fixed at 140 fs.

It turned out that after inclusion of a few control landscapes into the training data set (namely those with sine–parameters $A = 0.2$ and $A = 0.4$, shown in Fig. 7.20(a) and (b)), the network was quite capable of interpolating and extrapolating to the control landscapes which were not included in the training data. In Fig. 7.20(c) to (h) the control landscapes are depicted for sine–parameters $A = 0.1$, $A = 0.3$ and $A = 0.5$,

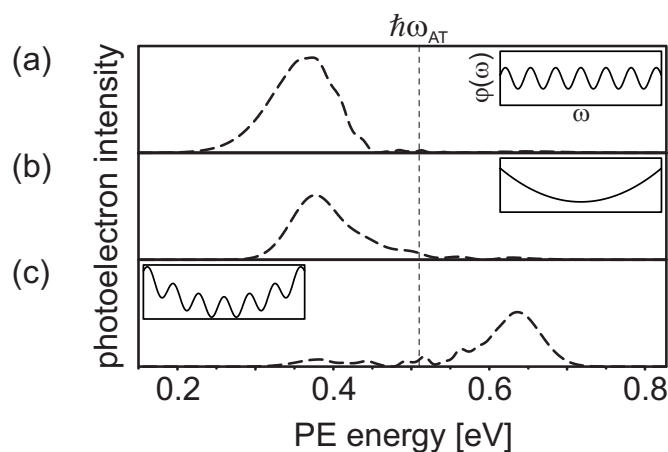


Figure 7.19: Selected photoelectron spectra corresponding to (a) sinusoidal phase modulation with parameters $A = 0.4$ rad, $\tau = 140$ fs and $\phi_0 = 1.02$ rad, (b) quadratic phase modulation with $\phi^{(2)} = 500$ fs² and (c) a linear combination of these two (see Eq. 7.7). The phase modulation functions $\varphi(\omega)$ are shown schematically in the insets and the energy $\hbar\omega_{AT}$ marks the center of the AT doublet, separating slow from fast photoelectrons.

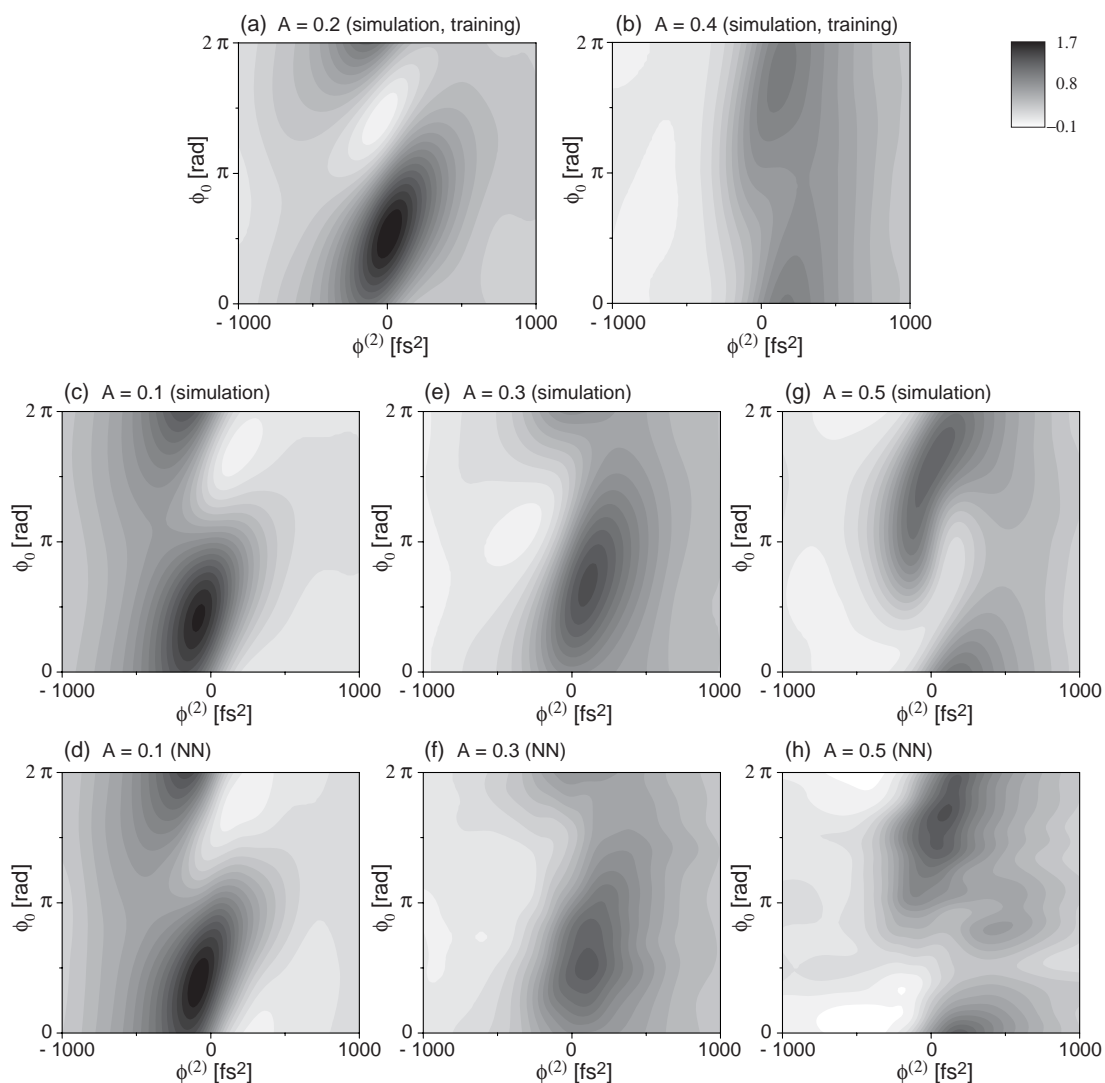


Figure 7.20: Control landscapes – the intensity of fast photoelectrons (confer Fig. 7.19) is shown as a function of the second order phase $\phi^{(2)}$ (from -1000 to $+1000$ fs²) and the varied sinusoidal phase parameter, here ϕ_0 (from 0 to 2π), with τ fixed at 140 fs. In the top row, the exact results of the numeric model that were used for the training process are shown for (a) $A = 0.2$ and (b) $A = 0.4$. The NN is then employed for interpolating the control landscapes for different values of A . The simulated landscapes are shown in the second row, the corresponding NN predictions in the bottom row for ((c) and (d)) $A = 0.1$, ((e) and (f)) $A = 0.3$ and ((g) and (h)) $A = 0.5$.

which show again the intensity of fast photoelectrons in dependence on the applied second-order phase coefficient $\phi^{(2)}$ and the sinusoidal phase parameter ϕ_0 . The exact control landscapes from the numeric model are shown in the second row, the corresponding control landscapes approximated by the network in the bottom row. Again, the agreement between the exact results and the network approximation is convincing

both qualitatively and quantitatively. Apparently, the coherent dynamics induced by shaped electromagnetic fields that were not included in the training data set can be predicted by the network, provided that the phase modulations of these new fields resemble at least to some extent the phase modulations encountered during the training process. It should be noted that the NN interpolation and extrapolation for pulses that were previously ‘unknown’ to the NN (Figs. 7.20(c) to (h)) works even if the landscapes differ significantly from those used during the training process (Figs. 7.20(a) and (b)).

7.5 Conclusion

The application of neural networks (NNs) for the automated generation of input–output maps of light–driven physical processes was demonstrated for the first time with great success for comparatively simple systems, namely second–harmonic generation (SHG) and molecular fluorescence yield (section 7.3). The employed network did not only learn from the corresponding training data, but it was also able to generalize beyond its teaching, as it was shown that the response of the investigated systems to arbitrarily shaped femtosecond laser pulses can indeed be predicted. As demonstrated with experimental data, different responses (SHG and fluorescence of the molecule NK88 in the case studied) to the same electric field can be described with a single input–output map generated by a neural network.

A neural network (NN) was also successfully employed for predicting photoelectron spectra from resonant strong–field ionization of potassium atoms (section 7.4). Compared to the rather simple test cases of SHG and molecular fluorescence, this model system is far more complex, as the outcome of the light–driven process depends critically on all details of the laser field. It turned out that the amount of data required for the training strongly increases with the complexity of the correlations which are to be modeled. Under such conditions, extrapolation to regions of the parameter space which were not covered at all by the training data is still a challenge. However, reproduction of the training data worked excellent, provided that an appropriate parametrization of the input fields was used. Moreover, when taking two–dimensional data the coherent strong–field dynamics could be predicted by the NN for laser pulse shapes not included in the training data set.

These successful demonstrations do not entail that mechanistic insights into the modeled processes are provided, as a direct understanding of the modeled function or process cannot be obtained by analyzing the NN weights. However, this was not the objective of this approach. We rather exploited the strength of NNs, namely their ability to generate quite accurate input–output maps in an automated fashion from a large data set. The described procedure can indeed provide an effective computer model of the real–world system that is then available for further investigations and applications. On more operational terms, the procedure demonstrated here can provide numerical

models for quantum systems in an automated fashion. This may be especially interesting for those cases where correct *ab initio* calculations are too difficult to accomplish, such as for large or interacting systems. In these cases, an effective input–output map that implicitly contains the exact experimental conditions may prove to be very helpful.

As a next step, it would be interesting to study the applicability of NNs to the field of non-linear spectroscopy, in order to see if a NN can model the response function from one spectroscopy technique (e.g., transient grating or photon echo), and if this response function could in turn be used to predict the outcome of different spectroscopy experiments based on a nonlinearity of the same order.

Chapter 8

Summary

With the advent of femtosecond laser pulses, it became possible to observe and investigate molecular dynamics directly. The development of pulse shapers that allow the ultrafast manipulation of these pulses opened up new perspectives for these new light sources. The ability to tailor electric fields on the natural timescale of molecular dynamics proved especially useful for achieving selective control over photophysical or photochemical processes. While most quantum systems are too complex to allow an accurate calculation of the electric fields required for achieving specific control objectives, numerous processes have been successfully controlled experimentally. Essential for this success was the concept of closed-loop adaptive quantum control introduced by Judson and Rabitz. Based on experimental feedback, which is used to evaluate the suitability of differently shaped laser pulses for achieving the desired outcome, the electric field of the applied laser pulses is iteratively improved by a learning algorithm. Without requiring detailed *a priori* knowledge, the search for the optimal pulse shape is guided by the quantum system itself with this method.

In this work, a variety of novel applications and techniques for the shaping of femtosecond laser pulses have been presented, both within and outside the context of adaptive quantum control.

Until recently, experiments for achieving selective control over quantum systems have been carried out only with linearly polarized light. This restriction means that only the scalar properties of the light-matter interaction were addressed, while the vectorial character of both the dipole moment $\mu(t)$ and the electric field $\mathbf{E}(t)$ that govern this interaction was neglected. The sensitivity of molecular dynamics to the polarization state of the light fields that drive these dynamics has been demonstrated here for a model quantum system, the potassium dimer K_2 . Pump-probe experiments with varying polarizations of the pump and probe pulses have shown that the molecular dynamics as well as the population of intermediate states depend strongly on the employed polarizations of the pump and probe pulses. Comparative optimizations of the multiphoton ionization of K_2 with either phase-only or polarization-and-phase

shaped laser pulses verified the superiority of polarization–and–phase pulse shaping, which allows the adaptation of the electric field to the spatio–temporal evolution of the transition dipole moments. Hence, the ability to manipulate the time–dependent polarization state of light gives access to a qualitatively new level of control over quantum systems.

The technique of ultrafast polarization pulse shaping was then extended to the ultraviolet. By employing a pair of nonlinear crystals with mutually perpendicular optical axes, polarization–shaped near–infrared pulses can be converted to the UV. For an accurate characterization of these pulses, dual–channel spectral interferometry was combined with FROG and XFROG techniques. It was shown that mixing effects between the two shaped polarization components can be minimized with an improved polarization pulse shaper setup that features volume phase holographic (VPH) gratings, in conjunction with a Berek compensator. Polarization–shaped pulses in the ultraviolet spectral region are of special interest in the context of stereo chemistry, e.g., as a novel tool for the control of ring–opening and isomerization reactions, or for enantiomer–selective excitation, transformation or production of chiral molecules. Further areas of application for ultrafast polarization shaping include the optical control of lattice vibrations, the generation and characterization of attosecond light pulses and the manipulation of forces on the nanometer scale. Thus, this new technique opens the door to a large variety of new experiments which either require or benefit greatly from the possibility to modify the polarization state of UV laser pulses on an ultrafast timescale.

While the closed–loop adaptive optimization of electric fields with learning algorithms has proven to be a powerful tool for reaching specific control objectives, it is often very difficult to extract information on the control mechanism or reaction pathways utilized by the optimal pulse shape. Systematic scans of different electric field parametrizations in open–loop experiments can be a valuable tool for the identification of important control mechanisms and for the interpretation of adaptively obtained optimal pulse shapes. In this context, sequences of differently colored double pulses were introduced in this thesis. By scanning the central wavelengths, the relative amplitudes or phases, or the temporal separation of the two pulses, illustrative fitness landscapes can be recorded, where the reaction outcome is visualized as a function of two pulse parameters. These landscapes can help to extract or confirm control mechanisms, which was first demonstrated for a purely optical experiment. For this purpose, a setup for the generation of the third harmonic of a Ti:sapphire laser system was designed, where certain double pulses will give the highest signal yield. Adaptive optimization experiments with the goal of maximizing the third harmonic yield were performed, and the optimal pulse shape was indeed found to lie in the vicinity of the maximum of the recorded fitness landscape. In a second experiment, the excitation efficiency of the dye molecule IR140 in solution was studied with transient absorption spectroscopy. It could be shown that very different pulse shapes, namely linearly chirped pulses and colored double pulses can utilize the same control mechanism, in this case a pump–dump scheme. More generally, a combination of several adequately chosen electric

field parameterizations can serve as a means to identify the control mechanisms involved in an optimal pulse found in a closed-loop optimization. With the assistance of parameter scans like the colored double pulses presented here, a better understanding of molecular systems and their controllability is a realistic objective.

Apart from the adaptive control of physical or chemical processes, the ability to shape femtosecond laser pulses can be used for a variety of purposes. For example, the response of quantum systems to a large number of different electric fields can be probed with shaped pulses. This information can in turn be used to obtain models for the interaction of light and matter. In this thesis, neural networks were introduced as a means for the automated generation of input-output maps capable of describing this interaction. This procedure worked especially well for comparatively simple systems, namely second harmonic generation (SHG) and molecular fluorescence. A neural network was also successfully employed for predicting photoelectron spectra from resonant strong-field ionization of potassium atoms. Compared to SHG and molecular fluorescence, this model system is far more complex, as the outcome of the light-driven process depends critically on all details of the laser field. While the amount of data required for modeling light-matter interactions with this method increases with the complexity of the correlations which are to be modeled, this procedure is nevertheless a promising approach, especially for large and/or interacting systems, where *ab initio* calculations are not feasible.

It can be concluded that this work has contributed to two major aspects in quantum control: the selective control of stereochemical reactions and the goal to obtain information about quantum systems and their interaction with light. The successful demonstration of adaptive polarization quantum control in a molecular system, and especially the novel technique for the generation of polarization-shaped pulses in the UV, are important steps towards the coherent control of chirality. While the systematic parameter scans and experimentally determined fitness landscapes presented here can help to shed light on reaction pathways and control mechanisms in adaptive control experiments, neural networks, as demonstrated for the first time within this thesis, can be employed for the generation of numerical models for light-matter interactions.

*While there is light, there is life.
While there is life, there is hope.*

Chapter 9

Zusammenfassung

Mit Hilfe von Femtosekunden-Lasersystemen ist es möglich, die Dynamik in Molekülen direkt zu beobachten und zu untersuchen. Die Entwicklung von Laserpulsformern, welche eine ultraschnelle Manipulation dieser Laserpulse gestatten, eröffnete weitere Perspektiven für diese neuartigen Lichtquellen. Die Fähigkeit, elektrische Felder auf der natürlichen Zeitskala molekularer Dynamik beeinflussen zu können, erwies sich insbesondere im Hinblick auf die selektive Kontrolle von photophysikalischen oder photochemischen Prozessen als äußerst nützlich. Obwohl die meisten Quantensysteme zu komplex sind, um die zum Erreichen bestimmter Kontrollziele notwendigen elektrischen Felder genau genug berechnen zu können, konnten zahlreiche Prozesse experimentell mit speziell geformten Femtosekunden-Laserpulsen erfolgreich kontrolliert werden. Entscheidend für diesen Erfolg war das Konzept der adaptiven Quantenkontrolle, das von Judson und Rabitz vorgeschlagen wurde. Hierbei werden experimentelle Rückkopplungssignale verwendet, um die Tauglichkeit verschieden geformter Laserpulse im Hinblick auf das gewünschte Reaktionsziel zu ermitteln. Ein lernfähiger Algorithmus nutzt diese Information, um das elektrische Feld iterativ zu verbessern, bis das gewünschte Ziel erreicht ist. Der Vorteil dieser Methode besteht darin, dass zur erfolgreichen Kontrolle keine detaillierten Vorkenntnisse über das untersuchte System benötigt werden, da die Suche nach der optimalen Pulsform vom Quantensystem selbst gesteuert wird.

In dieser Arbeit wurde eine Vielzahl neuartiger Anwendungen und Methoden der Femtosekunden-Pulsformung präsentiert, sowohl im Hinblick auf die adaptive Quantenkontrolle, als auch darüber hinaus.

Bis vor Kurzem wurden Experimente zur selektiven Kontrolle von Quantensystemen ausschließlich mit linear polarisiertem Licht durchgeführt. Diese Einschränkung bedeutet, dass im Experiment nur die skalaren Eigenschaften der Licht-Materie Wechselwirkung angesprochen und ausgenutzt wurden, während die vektoriellen Eigenschaften der für diese Wechselwirkung maßgeblichen Größen, des Dipolmomentes $\mu(t)$ und des elektrischen Feldes $\mathbf{E}(t)$, vernachlässigt wurden. Die

Abhängigkeit molekularer Dynamik vom Polarisationszustand des Lichtes, welches diese Dynamik antreibt, wurde hier für ein Modell-Quantensystem, das Kaliumdimer K_2 untersucht. Anrege-Abfrage Experimente mit unterschiedlichen Polarisierungen der Anrege- und Abfragepulse haben gezeigt, dass sowohl die molekulare Dynamik, als auch die Besetzung von Zwischenzuständen, stark von den verwendeten Polarisationszuständen abhängen. Um reine Phasenformung mit der gleichzeitigen Formung von Phase und Polarisation vergleichen zu können, wurden beide Optimierungen parallel durchgeführt, jeweils mit dem Ziel die Multiphotonen-Ionisation des K_2 Moleküls zu maximieren. Die Ergebnisse zeigen deutlich die Überlegenheit der gleichzeitigen Formung von Phase und Polarisation, welche die Anpassung des elektrischen Feldes an die räumliche und zeitliche Entwicklung der Dipolmomente ermöglicht. Somit konnte gezeigt werden, dass die Möglichkeit, den Polarisationszustand im Verlauf eines Laserpulses zu verändern, nicht nur eine quantitative Verbesserung, sondern eine qualitativ neue Art der Kontrolle über Quantensysteme darstellt.

Die verwendete Technik zur ultraschnellen Polarisationsformung konnte darüber hinaus auf den ultravioletten (UV) Spektralbereich erweitert werden. Mit Hilfe zweier nichtlinearer Kristalle, deren optische Achsen senkrecht aufeinander stehen, war es möglich, die polarisationsgeformten Nahinfrarot-Pulse ins UV zu konvertieren. Die präzise Charakterisierung dieser Pulse gelang mit einer Kombination von spektraler Interferometrie mit FROG- und XFROG-Techniken. Desweiteren konnte gezeigt werden, dass die Mischungseffekte zwischen den beiden geformten Polarisationskomponenten mit Hilfe eines neuen Pulsformeraufbaus minimiert werden können, unter Verwendung von holographischen Phasengittern sowie eines Berek-Kompensators. Polarisationsgeformte Laserpulse im ultravioletten Spektralbereich sind insbesondere für stereochemische Anwendungen von Interesse, beispielsweise als neuartiges Werkzeug zur Kontrolle von Ringöffnungs- oder Isomerisierungsreaktionen, oder zur Enantiomer-spezifischen Anregung, Umwandlung oder Produktion von chiralen Molekülen. Weitere Anwendungsgebiete umfassen die Kontrolle von Gitterschwingungen, die Erzeugung und Charakterisierung von Attosekunden-Laserpulsen, sowie die Kontrolle von Kräften im Nanometer-Bereich. Diese neuartige Technik ermöglicht somit den Zugang zu einer Fülle neuartiger Anwendungen, welche entweder auf polarisationsgeformte UV Laserpulse angewiesen sind, oder stark von deren Verwendung profitieren.

Ogleich sich die adaptive Optimierung elektrischer Felder mit lernfähigen Algorithmen als außerordentlich erfolgreich zum Erreichen spezieller Kontrollziele erwiesen hat, ist es meist sehr schwierig, Informationen über den Kontrollmechanismus oder den Reaktionsweg aus der optimalen Pulsform zu extrahieren. Die systematische Abtastung verschiedener Parametrisierungen des elektrischen Feldes kann wertvolle Beiträge zur Identifizierung wichtiger Kontrollmechanismen und zur Interpretation von adaptiv ermittelten optimalen Pulsformen liefern. In diesem Zusammenhang wurden in dieser Arbeit Sequenzen von farbigen Doppelpulsen vorgestellt. Durch Variation der Zentralwellenlängen, der relativen Amplituden und Phasen, sowie

des zeitlichen Pulsabstands können aussagekräftige Fitnesslandschaften aufgenommen werden, in welchen die Reaktionsausbeute als Funktion von zwei variierten Parametern dargestellt wird. Diese Fitnesslandschaften können dabei helfen, wichtige Kontrollmechanismen zu bestätigen oder erstmals zu erkennen. Dies wurde zunächst in einem rein optischen Demonstrationsexperiment gezeigt. Zu diesem Zweck wurde ein Aufbau zur Erzeugung der dritten Harmonischen des Titan–Saphir Lasersystems so konzipiert, dass bestimmte Doppelpulse die höchste Signalausbeute liefern. Es wurden adaptive Kontrollexperimente durchgeführt, mit dem Ziel, das Signal der dritten Harmonischen zu maximieren. Dabei konnte gezeigt werden, dass die adaptiv ermittelte optimale Pulsform in der Tat in der Nähe des Maximums der ebenfalls aufgezeichneten Fitnesslandschaft liegt. In einem zweiten Experiment wurde die Anregungseffizienz des Farbstoffmoleküls IR140 in Lösung mit transientser Absorptionsspektroskopie untersucht. Es stellte sich heraus, dass sehr unterschiedliche Pulsformen, nämlich linear geschirpte Pulse und farbige Doppelpulse, sich des gleichen Kontrollmechanismus bedienen können. In beiden Fällen konnte ein Anrege–Abrege–Mechanismus identifiziert werden. Allgemeiner betrachtet kann eine adäquate Kombination verschiedener Parametrisierungen des elektrischen Feldes dabei helfen, die Kontrollmechanismen einer adaptiv erhaltenen optimalen Pulsform aufzudecken. Ein verbessertes Verständnis molekularer Systeme und ihrer Kontrollierbarkeit rückt dadurch in greifbare Nähe.

Die Fähigkeit, Femtosekunden–Laserpulse beinahe willkürlich formen zu können, eröffnet weitere faszinierende Möglichkeiten jenseits der adaptiven Kontrolle. So ist es mit Hilfe geformter Laserpulse möglich, die Antwort von Quantensystemen auf eine Vielzahl von elektrischen Feldern zu untersuchen. Diese Information kann dazu dienen, Modelle für die Wechselwirkung von Licht und Materie zu erhalten bzw. zu verbessern. In dieser Arbeit wurden Neuronale Netzwerke zur automatischen Erzeugung von Abbildungen verwendet, welche diese Wechselwirkung beschreiben. Diese Methode erwies sich insbesondere für relativ einfache Systeme, nämlich die Erzeugung der zweiten Harmonischen (SHG) und laserinduzierte molekulare Fluoreszenz, als sehr erfolgreich. Neuronale Netzwerke konnten auch erfolgreich auf die Vorhersage von Photoelektronenspektren aus der resonanten Starkfeld–Ionisation von Kaliumatomen angewendet werden. Verglichen mit SHG und molekularer Fluoreszenz ist dieses Modellsystem weitaus komplexer, da der Ausgang des lichtinduzierten Prozesses praktisch von allen Details des Lichtfeldes abhängt. Während die Datenmenge, welche für die Modellierung von Licht–Materie Wechselwirkungen mit dieser Methode benötigt wird, mit der Komplexität der zu modellierenden Korrelationen anwächst, ist dieser Ansatz dennoch vielversprechend, insbesondere für große und/oder wechselwirkende Systeme, bei denen *ab initio* Rechnungen (noch) nicht durchführbar sind.

Zusammenfassend läßt sich sagen, dass diese Arbeit zwei wesentliche Anliegen der Quantenkontrolle vorangebracht hat: zum einen die selektive Kontrolle stereochemischer Reaktionen und zum anderen die Gewinnung von Informationen über Quan-

tensysteme und ihre Wechselwirkung mit Licht. Die erfolgreiche Demonstration der adaptiven Polarisationspulsformung an einem molekularen System, und insbesondere die neuartige Methode zur Erzeugung polarisationsgeformter Laserpulse im UV, sind wichtige Schritte auf dem Weg zur kohärenten Kontrolle chiraler Systeme. Die hier präsentierten systematischen Abtastungen verschiedener Parametrisierungen des elektrischen Feldes und experimentell ermittelte Fitnesslandschaften können zu einem verbesserten Verständnis von Kontrollmechanismen und Reaktionswegen in adaptiven Kontrollexperimenten beitragen. Wie in dieser Arbeit erstmals gezeigt wurde, können Neuronale Netzwerke verwendet werden, um numerische Modelle für Licht–Materie Wechselwirkungen zu erhalten.

Bibliography

- [1] A. H. Zewail.
Femtochemistry.
World Scientific, Singapore (1994).
- [2] A. H. Zewail.
Femtochemistry: Recent progress in studies of dynamics and control of reactions and their transition states.
J. Phys. Chem. **100**, 12701 (1996).
- [3] J. Jortner, R. D. Levine, and S. A. Rice (Eds.).
Photoselective Chemistry, volume 47 of *Advances in Chemical Physics*.
Wiley, New York (1981).
- [4] N. Bloembergen and A. H. Zewail.
Energy redistribution in isolated molecules and the question of mode-selective laser chemistry revisited.
J. Phys. Chem. **88**, 5459–5465 (1984).
- [5] T. Elsaesser and W. Kaiser.
Vibrational and vibronic relaxation of large polyatomic molecules in liquids.
Annu. Rev. Phys. Chem. **42**, 83–107 (1991).
- [6] M. Gruebele and R. Bigwood.
Molecular vibrational energy flow: Beyond the golden rule.
Int. Rev. Phys. Chem. **17**, 91–145 (1998).
- [7] M. Shapiro and P. Brumer.
Principles of the quantum control of molecular processes.
Wiley-Interscience, Hoboken, NJ (2003).
- [8] M. Shapiro and P. Brumer.
Coherent control of molecular dynamics.
Rep. Prog. Phys. **66**, 859–942 (2003).
- [9] P. Brumer and M. Shapiro.
Control of unimolecular reactions using coherent light.
Chem. Phys. Lett. **126**, 541–546 (1986).
- [10] M. Shapiro, J. W. Hepburn, and P. Brumer.

- Simplified laser control of unimolecular reactions: Simultaneous (ω_1 , ω_3) excitation.*
Chem. Phys. Lett. **149**, 451–454 (1988).
- [11] C. Chen, Y.-Y. Yin, and D. S. Elliott.
Interference between optical transitions.
Phys. Rev. Lett. **64**, 507–510 (1989).
- [12] S. M. Park, S. P. Lu, and R. J. Gordon.
Coherent laser control of the resonance-enhanced multiphoton ionization of HCl.
J. Chem. Phys. **94**, 8622–8624 (1991).
- [13] S.-P. Lu, S. M. Park, Y. Xie, and R. J. Gordon.
Coherent laser control of bound-to-bound transitions of HCl and CO.
J. Chem. Phys. **96**, 6613–6620 (1992).
- [14] G. Xing, X. Wang, X. Huang, R. Bersohn, and B. Katz.
Modulation of resonant multiphoton ionization of CH₃I by laser phase variation.
J. Chem. Phys. **104**, 826–831 (1995).
- [15] D. Meshulach and H. Silberberg.
Coherent quantum control of two-photon transitions by a femtosecond laser pulse.
Nature **396**, 239–242 (1998).
- [16] D. Meshulach and H. Silberberg.
Coherent quantum control of multiphoton transitions by shaped ultrashort optical pulses.
Phys. Rev. A **60**, 1287–1292 (1999).
- [17] D. J. Tannor and S. A. Rice.
Control of selectivity of chemical reaction via control of wavepacket evolution.
J. Chem. Phys. **83**, 5013–5018 (1985).
- [18] D. J. Tannor, R. Kosloff, and S. A. Rice.
Coherent pulse sequence induced control of selectivity of reactions: Exact quantum mechanical calculations.
J. Chem. Phys. **85**, 5805–8520 (1986).
- [19] T. Baumert, M. Grosser, R. Thalweiser, and G. Gerber.
Femtosecond time-resolved molecular multiphoton ionization: The Na₂ system.
Phys. Rev. Lett. **67**, 3753–3756 (1991).
- [20] E. D. Potter, J. L. Herek, S. Pedersen, O. Liu, and A. H. Zewail.
Femtosecond laser control of a chemical reaction.
Nature **355**, 66–68 (1992).
- [21] T. Baumert and G. Gerber.

- Fundamental interactions of molecules (Na_2 , Na_3) with intense femtosecond laser pulses.*
Isr. J. Chem. **34**, 103–114 (1994).
- [22] S. L. Logunov, V. V. Volkov, M. Braun, and M. A. El-Sayed.
The relaxation dynamics of the excited electronic states of retinal in bacteriorhodopsin by two-pump-probe femtosecond studies.
PNAC **98**, 8475–8479 (2001).
- [23] C. J. Bardeen, Q. Wang, and C. V. Shank.
Femtosecond chirped pulse excitation of vibrational wave packets in LD690 and bacteriorhodopsin.
J. Phys. Chem. A **102**, 2759–2766 (1998).
- [24] C. J. Bardeen, J. Che, K. R. Wilson, V. V. Yakovlev, C. C. M. V. A. Apkarian, R. Zadoyan, B. Kohler, and M. Messina.
Quantum control of I_2 in the gas phase and in condensed phase solid Kr matrix.
J. Chem. Phys. **106**, 8486–8503 (1997).
- [25] B. Kohler, V. V. Yakovlev, J. Che, J. L. Krause, M. Messina, K. R. Wilson, N. Schwentner, R. M. Witnell, and Y. J. Yan.
Quantum control of wave packet evolution with tailored femtosecond pulses.
Phys. Rev. Letters **74**, 3360–3363 (1995).
- [26] U. Gaubatz, P. Rudecki, M. Becker, S. Schiemann, M. Kulz, and K. Bergmann.
Population switching between vibrational levels in molecular beams.
Chem. Phys. Lett. **149**, 463–468 (1988).
- [27] U. Gaubatz, P. Rudecki, S. Schiemann, and K. Bergmann.
Population transfer between molecular vibrational levels by stimulated Raman scattering with partially overlapping laser fields: A new concept and experimental results.
J. Chem. Phys. **92**, 5363–5376 (1990).
- [28] A. Shi, A. Woody, and H. Rabitz.
Optimal control of selective vibrational excitation in harmonic linear chain molecules.
J. Chem. Phys. **88**, 6870–6883 (1988).
- [29] A. P. Peirce, M. Dahleh, and H. Rabitz.
Optimal control of quantum-mechanical systems: Existence, numerical approximation, and applications.
Phys. Rev. A **37**, 4950–4964 (1988).
- [30] R. Kosloff, S. A. Rice, P. Gaspard, S. Tersigni, and D. J. Tannor.
Wavepacket dancing: Achieving chemical selectivity by shaping light pulses.
Chem. Phys. **139**, 201–220 (1989).
- [31] D. Gerbasi, M. Shapiro, and P. Brumer.
Theory of enantiomeric control in dimethylallene using achiral light.

- J. Chem. Phys. **115**, 5349–5352 (2001).
- [32] E. Frishman, M. Shapiro, D. Gerbasi, and P. Brumer.
Enantiomeric purification of nonpolarized racemic mixtures using coherent light.
J. Chem. Phys. **119**, 7237–7246 (2003).
- [33] S. Bychkov, B. Grishanin, and V. Zadkov.
Laser synthesis of chiral molecules in isotropic racemic media.
J. Exp. Theor. Phys. **93**, 24 (2001).
- [34] L. González, K. Hoki, D. Kroner, A. S. Leal, J. Manz, and Y. Ohtsuki.
Selective preparation of enantiomers by laser pulses: From optimal control to specific pump and dump transitions.
J. Chem. Phys. **113**, 11134–11142 (2000).
- [35] Y. Fujimura, L. González, K. Hoki, D. Kroner, J. Manz, and Y. Ohtsuki.
From a racemate to a pure enantiomer by laser pulses: Quantum model simulations for H₂POSH.
Angewandte Chemie-International Edition **39**, 4586–+ (2000).
- [36] K. Hoki, L. González, and Y. Fujimura.
Quantum control of molecular handedness in a randomly oriented racemic mixture using three polarization components of electric fields.
J. Chem. Phys. **116**, 8799–8802 (2002).
- [37] S. P. Shah and S. A. Rice.
A test of the dependence of an optimal control field on the number of molecular degrees of freedom: HCN isomerization.
J. Chem. Phys. **113**, 6536–6541 (2000).
- [38] R. S. Judson and H. Rabitz.
Teaching lasers to control molecules.
Phys. Rev. Lett. **68**, 1500–1503 (1992).
- [39] S. Kirkpatrick, C. D. Gelatt, and M. P. Vecchi.
Optimization by simulated annealing.
Science **220**, 671–680 (1983).
- [40] D. E. Goldberg.
Genetic Algorithms in Search, Optimization, and Machine Learning.
Addison-Wesley, Reading (1993).
- [41] H.-P. Schwefel.
Evolution and Optimum Seeking.
Wiley, New York (1995).
- [42] V. Seyfried.
Beobachtung und Kontrolle molekularer Dynamik durch Femtosekundenlaserpulse.
Dissertation, Universität Würzburg (1998).

- [43] T. Brixner.
Adaptive Femtosecond Quantum Control.
Dissertation, Universität Würzburg (2001).
- [44] T. Baumert, T. Brixner, V. Seyfried, M. Strehle, and G. Gerber.
Femtosecond pulse shaping by an evolutionary algorithm with feedback.
Appl. Phys. B **65**, 779–782 (1997).
- [45] C. J. Bardeen, V. V. Yakovlev, K. R. Wilson, S. D. Carpenter, P. M. Weber, and W. S. Warren.
Feedback quantum control of molecular electronic population transfer.
Chem. Phys. Lett. **280**, 151–158 (1997).
- [46] D. Yelin, D. Meshulach, and Y. Silberberg.
Adaptive femtosecond pulse compression.
Opt. Lett. **22**, 1793–1795 (1997).
- [47] A. Efimov, M. D. Moores, N. M. Beach, J. L. Krause, and D. H. Reitze.
Adaptive control of pulse phase in a chirped-pulse amplifier.
Opt. Lett. **23**, 1915–1917 (1998).
- [48] T. Brixner, M. Strehle, and G. Gerber.
Feedback-controlled optimization of amplified femtosecond laser pulses.
Appl. Phys. B **68**, 281–284 (1999).
- [49] A. Assion, T. Baumert, M. Bergt, T. Brixner, B. Kiefer, V. Seyfried, M. Strehle, and G. Gerber.
Control of chemical reactions by feedback-optimized phase-shaped femtosecond laser pulses.
Science **282**, 919–922 (1998).
- [50] M. Bergt, T. Brixner, B. Kiefer, M. Strehle, and G. Gerber.
Controlling the femtochemistry of Fe(CO)₅.
J. Phys. Chem. A **103**, 10381–10387 (1999).
- [51] N. H. Damrauer, C. Dietl, G. Krampert, S. H. Lee, K. H. Jung, and G. Gerber.
Control of bond-selective photochemistry in CH₂BrCl using adaptive femtosecond pulse shaping.
EPJ D **103**, 71–76 (2002).
- [52] R. J. Levis, G. M. Menkir, and H. Rabitz.
Selective bond dissociation and rearrangement with optimally tailored, strong-field laser pulses.
Science **292**, 709–713 (2001).
- [53] J. L. Herek, W. Wohlleben, R. J. Cogdell, D. Zeidler, and M. Motzkus.
Quantum control of energy flow in light harvesting.
Nature **417**, 533–535 (2002).
- [54] T. Hornung, R. Meier, and M. Motzkus.

- Optimal control of molecular states in a learning loop with a parameterization in frequency and time domain.*
Chem. Phys. Lett. **326**, 445 (2000).
- [55] T. C. Weinacht, J. L. White, and P. H. Bucksbaum.
Toward strong field mode-selective chemistry.
J. Phys. Chem. A **103**, 10166–10168 (1999).
- [56] G. Vogt, G. Krampert, P. Niklaus, P. Nuernberger, and G. Gerber.
Optimal Control of Photoisomerization.
Phys. Rev. Lett. **94**, 068305 (2005).
- [57] M. Sukharev, E. Charron, and A. Suzor-Weiner.
Quantum control of double ionization of calcium.
Phys. Rev. A **66**, 053407 (2002).
- [58] E. Papastathopoulos, M. Strehle, and G. Gerber.
Optimal control of femtosecond multiphoton double ionization of atomic calcium.
Chem. Phys. Lett. **408**, 65–70 (2005).
- [59] C. Daniel, J. Full, L. González, C. Lupulescu, J. Manz, A. Merli, Š. Vajda, and L. Wöste.
Deciphering the reaction dynamics underlying optimal control laser fields.
Science **299**, 536–539 (2003).
- [60] A. Lindinger, C. Lupulescu, M. Plewicky, F. Vetter, A. Merli, S. M. Weber, and L. Wöste.
Isotope selective ionization by optimal control using shaped femtosecond laser pulses.
Phys. Rev. Lett. **93**, 033001 (2004).
- [61] Š. Vajda, A. Bartelt, E.-C. Kaposta, T. Leisner, C. Lupulescu, S. Minemoto, P. Rosendo-Francisco, and L. Wöste.
Feedback optimization of shaped femtosecond laser pulses for controlling the wavepacket dynamics and reactivity of mixed alkaline clusters.
Chem. Phys. **267**, 231–239 (2001).
- [62] T. Hornung, R. Meier, R. de Vivie-Riedle, and M. Motzkus.
Coherent control of the molecular four-wave-mixing response by phase and amplitude shaped pulses.
Chem. Phys. **267**, 261–276 (2001).
- [63] T. Fuji, A. Apolonski, and F. Krausz.
Self-stabilization of carrier-envelope offset phase by use of difference-frequency generation.
Opt. Lett. **29**, 632 (2004).
- [64] T. Fuji, J. Rauschenberger, A. Apolonski, V. Yakovlev, G. Tempea, T. Udem, C. Gohle, T. Hänsch, W. Lehnert, M. Scherer, and F. Krausz.

- Monolithic carrier-envelope phase-stabilization scheme.*
Opt. Lett. **29**, 632 (2004).
- [65] J. Diels and W. Rudolph.
Ultrashort laser pulse phenomena: fundamentals, techniques, and applications on a femtosecond time scale.
Academic Press (1995).
- [66] P. F. Moulton.
Spectroscopic and Laser Characteristics of Ti:Al₂O₃.
J. Opt. Soc. Am. B **3**, 125–133 (1986).
- [67] D. E. Spence, P. N. Kean, and W. Sibbett.
60 fs pulse generation from a self-mode-locked Ti:sapphire laser.
Opt. Lett. **16**, 42–44 (1991).
- [68] J. M. Hopkins and W. Sibbett.
Ultrashort-pulse lasers: Big payoffs in a flash.
Scientific American **283**, 72–79 (2000).
- [69] D. Strickland and G. Mourou.
Compression of Amplified Chirped Optical Pulses.
Opt. Commun. **56**, 219–221 (1985).
- [70] Y. R. Shen.
The principles of nonlinear optics.
John Wiley & Sons Inc. (1994).
- [71] P. N. Butcher and D. Cotter.
The elements of nonlinear optics.
Cambridge University Press (1990).
- [72] M. Bass, P. A. Franken, J. F. Ward, and G. Weinreich.
Optical rectification.
Phys. Rev. Lett. **9**, 446–448 (1962).
- [73] L. Bergmann and Schaefer.
Optik.
Walter de Gruyter (1993).
- [74] G. Vdovin and P. M. Sarro.
Flexible Mirror Micromachined in Silicon.
Appl. Opt. **34**, 2968–2972 (1995).
- [75] C. W. Hillegas, J. X. Hull, D. Goswami, D. Strickland, and W. S. Warren.
Femtosecond laser pulse shaping by use of microsecond radio-frequency pulses.
Opt. Lett. **19**, 737–739 (1994).
- [76] M. A. Dugan, J. X. Tull, and W. S. Warren.

- High-resolution acousto-optic shaping of unamplified and amplified femtosecond laser pulses.*
J. Opt. Soc. Am. B. **14**, 2348–2358 (1997).
- [77] M. Roth, M. Mehendale, A. Bartelt, and H. Rabitz.
Acousto-optical shaping of ultraviolet femtosecond pulses.
Appl. Phys. B **80**, 441–444 (2005).
- [78] H. Kuck, W. Doleschal, A. Gehner, W. Grundke, R. Melcher, J. Paufler, R. Seltmann, and G. Zimmer.
Deformable micromirror devices as phase-modulating high-resolution light valves.
Sensors and Actuators A-Physical **54**, 536–541 (1996).
- [79] M. Hacker, G. Stobrawa, R. Sauerbrey, T. Buckup, M. Motzkus, M. Wildenhain, and A. Gehner.
Micromirror SLM for femtosecond pulse shaping in the ultraviolet.
Appl. Phys. B **76**, 711–714 (2003).
- [80] M. Hacker, R. Netz, G. Stobrawa, T. Feurer, and R. Sauerbrey.
Frequency doubling of phase-modulated ultrashort laser pulses.
Appl. Phys. B **73**, 273–277 (2001).
- [81] M. Hacker, T. Feurer, R. Sauerbrey, T. Lucza, and G. Szabo.
Programmable femtosecond laser pulses in the ultraviolet.
J. Opt. Soc. Am. B **18**, 866–871 (2001).
- [82] P. Nuernberger, G. Vogt, R. Selle, S. Fechner, T. Brixner, and G. Gerber.
Generation of femtosecond pulse sequences in the ultraviolet by spectral phase modulation.
In J. T. Sheridan and F. Wyrowski (Eds.), Photon Management II, *Proceedings of SPIE*, volume 6187 (2006).
- [83] P. Nuernberger, G. Vogt, R. Selle, S. Fechner, T. Brixner, and G. Gerber.
Generation of shaped ultraviolet pulses at the third harmonic of titanium–sapphire femtosecond laser radiation.
Appl. Phys. B **88**, 519 (2007).
- [84] E. Sidick, A. Dienes, and A. Knoesen.
Ultrashort-Pulse Second-Harmonic Generation. 2. Non-Transform-Limited Fundamental Pulses.
J. Opt. Soc. Am. B **12**, 1713–1722 (1995).
- [85] A. M. Weiner.
Femtosecond pulse shaping using spatial light modulators.
Rev. Sci. Instrum. **71**, 1929 (2000).
- [86] P. Nuernberger.
Formung und Charakterisierung von Femtosekunden-Laserimpulsen im Ultravioletten.

- Diplomarbeit, Universität Würzburg (2004).
- [87] O. E. Martínez.
Matrix formalism for pulse compressors.
IEEE J. Quantum Elec. **24**, 2530–2536 (1988).
- [88] T. Brixner.
Kohärente Kontrolle von Photodissoziationsreaktionen mit optimal geformten ultrakurzen Laserpulsen.
Diplomarbeit, Universität Würzburg (1998).
- [89] A. M. Weiner, D. E. Leaird, A. Patel, and J. R. Wullert.
Programmable shaping of femtosecond optical pulses by use of 128-element liquid-crystal phase modulator.
IEEE J. Quantum Electron. **28**, 908–920 (1992).
- [90] M. M. Wefers and K. A. Nelson.
Analysis of programmable ultrashort waveform generation using liquid-crystal spatial light modulators.
J. Opt. Soc. Am. B **12**, 1343–1362 (1995).
- [91] G. Krampert.
Femtosecond Quantum Control and Adaptive Polarization Pulse Shaping.
Dissertation, Universität Würzburg (2004).
- [92] M. Kakehata, R. Ueda, H. Takada, K. Torizuka, and M. Obara.
Combination of high-intensity femtosecond laser pulses for generation of time-dependent polarization pulses and ionization of atomic gas.
Appl. Phys. B **70**, S207 (2000).
- [93] M. Plewicky, F. Weise, S. M. Weber, and A. Lindinger.
Phase, amplitude, and polarization shaping with a pulse shaper in a MachZehnder interferometer.
Appl. Opt. **45**, 8354 (2006).
- [94] S. M. Weber, F. Weise, M. Plewicky, and A. Lindinger.
Interferometric generation of parametrically shaped polarization pulses.
Appl. Opt. **46**, 5987 (2007).
- [95] S. Fechner.
Aufbau eines Polarisationsimpulsformers zur optimalen Kontrolle chemischer Reaktionen.
Diplomarbeit, Universität Würzburg (2005).
- [96] J. A. Arns, W. S. Colburn, and S. C. Barden.
Volume Phase Holographic Gratings: Polarization Properties and Diffraction Efficiency.
Proc. SPIE **3779**, 31 (1999).
- [97] M. V. Klein and T. E. Furtak.

- Optics*.
Second edition. Wiley, New York (1986).
- [98] A. Gerrard and J. M. Burch.
Introduction to Matrix Methods in Optics.
Wiley, New York (1975).
- [99] *Polarization and Polarization Control*, pp. 1–8.
New Focus (2003).
- [100] R. Trebino, K. W. DeLong, D. N. Fittinghoff, J. N. S. abd M. A. Krumbügel,
and B. A. Richman.
*Measuring ultrashort laser pulses in the time-frequency domain using
frequency-resolved optical gating*.
Rev. Sci. Inst. **68**, 3277–3295 (1997).
- [101] D. Kane and R. Trebino.
*Characterization of arbitrary femtosecond pulses using frequency-resolved
optical gating*.
IEEE J. Quantum Electron. **29**, 571–579 (1993).
- [102] A. Baltuška, M. S. Pshenichnikov, and D. O. Wiersma.
*Second-harmonic generation frequency-resolved optical gating in the
single-cycle regime*.
IEEE J. Quantum Electron. **35**, 459–478 (1999).
- [103] L. Lepetit, G. Chériaux, and M. Joffre.
*Linear techniques of phase measurement by femtosecond spectral
interferometry for applications in spectroscopy*.
J. Opt. Soc. Am. B **12**, 2467–2474 (1995).
- [104] M. Hirasawa, N. Nakagawa, K. Yamamoto, R. Molita, H. Shigekawa, and
M. Yamashita.
*Sensitivity improvement of spectral phase interferometry for direct electric-field
reconstruction for the characterisation of low-intensity femtosecond pulses*.
Appl. Phys. B. Suppl. **74**, 225–229 (2002).
- [105] C. Dorrer and I. A. Walmsley.
*Accuracy criterion for ultrashort pulse characterisation techniques:
application to spectral phase interferometry for direct electric field
reconstruction*.
J. Opt. Soc. Am. B **19**, 1019–1029 (2002).
- [106] M. E. Anderson, L. E. E. de Araujo, E. M. Kosik, and I. A. Walmsley.
The effects of noise on ultrashort-optical-pulse measurement using SPIDER.
Appl. Phys. B. Suppl. **70**, 85–93 (2000).
- [107] C. Dorrer, B. de Beauvoir, C. L. Blanc, S. Ranc, J. P. Rousseau, P. Rousseau,
J. P. Chambaret, and F. Salin.

- Single-shot real-time characterization of chirped-pulse amplification systems by spectral phase interferometry for direct electric-field reconstruction.*
Opt. Lett. **24**, 1644–1646 (1999).
- [108] C. Dorrer.
Implementation of spectral phase interferometry for direct electric-field reconstruction with a simultaneously recorded reference interferogram.
Opt. Lett. **24**, 1432–1434 (1999).
- [109] C. Iaconis and I. A. Walmsley.
Spectral phase interferometry for direct electric-field reconstruction of ultrashort optical pulses.
Opt. Lett. **23**, 1030–1038 (1998).
- [110] L. Li, S. Kusaka, N. Karasawa, R. Morita, H. Shigekawa, and M. Yamashita.
Amplitude and phase characterisation of 5.0fs optical pulses using spectral phase interferometry for direct electric-field reconstruction.
Jap. J. Appl. Phys. **40**, L684–L687 (2001).
- [111] R. Trebino.
Frequency-Resolved Optical Gating: The Measurement of Ultrashort Laser Pulses.
Kluwer Academic Publishers, Boston / Dordrecht / London (2000).
- [112] K. W. DeLong, D. N. Fittinghoff, R. Trebino, B. Kohler, and K. R. Wilson.
Pulse retrieval in frequency-resolved optical gating based method of generalized projections.
Opt. Lett. **19**, 2152–2154 (1994).
- [113] K. W. DeLong and R. Trebino.
Improved ultrashort pulse-retrieval algorithm for frequency-resolved optical gating.
J. Opt. Soc. Am. A **11**, 2429–2437 (1994).
- [114] Femtosoft technologies.
FROG (2004).
- [115] C. Froehly, A. Lacourt, and J. C. Vienot.
Notions de réponse impulsionnelle et de fonction de transfert temporelles des pupilles optiques, justifications expérimentales et applications.
J. Opt. (Paris) **4**, 183 (1973).
- [116] J. Piasecki, B. Colombeau, M. Vampouille, C. Froehly, and J. A. Arnaud.
Nouvelle méthode de mesure de la réponse impulsionnelle des fibres optiques.
Appl. Opt. **19**, 3749 (1980).
- [117] D. N. Fittinghoff, J. L. Bowie, J. N. Sweetser, R. T. Jennings, M. A. Krumbugel, K. W. DeLong, R. Trebino, and I. A. Walmsley.
Measurement of the intensity and phase of ultraweak, ultrashort laser pulses.
Opt. Lett. **21**, 884–886 (1996).

- [118] W. J. Walecki, D. N. Fittinghoff, A. L. Smirl, and R. Trebino.
Characterization of the polarization state of weak ultrashort coherent signals by dual-channel spectral interferometry.
Opt. Lett. **22**, 81 (1997).
- [119] L. Cohen.
Time Frequency-Distributions - A Review.
Proc. IEEE **77**, 941–981 (1989).
- [120] E. Wigner.
On the Quantum Correction For Thermodynamic Equilibrium.
Phys. Rev. **40**, 749–759 (1932).
- [121] S. Mukamel, C. Ciordas-Ciurdariu, and V. Khidekel.
Wigner spectrograms for femtosecond pulse-shaped heterodyne and autocorrelation measurements.
IEEE J. Quantum Electron. **32**, 1278–1288 (1996).
- [122] R. Gase.
Ultrashort-pulse measurements applying generalized time-frequency distribution functions.
JOSA B **14**, 2915 (1997).
- [123] C. E. Heil and D. Walnut.
Continuous and Discrete Wavelet Transforms.
SIAM Review **31**, 628 (1989).
- [124] C. Hirlimann and J. G. Morhange.
Wavelet Analysis of Short Light Pulses.
Applied Optics **31**, 3263 (1992).
- [125] K. Husimi.
Some Formal Properties of the Density Matrix.
Proc. Phys. Math. Soc. Jpn. **22**, 264 (1940).
- [126] S. Fechner, F. Dimler, T. Brixner, G. Gerber, and D. J. Tannor.
The von Neumann picture: a new representation for ultrashort laser pulses.
Opt. Express **15**, 15387 (2007).
- [127] T. Brixner and G. Gerber.
Quantum control of gas-phase and liquid-phase femtochemistry.
ChemPhysChem **4**, 418 (2003).
- [128] C. Altucci, C. Delfin, L. Roos, M. B. Gaarde, A. L'Huillier, I. Mercer, T. Starczewski, and C.-G. Wahlström.
Frequency-resolved time-gated high-order harmonics.
Phys. Rev. A **58**, 3934 (1998).
- [129] D. N. Villeneuve, S. A. Aseyev, P. Dietrich, M. Spanner, M. Y. Ivanov, and P. B. Corkum.

- Forced molecular rotation in an optical centrifuge.*
Phys. Rev. Lett. **85**, 542 (2000).
- [130] P. B. Corkum, N. H. Burnett, and M. Y. Ivanov.
Subfemtosecond pulses.
Opt. Lett. **19**, 1870 (1994).
- [131] M. Y. Ivanov, P. B. Corkum, T. Zuo, and A. D. Bandrauk.
Routes to control of intense-field atomic polarizability.
Phys. Rev. Lett. **74**, 2933 (1995).
- [132] E. Constant, V. D. Taranukhin, A. Stolow, and P. B. Corkum.
Methods for the measurement of the duration of high-harmonic pulses.
Phys. Rev. A **56**, 3870 (1997).
- [133] M. M. Wefers, H. Kawashima, and K. A. Nelson.
Optical control over two-dimensional lattice vibrational trajectories in crystalline quartz.
J. Chem. Phys. **108**, 10248 (1998).
- [134] T. Brixner, N. H. Damrauer, G. Krampert, P. Niklaus, and G. Gerber.
Adaptive shaping of femtosecond polarization profiles.
J. Opt. Soc. Am. B **20**, 878 (2003).
- [135] D. Oron, N. Dudovich, and Y. Silberberg.
Femtosecond phase-and-polarization control for background-free coherent anti-Stokes Raman spectroscopy.
Phys. Rev. Lett. **90**, 213902 (2003).
- [136] T. Brixner, G. Krampert, T. Pfeifer, R. Selle, G. Gerber, M. Wollenhaupt, O. Graefe, C. Horn, D. Liese, and T. Baumert.
Quantum control by ultrafast polarization shaping.
Phys. Rev. Lett. **92**, 208301 (2004).
- [137] T. Suzuki, S. Minemoto, T. Kanai, and H. Sakai.
Optimal Control of Multiphoton Ionization Processes in Aligned I₂ Molecules with Time-Dependent Polarization Pulses.
Phys. Rev. Lett. **92**, 133005 (2004).
- [138] T. Polack, D. Oron, and Y. Silberberg.
Control and measurement of a nonresonant Raman wavepacket using a single ultrashort pulse.
Chem. Phys. **318**, 163 (2005).
- [139] F. Weise, S. M. Weber, M. Plewicky, and A. Lindinger.
Application of phase, amplitude, and polarization shaped pulses for optimal control on molecules.
Chem. Phys. **332**, 313 (2007).
- [140] R. de Vivie-Riedle, B. Reischl, S. Rutz, and E. Schreiber.

- Femtosecond Study of Multiphoton Ionization Processes in K_2 at Moderate Laser Intensities.*
J. Phys. Chem. **99**, 16829 (1995).
- [141] R. de Vivie-Riedle, K. Kobe, J. Manz, W. Meyer, B. Reischl, S. Rutz, E. Schreiber, and L. Wöste.
Femtosecond study of multiphoton ionization processes in K_2 : From pump-probe to control.
J. Phys. Chem. **100**, 7789 (1996).
- [142] S. Rutz, R. deVivieRiedle, and E. Schreiber.
Femtosecond wave-packet propagation in spin-orbit-coupled electronic states of $^{39,39}K_2$ and $^{39,41}K_2$.
Phys. Rev. A **54**, 306 (1996).
- [143] H. Schworer, R. Pausch, M. Heid, V. Engel, and W. Kiefer.
Femtosecond time-resolved two-photon ionization spectroscopy of K_2 .
J. Chem. Phys. **107**, 9749 (1997).
- [144] H. Schworer, R. Pausch, M. Heid, and W. Kiefer.
Femtosecond vibrational wavepacket spectroscopy in the electronic ground state of K_2 .
Chem. Phys. Lett. **285**, 240 (1998).
- [145] R. Pausch, M. Heid, T. Chen, W. Kiefer, and H. Schworer.
Selective generation and control of excited vibrational wave packets in the electronic ground state of K_2 .
J. Chem. Phys. **110**, 9560 (1999).
- [146] C. Nicole, M. A. Bouchene, C. Meier, S. Magnier, E. Schreiber, and B. Girard.
Competition of different ionization pathways in K_2 studied by ultrafast pump-probe spectroscopy: A comparison between theory and experiment.
J. Chem. Phys. **111**, 7857 (1999).
- [147] H. Stapelfeldt and T. Seideman.
Colloquium: Aligning molecules with strong laser pulses.
Rev. Mod. Phys. **75**, 543–557 (2003).
- [148] A. Ulman.
Formation and structure of self-assembled monolayers.
Chem. Rev. **96**, 1533–1554 (1996).
- [149] U. Hefter, G. Ziegler, A. Mattheus, A. Fischer, and K. Bergmann.
Preparation and detection of alignment with high m -selectivity by saturated laser optical pumping in molecular beams.
J. Chem. Phys. **85**, 286 (1986).
- [150] D. P. Pullman, B. Friedrich, and D. R. Herschbach.
Facile alignment of molecular rotation in supersonic beams.
J. Chem. Phys. **93**, 3224 (1990).

- [151] V. Aquilanti, D. Ascenzi, M. de Castro Vitores, and F. P. und D. Cappelletti.
A quantum mechanical view of molecular alignment and cooling in seeded supersonic expansions.
J. Chem. Phys. **111**, 2620 (1999).
- [152] C. J. Gorter.
Zur Interpretierung des Senfbleben-Effektes.
Naturwissenschaften **26**, 140 (1938).
- [153] M. Sinha, C. D. Caldwell, and R. N. Zare.
Alignment of molecules in gaseous transport: Alkali dimers in supersonic nozzle beams.
J. Chem. Phys. **61**, 491 (1974).
- [154] T. Brixner, B. Kiefer, and G. Gerber.
Problem complexity in femtosecond quantum control.
Chem. Phys. **267**, 241 (2001).
- [155] T. Baumert, B. Bühler, R. Thalweiser, and G. Gerber.
Femtosecond spectroscopy of molecular autoionization and fragmentation.
Phys. Rev. Lett. **64**, 733–736 (1990).
- [156] T. Feurer, J. C. Vaughan, and K. A. Nelson.
Spatiotemporal coherent control of lattice vibrational waves.
Science **299**, 374–377 (2003).
- [157] New Focus.
The Berek Polarization Compensator.
- [158] F. J. G. Abajo, T. Brixner, and W. Pfeiffer.
Nanoscale force manipulation in the vicinity of a metal nanostructure.
J. Phys. B **40**, S249 (2007).
- [159] T. Brixner, N. H. Damrauer, P. Niklaus, and G. Gerber.
Photoselective adaptive femtosecond quantum control in the liquid phase.
Nature **414**, 57–60 (2001).
- [160] H. A. Rabitz, M. M. Hsieh, and C. M. Rosenthal.
Quantum optimally controlled transition landscapes.
Science **303**, 1998–2001 (2004).
- [161] H. A. Rabitz, M. Hsieh, and C. Rosenthal.
Optimal control landscapes for quantum observables.
J. Chem. Phys. **124**, 204107 (2006).
- [162] A. Rothman, T. S. Ho, and H. A. Rabitz.
Exploring the level sets of quantum control landscapes.
Phys. Rev. A **73**, 053401 (2006).
- [163] S.-H. Lee, K.-H. Jung, J.-H. Sung, K.-H. Hong, and C. H. Nam.
Adaptive quantum control of DCM fluorescence in the liquid phase.

- J. Chem. Phys. **117**, 9858 (2002).
- [164] A. M. Weiner, D. E. Leaird, G. P. Wiederrecht, and K. A. Nelson.
Femtosecond Pulse Sequences Used for Optical Manipulation of Molecular Motion.
Science **247**, 1317 (1990).
- [165] F. Langhojer, D. Cardoza, M. Baertschy, and T. Weinacht.
Gaining mechanistic insight from closed loop learning control: The importance of basis in searching the phase space.
J. Chem. Phys. **122**, 014102 (2005).
- [166] D. Cardoza, C. Trallero-Herrero, F. Langhojer, H. Rabitz, and T. Weinacht.
Transformations to diagonal bases in closed-loop quantum learning control experiments.
J. Chem. Phys. **122**, 124306 (2005).
- [167] D. Zeidler, S. Frey, K. L. Kompa, and M. Motzkus.
Evolutionary algorithms and their application to optimal control studies.
Phys. Rev. A **64**, 023420 (2001).
- [168] D. Zeidler, S. Frey, W. Wohlleben, M. Motzkus, F. Busch, T. Chen, W. Kiefer, and A. Materny.
Optimal control of ground-state dynamics in polymers.
J. Chem. Phys. **116**, 5231–5235 (2002).
- [169] T. Okada, I. Otake, R. Mizoguchi, K. Onda, S. S. Kano, and A. Wada.
Optical control of two-photon excitation efficiency of α -perylene crystal by pulse shaping.
J. Chem. Phys. **121**, 6386 (2004).
- [170] D. Cardoza, F. Langhojer, C. Trallero-Herrero, O. L. A. Monti, and T. Weinacht.
Changing pulse-shape bases for molecular learning control.
Phys. Rev. A **70**, 053406 (2004).
- [171] A. F. Bartelt, T. Feurer, and L. Wöste.
Understanding optimal control results by reducing the complexity.
Chem. Phys. **318**, 207 (2005).
- [172] W. Wohlleben, T. Buckup, J. L. Herek, and M. Motzkus.
Coherent Control for Spectroscopy and Manipulation of Biological Dynamics.
ChemPhysChem **6**, 850 (2005).
- [173] M. Montgomery, R. Meglen, and N. Damrauer.
General Method for the Dimension Reduction of Adaptive Control Experiments.
J. Phys. Chem. A **110**, 6391 (2006).
- [174] M. Wollenhaupt, A. Präkelt, C. Sarpe-Tudoran, D. Liese, and T. Baumert.

- Quantum control and quantum control landscapes using intense shaped femtosecond pulses.*
J. Mod. Opt. **52**, 2187 (2005).
- [175] M. Wollenhaupt, D. Liese, A. Präkelt, C. Sarpe-Tudoran, and T. Baumert.
Quantum control by ultrafast dressed states tailoring.
Chem. Phys. Lett. **419**, 184 (2006).
- [176] G. Cerullo, C. J. Bardeen, Q. Wang, and C. V. Shank.
High-power femtosecond chirped pulse excitation of molecules in solution.
Chem. Phys. Lett. **262**, 362 (1996).
- [177] C. J. Bardeen, V. V. Yakovlev, J. A. Squier, and K. R. Wilson.
Quantum control of population transfer in green fluorescent protein by using chirped femtosecond pulses.
J. Am. Chem. Soc. **120**, 13023–13027 (1998).
- [178] K. Misawa and T. Kobayashi.
Wave-packet dynamics in a cyanine dye molecule excited with femtosecond chirped pulses.
J. Chem. Phys. **113**, 7546 (2000).
- [179] J. Cao, C. J. Bardeen, and K. R. Wilson.
Molecular π pulses: Population inversion with positively chirped short pulses.
J. Chem. Phys. **113**, 1898–1908 (2000).
- [180] S. Ruhman, B. Hou, N. Friedman, M. Ottolenghi, and M. Sheves.
Following evolution of bacteriorhodopsin in its reactive excited state via stimulated emission pumping.
J. Am. Chem. Soc. **124**, 8854–8858 (2002).
- [181] F. Gai, J. C. McDonald, and P. A. Anfinrud.
Pump-Dump-Probe spectroscopy of bacteriorhodopsin: Evidence for a Near-IR excited state absorbance.
J. Am. Chem. Soc. **119**, 6201–6202 (1997).
- [182] M. Renard, R. Chaux, B. Lavorel, and O. Faucher.
Pulse trains produced by phase-modulation of ultrashort optical pulses: tailoring and characterization.
Optics Express **12**, 473–482 (2004).
- [183] S. H. Ashworth, T. Hasche, M. Woerner, E. Riedle, and T. Elsaesser.
Vibronic excitations of large molecules in solution studied by two-color pump-probe experiments on the 20 fs time scale.
J. Chem. Phys. **104**, 5761–5769 (1996).
- [184] Y. H. Meyer, M. Pittman, and P. Plaza.
Transient absorption of symmetrical carbocyanines.
J. Photochem. Photobio. A **114**, 1–21 (1998).

- [185] P. Nuernberger.
Adaptive Control of Quantum Systems with Femtosecond Laser Pulses.
Dissertation, Universität Würzburg (2007).
- [186] M. Phan and H. Rabitz.
A self-guided algorithm for learning control of quantum-mechanical systems.
J. Chem. Phys. **110**, 34 (1999).
- [187] J. Geremia, E. Weiss, and H. Rabitz.
Achieving the laboratory control of quantum dynamics phenomena using nonlinear functional maps.
Chem. Phys. **267**, 209 (2001).
- [188] J. Hertz, A. Krogh, and R. Palmer.
Introduction to the Theory of Neural Computation.
Perseus Books Group, New York (1991).
- [189] J. A. Freeman and D. M. Skapura.
Neural Networks: Algorithms, Applications, and Programming Techniques (Computation and Neural Systems Series).
Addison–Wesley Longman Publishing Co., Inc., Redwood City (1991).
- [190] D. Patterson.
Künstliche neuronale Netze.
Prentice Hall Verlag GmbH, München (1997).
- [191] P. Nuernberger, G. Vogt, G. Gerber, R. Improta, and F. Santoro.
Femtosecond study on the isomerization dynamics of NK88: I. Ground state dynamics after photoexcitation.
J. Chem. Phys. **125**, 044512 (2006).
- [192] G. Vogt, P. Nuernberger, G. Gerber, R. Improta, and F. Santoro.
Femtosecond study on the isomerization dynamics of NK88: II. Excited state dynamics.
J. Chem. Phys. **125**, 044513 (2006).
- [193] M. Wollenhaupt, V. Engel, and T. Baumert.
Femtosecond laser photoelectron spectroscopy on atoms and small molecules: Prototype Studies in Quantum Control.
Annu. Rev. Phys. Chem. **56**, 25 (2005).
- [194] M. Wollenhaupt, A. Prækelt, C. Sarpe-Tudoran, D. Liese, and T. Baumert.
Quantum control by selective population of dressed states using intense chirped femtosecond laser pulses.
Appl. Phys. B **82**, 183 (2006).
- [195] M. Wollenhaupt, A. Prækelt, C. Sarpe-Tudoran, D. L. T. Bayer, and T. Baumert.
Femtosecond strong-field quantum control with sinusoidally phase-modulated pulses.
Phys. Rev. A **73**, 063409 (2006).

- [196] M. Wollenhaupt, A. Assion, O. Bazhan, C. Horn, D. Liese, C. Sarpe-Tudoran, M. Winter, and T. Baumert.
Control of interferences in an Autler-Townes doublet: Symmetry of control parameters.
Phys. Rev. A. **68**, 015401 (2003).
- [197] N. V. Vitanov, T. Halfman, B. W. Shore, and K. Bergmann.
Laser-induced population transfer by adiabatic passage techniques.
Annu. Rev. Phys. Chem. **52**, 763 (2001).
- [198] E. T. Sleva, I. M. X. Jr., and A. H. Zewail.
Photon locking.
J. Opt. Soc. Am. B **3**, 483 (1985).
- [199] R. Kosloff, A. D. Hammerich, and D. Tannor.
Excitation without demolition: Radiative excitation of ground-surface vibration by impulsive stimulated Raman scattering with damage control.
Phys. Rev. Lett. **69**, 2172 (1992).
- [200] G. Vogt, P. Nuernberger, R. Selle, F. Dimler, T. Brixner, and G. Gerber.
Analysis of femtosecond quantum control mechanisms with colored double pulses.
Phys. Rev. A **74**, 033413 (2006).
- [201] J. C. Shane, V. V. Lozovoy, and M. Dantus.
Search Space Mapping: Getting a Picture of Coherent Laser Control.
J. Phys. Chem. A **110**, 11388 (2006).
- [202] S. H. Autler and C. H. Townes.
Stark effect in rapidly varying fields.
Phys. Rev. **100**, 703 (1955).
- [203] B. W. Shore.
Theory of Coherent Atomic Excitation, Volume 1.
John Wiley & Sons, New York (1990).
- [204] C. Meier and V. Engel.
Interference Structure in the Photoelectron Spectra Obtained from Multiphoton Ionization of Na₂ with a Strong Femtosecond Laser Pulse.
Phys. Rev.Lett. **73**, 3207 (1994).
- [205] M. Wollenhaupt, A. Assion, and T. Baumert.
In: Springer Handbook of Lasers and Optics.
Springer, New York (2007).

Acknowledgements

At this point, I want to emphasize that many people have contributed to this work in one way or the other. Many of the achievements reported in this thesis have been the result of outstanding teamwork and several fruitful collaborations.

I want to thank all the members of ‘Experimentelle Physik I’, especially the ‘Labor B’ crew, for the friendly and cooperative atmosphere that made it a pleasure to work here and that helped to overcome many difficulties and set-backs. In particular I want to thank the following people:

- Prof. Dr. Tobias Brixner for giving me the opportunity to work in this exciting research field, for the freedom to pursue own ideas and projects, for many valuable discussions, for the excellent coordination of the laboratory and of the variety of projects, and for the financial support throughout this thesis,
- Prof. Dr. Gustav Gerber for the opportunity to work in his group, for his enthusiasm for physics, for his encouragement, for the opportunity to visit national and international conferences and summer schools, and also for the financial support,
- Prof. Dr. Thomas Baumert and Dr. Matthias Wollenhaupt for the fruitful collaboration concerning both the polarization shaping experiments on the potassium dimer carried out at the Universität Kassel and the modeling of strong-field dynamics in potassium atoms with neural networks,
- Dr. Gerhard Krampert for the excellent teamwork in the polarization shaping experiments on the potassium dimer, for his expertise in LabView and his machine-shop skills,
- Dr. Christian Horn, Dr. Dirk Liese, Dr. Oksana Graefe, and the rest of the Kassel crew for their essential contributions to the success of the potassium dimer experiment, especially their endurance in achieving stable molecular beam conditions,
- Prof. Dr. Wolfgang Kinzel and Dr. Richard Metzler for the fruitful discussions and their highly appreciated assistance concerning the implementation of neural networks,

- Dr. Gerhard Vogt for his great support concerning experimental tests of the neural network approach, the excellent teamwork in experiments with double pulses and on the dynamics of I_3^- (not shown here), for many valuable discussions, and for much appreciated advice on both professional and private matters,
- Dr. Gerhard Vogt, Dr. Patrick Nürnberger and Frank Dimler for the highly enjoyable teamwork on the analysis of femtosecond quantum control mechanisms with colored double pulses,
- Dr. Patrick Nürnberger for his expertise, ideas and assistance that were essential for the success of the UV polarization shaping experiment, to which Frank Dimler, Florian Langhojer, and Susanne Fechner also contributed,
- Susanne Fechner for the construction and maintenance of the revised polarization pulse shaper setup,
- Tim Bayer from the group of Prof. Dr. Thomas Baumert for the efficient and productive cooperation regarding the modeling of strong-field dynamics in potassium atoms with neural networks,
- Florian Langhojer and especially Dr. Patrick Nürnberger for the diligent and thorough review of earlier versions of this manuscript,
- Frank Dimler, Dr. Gerhard Krampert, Florian Langhojer, Dr. Patrick Nürnberger, Dr. Gerhard Vogt, and Daniel Wolpert for the good cooperation while rebuilding and improving the laser system,
- Ulrike Selig and Alexander Paulus for many enjoyable and helpful conversations and discussions,
- the computer administration team Dr. Christian Dietl, Dr. Patrick Niklaus, Dr. Sandra Dantscher, Dr. Domink Walter, and especially Robert Spitzenfeil, for ensuring the reliable working condition of our computational facilities,
- our technical assistants Monika Seifer, Helga Schwark, and Valentin Bajanov, as well as our secretary Diep Phan for their prompt assistance,
- the staff of the machine shop for the accurate realization of various mechanical parts needed for the experiments,
- my highschool physics teachers, especially Siegfried Hofmann, for awakening and kindling my interest in physics,
- my friends for many joyful hours, and especially for lending an ear or a hand when it was most needed.

Finally, and most important, I want to thank my parents Dietrich and Renate Selle, my sister Ulrike and her husband Armin Dertinger for their unlimited love and faith, and for the invaluable encouragement and support throughout my life in general, and during my studies in particular.

Lebenslauf

Persönliche Daten

Name: Reimer Andreas Selle
Wohnort: Scherenbergstr. 5, 97082 Würzburg
geboren am: 22. Februar 1974 in Hof
Staatsangehörigkeit: deutsch
Familienstand: ledig

Schulausbildung und Zivildienst

09/1980 – 07/1984 Grundschole Geroldsgrün
09/1984 – 07/1993 Gymnasium Naila
Juli 1993 Abitur mit der Gesamtnote 1.1
09/1993 – 11/1994 Zivildienst, Blindeninstitut Würzburg

Studium der Physik

11/1994 - 03/2001 Julius-Maximilians-Universität Würzburg
Diplomarbeit bei Prof. Dr. H. Fraas:
*Produktion und Zweikörperzerfall von Neutralinos:
Effekte CP-verletzender Phasen*

März 2001 Abschluss: Diplom-Physiker
Gesamtnote: *Mit Auszeichnung*

10/1997 - 07/1998 Auslandsstudienjahr an der University of Edinburgh (Schottland)

seit 04/02 Julius-Maximilians-Universität Würzburg
Promotion bei Prof. Dr. T. Brixner

Lehr- und Berufserfahrung, Praktika

- | | |
|--------------------------------------|---|
| 08/1997 - 10/1997 | Sommerstudent am Deutschen Elektronensynchrotron (DESY) in Hamburg, Programmierung von Tools zur Datenauswertung |
| 11/1999 - 07/2000 | Ausarbeitung und Durchführung einer Vorlesung mit dem Thema <i>Gruppen und Symmetrien</i> an der Universität Würzburg |
| 11/1999 - 07/2001
04/2002 - heute | Studien- und promotionsbegleitende Leitung von Übungsgruppen und Praktika |
| 09/2001 - 03/2002 | Wissenschaftlicher Mitarbeiter am DESY in Hamburg, Detektorsimulation |

Würzburg, den 16.11.2007

Reimer Selle